

**Measurement of longitudinal spin asymmetry
in production of muons from W/Z boson decays
in polarized p+p collisions at $\sqrt{s} = 500$ GeV
with the PHENIX detector at RHIC**

Hideyuki Oide
Department of Physics
The University of Tokyo

A thesis submitted for the degree of
Doctor of Science
December 2012

Abstract

Measurement of polarized parton distribution functions (PDF) of the proton is a key experimental knowledge to understand the spin structure of the proton. A measurement of single spin asymmetry of the production cross section of W^\pm/Z bosons in longitudinally polarized proton-proton collision presents a distinctive way to constrain the flavor-separated polarized PDF of quarks of the proton by taking advantage of $V - A$ interactions of weak bosons. This approach is striking to give another measurements of for \bar{u} and \bar{d} quark polarized parton distributions in addition to the existing measurements with semi-inclusive polarized deep inelastic scattering experiments that needs to employ the knowledge about fragmentation functions to interpret the experimental results.

In this thesis, the first measurement of longitudinal spin asymmetries of muon production in W^\pm/Z boson decays in longitudinally polarized proton-proton collisions at $\sqrt{s} = 500$ GeV is presented. The proton-proton collision was produced at the RHIC accelerator, and the data were taken at the PHENIX detector, which covers pseudorapidity region of $-2.2 < \eta < -1.4$ and $1.4 < \eta < 2.4$. A likelihood-based analysis was performed to extract $W^\pm/Z \rightarrow \mu^\pm$ signal. As a result, with using single muon events in $16 < p_T < 60$ GeV/ c the total production cross section of $W^\pm \rightarrow \mu^\pm$ was obtained as

$$\begin{aligned}\sigma(pp \rightarrow W^-) \times \mathcal{BR}(W^- \rightarrow \mu^-) &= 47.8^{+25.0}_{-11.8} \text{ (pb)} \text{ (68 \% C.L.)}, \\ \sigma(pp \rightarrow W^+) \times \mathcal{BR}(W^+ \rightarrow \mu^+) &= 129.5^{+102.0}_{-33.5} \text{ (pb)} \text{ (68 \% C.L.)}\end{aligned}$$

as the combined values of the measurements in two Muon Arms. The major systematic uncertainty comes from MuTr position resolution and the estimation of the shape of hadronic background events at the signal region, and the size of systematic these uncertainties were larger than statistical uncertainty. Still, we conclude that we observed $W^\pm \rightarrow \mu^\pm$ events in the data sample used in this thesis. The above statement is also supported by the result that the obtained cross section was consistent with NLO or higher-order theoretical calculations for both W^+ and W^- .

Following the extraction of $W^\pm/Z \rightarrow \mu^\pm$ signal, we obtained single spin asymmetry of muons from inclusive W^\pm/Z bosons as

$$\begin{aligned}A_L^{\mu^-} &= 0.15^{+0.47}_{-0.47}(\text{stat})^{+0.06}_{-0.06}(\text{sys}) \quad (\eta = -1.72), \\ A_L^{\mu^-} &= 0.35^{+0.46}_{-0.47}(\text{stat})^{+0.16}_{-0.12}(\text{sys}) \quad (\eta = 1.72), \\ A_L^{\mu^+} &= 0.56^{+0.53}_{-0.55}(\text{stat})^{+0.57}_{-0.14}(\text{sys}) \quad (\eta = -1.61), \\ A_L^{\mu^+} &= 0.07^{+0.55}_{-0.54}(\text{stat})^{+0.22}_{-0.11}(\text{sys}) \quad (\eta = 1.61).\end{aligned}$$

The current uncertainty on $A_L^{\mu^\pm}$ is highly dominated by statistics and we need more of data to constrain polarized sea quark PDFs. This is the world first measurement of single spin asymmetry of charged leptons from W^\pm/Z bosons at the given pseudorapidity regions.

Contents

1	Introduction	1
2	Physics Backgrounds	7
2.1	Quantum chromodynamics	7
2.1.1	QCD Lagrangian	7
2.1.2	Asymptotic freedom and color confinement	8
2.2	Parton model	9
2.2.1	Partons	9
2.2.2	Hadron structure functions	10
2.2.3	Validation of the parton model	11
2.3	Fundamental theorems of pQCD	12
2.3.1	Factorization theorem	12
2.3.2	Evolution	13
2.4	Spin structure of the nucleon	15
2.4.1	Polarized DIS	15
2.4.2	Sum rules	16
2.4.3	Determination of polarized quark and antiquark PDFs	16
2.5	Production and decays of W/Z bosons in proton-proton collisions	19
2.5.1	W bosons and Z boson	19
2.5.2	Hadronic production and decays of W/Z bosons	21
2.5.2.1	W boson productions and decays	21
2.5.2.2	Z boson productions and decays	27
2.6	Probing sea quark polarization via W/Z bosons	28
2.6.1	Longitudinal single spin asymmetry	28
2.6.2	Results of $A_L^{\ell\pm}$ at mid-rapidity	31
2.6.3	Impact of $A_L^{\ell\pm}$ on determining polarized PDFs	33
2.6.4	Measurement of $W^\pm/Z \rightarrow \mu^\pm$ at forward rapidity	34
2.6.4.1	Signal distribution	34
2.6.4.2	Backgrounds	35
3	Apparatus	37
3.1	RHIC as a polarized proton collider	37
3.1.1	Polarized Beam source	37
3.1.2	Accelerator complex	37
3.1.3	Control and measurement of polarization	39
3.1.3.1	Siberian Snakes and Spin Rotators	39
3.1.3.2	Polarimetry	40
3.2	PHENIX detector	44
3.2.1	Overview	44
3.2.2	Magnets and hadron absorbers	48

CONTENTS

3.2.3	Detector subsystems	51
3.2.3.1	Muon Identifier (MuID)	51
3.2.3.2	Muon Tracker (MuTr)	53
3.2.3.3	Resistive Plate Chamber (RPC3)	58
3.2.3.4	Beam Beam Counters (BBC)	61
3.2.3.5	Zero Degree Calorimeter (ZDC)	62
3.3	Data taking	63
3.3.1	DAQ	63
3.3.2	Triggers	64
3.3.2.1	Minimum bias triggers (BBCLL1)	66
3.3.2.2	MuIDLL1	66
3.3.2.3	Mutrg-LL1	67
3.3.2.4	Physics triggers for $W^\pm \rightarrow \mu^\pm$	69
3.4	Software and simulation framework	71
4	Reconstruction	73
4.1	Vertex reconstruction with the BBC	73
4.1.1	Conventional BBC reconstruction algorithm	73
4.1.2	Reconstruction of multiple vertices with BBC	74
4.2	Muon Arm tracking	77
4.2.1	MuID road reconstruction	77
4.2.2	MuTr hit reconstructions	78
4.2.3	Track finding	80
4.2.4	Kalman fitting	80
4.2.5	MuID and RPC3 association	81
4.3	Tracking variables	83
5	Data set	87
5.1	Luminosity	87
5.1.1	van der Meer scan	88
5.1.2	Multiple collision correction	89
5.1.3	Bunch-by-bunch fluctuation	91
5.2	Beam polarization	93
5.2.1	Absolute polarization	93
5.2.2	Transverse polarization	93
5.3	Vertex distribution	94
5.4	Overview of the detector status and data quality	95
6	Detector performances	101
6.1	Momentum resolution	101
6.1.1	J/ψ and Υ mass peak	101
6.1.2	Estimation with cosmic rays	102
6.1.3	Direct measurement of the position resolution of MuTr chambers	105
6.2	MuID and MuTr hit efficiencies	106
6.2.1	MuID hit efficiency	106
6.2.1.1	Procedure	106
6.2.1.2	Results	106
6.2.1.3	Crosschecks	108
6.2.2	MuTr hit efficiency	111
6.3	Estimation of trigger efficiencies	114
6.3.1	BBC(novtx) trigger	114
6.3.1.1	Data-driven method	114

6.3.1.2	Simulation	114
6.3.1.3	Multiple collision effect	115
6.3.2	MuID-1D trigger	116
6.3.2.1	Toy MC Simulation	116
6.3.2.2	Adjustment of t_{prob} using BBC trigger data	118
6.3.2.3	Simulation of MuID-1D trigger efficiency	119
6.3.2.4	MuID-1D trigger efficiency estimation with ERT triggers	121
6.3.2.5	Conclusion	121
6.3.3	Mutrg-SG1 trigger	123
6.3.3.1	Estimation with Mutrg simulator	123
6.3.3.2	Mutrg-SG1 trigger efficiency estimation with data	125
6.3.3.3	Luminosity dependence	126
6.4	RPC aefficiency	127
6.4.1	Absolute RPC efficiency estimation with dimuon data	127
6.4.2	Relative RPC efficiency correction using single track data	128
6.5	Tracking efficiency	130
6.5.1	Tuning of the PISA simulation	130
6.5.2	Crosscheck: Relative yield of $J/\psi \rightarrow \mu^+\mu^-$	131
6.5.3	Uncertainty of the absolute tracking efficiency	133
6.6	Effect of vertex distribution on acceptance	133
7	Extraction of $W^\pm/Z \rightarrow \mu^\pm$	135
7.1	Introduction	135
7.2	Topology of $W^\pm \rightarrow \mu^\pm$ signal	137
7.3	Backgrounds	139
7.3.1	Muon backgrounds	139
7.3.2	Hadronic backgrounds	139
7.4	Preselection of $W^\pm/Z \rightarrow \mu^\pm$ candidates	145
7.4.1	Run selection	145
7.4.2	Quality cut	145
7.4.3	Selection of p_T range	146
7.4.4	Likelihood-based preselection	148
7.5	Signal extraction	154
7.5.1	Fitting variables	154
7.5.2	Composing PDFs	154
7.5.3	Extended unbinned maximum likelihood fitting	161
7.5.4	Results	161
7.5.5	Acceptance and efficiency	164
7.5.6	Systematic uncertainties	166
7.5.6.1	Position resolution of MuTr	166
7.5.6.2	PDF of hadronic backgrounds	169
7.5.6.3	Signal shape uncertainty	171
7.5.6.4	Muon background uncertainties	171
7.6	Cross section of $W^\pm \rightarrow \mu^\pm$	173

CONTENTS

8 Measurement of longitudinal single spin asymmetry of $W^\pm/Z \rightarrow \mu^\pm$	177
8.1 Introduction	177
8.2 Dilution factor	179
8.2.1 Signal selection and signal efficiency	179
8.2.2 Final signal candidates	180
8.2.3 Error propagation	180
8.3 Beam polarization	184
8.4 Relative luminosity	184
8.5 Maximum likelihood fitting for spin asymmetry	185
9 Discussion and conclusion	189
9.1 Cross section of $W^\pm \rightarrow \mu^\pm$	189
9.2 $A_L^{\mu\pm}$ measurement	191
9.3 Future prospect	192
9.4 Conclusion	194
A Muon background estimation with dimuon events	197
A.1 Data analysis	197
A.1.1 Triggers	197
A.1.2 Integrated luminosity	197
A.1.3 Cuts	197
A.1.4 Subtraction of combinatorial backgrounds	198
A.1.5 Acceptance and efficiency	198
A.1.5.1 Relative efficiency correction	198
A.2 Simulation	198
A.2.1 General framework	199
A.2.2 Parameterization of mass spectra and notes	199
A.2.2.1 Open charm	199
A.2.2.2 Open bottom	199
A.2.2.3 Drell-Yan + Z^0	200
A.2.2.4 J/ψ , ψ' (Charmonia)	200
A.2.2.5 Upsilon states	200
A.2.3 Effect of Mutrg-SG1 trigger to different physics processes	203
A.3 Fitting of dimuon mass spectrum	204
A.3.1 Procedure	204
A.3.2 Results	206
B Development of Mutrg simulator	207
B.1 Drift of ionized electrons in the gap	207
B.1.1 Selection of arrival time of ionized electrons	207
B.1.2 Time walk, jitter	208
B.2 Hit efficiency	208
B.2.1 GTM tuning	208
B.2.2 LL1 width, AND/OR logic, clustering	209
B.2.3 Trigger Map	209
C Variable distributions for $J/\psi \rightarrow \mu^+\mu^-$ events	211
D Pseudo multiple vertex simulation and DCA_z	213
D.1 Simulation of multiple collision events	213
D.2 DCA_z with multiple vertices	215
D.3 DCA_z afterburner	215

E Determination of unpolarized PDFs	219
E.1 Sum rules	220
E.2 Valence quarks and sea quarks	220
E.3 Electromagnetic DIS	221
E.4 Neutrino DIS	221
E.5 Drell-Yan process	221
E.6 Jet productions	222
E.7 Summary of unpolarized PDFs	222
References	225
List of Figures	229
List of Tables	235
Acknowledgments	237
Index	240

CONTENTS

Chapter 1

Introduction

Baryons are bound states of three quarks. In particular the proton and the neutron (the nucleon) make up the most part of the mass of the matter as the atomic nucleus. Through the history, baryons and nucleons have had essential roles to establish the Standard Model of the particle physics. In the early years of the particle physics, people did not know whether the nucleons have substructure. At first, the proton and the neutron was considered to be the spin-1/2 fundamental particle described by the Dirac equation. Later in the 1930s, the magnetic moment of the proton and the neutron was independently measured and the existence of the anomalous magnetic moment of the nucleons turned out[1]. Particularly the finite magnetic moment of the neutron had been a long-standing problem, since the electric charge of the neutron is zero so that the existence of the magnetic moment should imply the substructural “electric current” inside the nucleons.

In the 1960s, a model to describe baryons and mesons with the spin-1/2 Dirac particles (“quarks”) which have fractional number electric charges as well as the degree of freedom of color charges was proposed by M.Gell-Mann and K.Nishijima[2, 3]. The model describes well – despite its simplicity – to estimate the mass and the magnetic moment of each baryon consistently by assigning particular masses and fractional charges to the constituent three quarks of the baryon. Shortly, development of accelerator technologies achieved direct probings of the substructure of the nucleons by injecting high energy electrons into fixed targets, called as deep inelastic scattering (DIS) experiments. Measurements of differential cross section in electron-nucleon scattering agreed with the model that the injecting electron interacts with the point-like charged particle (“parton”) in the nucleons (Sec. 2.2.1), which predicts the Bjorken scaling, that the differential cross section is universal for the momentum transfer of the scattering Q^2 (Sec. 2.2.3). The Bjorken scaling is an approximate law in the limit that partons are free each other in the nucleons, and actually the breaking of Bjorken scaling was also observed, which implies the dynamical interaction between partons. On the other hand, applying the SU(3) gauge symmetry to the color charges of quarks predicts a strong interaction between quarks mediated by gluons and gluon-gluon interactions, known as quantum chromodynamics (QCD) (Sec. 2.1). The QCD theory predicts the breaking of Bjorken scaling as described by DGLAP evolution equations (Sec. 2.3.2), and the experimental data agreed well with the DGLAP equation. This strongly justified the QCD theory with the direct observation of gluons in electron-positron colliders as a 3-jet events. The parton distribution function (PDF) was calculated from DIS experiments, which showed the valence quarks convey only about 1/3 of the total momentum of the nucleon, and the others are carried by gluons and sea quarks. The successful determination of parton distribution functions of the proton enabled us to calculate the cross section of hard process such as Drell-Yan process in proton-proton collisions with the foundation of the factorization theorem (Sec. 2.3.1). The parton model founded the base of hadron colliders to predict the

CHAPTER 1. INTRODUCTION

cross section of hard processes such as W/Z bosons, t -quark, Higgs production and so forth, and its contribution to the establishment of the Standard Model is enormous.

Spin of the nucleon The quark model, the QCD as the dynamics between quarks and gluons, and the empirical parton distribution of quarks and gluons have achieved to describe the high energy interaction of the nucleons. On the contrary, the spin structure of the nucleon is not fully understood. The spin structure of the nucleons seemed simple at first. In the constituent quark model, the spin-up state of the proton is described as

$$p^\uparrow = \sqrt{\frac{1}{18}} [u^\uparrow u^\downarrow d^\uparrow + u^\downarrow u^\uparrow d^\uparrow - 2u^\uparrow u^\uparrow d^\downarrow + (\text{permutations})] . \quad (1.1)$$

In the representation above, the expectation value of the magnetic moment of the proton at the non-relativistic limit is given as

$$\mu_p = \frac{4}{3}\mu_u - \frac{1}{3}\mu_d \quad (1.2)$$

where μ_p , μ_u , μ_d is the magnetic moment of the proton, u -quark, d -quark, respectively. Similarly the magnetic moment of the neutron is given as

$$\mu_n = \frac{4}{3}\mu_d - \frac{1}{3}\mu_u \quad (1.3)$$

by taking the isospin symmetry between the proton and the neutron. If we assume that quarks are spin-1/2 Dirac particles and that the effective mass of u -quark and d -quark as $m_u \approx m_d \approx 330 \text{ MeV}/c^2$, we obtain the proper estimation of the absolute value of magnetic moment of the proton and the neutron, and the relative fraction of the magnetic moment of the neutron to the proton to be -2/3. This constituent model is also applicable for other baryons including strange hyperons.

In parallel to the case of the magnetic moment calculation, in the constituent quark model the spin of the proton is calculated as

$$\left(\frac{1}{2}\right)_p = \frac{1}{2} \left[\left(\frac{4}{3}\right)_u + \left(-\frac{1}{3}\right)_d \right] \quad (1.4)$$

which means the (two) u -quarks carry 4/3 of the spin of the proton, and the d -quark carries -1/3 of the spin of the proton. Despite the constituent quark model does not take into account of the dynamics in the nucleons, it seemed the above prediction about the nucleon spin that the sum of the spin of constituent valence quarks equals the total spin of the nucleon was somewhat persuasive at least the first guess, since the estimation of the magnetic moment of the nucleons is successful.

The first determination of the contribution of the spin of quarks to the spin of the nucleons was performed by measuring the spin asymmetry in a polarized DIS experiment in 1988 at CERN, called European Muon Collaboration (EMC) [15, 16]. In a deep inelastic scattering of a longitudinally polarized charged lepton beam and a longitudinally polarized nucleon with a virtual photon, because of the polarization of the virtual photon the helicity of the quarks allowed to couple with is restricted. If there is a correlation between the polarization of the nucleon and the polarization of quarks, we observe a double spin asymmetry A_{LL} by flipping the direction of the polarization of the target nucleons:

$$A_{LL} = \frac{d\sigma_{\leftarrow\leftarrow} - d\sigma_{\leftarrow\rightarrow}}{d\sigma_{\leftarrow\leftarrow} + d\sigma_{\leftarrow\rightarrow}} \quad (1.5)$$

where $d\sigma$ is the differential cross section, and the first single arrow, the second double arrow in the index denotes the direction of the polarization of the charged lepton beam, the direction of the polarization of the target nucleons, respectively. Phenomenologically the description of unpolarized DIS cross section is possible with two hadron structure functions $F_1(x, Q^2)$, $F_2(x, Q^2)$ where x is the Bjorken- x and the Q^2 is the momentum transfer of the scattering charged lepton. In the polarized DIS case generally we need additional two polarized hadron structure functions $g_1(x, Q^2)$, $g_2(x, Q^2)$. By measuring the double spin asymmetry above, we can access to $g_1(x, Q^2)$. Considering the gluon does not couple with photons since it is neutral, the polarized DIS experiment is only sensitive to quarks and anti-quarks. $g_1(x, Q^2)$ is described with the sum of the polarized quark and anti-quark PDFs:

$$g_1(x, Q^2) = \frac{1}{2} \sum_f e_f^2 [\Delta q_f(x, Q^2) + \Delta \bar{q}_f(x, Q^2)] \quad (1.6)$$

where the index f denotes the flavor of the quarks ($f = u, d, s$), and e_f is the electric charge of the quark flavor, and Δq_f , $\Delta \bar{q}_f$ is the polarized PDF of quark and anti-quark of the flavor f , respectively. By measuring $g_1(x, Q^2)$ for the proton and the neutron separately and by assuming the polarized PDF is isospin symmetric between $u \leftrightarrow d$ exchange, one can obtain the polarized PDF of the sum of $(\Delta u + \Delta \bar{u})$ and $(\Delta d + \Delta \bar{d})$ respectively. Ignoring the small Q^2 -dependence, the total spin contribution of the quarks in the proton is given as

$$\Delta \Sigma \equiv \int_0^1 dx \sum_{f=u,d,s} [\Delta q_f(x) + \Delta \bar{q}_f(x)] . \quad (1.7)$$

The EMC experiment (1988) was the polarized DIS experiment to give the first result of the measurement of the polarization of the quarks, and what the collaboration reported was $\Delta \Sigma$ is obviously small compared to the total spin of the proton. At the latest knowledge, $\Delta \Sigma$ is measured as $\simeq 0.25$, meaning that the sum of quark and anti-quark spin covers about 25 % of the total spin of the proton. The result of the EMC experiment triggered lots of theoretical and experimental developments since then in this field, because the result was astonishing¹ compared with the consequence of the constituent quark model of Eq (1.4). However, it has not been established to clearly relate the dynamical polarized PDFs obtained from large- Q^2 scattering and the static constituent quark model. In the modern viewpoint, it is considered that the spin of the proton is composed of not only quarks and anti-quarks, but also gluons and relative orbital angular momenta between quarks:

$$\begin{aligned} \frac{1}{2} &= \frac{1}{2} \Delta \Sigma + \Delta G + L_q \\ &= \frac{1}{2} \int_0^1 dx \sum_{f=u,d,s} [\Delta q_f(x) + \Delta \bar{q}_f(x)] + \int_0^1 dx \Delta g(x) + L_q, \end{aligned} \quad (1.8)$$

where ΔG denotes the sum of the spin from the contribution of gluons, L_q is the sum of the relative orbital angular momenta between quarks and anti-quarks. At present, the polarized PDF of the sum of $u(d)$ -quark and anti- $u(d)$ -quark is relatively determined well by polarized DIS experiments. On the other hand, differentiating anti-quark polarized PDFs from quark polarized PDFs has much larger uncertainties, and this is the main topic of this thesis. For the gluon polarized PDF, longitudinally polarized proton-proton collisions at RHIC has started to constrain it. The orbital angular momenta of quarks has never been measured yet, but it is considered to take vast data of deep virtual Compton scattering (DVCS) to measure the total angular momenta of quarks J_q and subtract the quark spin $\Delta \Sigma/2$ to obtain L_q in the future.

¹The result of the EMC experiment is sometimes called as “the spin crisis”.

Production of W bosons in proton-proton collisions In polarized DIS experiments only the scattered charged leptons are measured, it is essentially impossible to differentiate $\Delta u(x)$ from $\Delta \bar{u}(x)$, or $\Delta d(x)$ from $\Delta \bar{d}(x)$. There is an extended method of polarized DIS called as semi-inclusive DIS (SIDIS), where a charged hadron is measured in addition to the scattered charged lepton:

$$\ell + p \rightarrow \ell + h^\pm + X \quad (1.9)$$

where h^\pm denotes π^\pm or K^\pm . In polarized SIDIS experiments it is possible to differentiate quark polarized PDFs from anti-quark polarized PDFs, as well as $s(\bar{s})$ -quark polarized PDFs via K^\pm . At present, constraints on the anti-quark polarized PDFs rely on the result of polarized SIDIS experiments. To interpret the results of polarized SIDIS experiments, it is necessary to employ the knowledge of the fragmentation functions which describe how the final-state partons decay to hadrons. However, the current global analysis result highly depends on which fragmentation function analysis result to employ: the determination of anti-quark polarized PDFs are sensitive to the knowledge of the fragmentation functions. For this reason, current uncertainties of the anti-quark polarized PDFs by SIDIS data are limited by the uncertainties of the fragmentation functions.

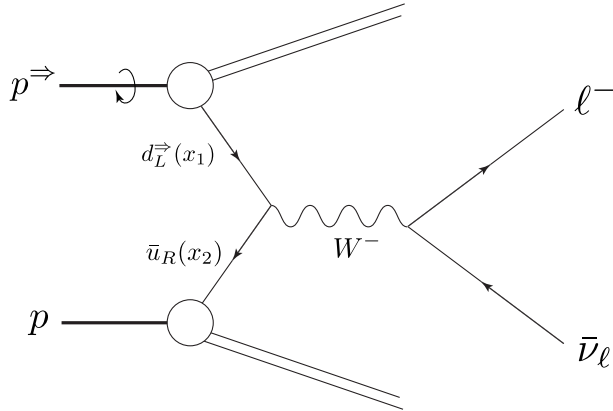


Figure 1.1: A Feynman diagram to produce $W^- \rightarrow \ell^- \bar{\nu}_\ell$ in $p^> + p$ collisions.

Another way to constrain the anti-quark polarized PDFs is to use the production of W bosons in proton-proton collisions. W bosons are weak interacting particles which couple with a different-flavor quark-anti-quark pair in the production at proton-proton collisions. Let us suppose the case that one of the two protons in the collision is longitudinally polarized, and the other one is unpolarized and they collide to produce W^- boson. As the W^- boson couples with only left-handed particles, if we neglect the small contribution from s -quark terms, the differential cross section of W^- production is written as

$$d\sigma(p^>p \rightarrow W^-) \equiv d\sigma^> \propto d_-^>(x_1)\bar{u}_+(x_2) + \bar{u}_+^>(x_1)d_-(x_2) \quad (1.10)$$

where \Rightarrow denotes the positive helicity state of the polarized proton, $x_1(x_2)$ is Bjorken- x of the parton coupled with W^- from polarized (unpolarized) proton. $d(x)$, $\bar{u}(x)$ is the parton distribution function of each flavor, and the index \pm denotes the probability to find helicity positive and negative state, respectively. Here the massless limit of the quarks is assumed, i.e. the helicity state and the chirality state is identical. If we flip the direction of polarization of the proton the helicity state becomes negative, and the differential cross section becomes

$$d\sigma(p^<p \rightarrow W^-) \equiv d\sigma^< \propto d_-^<(x_1)\bar{u}_+(x_2) + \bar{u}_+^<(x_1)d_-(x_2) . \quad (1.11)$$

The longitudinal single spin asymmetry is defined as

$$A_L^{pp \rightarrow W^-} \equiv \frac{d\sigma^{\Rightarrow} - d\sigma^{\Leftarrow}}{d\sigma^{\Rightarrow} + d\sigma^{\Leftarrow}} = \frac{-\Delta d(x_1)\bar{u}_+(x_2) + \Delta\bar{u}(x_1)d_-(x_2)}{d(x_1)\bar{u}_+(x_2) + \bar{u}(x_1)d_-(x_2)} \quad (1.12)$$

where $\Delta q(x) \equiv q_+^{\Rightarrow}(x) - q_+^{\Leftarrow}(x) = q_-^{\Leftarrow}(x) - q_-^{\Rightarrow}(x)$ ($q = d, \bar{u}$) is the polarized PDF. The longitudinal single spin asymmetry A_L does not vanish in the weak interaction as a consequence of parity violating $V - A$ coupling. Thus measurement of $A_L^{pp \rightarrow W^-}$ can constrain the polarized PDFs $\Delta d(x)$ and $\Delta\bar{u}(x)$. Similarly, measurement of $A_L^{pp \rightarrow W^+}$ can constrain the polarized PDFs $\Delta u(x)$ and $\Delta\bar{d}(x)$. In this measurement, we do not need to rely on fragmentation function to extract polarized PDFs. This is the motivation to measure the longitudinal spin asymmetry of W boson production in proton-proton collisions.

The RHIC accelerator is the unique facility to collide polarized protons in the world up to the center of mass energy (\sqrt{s}) of 510 GeV. One of the two large detectors at RHIC, the PHENIX detector (Figure 1.2) was used to take the data in this thesis. The PHENIX has ability to measure W bosons with either electron decay or muon decay, however it is impossible to reconstruct W bosons fully due to lacking ability to measure missing energy. Alternately we measure the A_L of single muons or single electrons from W boson decays. In this thesis, the single muon decay channel was analyzed. The acceptance of muon detectors in PHENIX is forward/backward rapidity regions, which are rather important kinematic regions to constrain polarized PDFs. On the other hand we must also include muons from Z boson decays as the signal because of the limited acceptance of muon detectors. The result presented in this thesis is the first measurement of A_L of muons from W/Z decays in the world based on the data amount of 25 pb^{-1} at $\sqrt{s} = 500 \text{ GeV}$ taken in year 2011 runs, and it is the first measurement of A_L of leptons from W/Z decays at the forward/backward rapidity regions.

Organization of the thesis In Chapter 2, the theoretical and experimental backgrounds of (un)polarized PDFs and the kinematics of $W^\pm/Z \rightarrow \mu^\pm$ in proton-proton collisions are described. Next, the RHIC accelerator and the PHENIX detector systems are described in Chapter 3 as well as data taking, triggering, and softwares/simulations. Event reconstructions are described in Chapter 4. In Chapter 5, overview of the data set and its quality are described. Chapter 6 treats various analyses about detector performances. Chapter 7 describes the main analysis about extracting muons from W/Z bosons. Following the cross section measurement the spin asymmetries are measured in Chapter 8. Chapter 9 is the conclusion of the thesis.

CHAPTER 1. INTRODUCTION

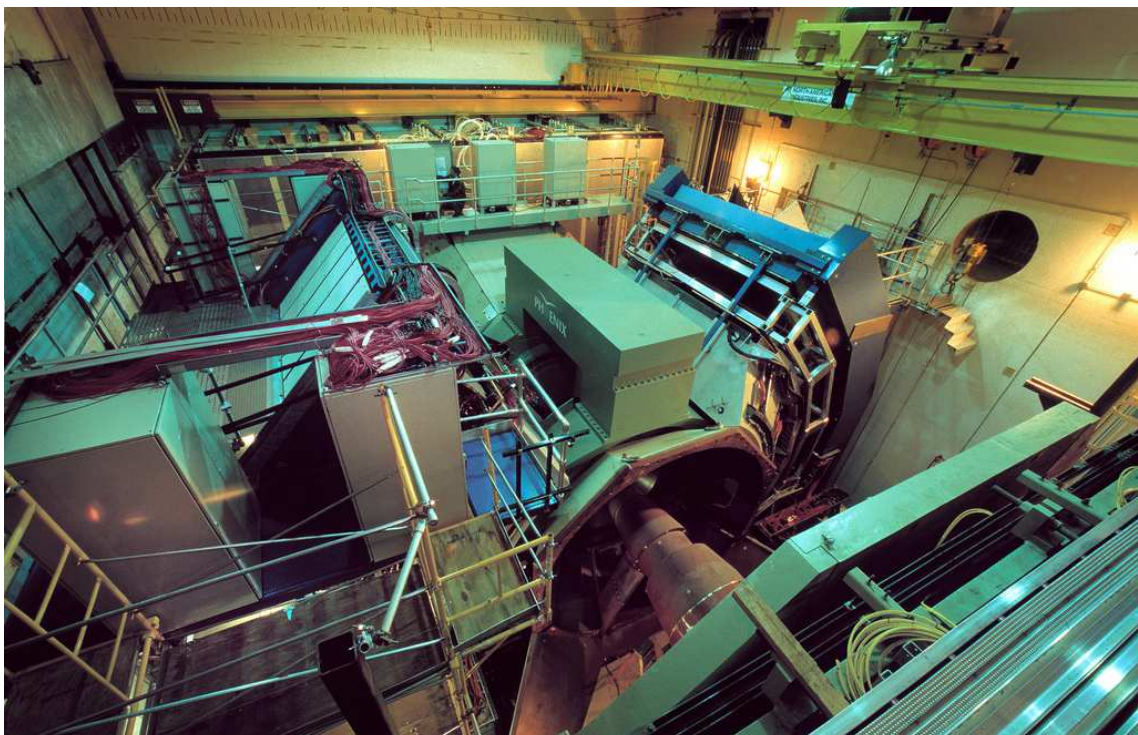


Figure 1.2: The PHENIX detector.

Chapter 2

Physics Backgrounds

2.1 Quantum chromodynamics

2.1.1 QCD Lagrangian

The quantum chromodynamics (QCD) is a non-Abelian gauge theory of color SU(3). The QCD Lagrangian is

$$\mathcal{L}_{\text{QCD}} = \sum_f \bar{\psi}_f (i\gamma^\mu D_\mu - m_f) \psi_f - \frac{1}{4} F_{a\mu\nu} F_a^{\mu\nu} \quad (2.1)$$

where the index a is summed over the generators of the SU(3) gauge group, and the fermion multiplet ψ_f has three irreducible degrees of freedom of colors. The field tensor $F_a^{\mu\nu}$ is

$$F_a^{\mu\nu} = \partial^\mu A_a^\nu - \partial^\nu A_a^\mu - g f_{abc} A_b^\mu A_c^\nu \quad (2.2)$$

where g is the SU(3) gauge coupling. Experimentally the gauge coupling g is related with the coupling constant of strong interaction α_s as $\alpha_s = g^2/4\pi$ in the convention of $\hbar = c = 1$. f_{abc} is the structure constants of SU(3) group generators T^a as

$$[T_a, T_b] = i f_{abc} T_c, \quad (2.3)$$

and D_μ is the covariant derivative defined by

$$D_\mu = \partial_\mu - ig A_a^\mu t_r^a \quad (2.4)$$

where t_r^a is the representation matrices of the SU(3) group. If we write out the nonlinear terms of the QCD Lagrangian, we obtain the vertices between fermions (quarks) and gauge fields (gluons):

$$\mathcal{L}_{\text{QCD}} = \mathcal{L}_{\text{free}} + g A_\mu^a \bar{\psi} \gamma^\mu t^a \psi - g f_{abc} (\partial_\mu A_\nu^a) A^{b\mu} A^{c\nu} = \frac{1}{4} g^2 (f^{eab} A_\mu^a A_\nu^b) (f^{ecd} A^{c\mu} A^{d\nu}) \quad (2.5)$$

where the first term $\mathcal{L}_{\text{free}}$ is the free field Lagrangian. The first nonlinear term is the quark-gluon vertex, the second is the gluon three-point vertex, and the third is the gluon four-point vertex, as shown in Figure 2.1. In contrast to quantum electrodynamics, the gauge field couples with itself in non-Abelian gauge theories.

Concrete calculations of Feynman diagrams in QCD such as $qq \rightarrow qq$ with the original Lagrangian (2.1) face a problem to produce unphysical states of time-like and longitudinal polarized gauge bosons, related with the additional degree of freedom compared with QED

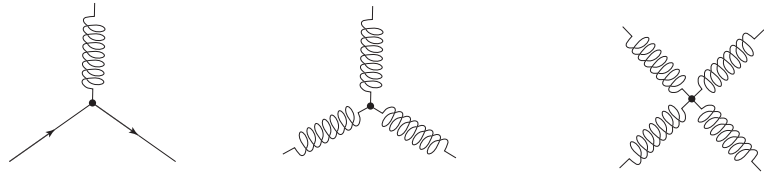


Figure 2.1: Couplings appearing in SU(3) QCD.

coupled with gauge-fixing. To avoid this situation we need to add additional terms to the original QCD Lagrangian which have negative degree of freedom to cancel out the unphysical states. The usual treatment is to introduce Faddeev-Popov ghost term as well as gauge-fixing term:

$$\mathcal{L}_{\text{ghost}} = \bar{c}^a (\partial^2 \delta^{ac} - g \partial^\mu f^{abc} A_\mu^b) c^c, \quad (2.6)$$

$$\mathcal{L}_{\text{gauge}} = -\frac{\lambda}{2} \sum_a (\partial_\mu A^{a\mu}), \text{ where } 1 \leq \lambda < \infty. \quad (2.7)$$

The gauge-fixing term is specifically called “covariant” gauges and taking $\lambda = 1$ is called Feynman gauge. Note that the gauge-fixing term has some arbitrariness. Another option of the gauge-fixing is called “axial” or “physical” gauge.

2.1.2 Asymptotic freedom and color confinement

As a consequence of discussions of renormalization, the effective coupling of a gauge theory differs by the scale of the interaction Q^2 , called as *running* coupling constant. The balance of how the coupling constant changes with the scale Q^2 is governed by the so-called β function as

$$\frac{\partial}{\partial \log(Q^2/M^2)} g = \beta(g). \quad (2.8)$$

The formula of β function depends on the structure of the gauge group. In $SU(N)$ non-Abelian gauge theory with fermions, the β function is given as

$$\beta(g) = -\frac{g^3}{(4\pi)^2} \left(\frac{11}{3}N - \frac{2}{3}n_f \right) \quad (2.9)$$

where n_f is the number of flavors which relate with the loop interaction in the given scale. As the number of flavors in the nature is less than 16, the β function of the QCD ($N = 3$) is negative. This results in that the coupling constant of the QCD becomes small as Q^2 increases. This phenomenon is referred as “asymptotic freedom.” The explicit formula of the running of α_s is then

$$\alpha_s(Q^2) = \frac{12\pi}{(33 - 2n_f) \log(Q^2/\Lambda_{\text{QCD}}^2)} \quad (2.10)$$

at the lowest order where Λ_{QCD} is called the renormalization scale, and is experimentally chosen to set the scale where the coupling is sufficiently strong. Typically Λ_{QCD} is the order of 200 MeV and is an indicator to separate the scale where perturbative QCD calculation works or not. In other words, Λ_{QCD} determines the characteristic size of hadrons.

The asymptotic freedom of the QCD coupling constant means the binding of two quarks by gluons becomes large when Q^2 is small (soft). Qualitatively this explains why the color charged particle is not observed directly: for example, if the distance of the quark and the antiquark of

a meson becomes larger, the potential becomes large enough to create a quark-antiquark pair (meson). Similar thing can be said for gluons. If we create a high energy quark or gluon, that will create lots of mesons as the final state, which is recognized as jets. This process is called hadronization. As a result, all hadrons we observe does not have any color charges, and this phenomenon is called “color confinement.”

2.2 Parton model

2.2.1 Partons

Baryons are bound states of three quarks (qqq) coupling with each other via gluons and virtual quark pairs. Essentially baryons are particles as a result of color confinement, and to describe baryons “as they are”, we need to consider all soft processes of QCD interaction, which is not calculable with perturbative field theory¹. Still, if we treat phenomena which are enough “hard”, namely the interaction scale is larger than roughly $\mathcal{O}(1 \text{ GeV})$, the perturbative QCD (pQCD) provides reliable calculations.

Experimentally it is possible to “probe” the substructure of the proton or the neutron by hammering quarks or gluons with hard scattering processes. Deep inelastic scattering (DIS) is classical one of them which high energy electrons or muon beams are injected into proton or neutron targets. Let us think of electron-proton scattering. In this case the injecting electron scatters with a charged constituent via virtual photon with momentum transfer Q^2 . Typically we consider the case which the center of mass energy of the system (\sqrt{s}) is sufficiently larger than the proton mass, and we set the frame that the electron and the proton collide head-on, and that the momenta of the constituents of the proton are almost collinear with the momentum of the proton. With these assumptions, a constituent receives a sizable transverse momentum only with the hard scattering process with the probing electron. The fraction of momentum of the interacting constituent with the electron to the momentum of the proton varies between 0 to 1, and let us call this fraction x . Every time of the scattering the fraction x is different, and we can think of the probability to find the constituent f has the momentum fraction x as $\phi_f(x, Q^2)dx$. The functions $\phi_f(x, Q^2)$ are called parton distribution functions (PDFs). If we sum up all of the momentum fractions carried by partons, that should be equal to the momentum of the proton. Thus PDFs satisfy the condition

$$\sum_f \int_0^1 x\phi_f(x, Q^2)dx = 1 \quad (2.11)$$

where the sum over f means summing up all contributions of the constituents (partons). The PDFs are determined by soft QCD quark and gluon processes in the proton, and are not calculated with the pQCD. Therefore PDFs should be determined by experiments. The parton model is a heuristic picture of hadron structures, but is fairly effective to describe hard hadronic processes. By using above notations, the cross section of the electron-proton scattering is given to leading order in α_s as

$$\sigma(e(k) + p(P) \rightarrow e(k') + X) = \int_0^1 dx \sum_f \phi_f(x, Q^2) \cdot \sigma(e(k) + f(xP) \rightarrow e(k') + f(p')) . \quad (2.12)$$

The above equation separates the “hard” elastic process of $e + f \rightarrow e + f$ and the “soft” partonic structure in the PDFs. This separation is called as *factorization*. Note that Eq. (2.12) is only the first term of an expansion in α_s . If we include the higher order QCD corrections to Eq. (2.12), not only the “hard” part correction but PDFs are needed to be corrected.

¹One powerful tool to solve QCD without perturbation is lattice QCD.

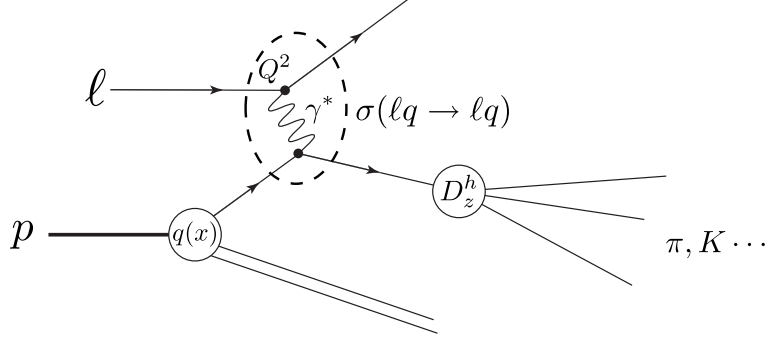


Figure 2.2: Deep inelastic scattering in charged lepton-proton scattering.

2.2.2 Hadron structure functions

Thinking of inclusive longitudinally (un)polarized electron-proton scattering $e^{(\rightarrow)} + p^{(\Rightarrow)} \rightarrow e+X$ via virtual photon exchange where X can be anything, it is phenomenologically possible to describe the cross section with a general formula of electromagnetic current-current interaction. Consider the interaction in the rest frame of the proton, and let the initial and final electron momenta and spins be $(k^\mu, s) = (E, \mathbf{k}, s)$ and $(k'^\mu, s') = (E', \mathbf{k}', s')$, respectively. Suppose the momentum and spin of the proton is $(P^\mu, \mathcal{S}) = (M, \mathbf{0}, \mathcal{S})$, then the differential cross section is written as

$$\frac{d\sigma}{d\Omega dE'} = \frac{\alpha^2}{2Mq^4} \frac{E'}{E} L_{\mu\nu} W^{\mu\nu} \quad (2.13)$$

where α is the electromagnetic coupling constant, and $q^2 \equiv (k - k')^2$ is the momentum transfer and

$$L_{\mu\nu} = [\bar{u}(k', s') \gamma_\mu u(k, s)]^* [\bar{u}(k', s') \gamma_\nu u(k, s)] \quad (2.14)$$

is called lepton tensor. Usually the spin of final state electrons are not measured, thus by taking the average of the spin of the final state electron, the lepton tensor becomes

$$L_{\mu\nu}(k, s; k') = 2 [L_{\mu\nu}^S(k; k') + iL_{\mu\nu}^A(k, s; k')] \quad (2.15)$$

where

$$L_{\mu\nu}^S = k_\mu k'_\nu + k'_\mu k_\nu - g_{\mu\nu}(k \cdot k' - m^2) \quad (2.16)$$

$$L_{\mu\nu}^A = m\epsilon_{\mu\nu\rho\sigma}s^\rho(k - k')^\sigma. \quad (2.17)$$

The corresponding hadron tensor $W^{\mu\nu}$ can generally be described (under the parity conservation) with four structure functions as

$$W_{\mu\nu}(q, P) = W_{\mu\nu}^S(q; P) + iW_{\mu\nu}^A(q; P, \mathcal{S}) \quad (2.18)$$

with

$$\begin{aligned} \frac{1}{2}W_{\mu\nu}^S(q; P) &= \left(-g_{\mu\nu} + \frac{q_\mu q_\nu}{q^2} \right) W_1(P \cdot q, q^2) \\ &\quad + \left[\left(P_\mu - \frac{P \cdot q}{q^2} q_\mu \right) \left(P_\nu - \frac{P \cdot q}{q^2} q_\nu \right) \right] \frac{W_2(P \cdot q, q^2)}{M^2} \end{aligned} \quad (2.19)$$

$$\frac{1}{2}W_{\mu\nu}^A(q; P, \mathcal{S}) = \epsilon_{\mu\nu\rho\sigma} q^\rho \left\{ M\mathcal{S}^\sigma G_1(P \cdot q, q^2) + [(P \cdot q)\mathcal{S}^\sigma - (\mathcal{S} \cdot q)P^\sigma] \frac{G_2(P \cdot q, q^2)}{M} \right\}. \quad (2.20)$$

$L_{\mu\nu}^S$, $W_{\mu\nu}^S$ are both spin-independent symmetric terms and asymmetric $L_{\mu\nu}^A$, $W_{\mu\nu}^A$ depends on spin of the electron and the proton, respectively. Then the differential cross section becomes

$$\frac{d\sigma}{d\Omega dE'} = \frac{\alpha^2}{Mq^4} \frac{E'}{E} [L_{\mu\nu}^S W^{S\mu\nu} - L_{\mu\nu}^A W^{A\mu\nu}] . \quad (2.21)$$

It is of the convention to use the following notations:

$$F_1 \equiv M W_1(P \cdot q, q^2) \quad (2.22)$$

$$F_2 \equiv \nu W_2(P \cdot q, q^2) \quad (2.23)$$

and

$$g_1(x, Q^2) \equiv \frac{(P \cdot q)^2}{\nu} G_1(P \cdot q, q^2) \quad (2.24)$$

$$g_2(x, Q^2) \equiv \nu(P \cdot q) G_2(P \cdot q, q^2) . \quad (2.25)$$

where $\nu \equiv E - E'$. $F_{1,2}$, $g_{1,2}$ are functions of $P \cdot q$ and q^2 , but we can also describe them as functions of x_B and Q^2 where

$$x_B \equiv -\frac{q^2}{2P \cdot q} = -\frac{q^2}{2M\nu}, \quad Q^2 \equiv -q^2 \quad (2.26)$$

x_B is called Bjorken- x , and this is identical to the momentum fraction of the parton x in the previous section if we assume the electron-parton scattering is elastic and the parton mass is negligible:

$$0 \approx (xP + q)^2 = 2x(P \cdot q) + q^2, \quad x = -\frac{q^2}{2P \cdot q} = x_B \quad (2.27)$$

In this case spin-dependent terms vanish and two independent hadron structure functions $W_1(P \cdot q, q^2)$ and $W_2(P \cdot q, q^2)$ remain. In the case of unpolarized inelastic scattering, Eq. (2.21) becomes

$$\frac{d\sigma}{d\Omega dE'} = \frac{4\alpha^2}{q^4} E'^2 \left[W_2(P \cdot q, q^2) \cos^2 \frac{\theta}{2} + 2W_1(P \cdot q, q^2) \sin^2 \frac{\theta}{2} \right] . \quad (2.28)$$

2.2.3 Validation of the parton model

Getting back to the parton model, if we identify partons as spin-1/2 Dirac particle with fractional electric charge, we can calculate the elastic scattering cross section of unpolarized electron-parton scattering for given parton x as

$$\frac{d\sigma^{\text{point}}}{d\Omega dE'}(x, Q^2) = \frac{4\alpha^2 e_f^2}{Q^4} E'^2 \left[\frac{x}{\nu} \cos^2 \frac{\theta}{2} + \frac{1}{M} \sin^2 \frac{\theta}{2} \right] \delta \left(x - \frac{Q^2}{2M\nu} \right) \quad (2.29)$$

where e_f is the fraction of the electric charge of the parton f by the unit of electron charge. Assuming the factorization (2.12), the total electron-proton cross section is

$$\begin{aligned} \frac{d\sigma}{d\Omega dE'} &= \int_0^1 dx \sum_f \phi_f(x, Q^2) \frac{d\sigma^{\text{point}}}{d\Omega dE'}(x, Q^2) \\ &= \frac{4\alpha^2}{Q^4} E'^2 \int_0^1 dx \sum_f \phi_f(x, Q^2) e_f^2 \left[\frac{x}{\nu} \cos^2 \frac{\theta}{2} + \frac{1}{M} \sin^2 \frac{\theta}{2} \right] \delta \left(x - \frac{Q^2}{2M\nu} \right) \\ &= \frac{4\alpha^2}{Q^4} E'^2 \sum_f \phi_f(x, Q^2) e_f^2 \left[\frac{x}{\nu} \cos^2 \frac{\theta}{2} + \frac{1}{M} \sin^2 \frac{\theta}{2} \right], \quad \text{where } x = \frac{Q^2}{2M\nu} . \end{aligned} \quad (2.30)$$

Then comparing the above equation with Eq. (2.28) one finds

$$F_1(x, Q^2) = \frac{1}{2x} \sum_f \phi_f(x, Q^2) e_f^2 \quad (2.31)$$

$$F_2(x, Q^2) = \sum_f \phi_f(x, Q^2) e_f^2 . \quad (2.32)$$

Here, the remarkable thing is that F_1 and F_2 are not independent of each other anymore and both essentially indicate the same parton distribution functions, although it is allowed to be independent at the first formalism (2.19). Experimentally F_1 and F_2 is possible to measure independently, and the result agrees well with the prediction of the parton model. This infers that the scattered electron interacts with spin-1/2 Dirac particles. Moreover, DIS experiments show F_1 and F_2 are approximately independent of Q^2 at $x \simeq 0.25$. This experimental fact is called Bjorken scaling. Bjorken scaling means the structure of the parton which interacts with the scattering electron does not change no matter how strongly hit it. This is the proof that there are point-like charged particles (=quarks) in the proton, and the factorization picture is valid. Precisely Bjorken scaling is violating at low x region, but this does not indicate the parton model is wrong. The violation of Bjorken scaling is explained by the evolution of parton distribution functions with Q^2 .

2.3 Fundamental theorems of pQCD

2.3.1 Factorization theorem

The heuristic model of factorization is realized in the pQCD as the theorem of factorization of long-distance (“soft”) from short-distance (“hard”) dependence for DIS. The theorem generalizes of the parton model results given by

$$F_1^{(Vh)}(x, Q^2) = \sum_f \int_0^1 \frac{d\xi}{\xi} C_1^{(Vf)} \left(\frac{x}{\xi}, \frac{Q^2}{\mu^2}, \frac{\mu_f^2}{\mu^2}, \alpha_s(\mu^2) \right) \phi_{f/h}(\xi, \mu_f, \mu^2) \quad (2.33)$$

$$F_2^{(Vh)}(x, Q^2) = \sum_f \int_0^1 d\xi C_2^{(Vf)} \left(\frac{x}{\xi}, \frac{Q^2}{\mu^2}, \frac{\mu_f^2}{\mu^2}, \alpha_s(\mu^2) \right) \phi_{f/h}(\xi, \mu_f, \mu^2) \quad (2.34)$$

where V, h denotes the coupling vector boson and the initial hadron respectively, $\phi_{f/h}$ is the PDF of the hadron h for the parton f , $C_{1,2}^{(Vf)}$ are generalized “hard-scattering” hadron structure functions at the parton level, and we have two independent mass scales μ , μ_f . The former scale μ is the renormalization scale, and the latter is called the factorization scale, which is specific to factorization calculation. μ_f separates the scale of short-distance and long-distance. The factorization theorem assures that each hard scattering function $C_{1,2}$ is infrared safe, i.e., it is calculable with the pQCD and is independent of long-distance effects. Also, the PDF $\phi_{f/h}$ contains all the infrared sensitivity of the original cross section. The PDF depends on μ_f , but it is universally applicable to any particular hard scattering process. The factorization is also valid to other hadronic processes other than DIS such as e^+e^- annihilation to hadronic final states. It is also applicable to polarized PDFs, which are the main topic of this thesis.

Factorization schemes If we calculate beyond the leading order, there is considerable ambiguity in separating the hard scattering functions from “soft” PDFs. Indeed we have arbitrariness how we split the short-distance “finite parts” at higher orders into the hard C functions and PDFs, and the selection of the method is a kind of taste. Thus we need to label to the calculations on which factorization scheme we base, and it is crucial to use consistent schemes. There are various common schemes called DIS, MS, $\overline{\text{MS}}$, etc.

2.3.2 Evolution

As written in Sec. 2.2.3, the DIS experiments support approximate Bjorken scaling, but precisely the Bjorken scaling is violating; the PDFs and hadron structure functions are functions of not only x but also the scale Q^2 . However, the Q^2 dependence is not freehand, and one remarkable consequence of the pQCD is that once we determined PDFs at a particular scale Q^2 as functions of x , ideally we can predict the PDFs for any other scale Q'^2 .

The evolution of the PDFs is described in terms of integro-differential equations known as DGLAP (Dokshitzer-Gribov-Lipatov-Altarelli-Parisi) equations,

$$\frac{d}{d \log Q^2} \phi_i(x, Q^2) = \sum_j \int_x^1 \frac{d\xi}{\xi} P_{ij} \left(\frac{x}{\xi}, \alpha_s(Q^2) \right) \phi_j(\xi, Q^2) \quad (2.35)$$

where P_{ij} are called splitting functions, or evolution kernels and j is over all constituent partons. The R.H.S. of the DGLAP equations is a convolution of PDFs and splitting functions. The splitting functions P_{ij} describe how a quark splits into a quark and a gluon, or how a gluon splits into a pair of quarks or gluons, and so forth. If we go to higher Q^2 scale, the length-scale of DIS probing becomes smaller. As a result the probability to observe quarks and gluons as separated ‘‘partons’’ especially in small x region increases logarithmically compared to lower Q^2 scales.

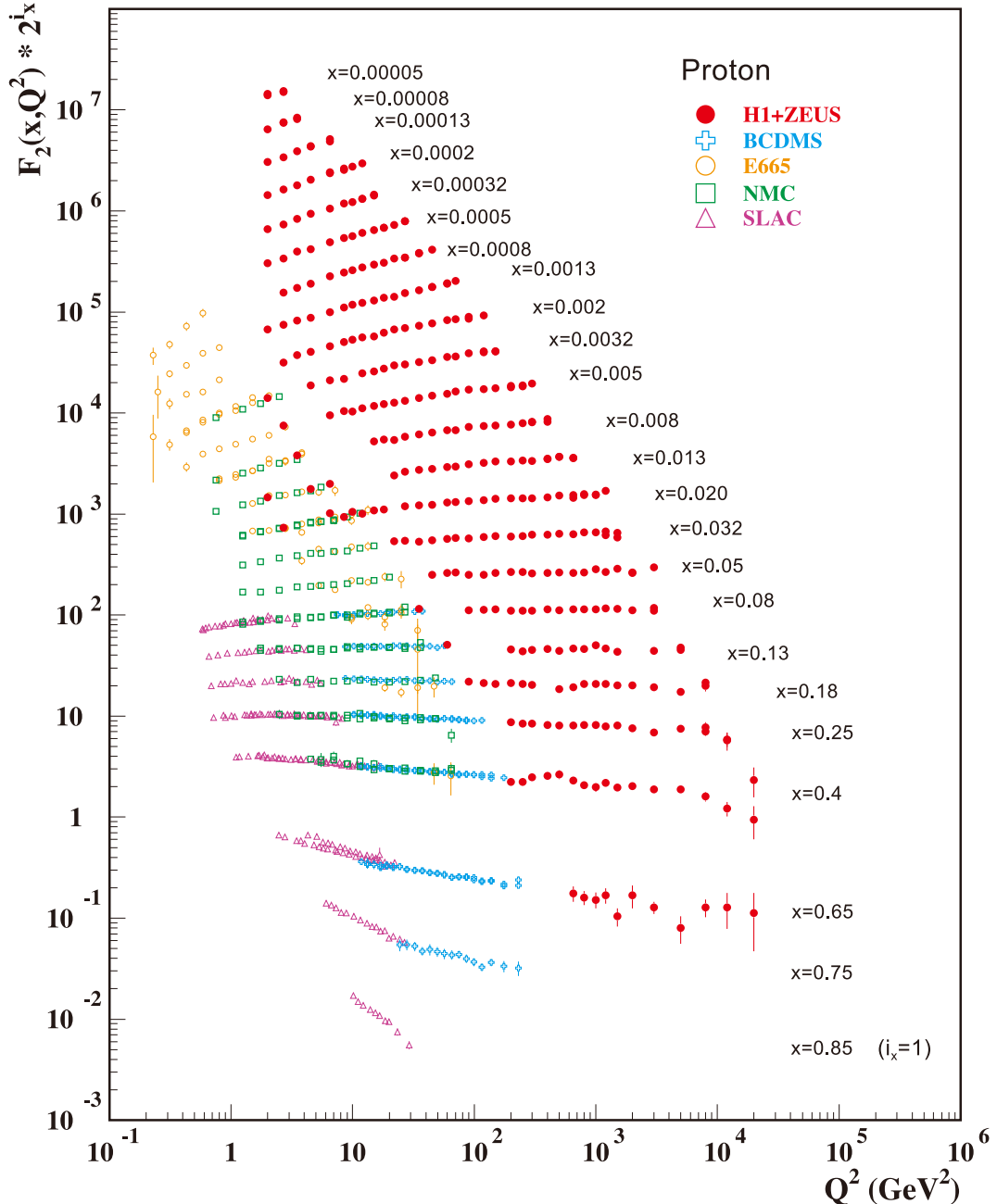


Figure 2.3: Q^2 dependence of $F_2(x, Q^2)$ at various x obtained by many experiments[9].

2.4 Spin structure of the nucleon

2.4.1 Polarized DIS

If we perform DIS experiments with both the electron and the proton polarized, we can probe another two hadron structure functions, $G_1(P \cdot q, q^2)$ and $G_2(P \cdot q, q^2)$ in Eq. (2.20). Let us consider the longitudinally polarized electron-proton collisions first. We discriminate the spin dependent cross sections by putting arrows like $d\sigma^{(\rightarrow\Rightarrow)}$, where the single arrow (\rightarrow) denotes the direction of electron polarization and the double arrow (\Rightarrow) denotes the direction of proton polarization. Right arrows denote positive helicities and left arrows denote negative helicities. (For transverse polarization we use up or down arrows.) Due to parity conservation in electromagnetic interactions, identities $d\sigma^{(\rightarrow\Rightarrow)} = d\sigma^{(\leftarrow\leftarrow)}$ and $d\sigma^{(\rightarrow\leftarrow)} = d\sigma^{(\leftarrow\rightarrow)}$ stand. The difference of the cross section by either flipping the electron polarization or flipping the proton polarization is

$$\begin{aligned}\frac{d\Delta\sigma}{d\Omega dE'} &\equiv \frac{d\sigma^{(\rightarrow\Rightarrow)}}{d\Omega dE'} - \frac{d\sigma^{(\rightarrow\leftarrow)}}{d\Omega dE'} \\ &= -\frac{4\alpha^2}{Q^2 M \nu} \frac{E'}{E} [(E + E' \cos \theta) g_1(x, Q^2) - 2x g_2(x, Q^2)]\end{aligned}\quad (2.36)$$

where

$$g_1(x, Q^2) \equiv \frac{(P \cdot q)^2}{\nu} G_1(P \cdot q, q^2) \quad (2.37)$$

$$g_2(x, Q^2) \equiv \nu(P \cdot q) G_2(P \cdot q, q^2) . \quad (2.38)$$

As well as the unpolarized case we would make correspondence between these structure functions and PDFs. Then we introduce polarized PDFs (or helicity PDFs in the literature). For a particular constituent quark PDF of the proton, we can think of the helicity-positive component and the helicity-negative component. Polarized PDFs is meaningful only when the proton is polarized. For example, we think of the helicity-positive component of PDF when the proton's helicity is positive, and write that component as

$$q_+^\Rightarrow(x, Q^2) \quad (2.39)$$

where the double right arrow (\Rightarrow) denotes the spin direction of the proton and the index “+” denotes the helicity-positive component. Summing up the helicity-positive and negative components gives the unpolarized PDF:

$$q_+^\Rightarrow(x, Q^2) + q_-^\Rightarrow(x, Q^2) = q^\Rightarrow(x, Q^2) = q(x, Q^2) \quad (2.40)$$

and the following equations stand.

$$q_-^\Leftarrow(x, Q^2) = q_+^\Rightarrow(x, Q^2), \quad q_+^\Leftarrow(x, Q^2) = q_-^\Rightarrow(x, Q^2) \quad (2.41)$$

We define the *polarized* PDF as

$$\begin{aligned}\Delta q(x, Q^2) &\equiv q_+^\Rightarrow(x, Q^2) - q_+^\Leftarrow(x, Q^2) \\ &= q_+^\Rightarrow(x, Q^2) - q_-^\Rightarrow(x, Q^2) .\end{aligned}\quad (2.42)$$

Similarly antiquark polarized PDFs are written as $\Delta \bar{q}(x, Q^2)$. The difference of spin-dependent cross sections of polarized electron-parton cross section is given as

$$\begin{aligned}\frac{d\Delta\sigma^{\text{point}}}{d\Omega dE'} &= \frac{d\sigma_{\text{point}}^{(\rightarrow\Rightarrow)}}{d\Omega dE'} - \frac{d\sigma_{\text{point}}^{(\rightarrow\leftarrow)}}{d\Omega dE'} \\ &= -\frac{4\alpha^2}{Q^2 M \nu} \frac{E'}{E} e_f^2 (E + E' \cos \theta) \delta\left(x - \frac{Q^2}{2M\nu}\right) .\end{aligned}\quad (2.43)$$

CHAPTER 2. PHYSICS BACKGROUNDS

If we compare the above equation with Eq. (2.36) with summing up all partons:

$$\frac{d\Delta\sigma}{d\Omega dE'} = \int_0^1 dx \sum_f \left[\Delta q_f(x) \frac{d\Delta\sigma^{\text{point}}}{d\Omega dE'} + \Delta \bar{q}_f(x) \frac{d\Delta\sigma^{\text{point}}}{d\Omega dE'} \right], \quad (2.44)$$

we find

$$g_1(x, Q^2) = \frac{1}{2} \sum_f e_f^2 (\Delta q_f(x, Q^2) + \Delta \bar{q}_f(x, Q^2)) \quad (2.45)$$

$$g_2(x, Q^2) = 0. \quad (2.46)$$

2.4.2 Sum rules

Some sum rules are employed to determine polarized PDFs.

Bjorken sum rule: isospin symmetry The Bjorken sum rule[4] is the most classical rule which bases on isospin symmetry between the proton and the neutron:

$$\int_0^1 [g_1^p(x) - g_1^n(x)] dx = \frac{1}{6} \left| \frac{g_A}{g_V} \right| \left(1 - \frac{\alpha_s(Q^2)}{\pi} + \dots \right) \quad (2.47)$$

where $g_1^p(x)$, $g_1^n(x)$ is $g_1(x)$ of the proton and the neutron, respectively, and g_V and g_A are the vector and axial-vector coupling constant of the neutron β -decay. The factor $(1 - \alpha_s(Q^2)/\pi + \dots)$ represents the higher order corrections. The Bjorken sum rule has been tested by many experiments[5, 6], and the experimental data verify the Bjorken sum rule well.

flavor SU(3) symmetry Similar to the Bjorken sum rule, the flavor SU(3) symmetry of baryon octets can be assumed. In the framework of the flavor SU(3), the β -decay of the hyperons are represented with two parameters F, D . And the following relations hold:

$$\int_0^1 ([\Delta u(x) + \Delta \bar{u}(x)] - [\Delta d(x) + \Delta \bar{d}(x)]) dx = F + D = \left| \frac{g_A}{g_V} \right| \quad (2.48)$$

$$\begin{aligned} \int_0^1 & [(\Delta u(x) + \Delta \bar{u}(x)) + (\Delta d(x) + \Delta \bar{d}(x)) - 2[\Delta s(x) + \Delta \bar{s}(x)]] dx \\ & = 3F - D = 0.586 \pm 0.031 \end{aligned} \quad (2.49)$$

It is noteworthy that the above relations are independent on Q^2 up to NLO corrections.

2.4.3 Determination of polarized quark and antiquark PDFs

Thus polarized DIS is sensitive to the sum of the quark and antiquark polarized PDFs. Experimental determination of $g_1(x)$ has been performed by many polarized DIS experiments. Following the pioneering experiments at the SLAC[11–14], the European Muon Collaboration (EMC) experiment in CERN[15, 16] measured $g_1(x)$ in the range of $0.01 < x < 0.7$. The result was interpreted with flavor SU(3) symmetry model as that the sum of quark and antiquark polarization is only about $\sim 10\%$ of the total proton spin. At that time of era the result was striking, and it urged to confirm the result of the EMC experiment[17–30]. Figure 2.4 summarizes many measurements of $g_1(x)$. The recent result of the sum of the polarization of quark and antiquark is determined to be about 20 to 35 % of the total proton spin. The remaining

of the proton spin is considered to be carried by gluons and orbital angular momenta between partons.

While the sum of quark and antiquark polarized PDFs has been measured by polarized DIS experiments to make it certain that the quark contribution to the proton spin is only partial, antiquark polarized PDFs are much more difficult to probe. Polarized semi-inclusive DIS (SIDIS) experiment is one technique to probe them, which detects not only scattered electrons but also detecting another hadron additionally. The limitation of the SIDIS is that one needs to interpret the final-state hadrons with the filter of fragmentation functions. Figure 2.5 shows one recent result of a global analysis of polarized PDFs. Compared to the sum of quark and antiquark PDFs, $\Delta\bar{u}(x), \Delta\bar{d}(x)$ have large relative uncertainties, which are mainly from the uncertainty of the fragmentation functions.

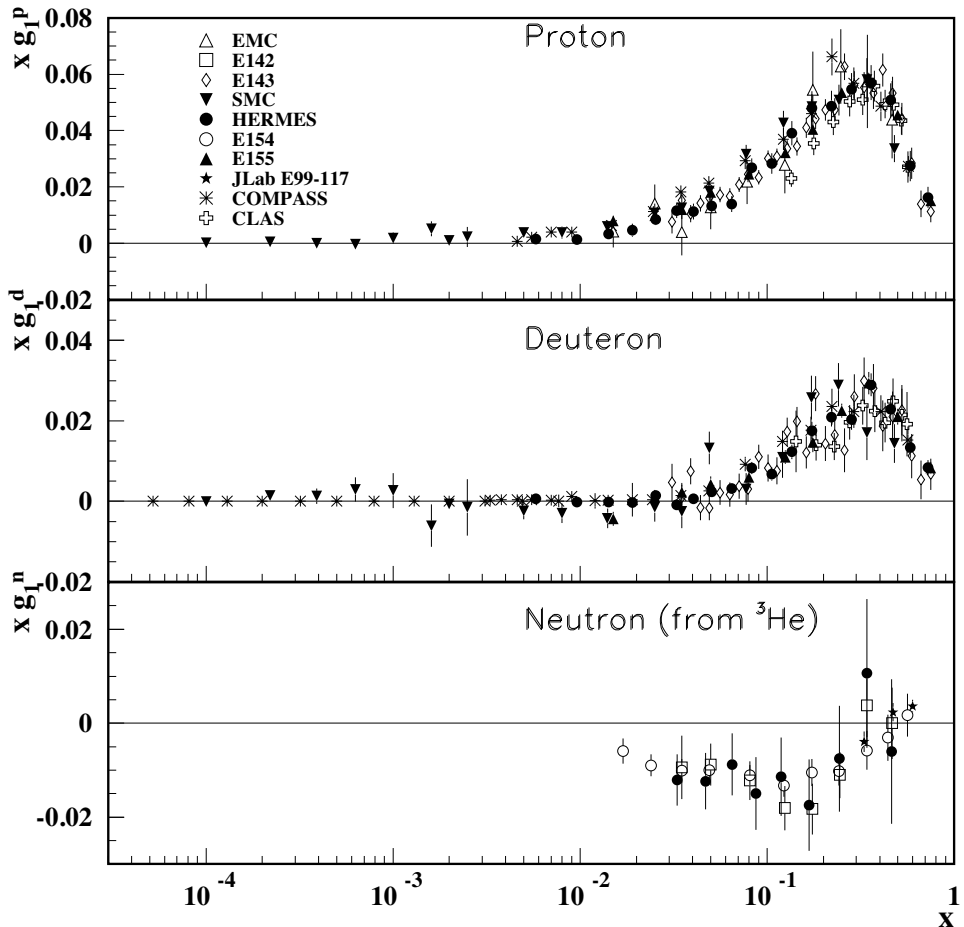


Figure 2.4: Summary of various $g_1(x)$ measurements for proton, deuteron, and neutron[9].

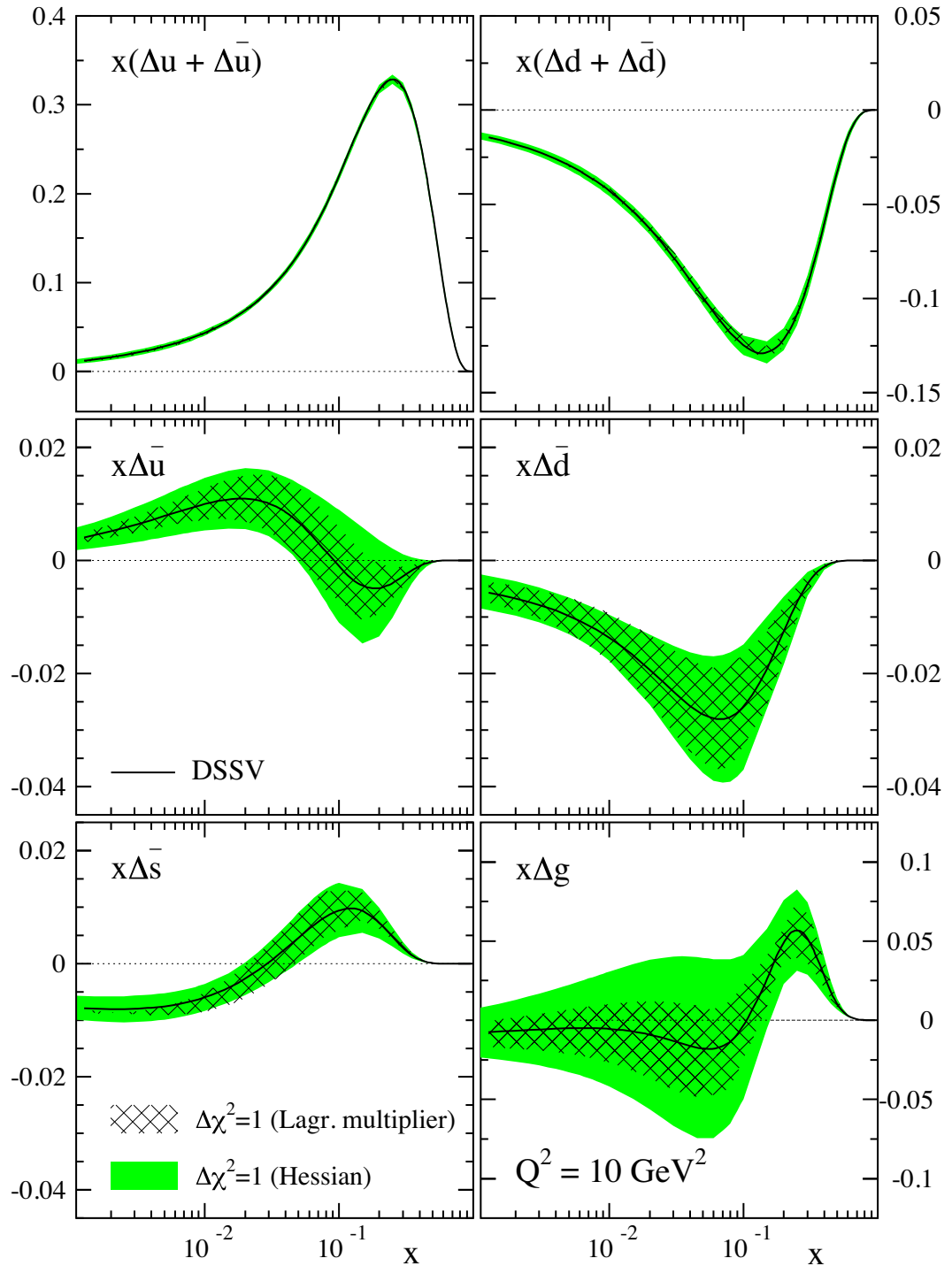


Figure 2.5: Result of the global analysis “DSSV” for the polarized PDFs [8].

2.5 Production and decays of W/Z bosons in proton-proton collisions

The production of W/Z bosons in proton-proton collision is sensitive to flavor-separating determination of PDFs. As mentioned in Appendix E, hadronic W/Z boson production constrains unpolarized PDFs. However for polarized PDFs, measurement of W/Z bosons has a seminal role for determining sea quark polarized PDFs due to the nature of the parity violation of weak interaction. In this section, we first discuss the hadronic production and decays of W bosons and its characteristic of kinematics. In the next section, we will see how W/Z bosons are sensitive to polarized sea quark PDFs.

2.5.1 W bosons and Z boson

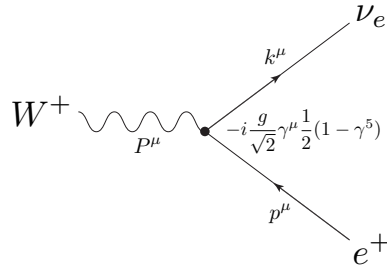


Figure 2.6: Leptonic decay mode $W^+ \rightarrow e^+ \nu_e$.

W bosons W bosons (W^+, W^-) are gauge bosons of $SU(2)_L$ weak interaction with mass of $80.40 \pm 0.02 \text{ GeV}/c^2$. W bosons couple with fermions with changing the charge and the flavor of the fermion. The coupling of W bosons with fermions is, unlike electromagnetic or strong gauge bosons, maximally parity-violating. Precisely the interaction of W bosons is called $V-A$ interaction. The leptonic decay of W bosons, for example $W^+ \rightarrow e^+ \nu_e$ is described with the matrix element

$$\mathcal{M} = -i \frac{g}{\sqrt{2}} \epsilon_\mu^\lambda(P) \bar{\nu}(k) \gamma^\mu \frac{1}{2} (1 - \gamma^5) e(p) \quad (2.50)$$

where the momenta and the vertex coupling are labelled in Figure 2.6. Averaging $|\mathcal{M}|^2$ over polarization of W^+ and summing over the fermion spins, at the massless limit of e^+ we obtain

$$\frac{1}{3} \sum_{\text{spin}} |\mathcal{M}|^2 = \frac{1}{3} g^2 M_W^2. \quad (2.51)$$

Consequently the partial decay width of $W^+ \rightarrow e^+ \nu_e$ is

$$\Gamma(W^+ \rightarrow e^+ \nu_e) = \frac{1}{48\pi} g^2 M_W = \frac{G_F}{\sqrt{2}} \frac{M_W^3}{6\pi} \equiv \Gamma_W^0 \quad (2.52)$$

where G_F is the Fermi coupling constant $g^2 = 8M_W^2 G_F / \sqrt{2}$. If the mass of leptons are negligible compared to M_W , the partial decay width is universal for other families of lepton pairs, $\mu^+ \nu_\mu, \tau^+ \nu_\tau$. The hadronic decays are mostly similar but we need to add the color factor and the flavor mixing factor:

$$\Gamma(W^+ \rightarrow q_i \bar{q}_j) = 3|V_{ij}|^2 \Gamma_W^0 \left(1 + \frac{\alpha_s(M_W)}{\pi} + \dots \right) \quad (2.53)$$

CHAPTER 2. PHYSICS BACKGROUNDS

where the factor 3 is the degree of freedom of color, V_{ij} is Cabibbo-Kobayashi-Maskawa (CKM) matrix element

$$V_{ij} \equiv \begin{pmatrix} V_{ud} & V_{us} & V_{ub} \\ V_{cd} & V_{cs} & V_{cb} \\ V_{td} & V_{ts} & V_{tb} \end{pmatrix} \approx \begin{pmatrix} 1 - \lambda^2/2 & \lambda & A\lambda^3(\rho - i\eta) \\ -\lambda & 1 - \lambda^2/2 & A\lambda^2 \\ A\lambda^3(1 - \rho - i\eta) & -A\lambda^2 & 1 \end{pmatrix}, \quad (2.54)$$

$$\lambda = 0.2257^{+0.0009}_{-0.0010}, \quad A = 0.814^{+0.021}_{-0.022}, \quad \rho = 0.135^{+0.031}_{-0.016}, \quad \eta = 0.349^{+0.015}_{-0.017}. \quad (2.55)$$

Here we take the Wolfenstein's approximation for the CKM matrix element. The parenthesis in Eq. (2.53) is the QCD correction. Note that the mass of t -quark is heavier than W bosons, the decay of $W^+ \rightarrow t\bar{b}, t\bar{s}, t\bar{d}$ is prohibited.

Neglecting the QCD correction factor and approximating the sum of hadronic decays by

$$\sum_{(i,j), i \neq t} |V_{ij}|^2 \simeq 2, \quad (2.56)$$

the branching ratio of $W^+ \rightarrow \ell^+ \bar{\nu}_\ell$ is about $1/9 \simeq 0.11$, where ℓ is any of the charged leptons. Table 2.1 summarizes the current experimental determination of the branching ratio of W^+ decays, and the above rough estimation gives a good picture of the decays of W bosons.

decay mode	\mathcal{BR}
$e^+\nu$	$(10.75 \pm 0.13) \%$
$\mu^+\nu$	$(10.57 \pm 0.15) \%$
$\tau^+\nu$	$(11.25 \pm 0.20) \%$
hadrons	$(67.60 \pm 0.27) \%$

Table 2.1: The decay modes and branching ratios of W^+ boson [9].

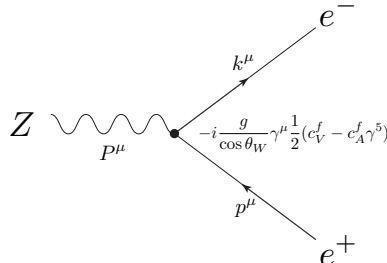


Figure 2.7: Leptonic decay mode $Z \rightarrow e^+ e^-$.

Z bosons Z boson is neutral massive electroweak gauge boson of $SU(2)_L \times U(1)_Y$ with the mass of $91.1876 \pm 0.0021 \text{ GeV}/c^2$. The coupling of Z boson with fermions is illustrated in Figure 2.7. The coupling of Z with fermions is similar to photon, but because of weak interaction coupling with Z violates parity conservation. The degree of parity violation differs by fermions, and it is parameterized with two coefficients c_V^f, c_A^f where f denotes the flavor of the fermion. The relative strength of the coupling constant of Z is different from that of W^\pm by factor $\sqrt{2}/\cos\theta_W$, where $\cos\theta_W$ is a fundamental constant of the Standard Model called the Weinberg angle. The matrix element of the leptonic decay of Z boson $Z \rightarrow e^+ e^-$ is

$$\mathcal{M} = -i \frac{g}{\cos\theta_W} \epsilon_\mu^\lambda(P) \bar{e}(k) \gamma^\mu \frac{1}{2} (c_V^e - c_A^e \gamma^5) e(p) \quad (2.57)$$

2.5 Production and decays of W/Z bosons in proton-proton collisions

and the following calculation is similar to W^\pm case. The decay width of each fermion pair is determined by c_V, c_A and at the leading order with the fermion massless limit they are

$$\Gamma(Z \rightarrow \bar{\nu}\nu) = \Gamma_Z^0 \equiv \frac{G_F M_Z^3}{12\pi\sqrt{2}} \quad (2.58)$$

$$\Gamma(Z \rightarrow \ell^+\ell^-) = \Gamma_Z^0 (1 - 4\sin^2\theta_W + 8\sin^4\theta_W) \quad (2.59)$$

$$\Gamma(Z \rightarrow \bar{u}u, \bar{c}c, \bar{b}b) = \Gamma_Z^0 \left(1 - \frac{8}{3}\sin^2\theta_W + \frac{32}{9}\sin^4\theta_W \right) \quad (2.60)$$

$$\Gamma(Z \rightarrow \bar{d}d, \bar{b}b) = \Gamma_Z^0 \left(1 - \frac{4}{3}\sin^2\theta_W + \frac{8}{9}\sin^4\theta_W \right) \quad (2.61)$$

where $\sin^2\theta_W \approx 0.23$. Note that $Z \rightarrow \bar{t}t$ is again prohibited. As a result, the branching ratio of $Z \rightarrow \ell^+\ell^-$ is about 3.36 %.

2.5.2 Hadronic production and decays of W/Z bosons

2.5.2.1 W boson productions and decays

Now let us think of the hadronic production of W bosons. The dominant production process is similar to the Drell-Yan process

$$q_i \bar{q}_j \rightarrow W^+$$

where q_i is u, c, t -quarks and \bar{q}_j is $\bar{d}, \bar{s}, \bar{b}$ -antiquarks. The matrix element is

$$\mathcal{M} = -i \frac{g}{\sqrt{2}} V_{ij} \epsilon_\mu^\lambda(P) \bar{q}_j(p_2) \frac{1}{2} \gamma^\mu (1 - \gamma^5) q_i(p_1) \quad (2.62)$$

where the momenta are labelled by Figure 2.8. The cross section of the subprocess is

$$\hat{\sigma}(q_i \bar{q}_j \rightarrow W^+) = 2\pi |V_{ij}|^2 \frac{G_F}{\sqrt{2}} M_W^2 \delta(\hat{s} - M_W^2) \quad (2.63)$$

where \hat{s} is square of the center of mass energy of the subprocess, $\hat{s} = (p_1 + p_2)^2$.

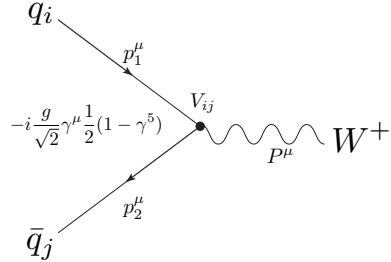


Figure 2.8: Hadronic production subprocess of W^+ .

According to the factorization theorem the total W^+ production cross section in proton-proton collision is at the leading order

$$\sigma(pp \rightarrow W^+) = \frac{K}{3} \int dx_1 dx_2 \sum_{i,j} q_i(x_1, M_W^2) \bar{q}_j(x_2, M_W^2) \hat{\sigma}(q_i \bar{q}_j \rightarrow W^+) \quad (2.64)$$

CHAPTER 2. PHYSICS BACKGROUNDS

where $q_i(x, M_W^2)$, $\bar{q}_j(x, M_W^2)$ are quark and antiquark PDFs at $Q^2 = M_W^2$. K is called the K -factor which includes the first order QCD corrections,

$$K = 1 + \frac{8\pi}{9}\alpha_s(M_W^2) + \dots \quad (2.65)$$

and the factor $1/3$ is the color factor.

Then if we introduce the *rapidity* of the W boson

$$y_W \equiv \frac{1}{2} \ln \left(\frac{E_W + p_z^W}{E_W - p_z^W} \right) \quad (2.66)$$

where E_W, p_z^W is the kinetic energy and the z -component of the momentum of W , we find the relation

$$dx_1 dx_2 = \frac{d\hat{s} dy_W}{s}. \quad (2.67)$$

and we can transform the integration of x_1, x_2 in Eq. (2.64) to that of \hat{s}, y_W . The integration over \hat{s} vanishes with the delta function in Eq. (2.63) and we obtain

$$\frac{d\sigma}{dy_W}(pp \rightarrow W^+) = K \frac{2\pi G_F}{3\sqrt{2}} \sum_{i,j} |V_{ij}|^2 x_1 x_2 q_i(x_1, M_W^2) \bar{q}_j(x_2, M_W^2) \quad (2.68)$$

$$\simeq K \frac{2\pi G_F}{3\sqrt{2}} x_1 x_2 [\cos^2 \theta_c \{u(x_1)\bar{d}(x_2) + \bar{d}(x_1)u(x_2)\} + \sin^2 \theta_c \{u(x_1)\bar{s}(x_2) + \bar{s}(x_1)u(x_2)\}] \quad (2.69)$$

where θ_c is the Cabibbo angle, and x_1, x_2 is related with y_W as

$$x_{1,2} = \frac{M_W}{\sqrt{s}} e^{\pm y_W}. \quad (2.70)$$

The Cabibbo angle suppresses the second term by factor ~ 18 and the production cross section is dominated by the first term. Integrating over y_W we obtain the total production cross section. Note that the condition $x_1, x_2 < 1$ imposes y_W to the kinematical limit

$$-\ln \left(\frac{\sqrt{s}}{M_W} \right) < y_W < \ln \left(\frac{\sqrt{s}}{M_W} \right). \quad (2.71)$$

In case of $\sqrt{s} = 500$ GeV this is $-1.83 < y_W < 1.83$. Figure 2.9 shows the total cross section of W^\pm times the branching ratio of $W^\pm \rightarrow \ell^\pm \nu_\ell$ as a function of \sqrt{s} for pp and $p\bar{p}$ collisions.

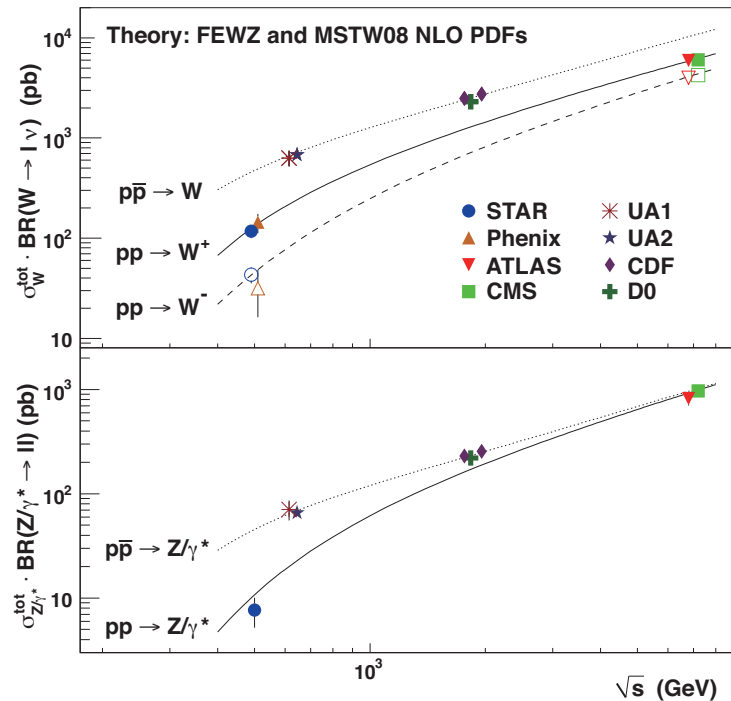


Figure 2.9: Measurements of production cross section of $W^\pm \rightarrow \ell^\pm \bar{\nu}$ and $Z \rightarrow \ell^+ \ell^-$ in proton-proton and proton-antiproton collisions at various \sqrt{s} [31–42].

CHAPTER 2. PHYSICS BACKGROUNDS

Kinematics of the leptonic decay The production and decay subprocess of $pp \rightarrow W^+ \rightarrow \ell^+ \bar{\nu}_\ell$ is typically

$$u\bar{d} \rightarrow W^+ \rightarrow \ell^+ \bar{\nu}_\ell . \quad (2.72)$$

The matrix element is

$$\mathcal{M} = i \frac{G_F}{\sqrt{2}} M_W^2 V_{ud} \frac{\bar{d}\gamma^\mu(1-\gamma^5)u\bar{\nu}\gamma_\mu(1-\gamma^5)\ell}{\hat{s} - M_W^2 + iM_W\Gamma_W} \quad (2.73)$$

where \hat{s} is square of the center of mass energy, M_W is the mass of W^+ , Γ_W is the decay width of W^+ , and $\bar{d}, u, \bar{\nu}, \ell$ are the fermion external lines of the corresponding flavors. In the $\ell^+\bar{\nu}_\ell$ rest frame, the center of mass scattering angle $\hat{\theta}$ is defined as the angle between u and ℓ^+ . With summing up the matrix element over the spin of the final states, we obtain

$$\frac{d\hat{\sigma}}{d\cos\hat{\theta}}(u\bar{d} \rightarrow W^+ \rightarrow \ell^+ \bar{\nu}_\ell) = \frac{|V_{ud}|^2}{8\pi} \left(\frac{G_F M_W^2}{\sqrt{2}} \right)^2 \frac{\hat{s}(1-\cos\hat{\theta})^2}{(\hat{s} - M_W^2)^2 + (\Gamma_W M_W)^2} . \quad (2.74)$$

The factor $(1-\cos\hat{\theta})^2$ is the direct result of parity violation. The $V-A$ interaction of W^+ boson couples only the left-handed u -quark and the right-handed \bar{d} -quark. Then the produced W^+ boson is perfectly polarized to the direction of \bar{d} -direction. The neutrino from the W^+ decay must be left-handed, then the charged lepton prefers to be emitted to \bar{d} -direction. For W^- production case, if we take $\hat{\theta}$ as the angle between d and ℓ^- , we obtain

$$\frac{d\hat{\sigma}}{d\cos\hat{\theta}} \propto (1+\cos\hat{\theta})^2. \quad (2.75)$$

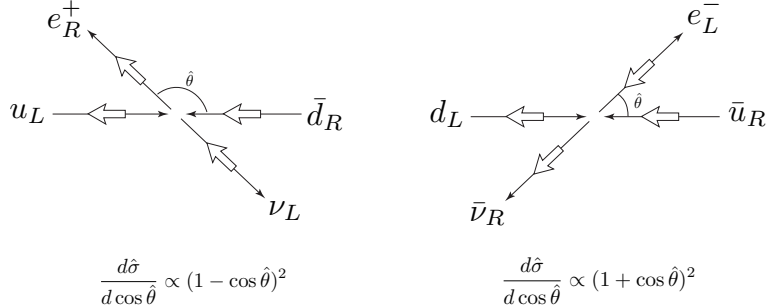


Figure 2.10: Helicity conservation in production and decay of W^\pm boson.

Let us denote the rapidity of ℓ^\pm at the center of mass frame of W production as $\hat{y}_{\ell\pm}$, then we find

$$\frac{d\hat{\sigma}}{d\hat{y}_{\ell\pm}} = \sin^2\hat{\theta} \frac{d\hat{\sigma}}{d\cos\hat{\theta}} \propto \sin^2\hat{\theta}(1 \mp \cos\hat{\theta})^2 \simeq \left(\frac{1 \mp \tanh\hat{y}_{\ell\pm}}{\cosh\hat{y}_{\ell\pm}} \right)^2, \quad (2.76)$$

and $\hat{y}_{\ell\pm}$ is related with the lepton rapidity at the lab frame $y_{\ell\pm}$ as

$$y_{\ell\pm} = y_{W\pm} + \hat{y}_{\ell\pm} = \frac{1}{2} \ln \left(\frac{x_1}{x_2} \right) + \hat{y}_{\ell\pm}. \quad (2.77)$$

Hence the lab frame ℓ^\pm rapidity distribution is given by

$$\frac{d\sigma}{dy_{\ell\pm}} = \frac{1}{3} \int dx_1 dx_2 \sum_{i,j} q_i(x_1) \bar{q}_j(x_2) \left[\frac{d\hat{\sigma}}{d\cos\hat{\theta}}(q_i \bar{q}_j \rightarrow \ell^\pm \nu) \sin^2\hat{\theta} \right]. \quad (2.78)$$

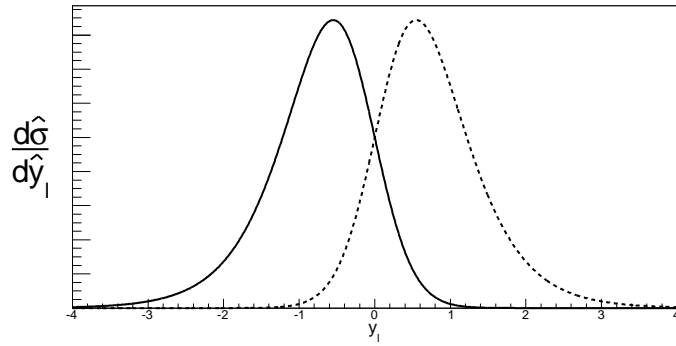


Figure 2.11: The rapidity distribution of the charged lepton from W decays at the center of mass frame. The solid line is of $W^+ \rightarrow \ell^+$ and the dotted line is of $W^- \rightarrow \ell^-$.

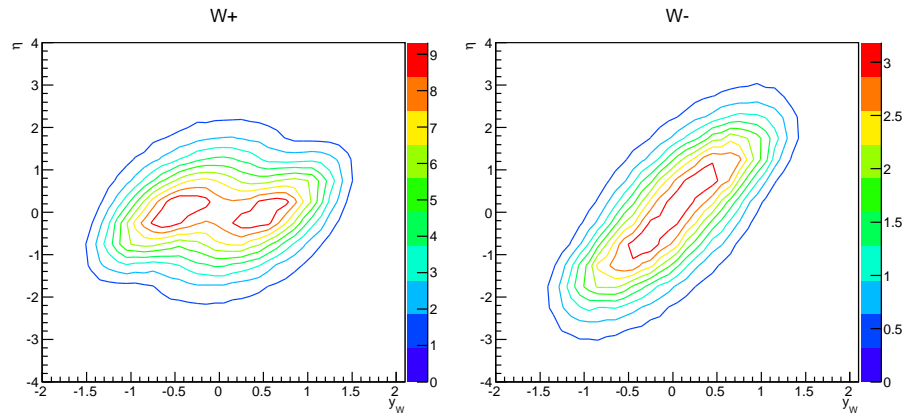


Figure 2.12: Distribution of y_W and η_ℓ for $W^+ \rightarrow \ell^+$ (left) and $W^- \rightarrow \ell^-$ (right). The correlation between y_W and η_ℓ is strong for $W^- \rightarrow \ell^-$, while it is weak for $W^+ \rightarrow \ell^+$.

Now considering the structures of PDFs, in the proton the quark PDFs have relatively high probability to have large x compared to the antiquark PDFs, since the quark PDFs are dominated by the contribution of valence quarks, while the antiquark PDFs are composed of sea quarks. Consequently, for the W boson production in proton-proton collisions the Bjorken- x of quark PDFs is much larger than that of antiquark PDFs. Then for W^+ production the rapidity of the W^+ tends to be along with the u -quark direction, while for W^- production the rapidity of the W^- tends to be along with the d -quark direction. Thus the direction of ℓ^+ from W^+ decay tends to be opposite to the boost of W^+ , and the direction of ℓ^- from W^- decay tends to be along with the boost of W^- (see Figure 2.12).

Jacobian peak The leptonic decay of W bosons is two-body decay, thus at the center of mass frame the charged lepton carries the half of the mass of the W boson. Then the transverse momentum of the charged lepton at the center of mass frame \hat{p}_T is

$$\hat{p}_T = \frac{\sqrt{s}}{2} \sin \hat{\theta} \quad \text{or} \quad \cos \hat{\theta} = \left(1 - 4 \frac{\hat{p}_T^2}{\hat{s}}\right)^{1/2}, \quad (2.79)$$

if we change the variable in the differential cross section from $d \cos \hat{\theta}$ to $d \hat{p}_T^2$, the Jacobian appears:

$$\frac{d \cos \hat{\theta}}{d \hat{p}_T^2} = -\frac{2}{\hat{s}} \left(1 - 4 \frac{\hat{p}_T^2}{\hat{s}}\right)^{1/2}. \quad (2.80)$$

The differential cross section is then

$$\frac{d\hat{\sigma}}{d\hat{p}_T^2} = 3 \frac{\hat{\sigma}}{\hat{s}} \frac{(1 - 2\hat{p}_T^2/\hat{s})}{(1 - 4\hat{p}_T^2/\hat{s})^{1/2}} \quad (2.81)$$

The above differential cross section has a singularity at $\hat{p}_T = \sqrt{\hat{s}}/2 = M_W/2$, and that is known as the Jacobian peak. It is clear that the Jacobian peak consists of charged leptons from W decays whose direction at the center of mass frame is perpendicular to the beam axis. If we restrict the rapidity of charged leptons within forward rapidity, that is the case of the measurement in this thesis, the probability of having the highest $p_T = M_W/2$ for charged leptons becomes rare.

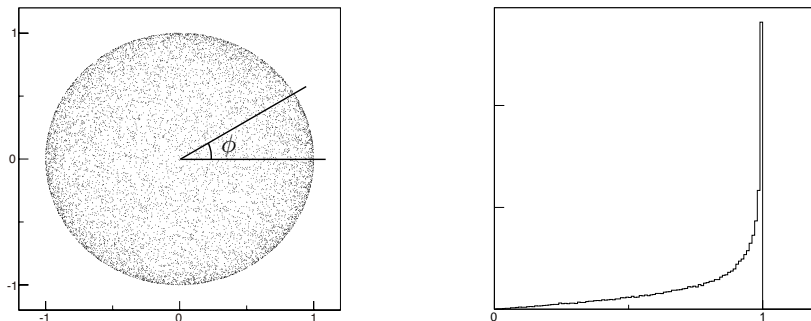


Figure 2.13: Geometrical explanation of the Jacobian peak. If we project a spherical shell in a plane, a dense edge appears at the rim of the projected disk. By integrating over ϕ , the Jacobian peak is obtained in radial distribution on the right figure.

2.5 Production and decays of W/Z bosons in proton-proton collisions

2.5.2.2 Z boson productions and decays

The Z boson production in proton-proton collision is similar to the W boson production. The production subprocess is

$$q\bar{q} \rightarrow Z \quad (2.82)$$

with the matrix element

$$|\mathcal{M}|^2 = 32 \frac{G_F}{\sqrt{2}} ((c_V^q)^2 + (c_A^q)^2) M_Z^4 \quad (2.83)$$

and the cross section of the subprocess is

$$\hat{\sigma}(q\bar{q} \rightarrow Z) = 8\pi \frac{G_F}{\sqrt{2}} ((c_V^q)^2 + (c_A^q)^2) M_Z^2 \delta(\hat{s} - M_Z^2). \quad (2.84)$$

The convoluted cross section is

$$\frac{d\sigma}{dy_Z}(pp \rightarrow Z) = K \frac{8\pi}{3} \frac{G_F}{\sqrt{2}} \sum_q ((c_V^q)^2 + (c_A^q)^2) x_1 x_2 q(x_1) \bar{q}(x_2). \quad (2.85)$$

Inputting concrete PDFs, we find the production cross section of Z is smaller than that of W production. If we focus on the leptonic decay, the ratio of $Z \rightarrow \ell^+ \ell^-$ to $W^\pm \rightarrow \ell^\pm \nu_\ell$ is about 1/10 due to the smaller production cross section and the smaller branching ratio.

2.6 Probing sea quark polarization via W/Z bosons

2.6.1 Longitudinal single spin asymmetry

Now let us consider to apply the production of W/Z bosons in proton-proton collisions to probe the polarized sea quark PDFs. We consider the longitudinally-polarized proton-proton collisions. The single spin asymmetry is defined as

$$A_L \equiv \frac{d\sigma^{\Rightarrow} - d\sigma^{\Leftarrow}}{d\sigma^{\Rightarrow} + d\sigma^{\Leftarrow}} \quad (2.86)$$

where $d\sigma^{\Rightarrow} = d\sigma(p^{\Rightarrow} p \rightarrow X)$, $d\sigma^{\Leftarrow} = d\sigma(p^{\Leftarrow} p \rightarrow X)$. Finite A_L appears only with parity-violating processes. The production cross section of ℓ^+ from W^+ decays in polarized proton-proton collisions is

$$\begin{aligned} d\sigma(p^{\Rightarrow} p \rightarrow W^+ \rightarrow \ell^+ \nu_{\ell}) &= \frac{K}{3} \int dx_1 dx_2 \sum_{i,j} (q_i^{\Rightarrow}(x_1) \bar{q}_{j+}(x_2) + \bar{q}_j^{\Rightarrow}(x_1) q_{i-}(x_2)) \\ &\quad \times d\hat{\sigma}(q_i \bar{q}_j \rightarrow W^+ \rightarrow \ell^+ \nu_{\ell}) \end{aligned} \quad (2.87)$$

$$\begin{aligned} d\sigma(p^{\Leftarrow} p \rightarrow W^+ \rightarrow \ell^+ \nu_{\ell}) &= \frac{K}{3} \int dx_1 dx_2 \sum_{i,j} (q_i^{\Leftarrow}(x_1) \bar{q}_{j+}(x_2) + \bar{q}_j^{\Leftarrow}(x_1) q_{i-}(x_2)) \\ &\quad \times d\hat{\sigma}(q_i \bar{q}_j \rightarrow W^+ \rightarrow \ell^+ \nu_{\ell}) . \end{aligned} \quad (2.88)$$

Here we implicitly assumed the massless limit of the quarks that the helicity state is identical to the chirality state. Then recalling the definition of polarized PDFs that $\Delta q(x) \equiv q_+^{\Rightarrow} - q_-^{\Rightarrow}$,

$$\begin{aligned} A_L(p^{\Rightarrow} p \rightarrow W^+ \rightarrow \ell^+ \nu_{\ell}) &= \frac{\int dx_1 dx_2 \sum_{i,j} (-\Delta q_i(x_1) \bar{q}_j(x_2) + \Delta \bar{q}_j(x_1) q_i(x_2)) \cdot d\hat{\sigma}}{\int dx_1 dx_2 \sum_{i,j} (q_i(x_1) \bar{q}_j(x_2) + \bar{q}_j(x_1) q_i(x_2)) \cdot d\hat{\sigma}} \\ &\approx \frac{\int dx_1 dx_2 (-\Delta u(x_1) \bar{d}(x_2) + \Delta \bar{d}(x_1) u(x_2)) \cdot d\hat{\sigma}}{\int dx_1 dx_2 (u(x_1) \bar{d}(x_2) + \bar{d}(x_1) u(x_2)) \cdot d\hat{\sigma}} \end{aligned} \quad (2.89)$$

Here we neglected the small contributions from $u\bar{s}$ and other channels, and only considered production in $u\bar{d}$. In particular, we focus on the charged lepton rapidity dependence of A_L . If we simply denote the A_L of $W^+ \rightarrow \ell^+ \nu_{\ell}$ as a function of y_{ℓ} as $A_L^{\ell^+}(y_{\ell})$, we obtain

$$A_L^{\ell^+}(y_{\ell}) = \frac{\int dx_1 dx_2 \left(-\Delta u(x_1) \bar{d}(x_2) (1 - \cos \hat{\theta})^2 + \Delta \bar{d}(x_1) u(x_2) (1 + \cos \hat{\theta})^2 \right)}{\int dx_1 dx_2 \left(u(x_1) \bar{d}(x_2) (1 - \cos \hat{\theta})^2 + \bar{d}(x_1) u(x_2) (1 + \cos \hat{\theta})^2 \right)} . \quad (2.90)$$

Note that in the above equation we re-defined $\hat{\theta}$ as the angle between the direction of the momentum of the polarized proton and the charged lepton at the center of mass frame. Therefore between the first term and the second term the sign before the $\cos \hat{\theta}$ becomes opposite. Consequently the rapidity y_{ℓ} is positive (negative) when $p_z^{\ell} > 0$ ($p_z^{\ell} < 0$), where the z -axis is parallel with the momentum of the polarized proton (Figure 2.14). Similarly for $W^- \rightarrow \ell^- \bar{\nu}_{\ell}$, we obtain

$$A_L^{\ell^-}(y_{\ell}) = \frac{\int dx_1 dx_2 \left(\Delta \bar{u}(x_1) d(x_2) (1 - \cos \hat{\theta})^2 - \Delta d(x_1) \bar{u}(x_2) (1 + \cos \hat{\theta})^2 \right)}{\int dx_1 dx_2 \left(\bar{u}(x_1) d(x_2) (1 - \cos \hat{\theta})^2 + d(x_1) \bar{u}(x_2) (1 + \cos \hat{\theta})^2 \right)} . \quad (2.91)$$

Eq. (2.90) and (2.91) are both convolutions over x_1 and x_2 , and quark PDFs and antiquark PDFs are coupled. Thus the antiquark PDFs are not directly extracted and we need to compare experimental data with numerical computations to constrain the antiquark PDFs. However it

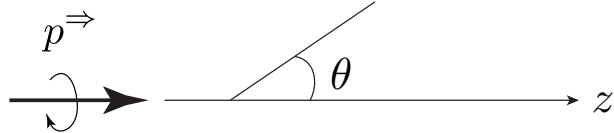


Figure 2.14: The convention of the coordinate system for spin asymmetry.

is possible to make some qualitative arguments about the sensitivity to the antiquark PDFs. For the $W^- \rightarrow \ell^- \nu_\ell$ case, consider measuring A_L at large negative y_ℓ . In this case $\hat{\theta} \sim \pi$ and $x_1 \ll x_2$ are expected then the convolution over x_1, x_2 is approximately decomposed. Then the second term of the $d\bar{u}$ coupling is highly suppressed compared to the first term because of the factor $(1 + \cos \hat{\theta})^2$, approximately we obtain

$$A_L^{\ell^-}(y_\ell \rightarrow \text{large neg.}) \approx \frac{\Delta \bar{u}(x_1)}{\bar{u}(x_1)} \quad (2.92)$$

thus we will see almost pure $\Delta \bar{u}(x)$ at medium Bjorken- x ($x \sim 0.05$). On the other hand, if we measure A_L at large positive y_ℓ , $\hat{\theta} \sim 0$ and $x_1 \gg x_2$. In this case, on the contrary, the second term dominates the first term then we obtain

$$A_L^{\ell^-}(y_\ell \rightarrow \text{large pos.}) \approx \frac{\Delta d(x_1)}{d(x_1)} \quad (2.93)$$

thus we will see almost pure $\Delta d(x)$ at large Bjorken- x ($x \sim 0.4$). Thus measuring the A_L of $W^- \rightarrow \ell^- \bar{\nu}_\ell$ at large (positive or negative) rapidity regions are very sensitive to $\Delta \bar{u}(x)$ and $\Delta d(x)$. For $W^+ \rightarrow \ell^+ \nu_\ell$ case, the convolution over x_1, x_2 is not decomposed, since the preference of the decay direction of ℓ^+ is opposite to the boost of the W^+ . If we select large negative or positive rapidity $A_L^{\ell^+}$, both the first term and the second term of Eq. (2.90) almost equally contribute. Thus measuring $A_L^{\ell^+}$ for wide rapidity range is desired to constrain on polarized PDFs. Figure 2.16 shows A_L of $W^\pm \rightarrow \ell^\pm$ at $\sqrt{s} = 500$ GeV with the CHE NLO generator[10] as a function of y_ℓ with DSSV08 global analysis of polarized PDFs[8].

Effect of Z boson on $A_L^{\ell^\pm}$ $Z \rightarrow \ell^\pm$ process also contributes to single spin asymmetry $A_L^{\ell^\pm}$ once one of two charged lepton is not observed in the detector. PHENIX is non-hermetic detector, and there are significant chance to observe only one charged lepton from Z boson. Due to the small production cross section of Z boson compared to W^\pm bosons, $A_L^{\ell^\pm}$ is dominantly determined by W^\pm bosons. In this thesis, both muons from W^\pm and Z are considered as signal, and the inclusive single spin asymmetry is measured. Figure 2.16 shows A_L of $Z^\pm \rightarrow \ell^\pm$ at $\sqrt{s} = 500$ GeV with the CHE NLO generator[10] as a function of y_ℓ with DSSV08 global analysis of polarized PDFs[8].

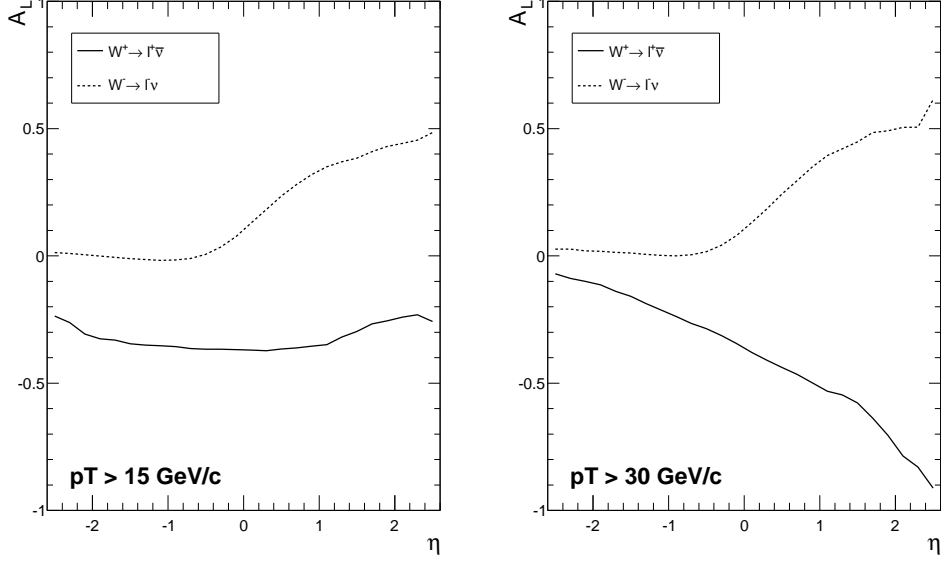


Figure 2.15: Estimation of A_L of $W^\pm \rightarrow \ell^\pm$ at $\sqrt{s} = 500$ GeV with the CHE NLO generator[10]. The DSSV08 PDFs[8] were used for polarized PDFs, and the MRST2002 PDFs[7] were used for unpolarized PDFs.

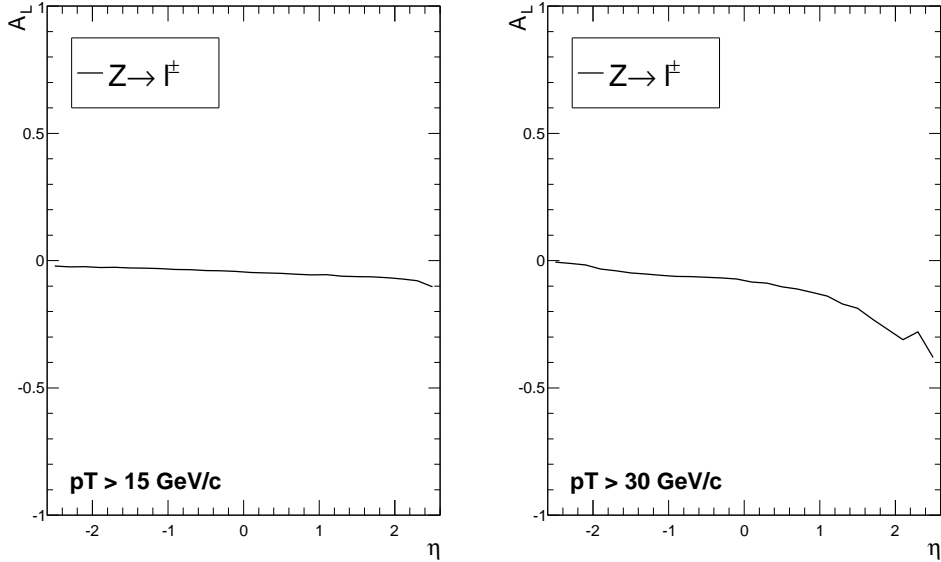


Figure 2.16: Estimation of A_L of $Z \rightarrow \ell^\pm$ at $\sqrt{s} = 500$ GeV with the CHE NLO generator[10]. The DSSV08 PDFs[8] were used for polarized PDFs, and the MRST2002 PDFs[7] were used for unpolarized PDFs.

2.6.2 Results of $A_L^{\ell\pm}$ at mid-rapidity

The RHIC started to take data for A_L of W^\pm at $\sqrt{s} = 500$ GeV in longitudinally polarized proton-proton collisions from 2009. Both the PHENIX and the STAR experiments of RHIC measured A_L at mid-rapidity. Table 2.2 summarizes the result, and Figure 2.17 and 2.18 shows the result plot of PHENIX and STAR, respectively. In both results the measured values of A_L have large statistical uncertainty, but the results are consistent with calculations with various global analyses of polarized PDFs. Both experiments are continuing to take data to improve the results.

experiment	mode	luminosity	$A_L(\eta = 0)$	$A_L(\eta = 0)$ 68 % C.L.
PHENIX	$W^+/Z \rightarrow e^+$	8.6	-0.88	[-1, -0.61]
	$W^-/Z \rightarrow e^-$		0.91	[0.20, 1]
$\int \mathcal{L} dt = 8.6 \text{ pb}^{-1}, 30 < p_T < 50 \text{ GeV}/c, \eta < 0.35$				
STAR	$W^+ \rightarrow e^+$	12	-0.27	$-0.27 \pm 0.11_{\text{(stat)}} \pm 0.02_{\text{(sys)}}$
	$W^- \rightarrow e^-$		0.14	$0.14 \pm 0.19_{\text{(stat)}} \pm 0.02_{\text{(sys)}}$
$\int \mathcal{L} dt = 12 \text{ pb}^{-1}, 25 < p_T < 50 \text{ GeV}/c, \eta < 1$				

Table 2.2: Results of A_L at mid-rapidity region with PHENIX and STAR[43, 44].

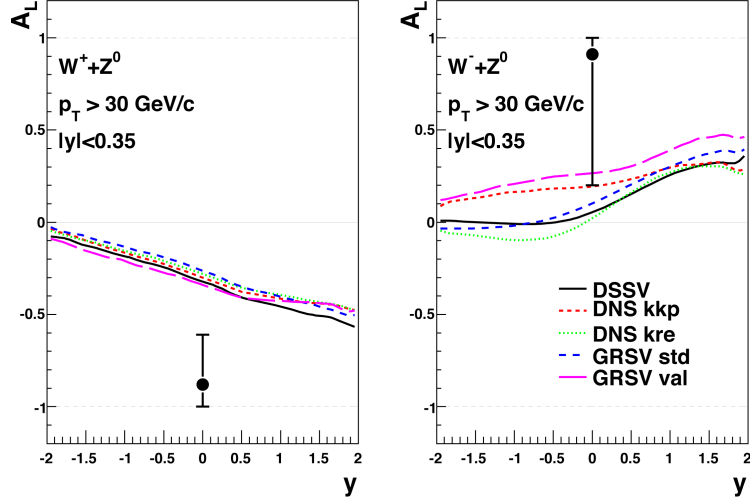


Figure 2.17: A_L for e^\pm from W^\pm/Z^0 boson decays for $|\eta| < 0.35$, $30 < p_T < 50 \text{ GeV}/c$ with PHENIX[43].

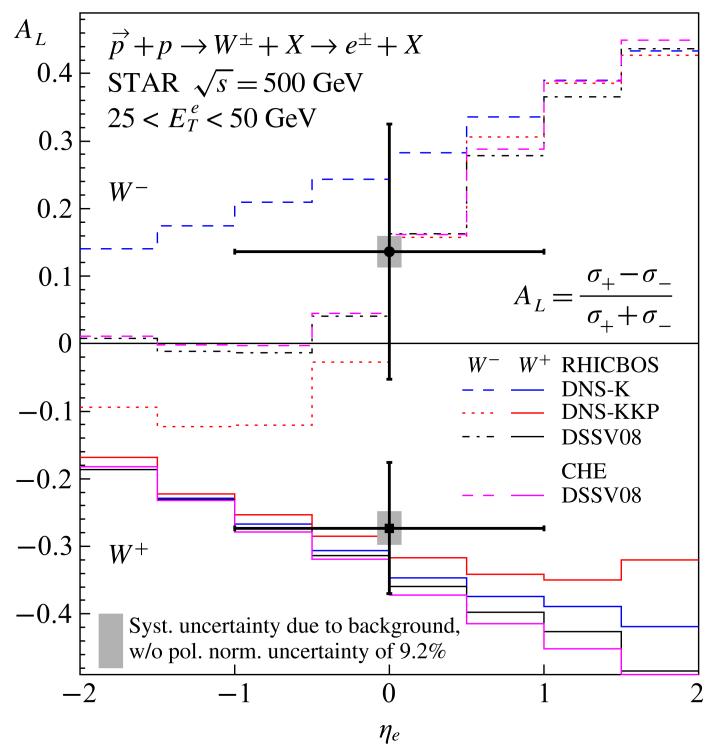


Figure 2.18: A_L for e^\pm from W^\pm boson decays for $|\eta| < 1$, $25 < p_T < 50$ GeV/c with STAR[44].

2.6.3 Impact of $A_L^{\ell\pm}$ on determining polarized PDFs

Figure 2.19 and 2.20 illustrate the impact of the measurement of $A_L^{\ell\pm}$ for constraining antiquark PDFs[8]. The former is the current DSSV global analysis. Both $\Delta\bar{u}(x)$ and $\Delta\bar{d}(x)$ have large uncertainties in $x \lesssim 0.3$. The latter is the same global analysis with assuming DSSV polarized PDFs and generating pseudo-experimental data of integrated luminosity of 200 pb^{-1} . The uncertainty becomes significantly small at wide range of x for both $\bar{u}(x)$ and $\bar{d}(x)$. It is important to obtain results at various rapidity points for better constraining of antiquark polarized PDFs.

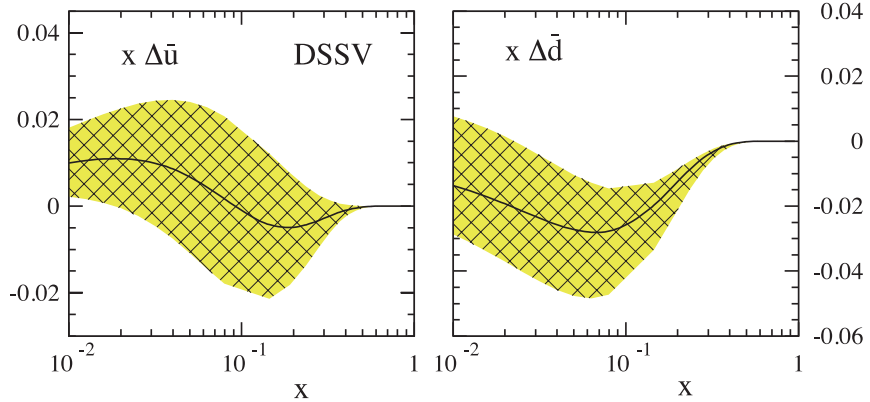


Figure 2.19: Global fit result of $\Delta u(x, Q^2)$ and $\Delta \bar{d}(x, Q^2)$ at $Q^2 = 10 \text{ GeV}^2$ obtained in the DSSV analysis[8].

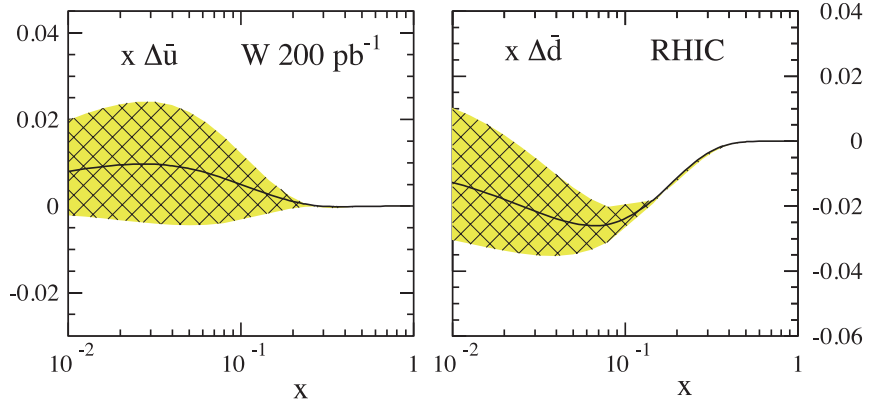


Figure 2.20: The same plot as Figure 2.19, but adding pseudo-data points to the DSSV data set which are expected to be obtained by the RHIC experiments (PHENIX and STAR), assuming the integrated luminosity of 200 pb^{-1} [8].

2.6.4 Measurement of $W^\pm/Z \rightarrow \mu^\pm$ at forward rapidity

In this thesis the PHENIX detector is used for the measurement of $W^\pm \rightarrow \mu^\pm$. The PHENIX detector has acceptance for muons in forward rapidity regions. The effective acceptance is $-2.2 < \eta < -1.4$ and $1.4 < \eta < 2.4$. The PHENIX detector is not a hermetic detector and it does not have ability to measure the missing energy taken by neutrinos from W decays. Also the limited acceptance allows to miss one of the two muons from Z decays. It is not easy to separate Z events from W^\pm , and both processes could produce parity-violating A_L . Thus we treat single muons from both W^\pm and Z bosons as signals. However the muon production cross section from W^\pm decays dominates the signal, and the contribution of Z events in the signal will be the order of 10 %.

2.6.4.1 Signal distribution

Figure 2.21 shows the distribution of μ^\pm in the transverse momentum p_T and the pseudorapidity η . The dense regions around $p_T \simeq 40$ GeV/c is the Jacobian peak. The Jacobian peak is significant at the mid-rapidity region of $|\eta| \lesssim 1.5$ for both W^+ and W^- , while it is less significant at forward rapidity. As shown in Figure 2.23, at the pseudorapidity region of $1.4 < \eta < 2.4$ the p_T spectrum of muons from W^\pm is rather continuum and the Jacobian peak barely remains only for W^+ . Next, seeing the signal distribution with projecting to pseudorapidity as Figure 2.23, for both W^+ and W^- the distribution decreases as the η increases. Precisely μ^+ from W^+ has steeper decreasing distribution than μ^- from W^- .

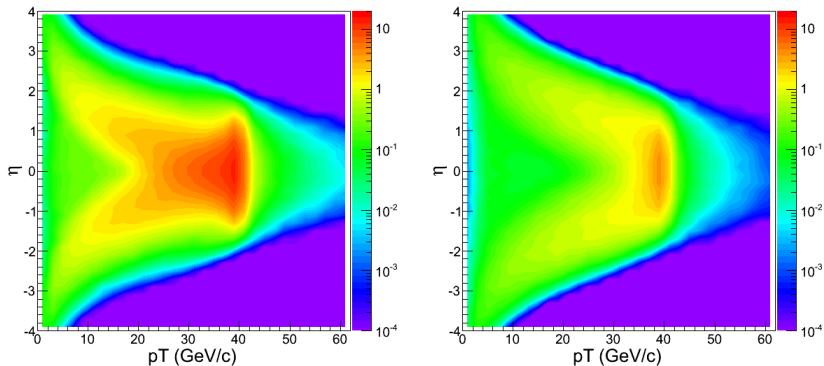


Figure 2.21: Distribution of muons from W^+ and W^- in p_T and η dimension.

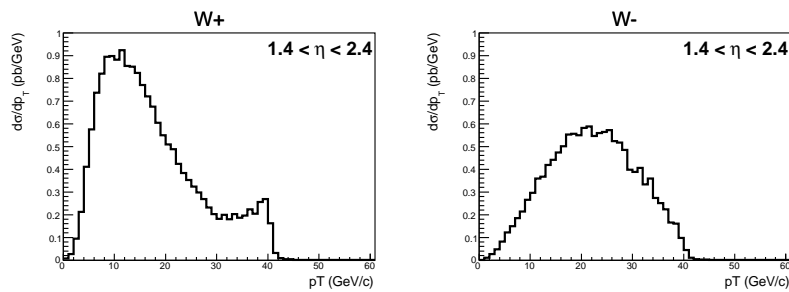


Figure 2.22: p_T distribution of μ^\pm from W^\pm in $1.4 < \eta < 2.4$.

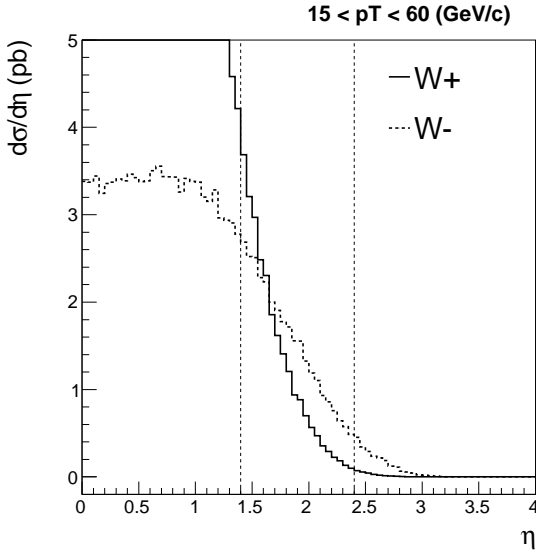


Figure 2.23: η distribution of μ^\pm from W^\pm in $15 < p_T < 60$ GeV/ c .

2.6.4.2 Backgrounds

The possible muon backgrounds of $W \rightarrow \mu$ signals are as follows:

- open heavy flavors (open bottom, open charm)
- quarkonia (J/ψ , Υ states)
- Drell-Yan
- Direct photon
- $W \rightarrow \tau \rightarrow \mu$
- $W \rightarrow \text{hadrons} \rightarrow \mu$

Figure 2.24 and 2.25 show the simulation of these backgrounds at $1.2 < \eta < 2.4$ with PYTHIA6 event generator[69]. The major muon backgrounds are open heavy flavors and quarkonia, and the p_T spectra of these processes are very similar and they decrease steeply with p_T . All background sources are well suppressed above $p_T > 20$ GeV/ c , then high p_T single muons are candidates of $W \rightarrow \mu$ events. $W \rightarrow \tau \rightarrow \mu$ could be a background which produces finite A_L , but its contribution is smaller than Drell-Yan and Z . Note that the finite momentum resolution of the detector smears the spectra then the $W \rightarrow \mu$ signals at high p_T region suffer more of backgrounds whose original momentum is lower than the reconstructed one. In addition to the above muon backgrounds, the signal would be buried by large amount of hadronic backgrounds (π^\pm, K^\pm), which will be described in the analysis part of this thesis. Indeed differentiating hadronic backgrounds is the most challenging issue of the experiment and the analysis in this thesis. We will confirm this in Sec. 7.3.2.

CHAPTER 2. PHYSICS BACKGROUNDS

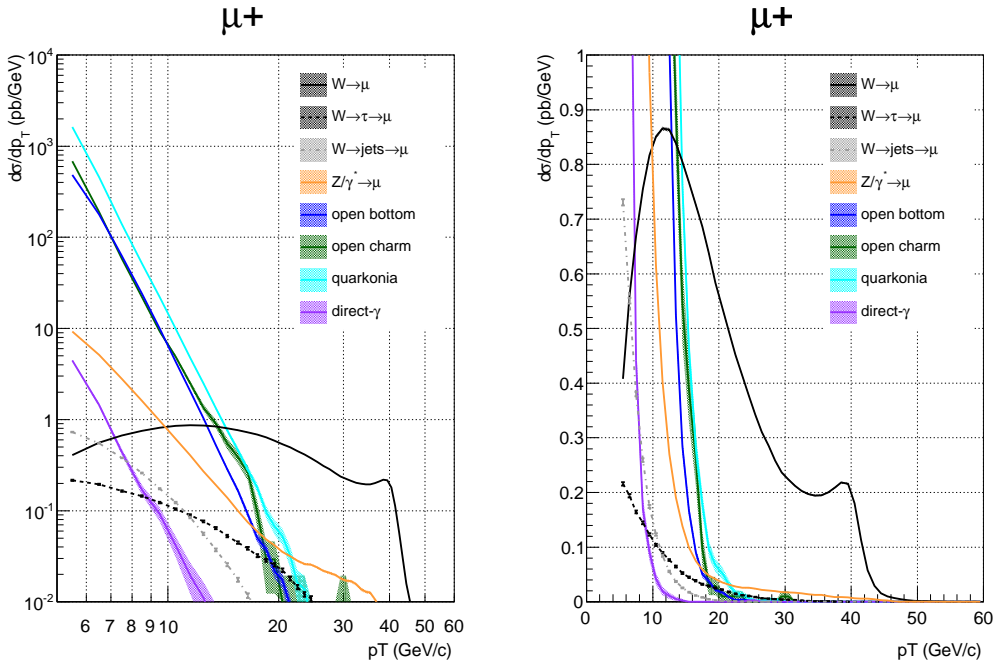


Figure 2.24: Simulated $W^+ \rightarrow \mu^+$ process and muon background processes at $1.4 < |\eta| < 2.4$ with PYTHIA.

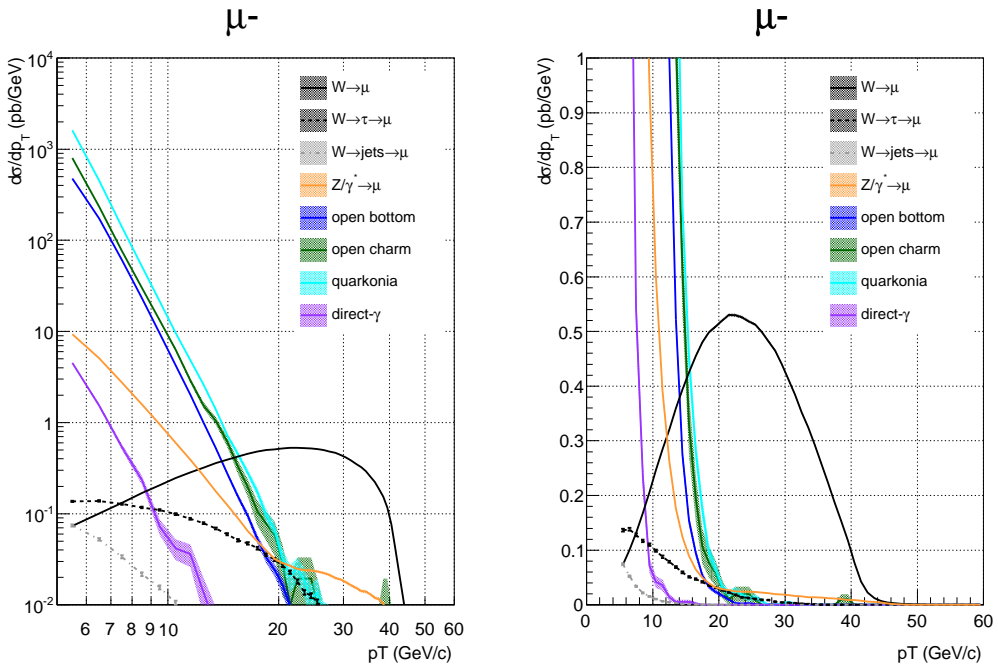


Figure 2.25: Simulated $W^- \rightarrow \mu^-$ process and muon background processes at $1.4 < |\eta| < 2.4$ with PYTHIA.

Chapter 3

Apparatus

In this chapter, experimental apparatus used in this thesis is described. In the first section the RHIC accelerator with respect to polarized proton collisions is described. In the second section the PHENIX detector is described. The third section describes the detail of the data acquisition (DAQ) and triggering. The last section is an overview of the simulations and the software framework.

3.1 RHIC as a polarized proton collider

The Relativistic Heavy Ion Collider (RHIC) at Brookhaven National Laboratory (BNL) is a unique collider which can collide heavy nuclei to create quark-gluon plasma state of matter as well as polarized protons for probing the spin structure of the proton. The RHIC is the first and only polarized proton-proton collider in the world. The RHIC can set the center of mass energy (\sqrt{s}) from 62.4 GeV up to 510 GeV for proton-proton collisions.

3.1.1 Polarized Beam source

The polarized proton beam source of the RHIC is called Optically-Pumped Polarized Ion Source (OPPIS)[45]. The OPPIS produces a $400 \mu\text{s}$ pulse of $\sim 10^{12}$ nuclearly polarized H^- ions with 35 keV of kinetic energy. H^- ions extracted from OPPIS are accelerated by RFQ to 750 keV and transferred to the LINAC. Several steps are there to obtain the nuclearly polarized H^- ions. First, H^+ ions are created with a 29 GHz Electric Cyclotron Resonance proton source. H^+ ions are accelerated to 3 keV to pass through a rubidium vapor cell in which polarized electrons created by a high-power titanium-sapphire 796 nm laser source with the optical-pumping mechanism are attached from rubidium ions to H^+ ions. The rubidium vapor cell is surrounded by a 2.5 T superconducting solenoid to prevent depolarization of polarized electrons. Then the H^0 gas is separated from remaining H^+ ions by deflection, and the polarization of the electron in the H^0 atom is transferred to the proton by the Sona transition[46]. The Sona transition is achieved by a adiabatic sweep of the external magnetic field from large positive to large negative values with small rapid oscillation within ± 1 gauss. Finally nuclearly polarized H^0 gas is attached an additional electron by spraying Na jet and H^- ions are transferred to the RFQ.

3.1.2 Accelerator complex

The RHIC accelerator complex consists of several components. Here the components related with acceleration and collision of polarized proton beams are briefly described.

CHAPTER 3. APPARATUS

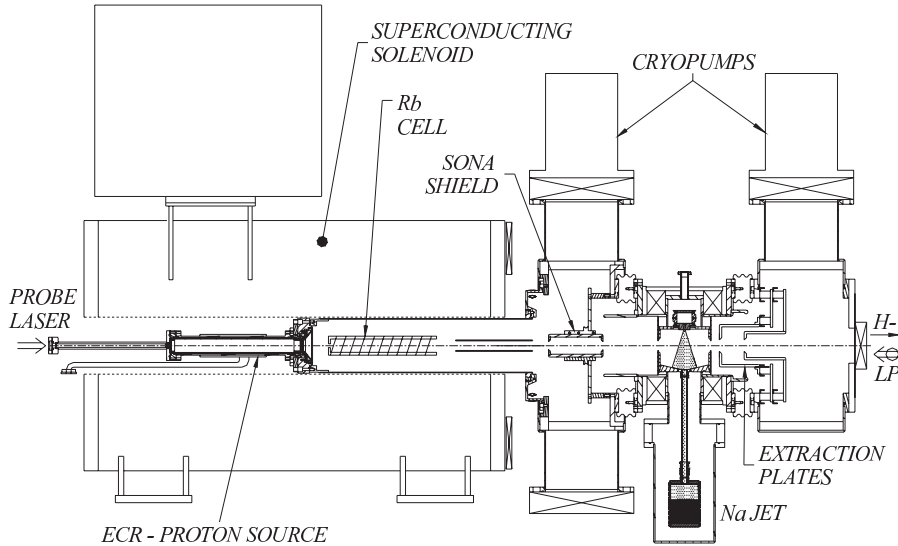


Figure 3.1: Schematic drawing of OPPIS[45].

LINAC The LINAC is a 200 MHz linear accelerator and it accelerates H^- ions to 200 MeV and strips the electrons away to inject proton beams into the Booster Synchrotron.

Booster Synchrotron The Booster Synchrotron accepts the proton beam from the LINAC of the $400 \mu s$ pulse into a single bunch, and it accelerates the proton bunch to 2.35 GeV and injects them into the AGS.

Alternating Gradient Synchrotron (AGS) The AGS is a pioneering accelerator operated since 1960, which employed the strong focusing principle with the concept of alternating gradient focusing. AGS accelerates polarized protons to 24.3 GeV and injects them to the RHIC.

Relativistic Heavy Ion Collider (RHIC) The RHIC is a double-ring superconducting collider which accelerates proton beams up to 255 GeV to achieve the center of mass energy (\sqrt{s}) from 62.4 GeV to 510 GeV. The circumference of the collider ring is 3.83 km, and each of two independent rings can fill maximally 120 proton bunches, namely the bunch crossing time period is 106 ns. As a matter of convention, the clockwise beam is named as “Blue beam”, and the counterclockwise beam is named as “Yellow beam”. In year 2011 runs, the RHIC achieved about 165×10^9 ions per bunch in proton-proton collisions, and the peak and average luminosity was $1.45 \times 10^{32} \text{ cm}^{-2}\text{s}^{-1}$ and $0.90 \times 10^{32} \text{ cm}^{-2}\text{s}^{-1}$, respectively. The typical lifetime of one fill is about 8 hours. There are six collision points in the RHIC. For each collision point two beams are merged with the DX dipole magnets and they make head-on collisions.

Pattern Name	Blue beam	Yellow beam
P1	+ - + - - + - + ...	+ + - - + + - - ...
P2	- + - + + - + - ...	+ + - - + + - - ...
P3	+ - + - - + - + ...	- - + + - - + + ...
P4	- + - + + - + - ...	- - + + - - + + ...

Table 3.1: The “spin patterns” used in year 2011 runs.

For each bunch the nominal direction of the polarization can be either vertical-up (+) or vertical-down (-). The pattern of the spin direction is selected so that all possible four pattern collisions, i.e., $\{++, +-, -+, --\}$ take place almost equally. Several patterns are provided by the accelerator group as shown in Table 3.1, and the pattern is usually different fill by fill. 10 packets out of 120 (#110 - #119) are reserved for utility time (“abort gap”), such as laser calibration of the detector, and each beam has two bunch-length blanks (“keys”) at different bunch crossings (#38 and #39 for the Blue beam, #78 and #79 for the Yellow beam) to crosscheck the pattern. The spin direction at the moment of the collision is controlled by the spin rotators which are set both outside the DX magnets with respect to the collision point, and longitudinal (spin oriented along with the beam axis), vertical (spin oriented perpendicularly), and radial (spin oriented along with radial axis) collisions are possible independently for each collision point. Controlling the spin of proton beams are described in the next subsection.

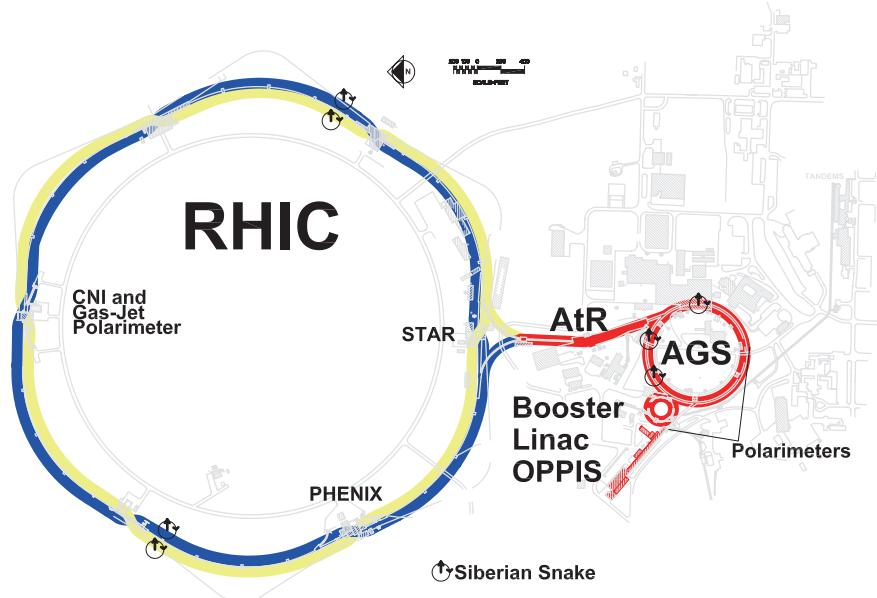


Figure 3.2: RHIC accelerator complex. 1) Tandem Van de Graaff used for heavy ions, 2a) Tandem-to-Booster line, 2b) Linac for polarized protons, 3) Booster Synchrotron, 4) Alternating Gradient Synchrotron (AGS), 5) AGS-to-RHIC Line, 6) RHIC.

3.1.3 Control and measurement of polarization

3.1.3.1 Siberian Snakes and Spin Rotators

The polarization of proton beams may be lost during acceleration and collision. The reason of depolarization is classified into two; one is due to imperfection of dipole and quadrupole magnetic field caused by mis-alignment, *etc.*, the other is due to the existence of intrinsic spin resonance cased by spin precession around the radial field components in the focusing magnets. Both of them can be prevented by inserting instruments named “Siberian snakes” [47, 48]. A Siberian Snake consists of helical dipoles, in which the direction of spin of the proton is rotated by 180° in the full Snake case or at a certain degree in the partial Snake case. By using Siberian Snakes, the effect of depolarizations in the beam path is cancelled out between one and the

next circulation of the beam. The AGS employs a 9° partial Snake, and the RHIC employs two full Snakes.

The Spin rotator is a similar instrument as the Siberian Snake, which consists of four helical dipoles, but the helicity of the two of them is opposite to the others. By tuning the current weaker than the Siberian Snake, it is possible to rotate the direction of spin of proton beams. Figure 3.4 shows the precession of the proton spin through a RHIC Siberian Snake and a Spin Rotator.

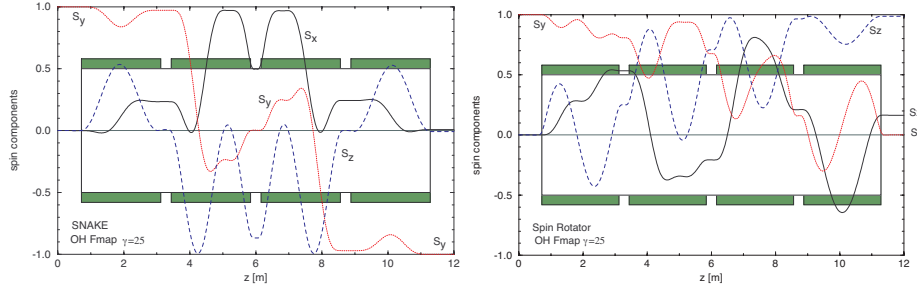


Figure 3.3: (Left) The spin precession at the Siberian Snake to flip the direction, (Right) The spin precession at the Spin Rotator from vertical to longitudinal direction. The figures are taken from[48].

3.1.3.2 Polarimetry

The RHIC employs three different types of polarimeters to measure the polarization of the beam. The principle of all three polarimeter is the same, i.e., to measure the transverse spin asymmetry. The transverse spin asymmetry and its raw asymmetry, denoted as A_N and ε_N respectively, are defined as

$$\varepsilon_N \equiv PA_N \equiv \frac{N_L - N_R}{N_L + N_R} \quad (3.1)$$

where P is the polarization of either the beam or the target, and $N_{L(R)}$ is the number of events detected at the left(right)-side detector with respect to the beam direction. The Coulomb-Nuclear Interference (CNI) polarimeter uses thin carbon ribbons to measure the polarization profile of the beam[50]. The CNI polarimeter gives the relative polarization precisely, however, the absolute polarization is not available. The Hydrogen jet (H-jet) polarimeter is provided to measure the absolute polarization of the beam with the polarized hydrogen gas jet[51, 52]. The H-jet polarimeter is used to calibrate the CNI polarimeter. These two polarimeters are globally used in the RHIC. Apart from these, the third polarimeter is set in the PHENIX detector, called as the Local polarimeter[53]. The local polarimeter is used to validate the polarization value obtained in the CNI and H-jet polarimeters in the vertical collision case, or to validate the spin direction is appropriately rotated in the longitudinal collision case. In particular, the Local polarimeter is important as the remaining transverse polarization of the beam could be a source of systematic uncertainties of the spin asymmetry measurement.

Coulomb-Nuclear Interference (CNI) polarimeter The Coulomb-Nuclear Interference (CNI) polarimeter measures the transverse spin asymmetry of recoil carbons scattered about 90° with respect to the beam direction in $p^\uparrow + C \rightarrow p + C$ Coulomb-nuclear interference elastic scattering by inserting horizontal and vertical thin carbon ribbons into the beam path. The recoil carbons are detected with six silicon detectors surrounding the beam path. The width

3.1 RHIC as a polarized proton collider

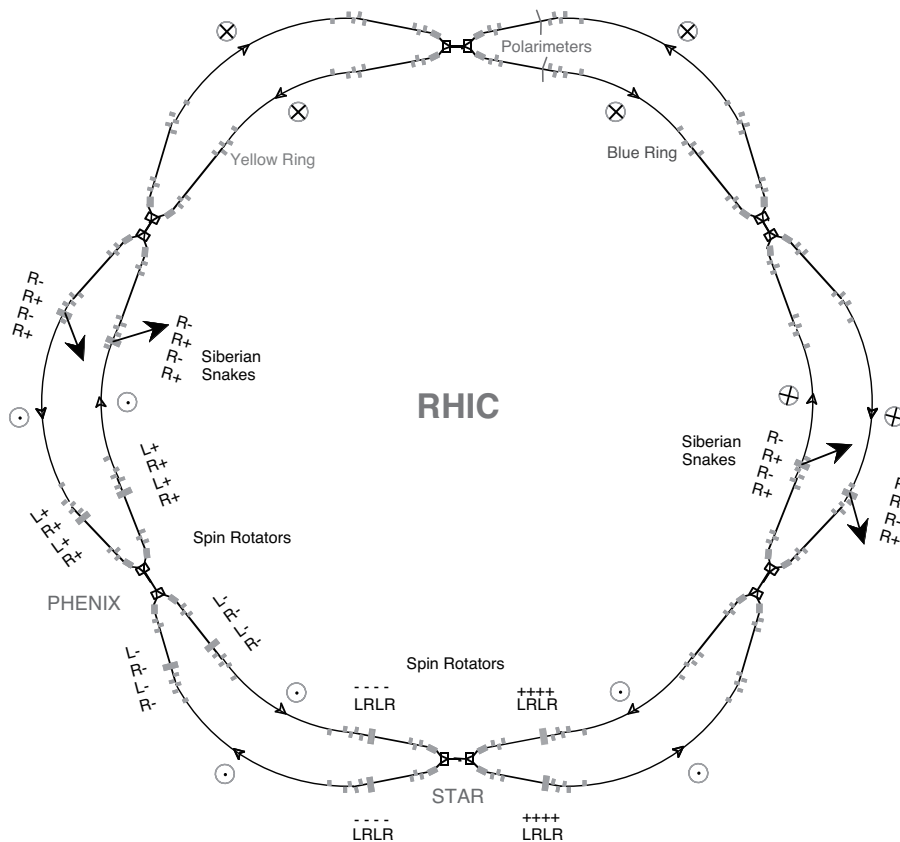


Figure 3.4: View of RHIC overemphasizing the interaction regions to show the location of the Siberian Snakes and the spin rotators placed around the collider experiments STAR and PHENIX. Also shown are the polarization directions around the rings and around the detectors for collisions with longitudinal polarization. The figure is taken from [49].

CHAPTER 3. APPARATUS

of the ribbon is $10 \mu\text{m}$, thus the CNI polarimeter is possible to scan the polarization profile of the beam. Thanks to the large cross section of proton-carbon elastic scattering, the CNI polarimeter collects about 4×10^6 recoil carbons per one scanning, which takes time about one minute. Consequently two or three times of polarization measurements are possible per one fill, which are used to chase the long-term polarization decrease during the fill. Since the true transverse asymmetry A_N for proton-carbon elastic scattering is not known, the CNI polarimeter measures polarization relatively. For the absolute calibration of the CNI polarimeter, the H-jet polarimeter is used, which is described in the next paragraph.

Hydrogen jet polarimeter The Hydrogen Jet (H-jet) polarimeter uses a polarized hydrogen gas jet stream as a target. The direction of the polarization of the gas is vertical and the direction is flipped to opposite in every 10 minutes. The event rate of H-jet polarimetry is about 5 Hz, and the dilution of the hydrogen gas is enough not to affect to the physics measurement of the collision. Thus the H-jet measurement is continuously taking during the fill. The absolute polarization of the hydrogen jets is absolutely measured with a Breit-Rabi polarimeter. The elastic scattering of the proton beam and the proton target is measured with silicon detectors similar to the CNI polarimeter. We can measure the raw transverse asymmetry for both the beam and the target by averaging the polarization of the other hand, thus we obtain the following relation:

$$A_N = \varepsilon_N^{\text{beam}} / P_{\text{beam}} = \varepsilon_N^{\text{target}} / P_{\text{target}} . \quad (3.2)$$

By using the polarization value of the jet target measured with the Breit-Rabi polarimeter, we obtain the absolute polarization of the beam.

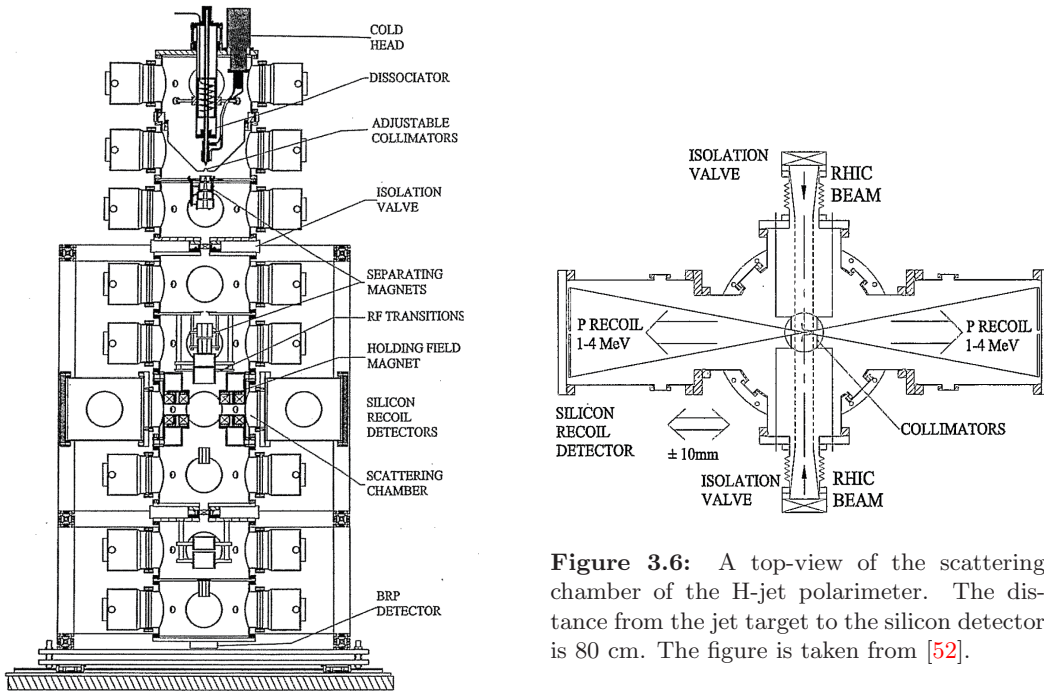


Figure 3.5: A general layout of the H-jet polarimeter. The figure is taken from [52].

Figure 3.6: A top-view of the scattering chamber of the H-jet polarimeter. The distance from the jet target to the silicon detector is 80 cm. The figure is taken from [52].

3.1 RHIC as a polarized proton collider

PHENIX local polarimeter For longitudinally polarized collisions, we need to rotate the spin of the beam from the nominal vertical orientation to the longitudinal orientation by the Spin rotators described in Sec. 3.1.3.1. To ensure that the spin orientation does not have residual transverse components, the local polarimeter is used at the PHENIX detector. As a hardware the local polarimeter is identical to the Zero Degree Calorimeter (ZDC) as a hardware which will be described in Sec. 3.2.3.5. These detectors are located between Blue and Yellow beam rings next to the DX magnets as shown in Figure 3.7, and the distance from the collision point of the PHENIX detector is about 18 m. Here all charged particles are deflected by the DX magnet, and only neutral particles inject to ZDCs. Substantially ZDCs detect neutrons produced by collisions mainly. The neutron production in proton-proton collision has a transverse single spin asymmetry of $A_N \sim 10\%$, but it should not have longitudinal single spin asymmetry, since the longitudinal single spin asymmetry is parity-violating. Thus we can measure the residual transverse polarization with ZDCs.

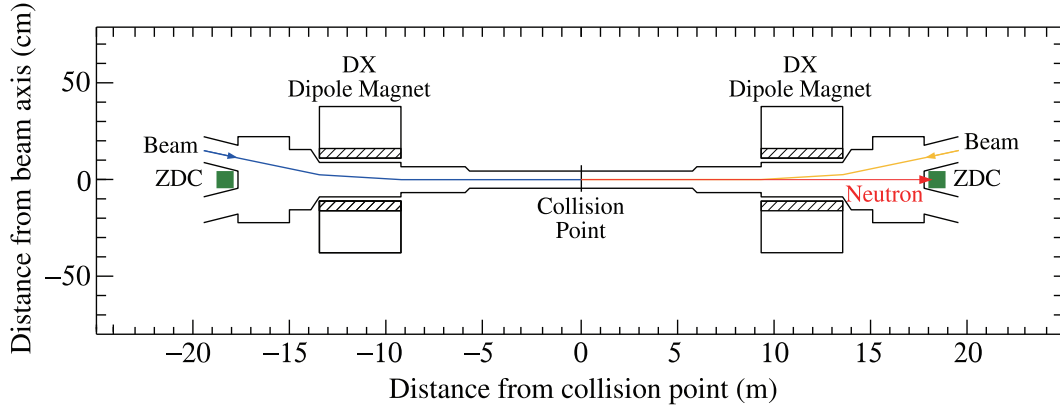


Figure 3.7: Geometric location of the Local polarimeter (ZDC,SMD) of the PHENIX detector.

3.2 PHENIX detector

3.2.1 Overview

The PHENIX is a large-scale multi-purpose detector system. It is located at one of 6 collision points of the RHIC called “8 o’clock”. It assembles four large spectrometers as well as complementing detectors. The four spectrometers cover different rapidity ranges. Two spectrometers which cover forward rapidity regions of about $-2.2 < \eta < 1.2$ and $1.2 < \eta < 2.4$ are called Muon Arms named after their specialization to detect muons. The other two spectrometers are called Central Arms which cover twice of 90° in azimuthal angle ϕ in the rapidity region of $|\eta| < 0.35$. The Central Arms are specialized to detect electrons, photons and hadrons with particle identification detectors. In addition to these large spectrometers, the PHENIX has the Muon Piston Calorimeters (MPC) which cover forward rapidity region of $3.1 < |\eta| < 3.7$. The PHENIX detector is applicable to measure both heavy ion collisions and polarized proton-proton collisions.

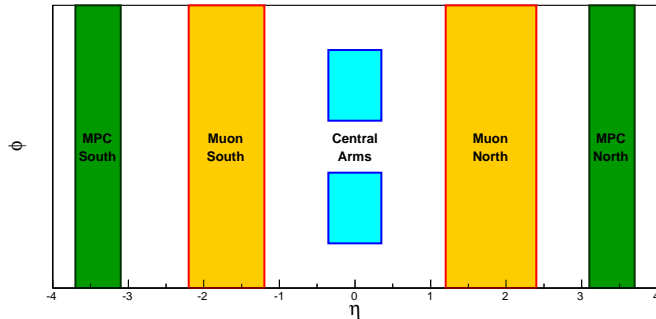


Figure 3.8: Geometrical acceptance of the PHENIX detector.

PHENIX coordinate system and conventions The PHENIX Cartesian coordinate system sets the origin at the nominal collision point at 8 o’clock of the RHIC. The z -axis is taken along the beam axis in clockwise, and its direction is clockwise seen from above. The y -axis perpendicular from bottom to top, and the x -axis is horizontal and it directs to the outside of the RHIC ring so that the resulting coordinate system is right-handed. The $-z$ direction is called “South” side and the $+z$ direction is called “North”, the $+x$ direction is called “West” and the $-x$ direction is called “East”, named after the geographical direction. We call a Muon Arm in the North (South) side “North (South) Arm”. Similarly, a Central Arm in the East (West) side is called “East (West) carriage”. The clockwise beam coming from $-z$ (South) to $+z$ (North) is called “Blue beam” and the counterclockwise beam from $+z$ (North) to $-z$ (South) is called “Yellow beam”. The radial distance r is defined as $\sqrt{x^2 + y^2}$. The polar angle θ is defined as the angle between the positive z -axis and the vector. The azimuthal angle ϕ is defined as the angle between the positive x -axis and the vector projected to the xy -plane. The pseudorapidity η is defined as $\eta = -\ln[\tan(\theta/2)]$. Note that for the longitudinal spin asymmetry calculation the polar angle is defined between the spin orientation of the polarized proton and the vector. Thus the definition of the polar angle changes which of two beams we take as the polarized beam. For the Blue beam case the definition of polar angle is the same as the PHENIX coordinate system. For the Yellow beam case we measure the polar angle as if the sign of z -axis is flipped then the sign of η becomes opposite. Hereafter we will use these conventions.

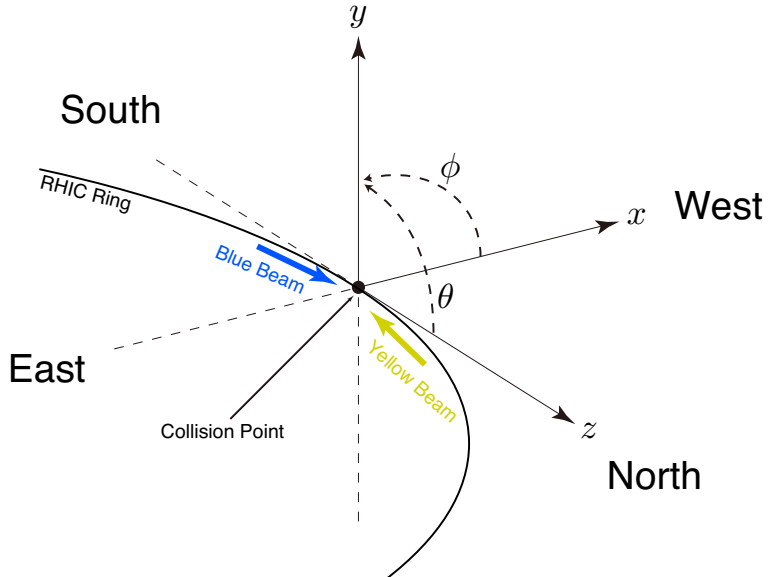


Figure 3.9: The coordinate system of the PHENIX detector.

Muon Arms The Muon Arms^[57] are specialized to measure muons. The acceptance of the South and the North Arms are not identical ($-2.2 < \eta < -1.2$ for the South and $1.2 < \eta < 2.4$ for the North). Muons or hadrons produced by collisions in the acceptance of Muon Arms first pass through the Central Magnet. The Central Magnet works as a hadron absorber, then small fraction of hadrons and muons traverse the Muon Trackers (MuTr), in which layered cathode strip chambers measure the position of the particles. After passing MuTr particles inject into the Muon Identifier (MuID). The MuID consists of five layers of alternate Iarocci tube detectors and steel walls. Most of surviving hadrons are absorbed gradually with the depth of layers. Both MuTr and MuID can issue triggers for the data taking. At the back of the fifth steel absorber wall the Resistive Plate Chamber (RPC3) is newly installed before year 2011 runs, which is also possible to trigger with a fast timing resolution of ~ 2 ns. Note that the acceptance of RPC3 is smaller than MuTr ($1.4 < |\eta| < 2.4$)¹. Details of sub-detectors of Muon Arms will be described in Sec. 3.2.3.

Central Arms The Central Arms^[54–56] measure electrons, charged hadrons, photons, π^0 at mid-rapidity of $|\eta| < 0.35$. The detailed specifications are different between the West and the East Carriage. The central Vertex detector (VTX) was newly installed in 2011 at the most inner part of the Central Arms to measure the primary vertex position and distance of closest approach of charged tracks². Particles passing the VTX inject a composite of the Pad Chambers (PC), the Ring Image Cherenkov Counters (RICH), the Drift Chambers (DC), and the Electromagnetic Calorimeters (EMCal). Depending on the ϕ -angle of the particle it may also pass through the Time Expansion Chambers (TEC), the Aerogel Cherenkov detectors (Aerogel), the Time-of-flight detector (TOF). Charged particles or photons are triggered by the cooperation of the EMCal and the RICH. Tracking is performed with the DC, PC, and VTX.

¹The missing coverage of the RPC3 is complemented from year 2012 runs by the RPC1 which sits in front of the MuTr.

²However during the proton-proton collision runs the VTX was under commissioning and it substantially did not take data in 2011.

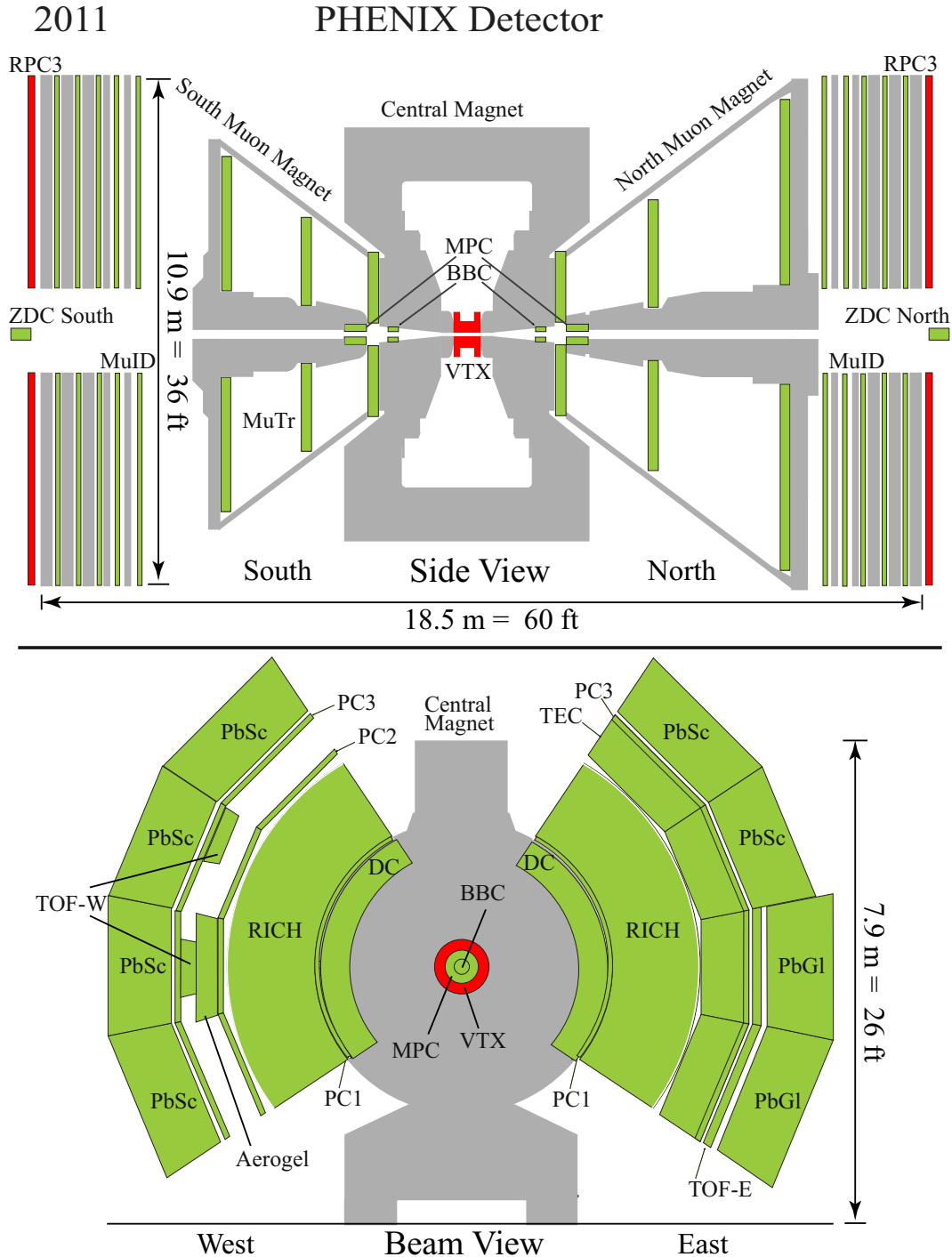


Figure 3.10: Detector subsystems of the PHENIX detector in year 2011 run setup. (Above): A side view featuring Muon Arm detectors and forward detectors. (Below): A beam view featuring Central Arm detectors. The Muon Arms cover 2π azimuthal (ϕ) angle in the rapidity ranges of $-2.2 < \eta < -1.2$ and $1.2 < \eta < 2.4$, whereas the Central Arms cover $2 \times 90^\circ$ in azimuthal (ϕ) angle in the rapidity range of $|\eta| < 0.35$.

Muon Piston Calorimeters (MPC) The Muon Piston Calorimeters cover forward rapidity of $3.1 < |\eta| < 3.7$, which is made of lead-tungsten glass (PbWO_4). The MPC mainly aims to reconstruct π^0 or η mesons.

Global detectors The Beam Beam Counters (BBC) and the Zero Degree Calorimeters (ZDC) are categorized as the global detectors in the meaning that those are commonly used by all measurements. The Beam Beam Counters (BBCs) are used to monitor the luminosity as well as to reconstruct the interaction point. The Zero Degree Calorimeter (ZDCs) was already introduced in Sec. 3.1.3.2. Details of the BBCs and the ZDCs are described in Sec. 3.2.3.4 and 3.2.3.5, respectively.

Configuration of the PHENIX in year 2011 runs The composition of sub-detectors is different almost year by year to adopt to different physics purposes with continuous upgrading. Related to the measurement of muons from W boson decays, the PHENIX collaboration has an upgrade program to install new detector subsystems listed as follows.

- MuTr trigger electronics (Mutrg)
- Resistive Plate Chambers (RPC3 and RPC1)
- Extension of hadron absorbers
- VTX and FVTX (forward vertex) detectors

The above upgrade program was in progress at the time of year 2011 runs, at that moment RPC1 and FVTX detectors had not been installed. Table 3.2 summarizes the installed detectors in year 2011 runs.

Abbr.	Name	Division	Purpose	Trigger
BBC	Beam Beam Counters	Global	luminosity monitoring	×
			minimum bias trigger	
			vertex determination	
			centrality ^a measurement	
ZDC	Zero Degree Calorimeters		neutron/local polarimetry	×
MuID	Muon Identifier	Muon	muon triggering and ID	×
RPC3	Resistive Plate Chambers-3		fast muon triggering and ID	×
MuTr	Muon Tracker		tracking and triggering	×
PC	Pad Chambers	Central	tracking/z-pos. determination	
DC	Drift Chambers		tracking	
TEC	Time Expansion Chambers		tracking	
RICH	Ring Image Cherenkov Counters		PID/triggering	×
Aerogel	Aerogel Counters		PID	
TOF	Time-of-flight counters		PID	
EMCal	Electromagnetic Calorimeters		calorimetry/ $e\pi$ -ID/triggering	×
VTX	Vertex (central)		primary vertex identification heavy flavor tagging	
MPC	Muon Piston Calorimeters	MPC	calorimetry (π^0, η)	×

^aA measure of overlapping of two colliding nuclei for heavy ion collisions.

Table 3.2: Detector subsystems installed in year 2011 runs.

CHAPTER 3. APPARATUS

Year		2009			2010		2011			2012				
Run Status		pp	HI	end	HI	end	pp	HI	end	pp	HI	end		
Muon	Mutrg		install/commissioning					operation (trigger)						
	RPC3	S	N/A				install	operation			operation (trigger)			
		N	N/A	install	commissioning				commissioning / operation					
	RPC1		N/A					install	commissioning / operation					
	FVTX		N/A						commissioning / operation		commissioning / operation			
Central	HBD	operation	removed											
	VTX	N/A			install	comm.	operation							

Figure 3.11: History of the PHENIX detector upgrades related with the measurement of muons from W/Z decays from 2009 to 2012.

3.2.2 Magnets and hadron absorbers

PHENIX magnets The magnet of the PHENIX consists of three parts; the Central Magnet and the two Muon Magnets (Figure 3.13). The Central Magnet creates the magnetic field along with the beam axis (z -direction) by two pairs of concentric coils, then charged particles bend in the azimuthal direction. As the Central Arms have PID detectors (RICH, TOF, Aerogel), it is desirable that the material between the collision point and the Central Arms is as low as possible. In addition, PMTs used in the RICH and the TOF should not be operated in strong magnetic fields. This is the major constraint to design the Central Magnet. The integrated magnetic field of the Central Magnet is $0.78 \text{ T} \cdot \text{m}$, while the field strength at the position of the RICH is about 200 gauss. The limited acceptance of the Central Arm detectors allows to put the return yokes at the top and the bottom of the Central Magnet to connect the two magnets at the both sides of the collision point surrounding the beam axis. While the Central Magnet is designed to minimize the materials through the path of particles flying to central rapidity region, it also works as a hadron absorber for forward rapidity. A Muon Magnet has two solenoidal coils in the tapered core of the Muon Arm called the Muon Piston to produce a radial field. The field flux is saturated in the Muon Piston and it diverges radially from the Muon Piston to the eight-frustum yoke called *lampshade*, then returns via a 30 cm thick endplate. The integrated magnetic field at $\theta = 15^\circ$ is $0.72 \text{ T} \cdot \text{m}$. Table 3.3 summarizes the key parameters of the magnets. Figure 3.13 shows the field lines of the PHENIX cut in the yz -plane.

parameters	Central Magnet	Muon Magnets
type	two pairs of concentric coils	solenoidal coils
field	solenoidal	radial
mass	500 tons	400 tons/arm
height	9 m	10 m
rapidity coverage	$ \eta < 0.35$	$1.1 < \eta < 2.4$
integrated field $\int \mathbf{B} \cdot d\mathbf{l}$	$0.78 \text{ T} \cdot \text{m}$	$0.72 \text{ T} \cdot \text{m}$ at $\theta = 15^\circ$

Table 3.3: The key parameters of the Central Magnet and the Muon Magnets.

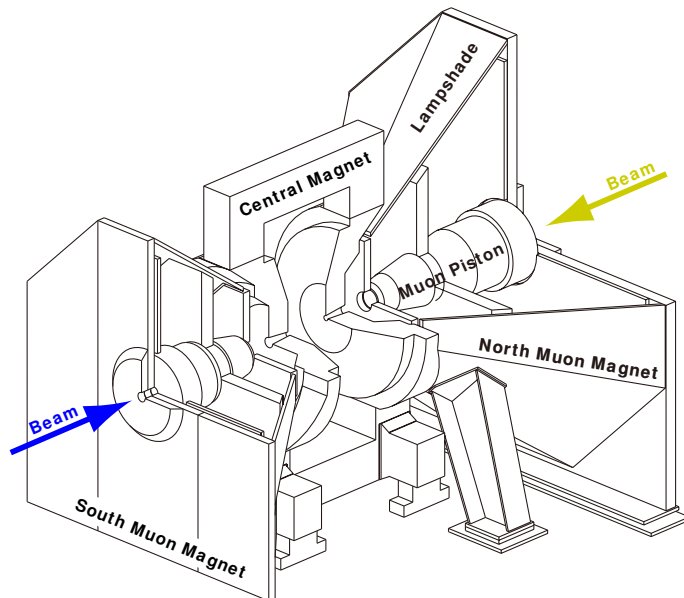
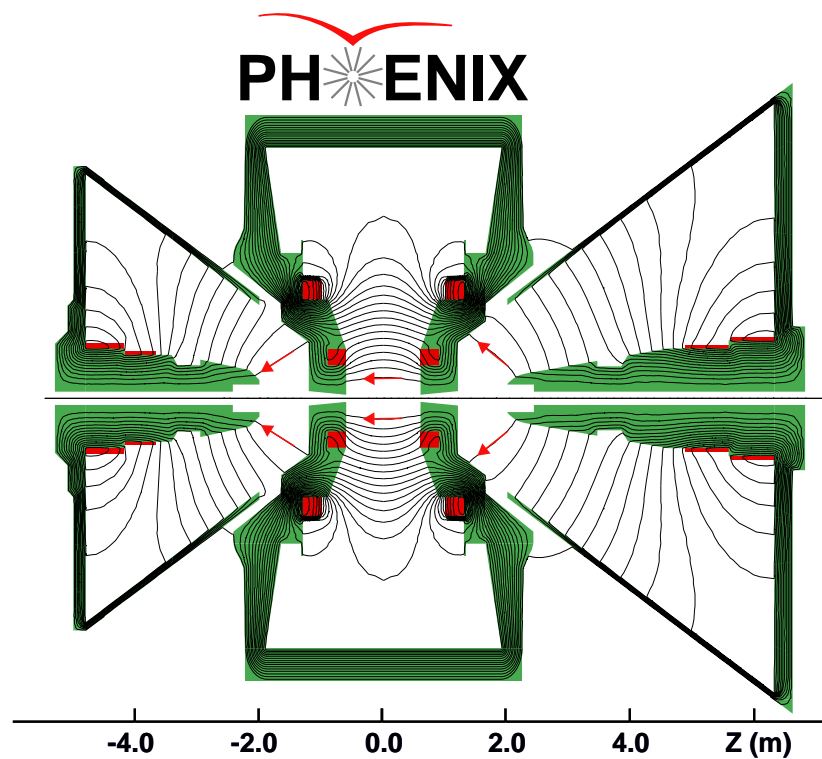


Figure 3.12: Overview of the PHENIX magnets.



Magnetic field lines for the two Central Magnet coils in combined (++) mode

Figure 3.13: PHENIX magnetic field lines in (++) mode.

CHAPTER 3. APPARATUS

Hadron absorbers As described above, the Central Magnet has a role of hadron absorber. At the inner surface of the Central Magnet 20 cm-thick copper nose cones are equipped. The Central Magnet steel has 60 cm thickness. The sum of these absorbers has hadronic interaction length of $4.9\lambda_I/\cos\theta$. In addition to these existing absorbers, new absorbers were installed at the rear surface of the Central Magnet for the measurement of $W^\pm \rightarrow \mu^\pm$ measurement (Figure 3.14). The new hadron absorber is the 35 cm-thick SS310 plates with 24 tons. SS310 is Cr (24 - 26 %) and Ni (19 - 22 %) enriched austenite phase stainless steel. By installing the new absorber, the pre-MuTr absorber presents a total thickness of $7.1\lambda_I/\cos\theta$, which corresponds to hadron reduction of $\sim 10^{-3}$.

Behind the MuTr there are also other absorbers as a part of the Muon Magnet and a part of the MuID. The thickness of the Muon Magnet Yoke (backplane) is 20 cm for the South Arm and 30 cm for the North Arm. The MuID has five steel walls in each arm. The total thickness of the MuID steel walls is 80 cm. The total interaction length from the origin to the rear of the MuID (at the location of the RPC3) is $13.0\lambda_I$ ($13.4\lambda_I$) for the South (North) Arm. Due to ionization energy loss, a particle must have a momentum at the vertex which exceeds $2.71/\cos\theta$ GeV/c ($2.85/\cos\theta$ GeV/c) to the location of the RPC3 for the South (North) Arm. Table 3.4 summarizes the specification of the hadron absorbers.

Location	Material	South	North	$\lambda_I/\cos\theta$
		Thickness (cm)	Thickness (cm)	
Nose cone	Copper	20	20	1.8
Central Magnet	Steel	60	60	3.1
New absorber	SS310	35	35	2.2
Sum of pre-MuTr	-	115	115	7.1
Muon Magnet Yoke	Steel	20	30	S:1.1, N:1.5
MuID 1st Layer	Steel	10	10	0.6
MuID 2nd Layer	Steel	10	10	0.6
MuID 3rd Layer	Steel	20	20	1.2
MuID 4th Layer	Steel	20	20	1.2
MuID 5th Layer	Steel	20	20	1.2
Total	-	215	225	S:13.0, N:13.4

Table 3.4: Parameters of hadron absorbers in the PHENIX detector.

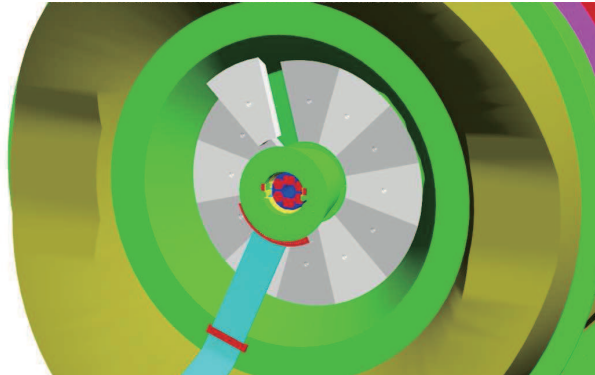


Figure 3.14: A layout of extended hadron absorbers.

3.2.3 Detector subsystems

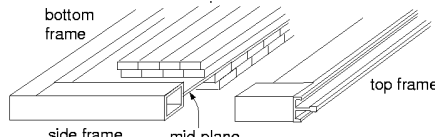
In this section details of detector subsystems used in this thesis are described.

3.2.3.1 Muon Identifier (MuID)

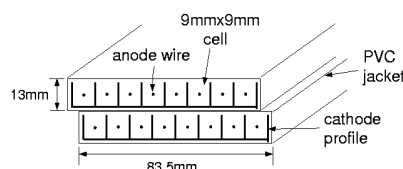
The Muon Identifier (MuID) is a trigger detector of the Muon Arm as well it provides the seed of the offline tracking. It is located behind the Muon Magnet of each arm. It has a sandwich structure of alternate five layers of steel walls and coarse gas chambers. The detector layer is also called as “gap”, named after that it is in the gap between the steel walls. The width and the height of the gap is about 15 m and 10 m, respectively. The depth of each steel wall is written in Table 3.4. The detector is composed of a aluminum-frame wire chamber called Iarocci streamer tube (Figure 3.15). A unit of the Iarocci tube used in the MuID is an array of nine 9×9 mm wire cells with a few meter length, and each cell has an anode wire surrounded by a square cathode. The gas is the mixture of 92 % CO₂ and 8 % isobutane. The applied high voltage is 4300 - 4500 V, which achieves the multiplication of $\sim 2 \times 10^4$. Two units of Iarocci tube arrays are bundled with shifting by a half cell each other, and this becomes the unit of the readout of one channel called “two-pack”. One gap of the MuID is divided in six panels as shown in Figure 3.16, and each panel has horizontal and vertical arrays of two-packs.

Parameter	Design
Width	13 m
Height	10 m
Gaps	5
Panels per gap	4 (large) + 2 (small)
Segmentation	8.35 cm (X,Y)
Gas constituent	CO ₂ (92 %) + isobutane (8 %)
Operational voltage	4300 - 4500 V
Multiplication	$\sim 2 \times 10^4$
Drift time	~ 60 ns

Table 3.5: Parameters of MuID.



Cross section of the MuID panel



Cross section of the plastic tube(2-pack)

Figure 3.15: A drawing of Iarocci streamer tubes in the MuID.

CHAPTER 3. APPARATUS

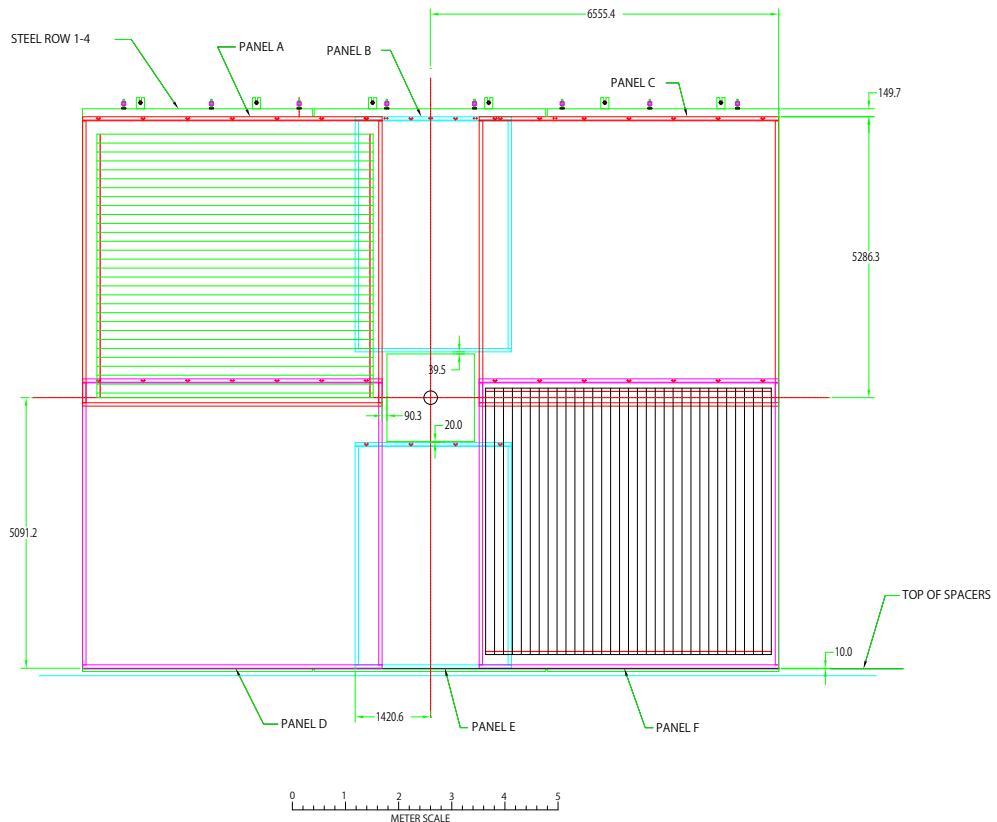


Figure 3.16: A drawing of one gap of the MuID. A gap consists of six panels. Each panel has a horizontal tube array and a vertical tube array of two-packs. Dimensions are in mm.

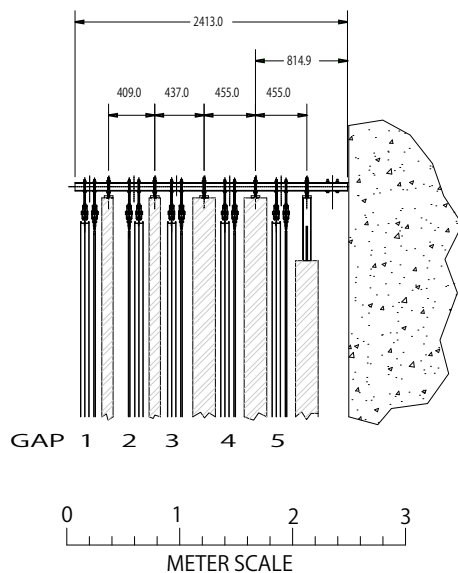


Figure 3.17: A side view drawing of the MuID gaps. The hatched materials are the steel wall absorbers. Dimensions are in mm.

MuID electronics The signal created at the two-pack wires is read with a differential-output preamplifier of a gain of ~ 150 , which gives about ± 20 mV pulse height for minimum ionization particles. The amplified analog signals are sent to the readout card (ROC) then converted into positive-going single-ended signals, then they are digitized to binaries with a constant fraction discriminator. The latch width is set 2 beam clocks. The digitized signals are buffered in the 64 beam-clock buffer, while the data are sent to the local level-1 (LL1) trigger board. The LL1 trigger board judges the trigger condition based on the hit pattern for each beam clock (see Sec. 3.3.2.2 in detail). If triggered, the data in the ROCs are multiplexed and transferred to the front-end module (FEM), and the data is formatted at the FEM. Finally the FEM sends data to the data collection module (DCM).

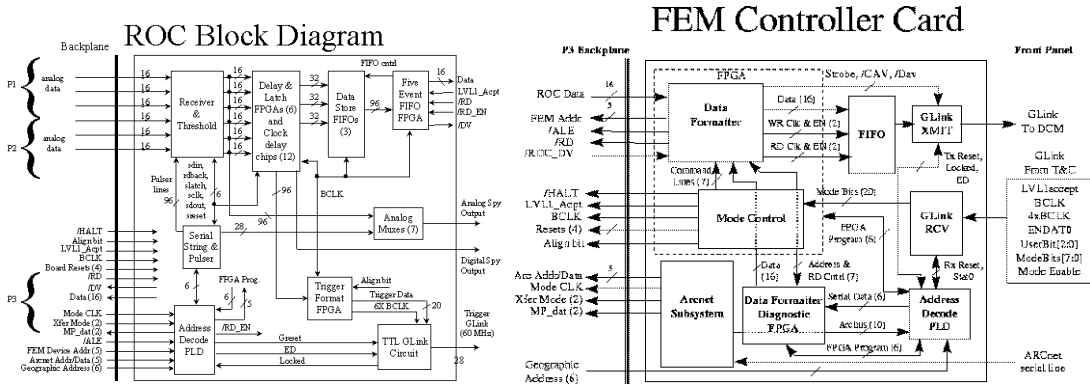


Figure 3.18: Block diagram of the MuID readout card (ROC) and front-end module (FEM).

3.2.3.2 Muon Tracker (MuTr)

The Muon Tracker (MuTr) is the main tracking detector of the Muon Arms. Three strata of cathode strip chambers called “stations” which cover most of the azimuths are built inside the “lampshade” of the Muon Magnets. The South MuTr covers $12.5^\circ - 35^\circ$ ($-2.2 < \eta < -1.1$), and the North MuTr covers $10^\circ - 35^\circ$ ($1.1 < \eta < 2.4$) of the polar angle. The z -position of the three stations are distant from the origin by 1.80, 3.00, 4.60 m for the South Arm and 1.80, 3.47, 6.12 m for the North Arm, respectively. The three stations are called Station-1,2,3 counting from inner to outer. The first station (Station-1) consists of four identical segments called “quadrants”, while the second and third stations (Station-2,3) consist of eight segments called “octants”. The stations consist of multi-layer cathode strip chambers. A quadrant of the Station-1 and an octant of the Station-2,3 are further segmented into two in azimuthal direction, each of them is called “octant” and “half octant”, respectively. A layer of a station is a cathode strip chamber and it is called “gap”. The distance between the two cathode planes of the gap is 6.4 mm. The number of layers of the Station-1,2,3 is 3, 3, 2, respectively. As the magnetic field is radial then charged tracks are bent in ϕ -direction, the cathode planes of the chamber is etched strips in roughly radial direction by 5 mm pitch, and the $\phi 20\text{ }\mu\text{m}$ gold-plated tungsten anode wires and $\phi 75\text{ }\mu\text{m}$ gold-plated copper-beryllium field wires are stretched to the azimuthal direction alternately. The distance between the anode and the field wire is 5.0 mm. Both side cathodes of the chamber is used for readout. The direction of one cathode plane strips of the chamber is exactly radial at the center of the half octant, and the direction of the other cathode plane is tilted relatively by a certain small angle to measure the radial position of the particle injection. The tilt angle is slightly different by chambers. The tilted planes are called “stereo planes”, and the radial planes are called “non-stereo planes” in the nomenclature. The

CHAPTER 3. APPARATUS

strips have no intersections and they run through the octant from the inner edge to the outer edge. Not all strips are read out, active strips and grounded strips come alternately. The gas mixture is Ar/CO₂/CF₄ = 50/30/20 %. The nominal high voltage applied to the anode wires is 1900 V and the typical multiplication gain is 2×10^4 .

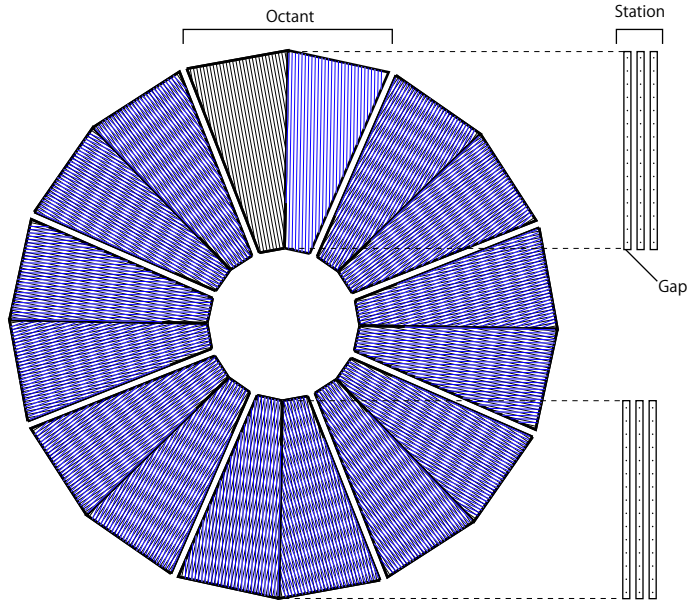


Figure 3.19: Schematic drawing of one chamber layer of the MuTr. The black lines represent the non-stereo plane and the blue lines represent the stereo plane.

Parameter	South (St. 1 / 2 / 3)	North (St. 1 / 2 / 3)
$ z (m)$	1.80 / 3.00 / 4.60	1.80 / 3.47 / 6.12
Radius (m)	1.26 / 2.10 / 3.22	1.26 / 2.43 / 4.29
Number of gaps	3 / 3 / 2	3 / 3 / 2
Number of cathode planes	6 / 6 / 4	6 / 6 / 4
Number of RO channels/octant/plane	96 / 160 / 256	96 / 192 / 320

Table 3.6: Parameters of the MuTr.

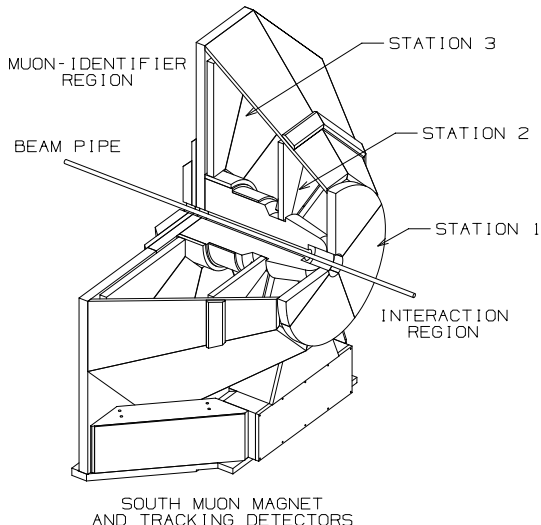


Figure 3.20: Drawing of the South Muon Magnet and the MuTr Stations.

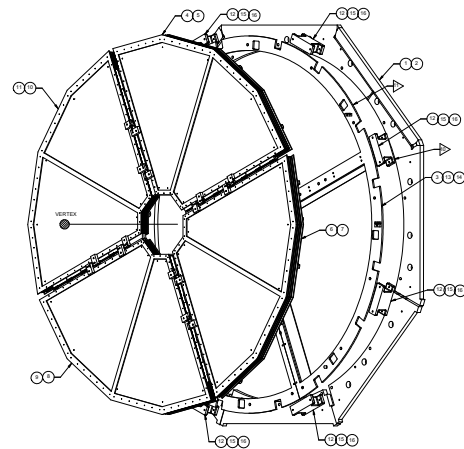


Figure 3.21: Mechanical drawing of the MuTr Station-1.

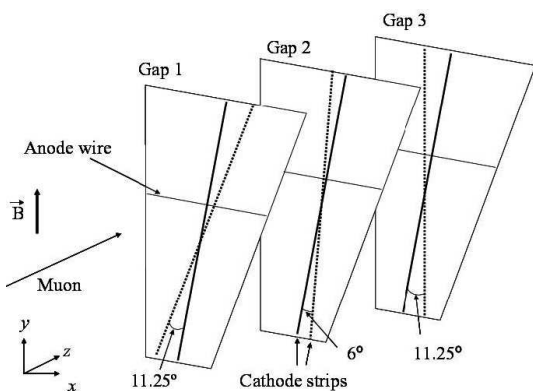


Figure 3.22: Illustration of stereo readout of the MuTr. The stereo angle is different by stations for eliminating ghosts.

Station	Gap	Angle (deg)
1	1	-11.25
	2	+6.00
	3	+11.25
2	1	+7.50
	2	+3.75
	3	+11.25
3	1	-11.25
	2	-11.25

Figure 3.23: The azimuthal offset angle of stereo cathode planes with respect to their corresponding non-stereo cathode planes.

CHAPTER 3. APPARATUS

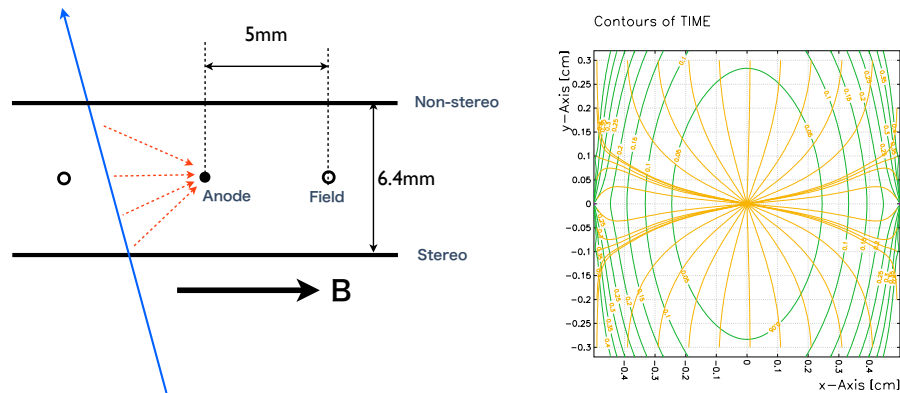


Figure 3.24: (Left) Schematic drawing of a MuTr cell. (Right) Contour plot of drift time in the MuTr cell simulated by Garfield.

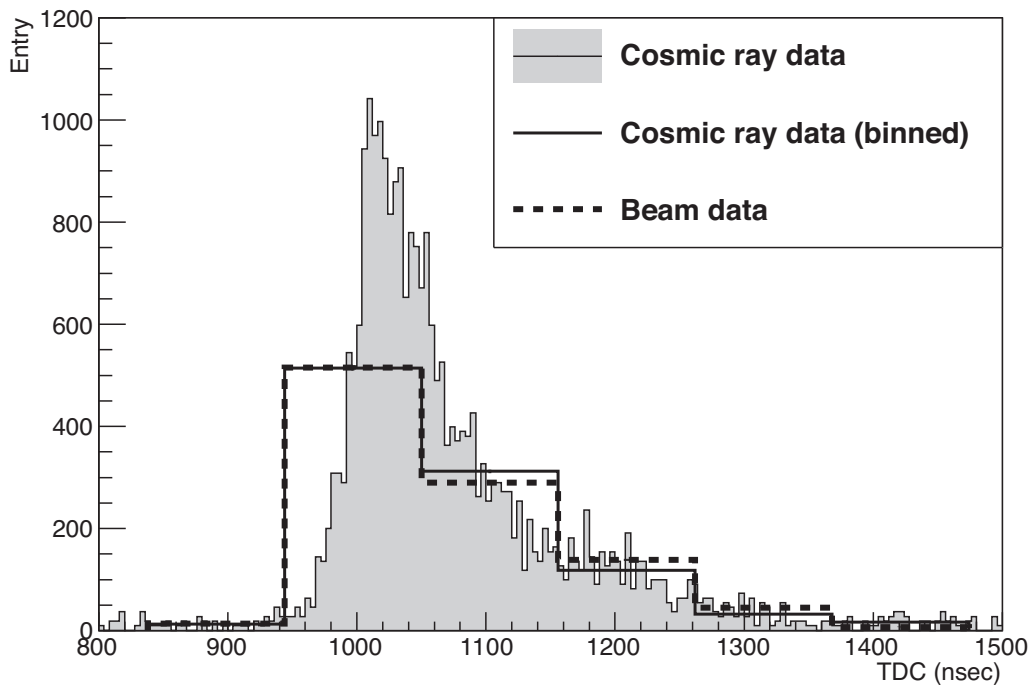


Figure 3.25: The arrival time distribution for different incident angles into MuTr based on Garfield simulation.

MuTr electronics Cathode strip chambers determine the position of particle injections by measuring the charge on each strip. The MuTr is also used to provide the local level-1 (LL1) trigger. For each cathode strip, the raw signal charge is split into two independent readout. About 90 % of the charge is read by the MuTr FEE which is for offline tracking, and the remaining is read by the Mutrg FEE which is for issuing trigger. The charge from the cathode strip is amplified and shaped by the charge preamplifier (CPA) with conversion factor of 3.5 mV/fC, then buffered in the analog memory unit (AMU) for 64 beam clocks. If triggered, the digitization is performed by the 11 bit ADC then the sampled waveform is sent to the data collection module (DCM) as shown in Figure 3.27. The DCM processes the zero suppression, and only signals greater than certain thresholds are recorded as data.

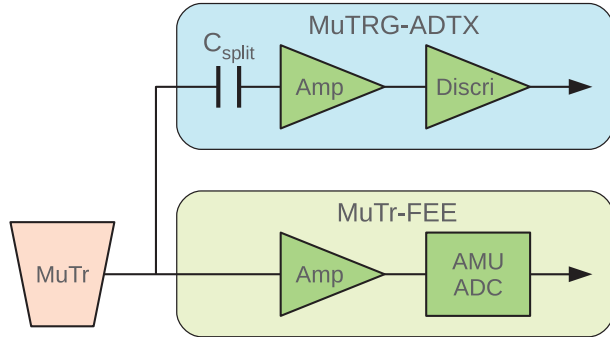


Figure 3.26: Analog readout diagram of the MuTr.

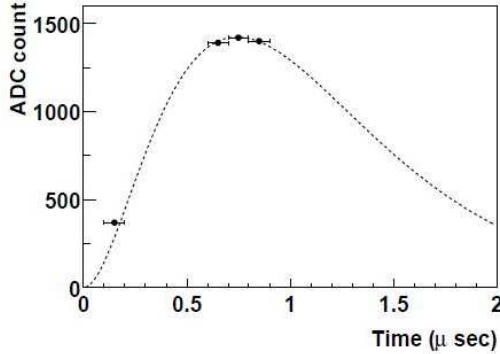


Figure 3.27: Sampling recording of the waveform of the signal with the MuTr FEE.

Mutrg electronics The Mutrg is the trigger electronics of the MuTr[58, 59]. As described in the previous section, the Mutrg uses about 10 % fraction of the total charge deposited at the cathode strips of the MuTr to provide the hit pattern for the triggering. The analog part of the electronics is called Mutrg-ADTX, which mounts signal amplifiers and discriminators. The digitized signals from multiple Mutrg-ADTX boards are sent to the merger board (Mutrg-MRG), which buffers the data and sends the hit pattern to the local-level1 (LL1) trigger board for the trigger decision. If triggered, the data in the Mutrg-MRG of the 7 beam clock patterns (from -3 beam clock before the trigger timing to +3 beam clock after the trigger timing) are

CHAPTER 3. APPARATUS

multiplexed and sent to the data collection module (DCM) via an interface board (Mutrg-DCMIF). The Mutrg electronics are implemented only for the non-stereo planes of the MuTr.

The Mutrg-ADTX board mounts signal amplifiers and discriminators. The signal amplifier uses two op-amps AD8038 and AD8065 of Analog Devices. Pulse height and peak time after the amplifier is about 300 mV and 200 ns with 100 fC charge deposit in MuTr. Noise after the amplifier is about 5 mV in root-mean-square (RMS). Two discriminators are implemented. One is level edge discriminator and the other is constant fraction discriminator.

The Mutrg-MRG board can extend the timing width of the hit to multiple beam clocks. Extending the timing width of the hit covers trigger inefficiencies due to the timing resolution of the MuTr longer than one beam clock of 106 ns. The Mutrg-MRG board can configure the condition of the hit of each station by changing the logic for hits in different planes of the same strip number. For example, taking the “OR” logic (true if any of the planes of the station has a hit) will increase the hit efficiency, while it will be fragile to noise hits. On the other hand, taking the “AND2” (true if more than two of the planes of the station have hits) or AND3 logic for planes will increase the tolerance to the noises but will sacrifice some of the hit efficiency.

Figure 3.28 shows the block diagram of the Mutrg FEE.

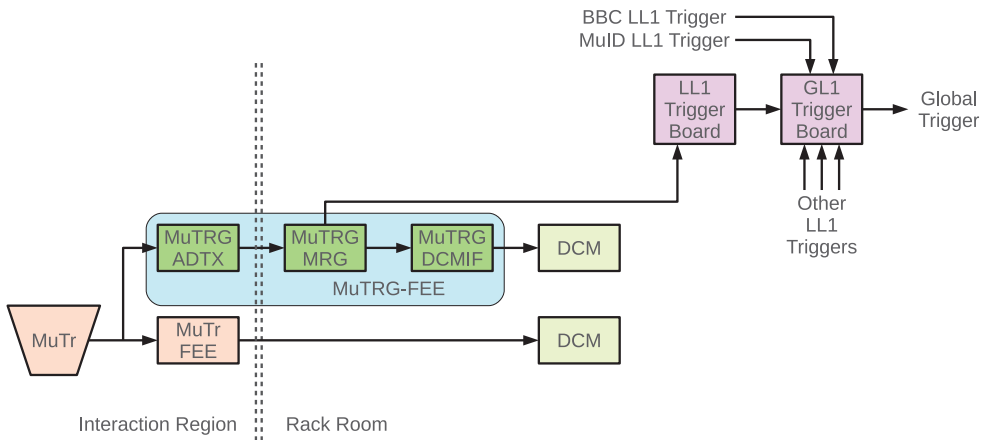


Figure 3.28: Block diagram of Mutrg FEE.

3.2.3.3 Resistive Plate Chamber (RPC3)

Motivation of installing the RPCs The primary motivation to install the Resistive Plate Chambers (RPCs)[60] to the existing PHENIX Muon Arms is to provide a dedicated trigger for the measurement of W bosons with the Muon Arms, which should have excellent timing resolution to identify the collision timing. In proton-proton collisions at $\sqrt{s} = 500$ GeV, the expected luminosity is so high to have collisions in almost every bunch crossing. This situation is crucial for measuring spin asymmetries with the Muon Arms. The spin pattern provided by the accelerator is different bunch by bunch (Table 3.1), thus the detector is expected to identify the bunch crossing of the event. The triggers using the Muon Arms (MuID trigger or Mutrg) do not have enough timing resolutions for bunch crossing ID, and without the RPCs we need to use the BBCs for bunch-crossing ID. However the BBCs would mix up the bunch crossing ID with the previous or the next bunch crossing, if the collision rate is too high. For this reason we need to introduce some less-occupied trigger detectors which have sufficiently fast time resolution to differentiate bunch crossing. Installing the RPCs is the solution to this issue, since the occupation of the RPCs is much less than the BBC and the time resolution satisfies to identify the collision.

Installation of the RPC detectors As the RPCs must be installed in addition to the existing PHENIX, the design on the RPCs suffers lots of constraints on their geometries. The candidate locations of installing the RPCs are three, one is the gap between the Central Magnet and the MuTr, two is the gap between the MuTr and the MuID, last is downstream the MuID. Correspondingly we have names of RPC-1,2,3. The RPC3 chambers must be installed through the RHIC beam tunnel and the radial length of the RPC3 is limited by the aperture of the tunnel (Figure 3.31). For this reason the RPC3 covers only the rapidity region of $|\eta| > 1.4$. Both the RPC1 and the RPC2 were planned to install³, which will cover the missing acceptance of the RPC3. As described in Sec. 3.2.1, the data used in this thesis were taken in year 2011 runs, at that moment only the RPC3 was finished to install, and the RPC1 had not installed yet. In year 2011 runs the RPC3 trigger system was under commissioning thus the RPC3s were not used for triggering. However the RPC3s took data passively using the other triggers. With requiring hits in the RPC3s for the track offline, the bunch crossing ID of the track is ensured.

Design of the RPCs The design of the RPCs used in the PHENIX is based on the one used in the CMS experiment in the LHC[61]. It employs a standard double-gap oil-coated bakelite resistive plates as Figure 3.30. The readout strips read induced charges generated by charges created at both of the two gaps. The readout strips are aligned in radial direction for each half-octant. The RPC3 is segmented into three regions in radial direction, called A,B,C from inner to outer as shown in Figure 3.29. The strip width is different by regions, inner regions have smaller strips. The gas mixture is 95/5 % C₂H₂F₄/isobutane, and the operating high voltage is about 9 kV.

RPC electronics The expected charge from the RPC ranges from 20 fC to 20 pC. The preamplifier used for readout has about 1.7 fC ENC for the case of a 15 Ω input impedance. The timing resolution of the amplifier is less than 0.6 ns for a 0.5 pC signal. The discrimination threshold is set around 100 fC. The discriminated signal is digitized at the TDC whose time bin size is 2.4 ns, which divides one beam clock (106 ns) into 44. The TDC data is processed the filter of timing window then transferred to the local level-1 board which is identical to the Mutrg-LL1, but this line was not used in year 2011 runs. The data are also buffered in the FPGA for 40 beam clocks, then once triggered the data at the trigger timing are sent to the data collection module (DCM). Figure 3.32 shows the block diagram of the RPC front-end electronics.

Bakelite thickness	2 mm
Bakelite bulk resistivity	$2.0 - 5.0 \times 10^{10} \Omega \text{ cm}$
Number of gaps	2
Gap width	2 mm
Gas mixture	95/5 % C ₂ H ₂ F ₄ /isobutane
HV	9 kV
Strip width (A/B/C)	37.8 / 50.6 / 64.8 mm
Time resolution	≤ 3 ns
Average cluster size	≤ 2 strip
Rate capability	0.5 kHz/cm ²
Number of streamers	< 10 %

Table 3.7: Performance requirements of the PHENIX RPC3 detectors.

³However the construction of the RPC2 was not approved.

CHAPTER 3. APPARATUS

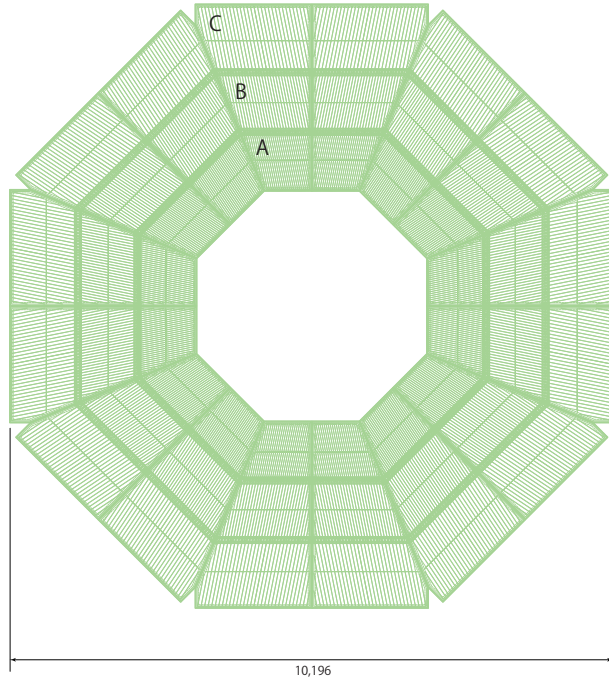


Figure 3.29: Geometry of the RPC3 strips. The width of the strip is different by regions A,B,C.

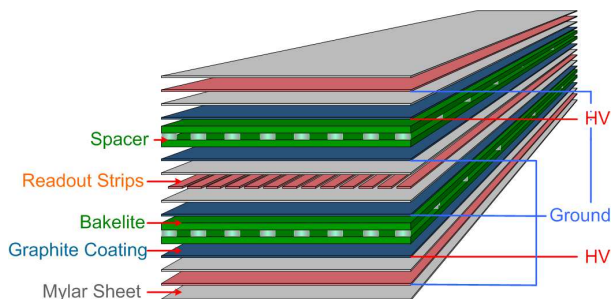


Figure 3.30: An exploded view of the layers of the RPCs.



Figure 3.31: RPC3 seen from the RHIC beam tunnel.

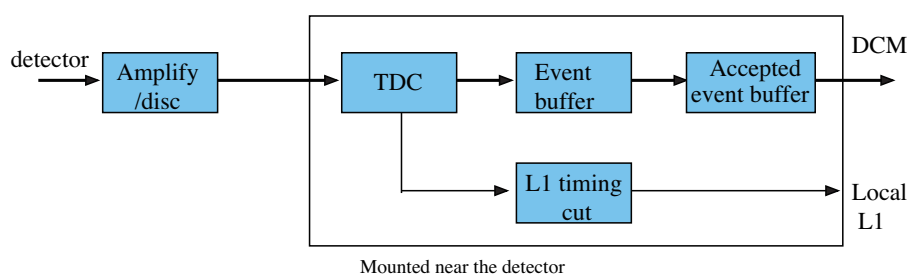


Figure 3.32: Diagram of the RPC front-end electronics.

3.2.3.4 Beam Beam Counters (BBC)

The Beam Beam Counters (BBC)[62] cover forward rapidity region of $3.1 < |\eta| < 3.9$. Two modules (South, North) are there, each of them consists of 64 quartz Cherenkov counters to surround the beam pipe in three layers (Figure 3.35). The inner diameter is 10 cm and the outer diameter is 30 cm. The width of the quartz crystal mounted on each photomultiplier tube is 3 cm, and the distance of the quartz crystals from the origin is 144 cm for both arm modules. Optical fibers branched from the two laser sources are mounted on quartz crystals to calibrate the gain and detection timing. The BBC detects charged particles with $\beta > 0.7$. The BBC are the luminosity monitor of the PHENIX, and it provides the minimum bias triggers. It also provides the primary vertex z -position and the timing of the collision by measuring time of flights. The vertex calculation is performed both offline and online. The online vertex calculation is used to issue the minimum bias triggers with limiting the vertex range to e.g. $|z_{\text{vtx}}| < 30$ cm. The precision of the vertex measurement is about 2 cm offline after calibrating time walks.

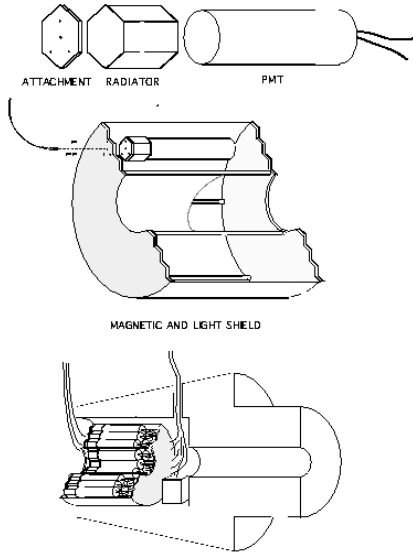


Figure 3.34: Picture of a BBC module.

Figure 3.33: Schematic Drawing of a BBC module.

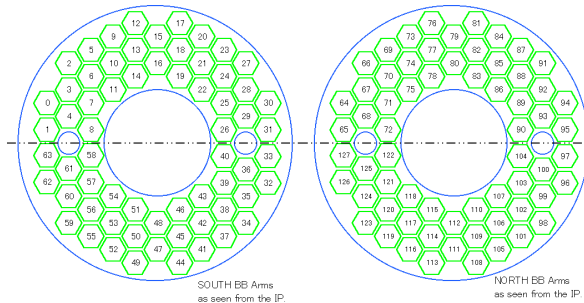


Figure 3.35: Arrangement of PMTs in the BBC. The blue circle blanks are the positions of laser sources.

3.2.3.5 Zero Degree Calorimeter (ZDC)

The Zero Degree Calorimeter (ZDC)[63] is a tungsten neutral hadron calorimeter located at the very forward region of $\theta \lesssim 2.8$ mrad i.e. $\sim 0^\circ$ behind the DX magnet. The distance from the origin to the ZDC is 18 m, the furthest detector of the PHENIX. Most charged particles are deflected by the DX magnet, and substantially neutrons and photons inject into the ZDC. One set of the ZDC is placed at each the South side and the North side. A ZDC consists of the three identical calorimeter modules and the Shower Maximum Detector. The calorimeter module is a sampling hadronic calorimeter made of tungsten plates and optical fibers. The hadronic interaction length of the 27 tungsten plates in one module is $2.0\lambda_I$. The fibers collect Cherenkov lights created by hadronic showers and the fibers are coupled to a $\phi 2\text{inch}$ standard PMT (Hamamatsu R329-02). The relative angle between the tungsten plates and neutron fluxes are set to 45° , which maximizes the light yield to achieve the best energy resolution. The energy resolution is $20 \cdot \sqrt{100 \text{ GeV}/E} \%$. Three modules are arrayed in beam direction, and mostly photons deposit all energy only on the first module, and neutrons deposit certain fraction of the energy on the second or the third modules. Between the first and the second module a 5 mm-thick X and Y orientation hodoscope called Shower Maximum Detector (SMD) is inserted. The segmentation of the SMD is 14 mm for X-direction and 19 mm for Y-direction. The position resolution of the SMD for injecting neutrons is about 1 cm. The ZDC can provide local level-1 triggers with requiring hits in both the South and North side detectors. It can also measure the collision vertex roughly by measuring time-of-flights as the BBC does. The precision of the vertex measurement is about 30 cm online and about 10 cm offline.

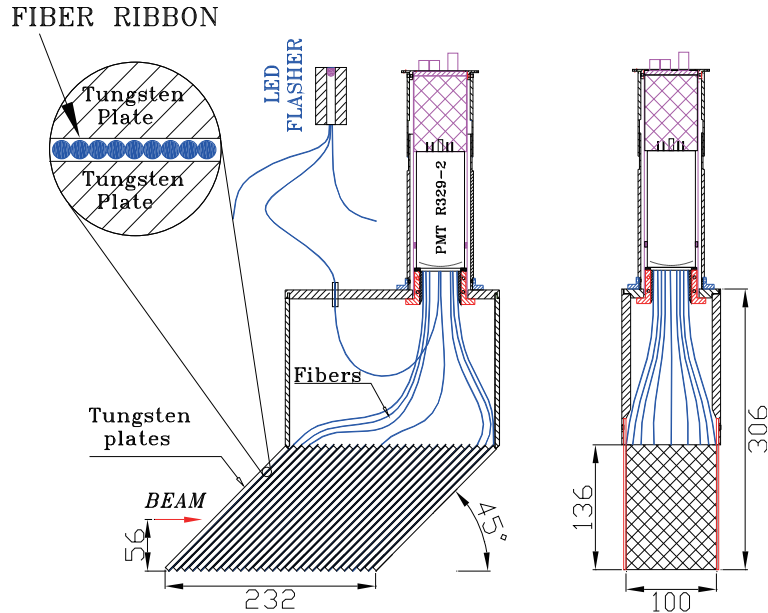


Figure 3.36: Drawing of a ZDC module. Dimensions are in mm.

3.3 Data taking

3.3.1 DAQ

The main design consideration on the PHENIX data acquisition (DAQ) system is to be compatible with both heavy ion collisions and proton-proton collisions. The characteristics of the two species of collisions are very different from the viewpoint of DAQ. The collision rate of heavy ion collisions is a few kHz while the multiplicity of tracks are enormous. On the other hand, the collision rate of proton-proton collisions are a few MHz, but the track multiplicity is not so large. To meet with the above condition, the PHENIX DAQ system employs non-dead-time front-end modules (FEMs) and the triggering system. Figure 3.37 illustrates the PHENIX DAQ system[65].

PHENIX DAQ system The root of the clock of the DAQ system is the RHIC original clock of 9.4 MHz which controls the beam bunches. At the PHENIX, the master timing module (MTM) receives the RHIC clock then distributes it to the global level-1 module (GL1) and the granule timing modules (GTMs). The GTMs distribute the clock to the assigned FEMs. The term “granule” stands for the minimal unit of the DAQ to take data, typically assigned for each detector subsystem. The GL1 manages the level-1 triggering. The GL1 receives the local level-1 (LL1) signals from individual subsystem, and when the pattern of LL1 matches with any of the level-1 trigger conditions, and if any of the GTMs is not busy, the GL1 issues a trigger signal to the GTMs and each GTM transmits it to the FEMs. The GTMs also send mode bit signals to control FEMs, and they receive the busy signal from the data collection modules (DCMs) and transfer it to the GL1. The GTMs also provide their own clock to the FEMs for the case that the RHIC original clock is absent.

The FEM operates the front-end electronics (FEE) boards of the detector subsystem. The FEM handles the raw signals of the detector, such as signal amplification and buffering, and it decides to issue the LL1 trigger bit. The buffering is either analog or digital, depending on the detector subsystems. The depth of the event buffer is 40 beam clocks for all detectors. If the GL1 trigger is fired, the FEM digitizes the corresponding timing event signals if they are analog, and sends data to the DCMs. The event-buffering system allows the FEMs to run without dead time. The FEEs and FEMs are located inside or beside the PHENIX detector, and the DCMs are located next to the counting room, and they are distant by about 20 m. The digitized data are transferred from the FEMs to the DCMs via optical fiber cables. The data transferred to the DCMs are processed for such as zero suppression, checking errors and formatting. The DCMs are on the data collection boards (DCBs), and the DCBs are grouped in a Partitioner.

The data at the DCMs are sent to the Partitioner and concatenated, then data packets are sent to the event builder (EvB), particularly the sub-event buffers (SEBs). The EvB consists of the SEBs and the assembly/trigger processors (ATPs), and the data packets temporarily stored in the SEBs are sent according to the request by the EvB controller to the ATPs via a 96-port gigabit switch with asynchronous transfer mode. The ATPs also judge the level-2 software trigger. Note that in the PHENIX the level-2 trigger is used subsidiarily, e.g. for the local polarimetry. The events assembled at the ATPs are called PRDF (PHENIX Raw Data File), and they are monitored online by shift crews and subsystem experts, and are stored to the event buffer boxes at the counting room. The PRDF files at the event buffer boxes are stored typically a few days while the online data production (fast production) is performed as much as time allows. If a set of the buffer boxes become full, the buffer box set is switched to another set. Meanwhile the PRDF data files at the buffer boxes are finally transferred to the tape data storage called HPSS (high performance storage system) and saved forever. The buffer boxes are cleared and reused for another runs.

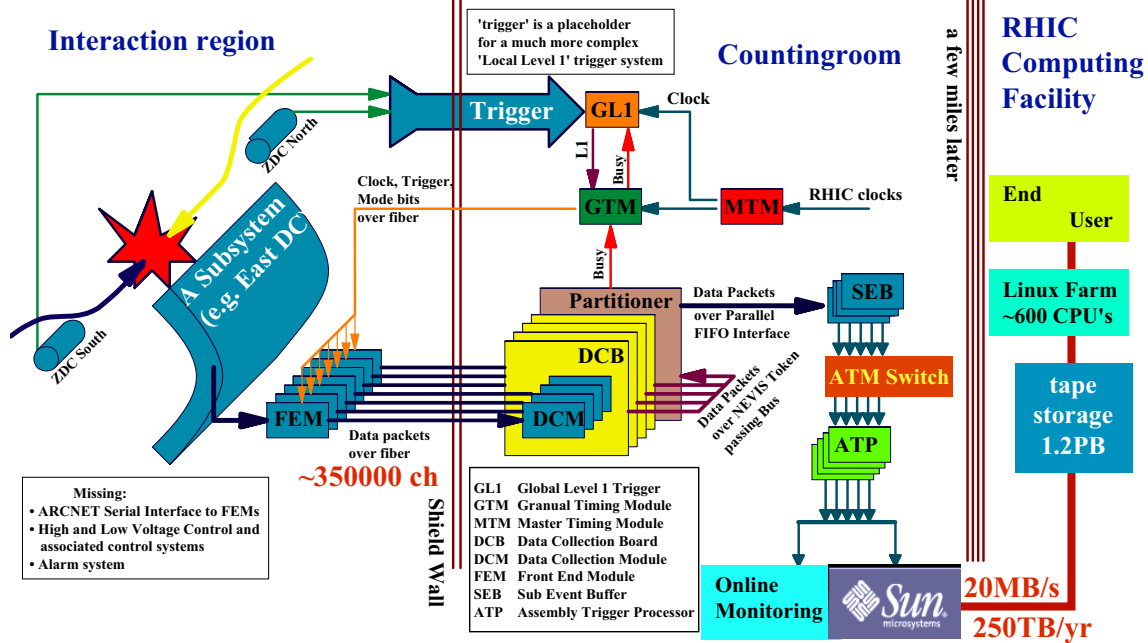


Figure 3.37: Illustration of the PHENIX DAQ system[65]. For the detail of the DAQ system, see the text.

3.3.2 Triggers

As a multi-purpose detector, the PHENIX uses various level-1 triggers. There are totally 32 slots of the level-1 triggers, and each trigger can take data separately. As the maximum bandwidth of the total data transfer is limited, triggers out of the interest of the physics measurements are reduced by pre-scaling. Table 3.8 shows the list of triggers employed in $\sqrt{s} = 500$ GeV proton-proton collisions in year 2011 runs as well as the scale down of each trigger for a particular run. The convention of the scale down is that for a scale down N , every $(N + 1)$ triggers the data is recorded once. The scale down is tuned run by run by monitoring the luminosity so that the individual trigger can take maximum data allowed within the bandwidth.

The number of triggered events are counted by a scaler called the GL1P scaler. Three kinds of triggers are counted for each trigger; raw, live, and scaled. The raw trigger means all number of events flagged by the trigger. If the GTMs are busy, the GL1 does not command FEMs to transfer data to the DCMs then the data are discarded. The live trigger means the events with the DAQ is ready for recording the data. The ratio of the live triggers to the raw triggers is called live-rate. As mentioned above, not all live triggers are recorded by pre-scaling. The scaled trigger is the recorded number of events. The DAQ rate is the total scaled trigger rate. The scale downs are determined to keep the live-rate as high as possible. Each trigger has its own trigger bit. For example the trigger bit of the “CLOCK” trigger is 0x00008000 in the octal system. Every event has raw, live, and scaled trigger bits to identify by which triggers the event is triggered. Note that the trigger bits of an event may contain more than one triggers.

The elements of the level-1 trigger is, as described in the previous section, called local level-1 (LL1) triggers. A LL1 trigger can be a standalone trigger, or it can be combined with other LL1 triggers to generate some elaborate triggers. In the following several LL1 triggers related with this thesis is described.

3.3 Data taking

Name	Short Name ^a	Scale Down	Class
BBCLL1(>0 tubes)	BBC(< 30cm)	12375	MB
BBCLL1(>0 tubes) novertex	BBC(novtx)	3991	
ZDCLL1wide	ZDC	1979	OT
BBCLL1(noVtx)&(ZDCN ZDCS)		4325	
MPC4x4b		0	MPC
BBCLL1(>0 tubes) narrowvtx	BBC(< 15cm)	6600	MB
ERTLL1_4x4b		0	ERT
ERTLL1_4x4a		3	
ERTLL1_4x4c&BBCLL1(narrow)		0	
ERTLL1_E&BBCLL1(narrow)		11	
MPC4x4a		3	MPC
MPC4x4c&ERTLL1_2x2		1	
((MUIDLL1_N2D S2D) ((N1D&S1D))&BBCLL1(noVtx)	MuID-2D	0	MUON
(MUIDLL1_N1H S1H)&BBCLL1(noVtx)	MuID-1H	130	
(MUIDLL1_N1D S1D)&BBCLL1(noVtx)	MuID-1D	86	
CLOCK		19959	OT
(NRPCA NRPCB NRPCC)&BBCLL1		1	MUON
MUON_N_RPCA		5	
MUON_N_RPCB		5	
MUON_N_RPCC		5	
MUON_N_SG1&BBCLL1(NoVtx)&MUIDLL1_N1D		0	
MUON_N_SG1		999999	
(SRPCA SRPCB SRPCC)&BBCLL1		0	
MUON_S_RPCA		0	
MUON_S_RPCB		0	
MUON_S_RPCC		0	
MUON_S_SG1&BBCLL1(NoVtx)&MUIDLL1_S1D		0	
MUON_S_SG1		999999	
PPG(Pedestal)		0	SERVICE
PPG(Test Pulse)		0	
PPG(Laser)		0	
Noise		not used	

^aThe convention only used in this thesis.

Table 3.8: The list of triggers employed for $\sqrt{s} = 500$ GeV proton-proton collisions in year 2011 runs. The scale down number is a typical one, and the number varies run by run with luminosity change.

3.3.2.1 Minimum bias triggers (BBCLL1)

The minimum bias (MB) triggers are used to monitor the luminosity, assures the collision and its timing. The MB triggers use the BBCs. The MB triggers issue the trigger bit when both the South and North BBC modules have more than one hits. Three triggers are provided. The first one has no requirements on the vertex position of the collision, and the second one requires the z -position of the collision vertex within 30 cm from the origin, and the last one requires the collision vertex within 15 cm from the origin. In the latter two cases, the time-of-flight (TOF) is calculated online. The first trigger is referred as “BBCLL1(> 0tubes) novertex” or shortly “BBC(novtx)” in this thesis, and the second is referred as “BBCLL1(> 0tubes)” or “BBC(< 30cm)”. The last is referred as “BBCLL1(> 0tubes) narrowvtx” or “BBC(< 15cm)”. The vertex cut of $|z_{\text{vtx}}| < 30$ cm roughly matches with the acceptance of the Central Arms, and $|z_{\text{vtx}}| < 15$ cm corresponds to the acceptance of the VTX detector. These triggers are not referred so much in this thesis, since the Muon Arms have much wider acceptance.

3.3.2.2 MuIDLL1

The MuID LL1 triggers (MuIDLL1) use the hit pattern of the MuID for triggering. For each orientation of x and y , the two packs in the same line of different panels are virtually grouped as a long detector through the MuID. This virtual long detector is called “logical tube”. For each logical tube in the gap-1, the line that connects the detector origin and the tube is considered, then the logical tubes in the other gaps which intersect with the line are grouped as a set called *symset* (Figure 3.39). The trigger condition is judged for each symset. Thus the MuID trigger secures some resistance to ghost tracks and tracks not from the vertex. If the five gaps of the same symset satisfy the specified condition, the orientation of the symset is flagged. The x -orientation and y -orientation layers separately judge the pattern, and the logical ‘AND’ of the two orientations is the final MuID trigger. Two symset logic conditions are provided. One is called “1D (one-deep)”, which is used for identifying muons, and the other is called “1H (one-hadron)”, which is used for identifying hadrons. The 1D algorithm requires at least one hit in the gap-4 or the gap-5, while the 1H algorithm requires no hits in the gap-5. The logic diagrams of the two conditions are shown in Figure 3.39.

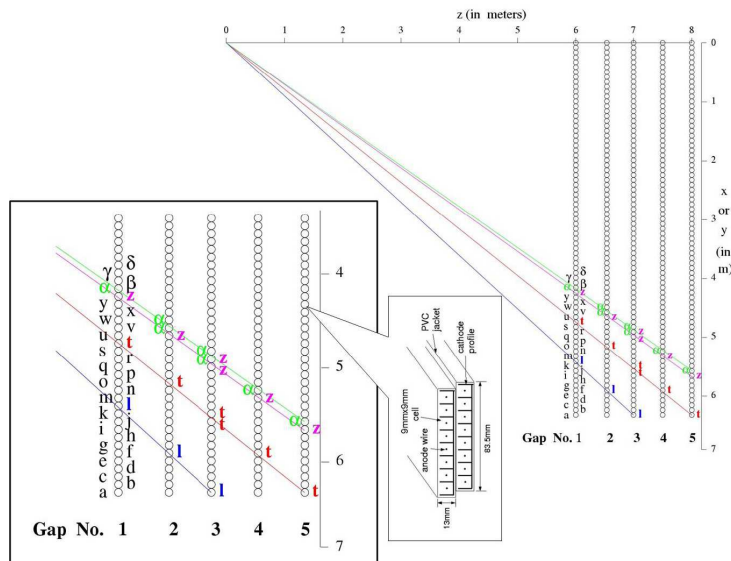


Figure 3.38: Defining symsets of the MuID trigger.

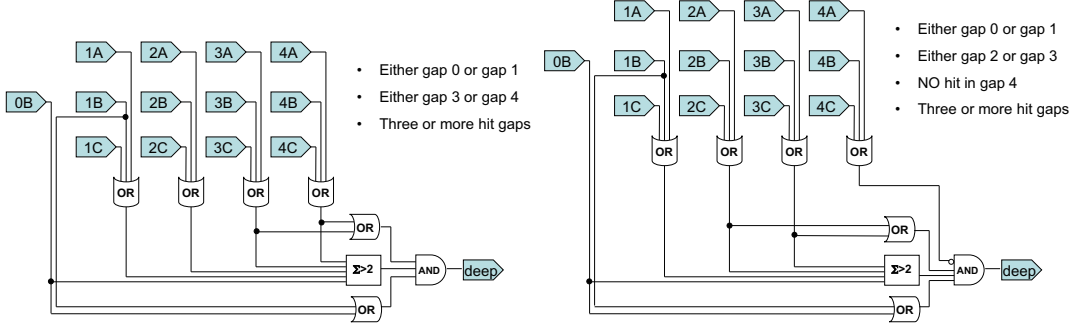


Figure 3.39: MuID symset logics. The left is MuID-1D (one-deep) logic and the right is MuID-1H (one-hadron) logic. Note that the numbering nomenclature is different from the text, i.e., the gap 1-5 is written as 0-4.

The MuIDLL1 can provide the trigger condition for plural tracks, called “2D (two-deep)” or “1D1H (one-deep,one-hadron)”, etc. Note that the 2D algorithm is not only the product of two 1D trigger conditions, but it considers the opening angle between the two tracks. In year 2011 runs, three triggers are MuIDLL1 triggers as follows:

- MuID-1D “(MUIDLL1_N1D||S1D)&BBCLL1(noVtx)”
This trigger is fired when either the South or North MuID satisfies the 1D condition as well as the BBC(novtx) condition. This trigger was scaled down.
- MuID-1H “(MUIDLL1_N1H||S1H)&BBCLL1(noVtx)”
This trigger is fired when either the South or North MuID satisfies the 1H condition as well as the BBC(novtx) condition. This trigger was scaled down.
- MuID-2D “((MUIDLL1_N2D||S2D))||(N1D&S1D))&BBCLL1(noVtx)”
This trigger is fired when either the South or North MuID satisfies the 2D condition, or both the South and North MuID satisfy the 1D condition. Also the BBC(novtx) condition is additionally required. This trigger was not scaled down.

Also the physics triggers for $W^\pm \rightarrow \mu^\pm$ used the MuID-1D trigger as a superset of the trigger.

3.3.2.3 Mutrg-LL1

The Mutrg-LL1 uses the hit patterns of the MuTr for triggering. The hit pattern is sent from the Mutrg-MRG boards to the LL1 board every beam clock. The timing width of the hit of a strip can be more than 1 beam clock. The Mutrg-LL1 has a function called clustering to keep high rejection. Usually a particle injection creates a series of a few strip hits in a station called a cluster. The clustering algorithm reduces cluster into single hits. The detail of the algorithm is as follows:

1. If successive hits are found, clustering starts.
2. If number of the successive hits is less than or equal to four, only the center hit is kept while other hits are discarded (Figure 3.40-(a)). If number of hits in the group is two or four, only one hit with smaller channel (arbitrary) near the center is kept (Figure 3.40-(b)).
3. Due to limited capacity of FPGA on the LL1 board, if number of the successive hits is more than four, the hits are divided into groups with less than or equal to four. Then, the same procedure of 2. is performed to each of divided sub-groups. (Figure 3.40-(c))

CHAPTER 3. APPARATUS

The Mutrg-LL1 module has trigger maps as look-up tables. An element of a trigger map is a set of the strip addresses of the station-1,2,3. If the MuTr hit pattern of the event matches with any of the trigger maps, the LL1 trigger bit is issued. There are several classes of trigger maps, classified with the size of sagitta. The sagitta is defined as the distance between the station-2 hit and the intersection point of the station-2 plane and the line which connects the station-1 hit and the station-3 hit digitized by the strip size. The trigger map which allows up to N -strip sagittas is classified as SG N . The trigger maps are determined based on the GEANT simulation (PISA, see Sec.3.4 in detail). The momentum threshold of the SG1 trigger map is $p_T \simeq 2.5$ (3.5) GeV/c for the South (North) Arm. In year 2011 runs the SG1 trigger map was employed for triggering $W^\pm \rightarrow \mu^\pm$ event candidates. Note that the larger N -strip trigger map includes the smaller N -strip trigger maps. For example, all strip combinations in the SG0 trigger map are included in the SG1 trigger map.

In year 2011 runs, the following configuration was used for the Mutrg FEE and the Mutrg-LL1.

- Using the leading edge discriminator
- 3-beam-clock LL1 width
- AND2 logic for Station-1, OR logic for Station-2 and Station-3
- Clustering ON
- SG1 trigger map

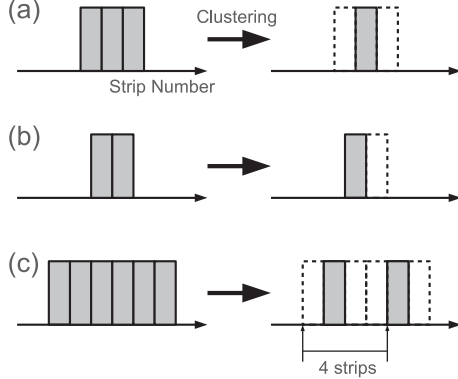


Figure 3.40: Explanatory drawings for the clustering.

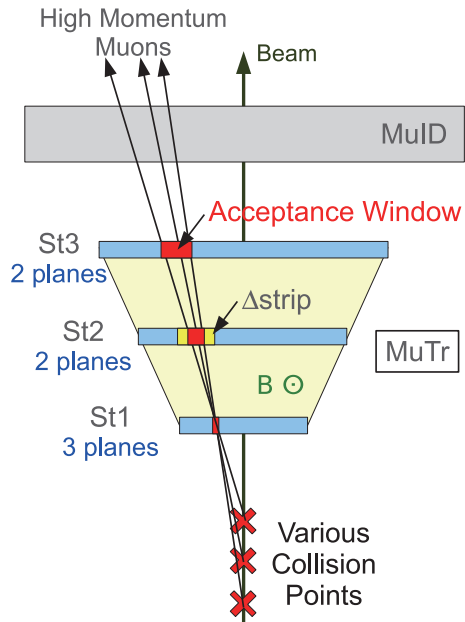


Figure 3.41: A schematic drawing of the Mutrg-LL1 trigger logic.

3.3.2.4 Physics triggers for $W^\pm \rightarrow \mu^\pm$

The physics triggers used in this thesis employ the coincidence of BBC(novtx), MuID-1D and Mutrg-SG1 LL1 triggers as schematically shown in Figure 3.42.

- South Arm: MUON_S_SG1&BBCLL1(NoVtx)&MUIDLL1_S1D
 - North Arm: MUON_N_SG1&BBCLL1(NoVtx)&MUIDLL1_N1D

For short, we use the conventions “WTRG(S)” and “WTRG(N)” hereafter.

The coincidence of the three LL1 components of the WTRG(S,N) triggers is judged for every BCLK. Both MuID-1D and Mutrg-SG1 LL1 triggers have more than 1 BCLK timing resolution, extension of the LL1 width is performed and the timing is tuned so that the probability of the coincidence is maximized. Figure 3.43 is the schematic illustration of the LL1 timing of the WTRG(S,N) triggers in year 2011 runs⁴.

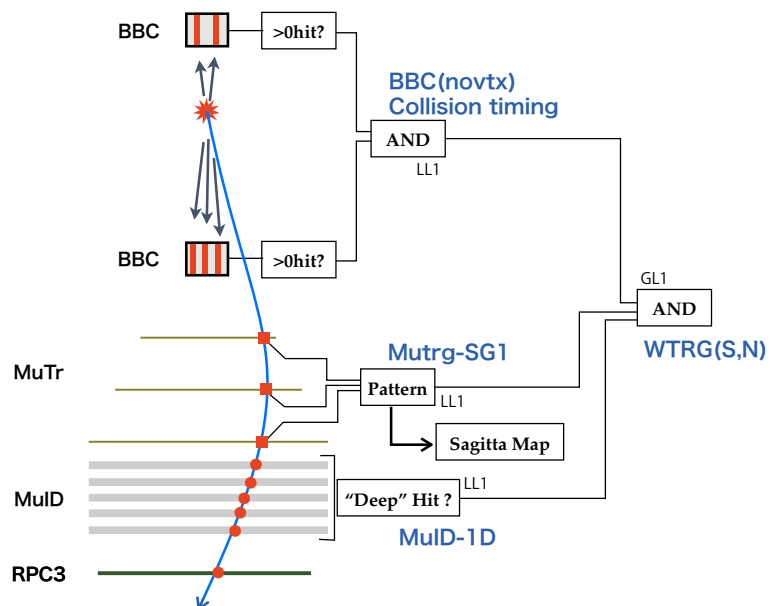


Figure 3.42: Schematic illustration of the physics trigger for $W^\pm \rightarrow \mu^\pm$ in year 2011 runs.

⁴This LL1 timing chart will be important in the analysis of MuID-1D trigger efficiency in Sec. 6.3.2.

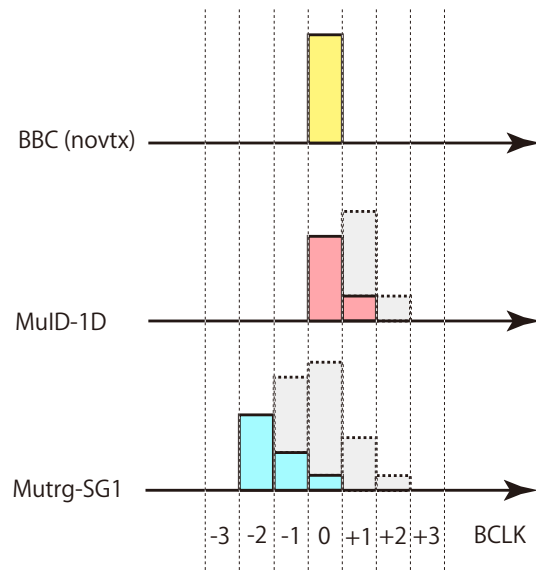


Figure 3.43: The configuration of the LL1 timing of the WTRG(S,N) trigger in year 2011 runs. The colored columns represent probabilities of having LL1 trigger bit without extending the LL1 width. The gray columns represent the probabilities of having LL1 trigger bit with extending the LL1 width. The LL1 width of the MuID-1D and Mutrg-SG1 is 2 and 3 BCLKs, respectively. At the BCLK-0 all of the tree LL1 trigger bits coincide and the WTRG trigger is issued at the GL1.

3.4 Software and simulation framework

The software framework is illustrated in Figure 3.44. The data taken in the run are stored temporarily at the buffer boxes in the counting room and permanently saved in the HPSS. The various online processing codes called OnCals are processed simultaneous with the data taking to read the packets in the acquired PRDF files directly to extract various parameters of the data which are referred at the time of data production and the analyses. The results of OnCal processes are stored in the database. At the period of data production, PRDF data in the HPSS storage are processed for reconstructions of data to extract DST (Data Summary Tape) which users can access frequently. A DST has a tree structure of objects for each event and the result of reconstruction in each subsystem is stored as a node. To save the disk space it is usual to select only essential nodes for the higher level analyses to save in the DST file, and several kinds of DST files exist for the same run, such as the DST specialized for the Muon Arm analyses, that for the local polarimetry, etc. The DST files may be further processed to extract more compact DSTs (nano-DSTs) or non-object tree files (pico-DSTs) for end-users in some working groups.

The simulation process passes through the same reconstruction algorithm to compare with data. Various physics processes can be fed into the detector simulations. In this analysis PYTHIA6 event generator[69], NLO generators, the single particle generator are used. The full detector simulation is called PISA (PHENIX Integrated Simulation Application) which is based on the GEANT3 framework[66, 67]. All detector geometries, materials and fields are implemented in the PISA, and interaction of particles with matters and particle decays are simulated in the PISA. Figure 3.45 shows a 3D rendering of the detector geometry implemented in the PISA. To obtain realistic detector response in the simulation, the output of the PISA is converted to detector hit data by applying detector response functions. This process is called digitization. At the digitization process, various detector qualities of a specified reference run stored in the database or user-defined tunings are referred. The intermediate data after the digitization can be recorded as PRDF files or DST-structure files. Finally the simulated detector hit data are processed by the same reconstruction codes as those used for the real data.

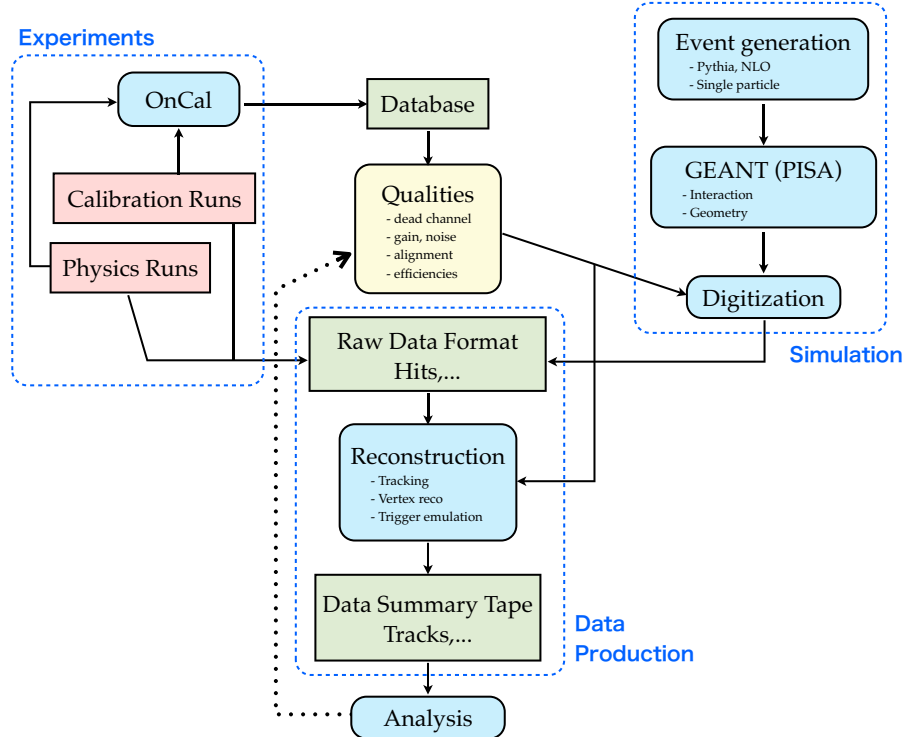


Figure 3.44: Illustration of the software framework.

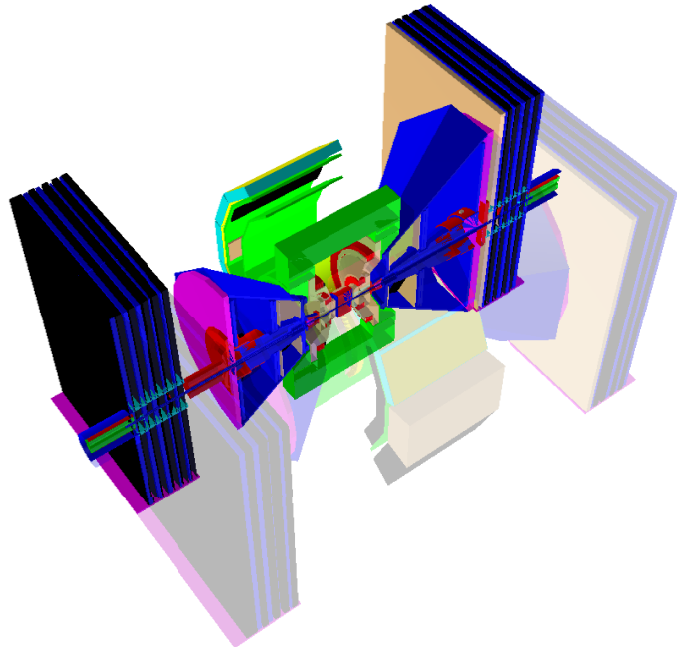


Figure 3.45: Geometry of the PHENIX built in the PISA simulation framework.

Chapter 4

Reconstruction

4.1 Vertex reconstruction with the BBC

In this thesis, the primary vertex z -position (z_{vtx}) is reconstructed with the BBC. The BBC gives the z -position and the timing (t_0) of the collision. The x, y -position cannot be reconstructed with the BBC, but the transverse size of the beam is small compared to the precision of the vertex reconstruction with the MuTr, we do not care the horizontal and vertical position of the collision point. The reconstruction of the vertex with the BBC is based on the comparison of time-of-flight between the South and North side BBC modules. Conventionally the reconstruction algorithm assumed to have only one collision at a time. As we will discuss in Sec. 5.1.2, however, for $\sqrt{s} = 500$ GeV proton-proton collisions in year 2011 runs used in this thesis, the significant fraction of the events has multiple collisions, and the conventional vertex reconstruction loses its accuracy. In the future runs we will expect higher luminosities, the situation would become worse. For this reason we developed a new vertex reconstruction algorithm of the BBC which partially improves the accuracy of the vertex reconstruction in case of multiple collisions¹.

4.1.1 Conventional BBC reconstruction algorithm

The basic concept of z_{vtx} reconstruction with the BBC is to measure the arrival time of particles injecting into the BBC from the collision vertex. Suppose that t_S (t_N) is the reconstructed timing of south (north) side BBC. The reconstructed z_{vtx} and t_0 are written as

$$z_{\text{vtx}} = \frac{c}{2}(t_S - t_N) \quad (4.1)$$

$$t_0 = \frac{t_S + t_N}{2} - \frac{L}{c} \quad (4.2)$$

respectively, where L is the distance between the origin and the BBC module ($L = 144$ cm), and the time-of-flight (TOF) for each module is defined as

$$\text{TOF}_{S,N} = t_{S,N} - t_0. \quad (4.3)$$

¹In 2011 and 2012 the PHENIX has installed the silicon VTX (vertex) and the FVTX (forward vertex) detector respectively around the collision point. The primary vertex reconstruction with these detectors is by far precise than that of the BBC. However the acceptance of these detectors does not cover the whole range of collisions. The measurement of spin asymmetry of $W^\pm \rightarrow \mu^\pm$ is limited mainly by the statistics, and it is considered that the whole acceptance of the Muon Arms should be used. For this reason the importance of the BBC for primary vertex reconstruction is kept even with the existence of these vertex detectors. Of course installation of these new detectors would partially improve the vertex reconstruction in the future runs.

The conventional BBC reconstruction algorithm employs the average of the arrival time of the hit channels as the $t_{S,N}$:

$$t_{S,N}^{\text{conv}} \equiv \bar{t}_{S,N} = \frac{1}{N_{S,N}^{\text{hit}}} \sum_j (t_j^{\text{hit}})_{S,N} . \quad (4.4)$$

One finds that in case of multiple collisions, the z_{vtx} given by the conventional reconstruction will be something middle point of the two collisions, as illustrated in Figure 4.1. Thus the conventional BBC reconstruction will degrade its accuracy when the luminosity is high to have significant multiple collisions.

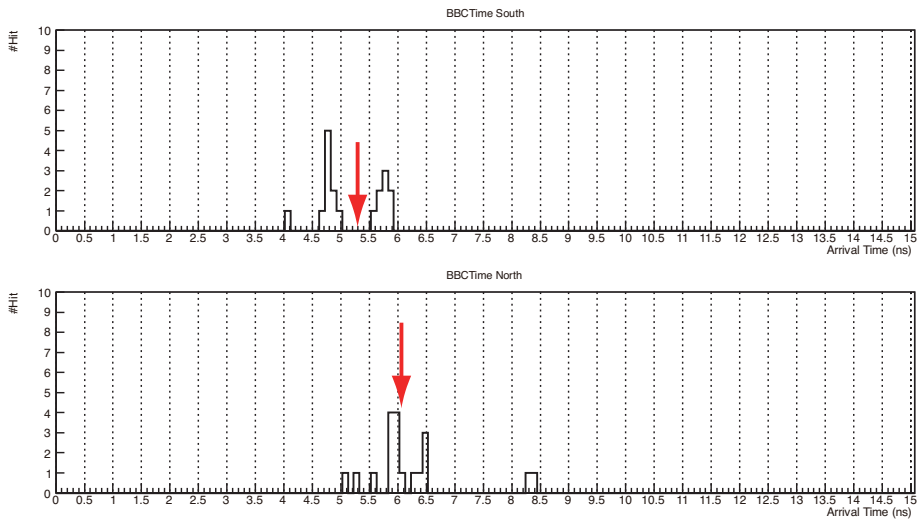


Figure 4.1: Timing histogram of the South and North BBC module for a typical event of double collision candidates. Red arrows show the average arrival time for each side BBC calculated by the conventional BBC reconstruction.

4.1.2 Reconstruction of multiple vertices with BBC

In $\sqrt{s} = 500$ GeV proton-proton collisions, the mean number of hits in one BBC module is 7 - 8 with the BBC(novtx) trigger. The occupancy is not serious compared to the total number of channels of one module of 64; it is estimated that the probability the a particular PMT detects particles from different collisions in the same bunch crossing is the order of 1 %. Then if the arrival time of the particles from different collisions is separated enough, the hit distribution as a function of arrival time will create clusters, each of them corresponds to each collision, as shown in Figure 4.1. If we differentiate clusters from different collisions, it is possible to obtain more accurate collision vertices. On the other hand, reconstruction of multiple vertices by BBC cannot be perfect in principle for following reasons:

1. limited collision detection efficiency,
2. impossibility to distinguish true vertex and ghost vertex,
3. clusters from different collisions are degenerated in time.

For the first case, if one BBC module had no particle injection or its signal was below the threshold, there is no way to determine the difference of arrival time. For the second case, let us think the case of double collision events for example. Both BBC modules detect two clusters ideally. The combination number of arrival time difference between south and north timing are 4, and two of these are true vertices and the other two are ghosts. However, we cannot guess which two vertices are true and which are ghosts solely with the BBC. Furthermore, the combination of the above 1. and 2. case, that loosing true vertices as well as reconstructing ghost vertices could happen. Despite such limited reconstruction ability, the attempt to find multiple vertices with the BBC will give better performance than simply using the conventional reconstruction.

The algorithm of the clustering used to reconstruct multiple vertices are the following:

1. Fill the hit timing of each PMT in a histogram with some adequate bin-size.
2. Find the maximum bin of the histogram.
3. Register hits in the range of [maxbin-2, maxbin+2] (5 bins) to a “cluster”.
4. Remove entries in that range from the histogram.
5. Return to 2.
6. Continue loop 2. - 5. until no hit remains.

We have some arbitrariness of choosing the bin-size of the histogram. After some tests of the performance we chose the bin-size of 0.2 ns in this thesis. The performance of the new reconstruction algorithm was evaluated with simulation, which is described in Appendix D.

CHAPTER 4. RECONSTRUCTION

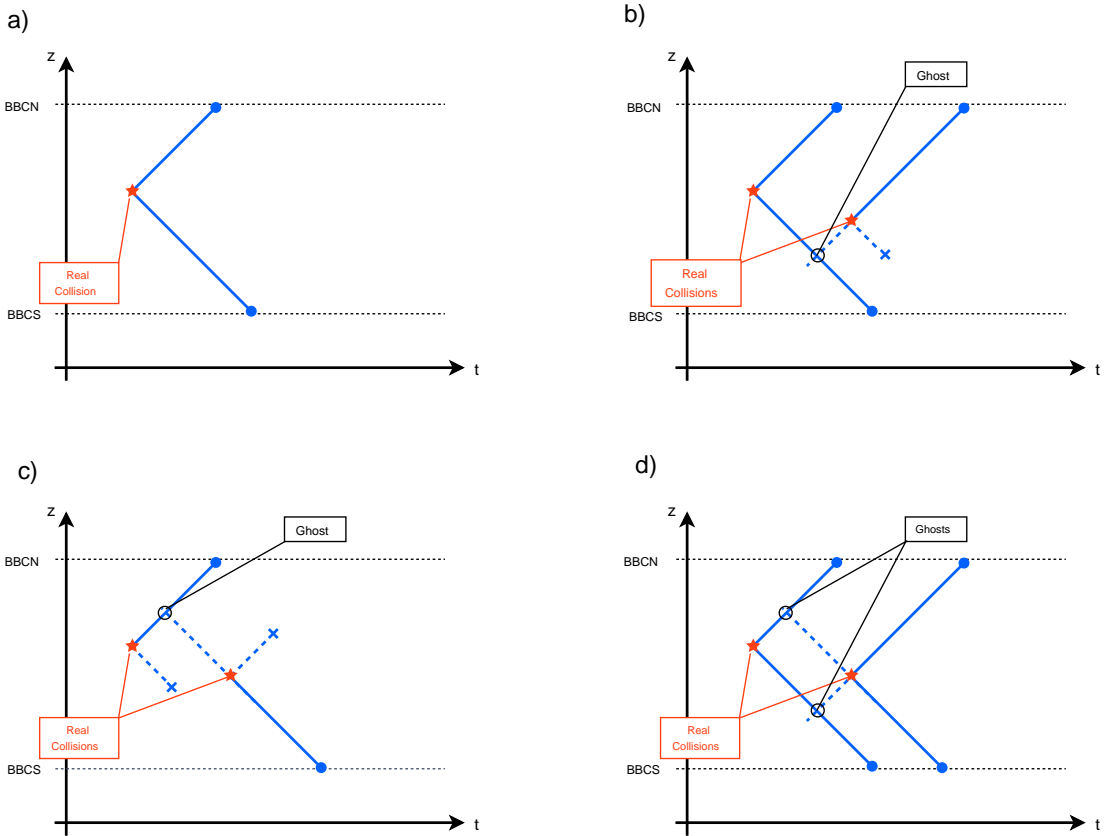


Figure 4.2: Diagrams of collision detection and reconstruction patterns of the BBC for typical cases. (a) A single collision event occurred, both BBC modules detected hits from the collision. (b) A double collision event occurred, one collision has hits for both modules, but the other collision has only hits in one module. Two vertices are reconstructed. One is the true vertex and the other is the ghost. The other true vertex is missed. (c) A double collision event occurred, one collision has hits in one module, and the other collision has hits in the other side module. One vertex is reconstructed, but this is a ghost. (d) A double collision event occurred, both collisions have hits in both modules. Totally $2 \times 2 = 4$ vertices are reconstructed. Two of them are true, and the two remainders are ghosts.

4.2 Muon Arm tracking

The procedure to find trajectories of charged particles and to determine their momenta and charges is called *tracking*. The tracking in the PHENIX Muon Arms is performed with outside-in process, i.e. the tracking starts from finding seeds in the MuID, then hits in the track are taken in from outer MuTr stations to inner stations. The determination of track momenta and charges is performed with the Kalman fit. Finally the vertex position and the associated RPC3 cluster hits are liked to the track and finally a set of tracking variables is constructed. The Muon Arm tracking has two strategies. One is the single-track strategy and the other is double-tracks strategy which assumes that the two tracks originate from the same vertex. Through this thesis we only use the single-track strategy, in the following we only focus on the single-track strategy.

4.2.1 MuID road reconstruction

The MuID is a coarse detector with position resolution of ~ 8 cm in horizontal (X) and vertical (Y) directions, and it is used to find the corridor of the particle which is used as the clue of precise tracking with the MuTr. The corridor of the particle identified by the MuID is called *road* in the PHENIX convention. The road finding is first performed for X and Y direction individually, then both are combined to construct a line in three dimensional space. Note that the MuID is located outside the magnetic field of the Muon Arm, bending is not considered. Moreover multiple scatterings in the absorber walls are sizable in case of low momentum tracks.

One-dimensional road finding The road finding algorithm is as follows. The unit of the readout is the two-pack tubes as mentioned in Sec. 3.2.3.1, and signals of the two-packs are called hits. Hits in the same panels are grouped to compose clusters. Here simply successive hits are connected as a cluster. The size of a cluster is maximally 2, and clusters whose number of hits is larger than 2 are split to small clusters. The clusters in the Gap-2 or the Gap-3 are used as the seed-cluster of constructing roads. Then two search orders are taken to connect clusters in different gaps to compose a one-dimensional road:

- Gap-2 \Rightarrow Gap-3 \Rightarrow Gap-1 \Rightarrow Gap-4 \Rightarrow Gap-5
- Gap-3 \Rightarrow Gap-2 \Rightarrow Gap-1 \Rightarrow Gap-4 \Rightarrow Gap-5

The search window is set as ± 60 cm from the projected position to the gap of interest for the case of associating the second gap, and is set as ± 30 cm for the other cases. The projection is performed based on the linear fit of the clusters associated to the road up to that time. Note that the vertex position reconstructed by the BBC is supplementally included when the number of associated clusters in the MuID at the fit is less than 3. The search of clusters goes over the adjacent panels, since panels are overlapped. If no cluster was found, the algorithm skips that gap then proceeds to the next gap. If more than one clusters were found in the search window, the road bifurcates to create another road. The maximum allowed skipped number of gaps is one.

Composing two-dimensional roads Once horizontal and vertical lists of one-dimensional roads are completed, next we move on combining one-dimensional roads to compose two-dimensional roads. Several conditions are imposed for two-dimensional roads:

- Total numbers of fired gaps of the horizontal and vertical roads do not differ by more than 1.
- The last fired gap of the horizontal and vertical roads do not differ by more than 1.

- Check of the geometrical intersection, i.e., the clusters are consistently in the same panel or in overlap region.
- The distance to closest approach of the road to the beam axis is less than ± 180 cm in both X and Y direction.
- The χ^2 value of the road fitting is less than 1000 for both X and Y directions.
- The last fired gap is deeper than Gap-2.

Grouping roads The two-dimensional roads which give similar tracking results combining with the MuTr hits are grouped as road groups, and only one representative road in the group is used as the seed of the tracking at the MuTr. The grouping contributes to reduce the computation time. To be specific, two roads are grouped in the following conditions:

- The hits of a road are all within the window of hits from the other road.
- The projection of a road to the MuTr Station-3 is in the window of the projection of the other road.

The representative road of the group has the closest Station-3 projection to the average of all Station-3 projections of the roads in the group.

4.2.2 MuTr hit reconstructions

Cluster finding and fitting The reconstruction of the MuTr starts with determination of the position of charged particle injection at the gap. Firstly hits on the strips are grouped as clusters. The procedure to make clusters is similar to the clustering in the MuID hits. The maximum size of a cluster is 4. The clustering is performed for each half-octant, does not go across the boundary of half-octants.

Next the position measurement is performed as follows. The injecting charged particle loses some of its energy in the gap with ionizing the gas, then ionized electrons drift to anode wires then occur avalanche multiplication. Electrons which are created by the avalanche drift to the anode wire while ions drift to the cathode planes, then the mirror charges on the cathode strips induced by drifting electrons and ions are detected as signals. The distribution of mirror charges on the cathode strips is determined by the geometry of the cell structure of the chamber as a consequence of the solution of the Poisson's equation. Especially in the case of multi-wire proportional chamber, the charge distribution $\rho(\lambda)$ is empirically described with a single parameter K_3 as

$$\frac{\rho(\lambda)}{q_{\text{tot}}} = K_1 \frac{1 - \tanh^2(K_2 \lambda)}{1 + K_3 \tanh^2(K_2 \lambda)}, \quad (4.5)$$

where

$$K_1 \equiv \frac{K_2 \sqrt{K_3}}{4 \tan^{-1}(\sqrt{K_3})}, \quad K_2 \equiv \frac{\pi}{2} \left(1 - \frac{\sqrt{K_3}}{2}\right), \quad (4.6)$$

and $\lambda = x/h$ is the reduced distance from the center of gravity of the distribution where h is the distance between the anode and the cathode plane. q_{tot} is the total charge created. Note that the parameter K_3 is determined by the geometry and is not a free parameter. The above relation is known as the Mathieson function[64], and we fit the charge distribution on the cathode strips with the Mathieson function to measure the particle injection position with respect to the strip-lined direction. Due to the read-out of every other strips, center of gravity approach does not provide precise center position. The measured position of the cathode plane is called *coordinate* in the nomenclature.

Coordinate matching The coordinates in the different planes of the same gap are coupled to reconstruct the full three-dimensional particle injection positions. The reconstructed three-dimensional positions are called *gap-coordinates*. Gap-coordinates are subsidiary variables in the process of the tracking.

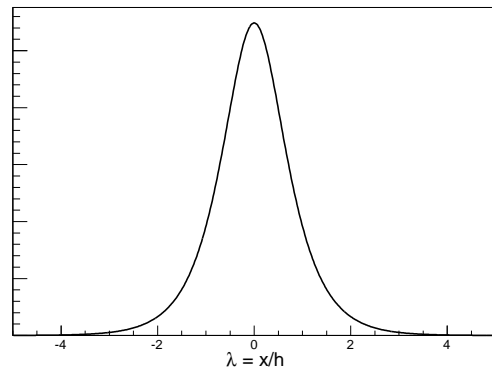


Figure 4.3: Mathieson function with $K_3 = 0.7$.

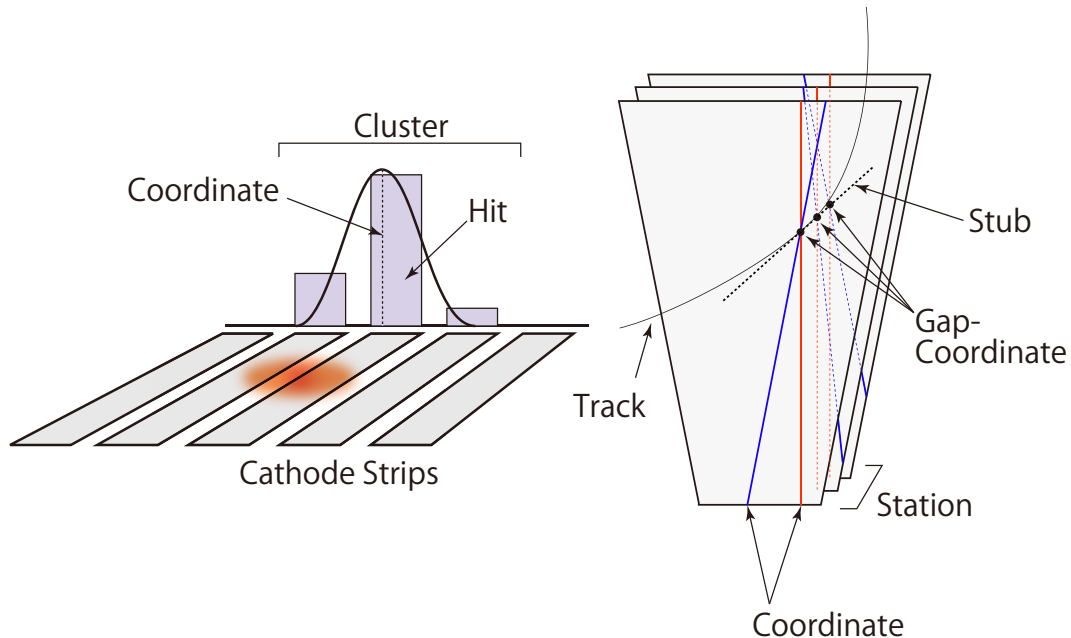


Figure 4.4: Nomenclatures of MuTr tracking.

4.2.3 Track finding

Track finding with stubs The track finding is the preliminary process before the track fitting to determine a set of coordinates used in the track fitting. As described above, the track finding employs the outside-in process and the MuID roads are used as seeds for the tracks. For each representative road in the road groups, a search window is set on the plane of the MuTr Station-3. The size of the search window is 50 cm (30 cm) for the South (North) Arm in both radial (θ) and azimuthal (ϕ) directions. The central point of the search window is the projection of the road to the Station-3. The coordinates of different cathode planes in the Station-3 in the search window are then grouped to compose possible particle passages called *stubs*. Coordinates in the same cathode plane cannot be included in the same stub. A stub must contain more than 2 coordinates. The coordinates which composes a stub are fitted with a three-dimensional line, and if the χ^2 of the fitting is too large the stub is rejected. Also the traverse angle of the stub with respect to the gap plane (dw/dz) must not be too large. The same quality cuts are also applied to the stubs in the other stations. If a Station-3 stub which satisfies above conditions, a new track is created with that stub and the seed MuID road. Next all qualified stubs in the Station-2 and Station-1 in the same octant are individually associated to the tracks. In this step no search window is imposed.

Bend-plane fitting, ghost rejection Once a set of three stubs of the track is completed, a fast bend-plane fitting is performed for the position of three stubs as well as the vertex position, to roughly obtain the track qualities, the momentum and the charge. In the bend-plane fitting, the θ angle of the track is roughly assumed as the θ angle between the line connecting the Station-2 stub and the origin and the beam axis. Based on the assumption that the track is along with the line of the origin - Station-2 stub line, the bend plane projected to the z -axis as well as transverse momentum kick are calculated for the Station-1,2 and Station-2,3 stub position differences. The bend-plane is fitted to the stub positions. Then ghost tracks are rejected, where relatively the best quality one track is selected among the tracks which share at least one common coordinate based on χ^2 value of the bend-plane fit and the number of coordinates included in the track.

4.2.4 Kalman fitting

The tracks which survived the ghost rejection are fitted with the Kalman fitter. In the Kalman fitting the coordinates included in the track are used to determine the position, momentum and the charge. The momentum and the charge estimated by the bend-plane fitting are used as the seed of the Kalman fitting. The key feature of the Kalman fitting is that it filters the parameter space every time the fitting includes the new coordinate, then it avoids to calculate the inversion of $n \times n$ matrix to obtain the most consistent set of parameters. Also the Kalman fitting is suitable to include the effect of multiple scattering and energy losses naturally. As the measured momentum in the MuTr is less than the true momentum by the amount of the energy loss at the hadron absorber in front of the MuTr, the fitted momentum is corrected for that energy loss. The correction is performed by extrapolating the track to the vertex z -position² with the Kalman filter with fixing the fitted parameters. The similar extrapolation is also performed to the MuID side up to the RPC3 plane, where multiple scattering and energy loss at the absorber walls are also taken into account.

²Here the conventional BBC reconstruction is used for the estimation of the vertex. If the BBC could not reconstruct the vertex, the origin is assumed.

4.2.5 MuID and RPC3 association

When the Kalman fitting is done, the reconstructed track is passed to MuID once again, and the reconstruction refines the MuID roads. In this second road finding, the condition of road finding is looser than the first in order not to miss true hits in the MuID. Maximally three roads can be selected to associate with the track corresponding the depth of the road, where the road depth is either of 2,3,4 and the depth of the associated roads must be different each other. Finally the best matching road amongst the three roads is associated to the track. The matching is evaluated using DG0 and DDG0 variable which will be introduced in the next section.

The reconstructed MuTr track is linearly extrapolated outside from the Station-3, and the intersection point with the RPC3 is calculated. The association of RPC3 clusters to the track is performed by searching the closest RPC3 clusters. The clustering in RPC3 is simply concatenating successive hit strips. The timing of the cluster is the average of the hit strips in the cluster. The closest RPC cluster is associated to the track.

CHAPTER 4. RECONSTRUCTION

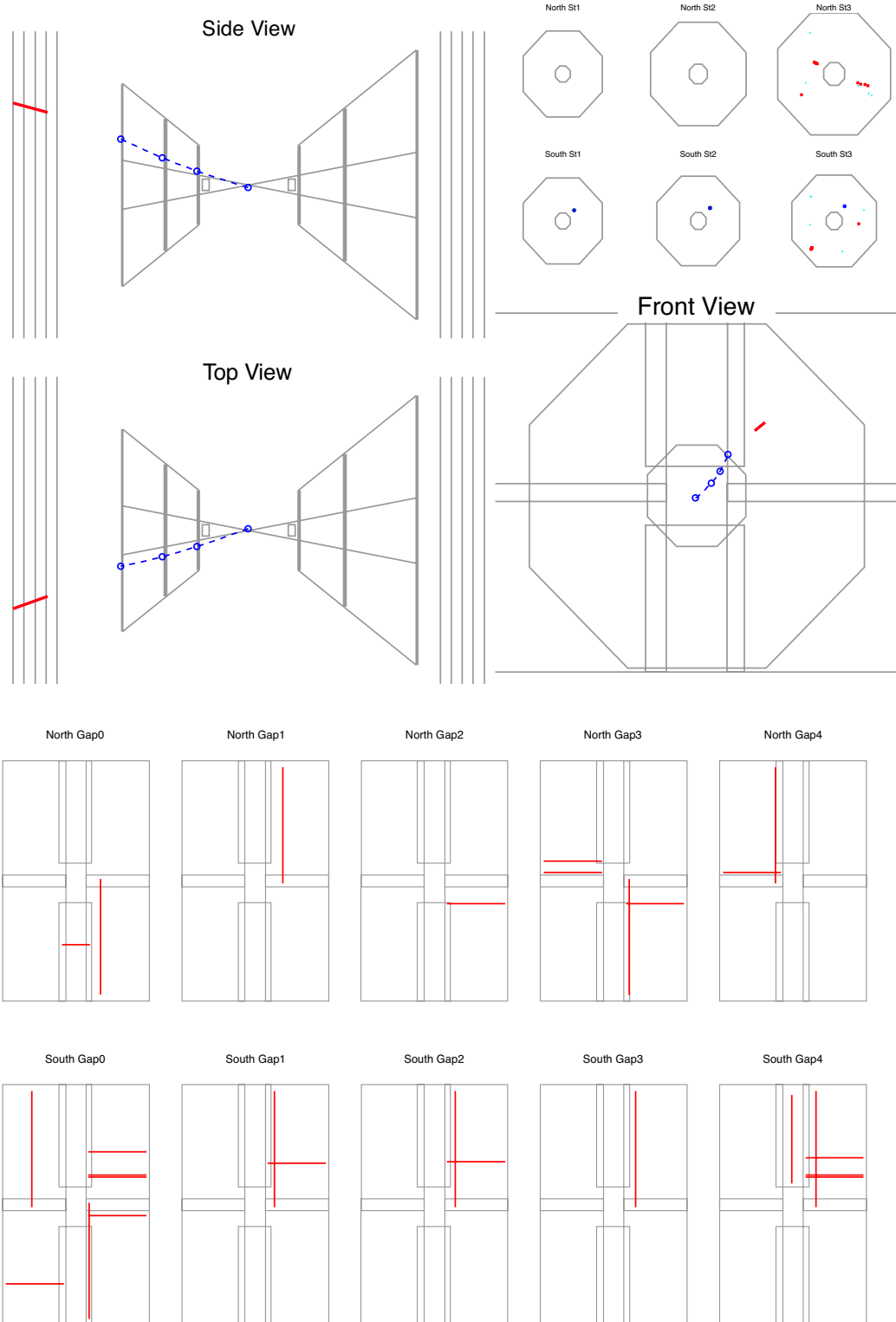


Figure 4.5: A visualization of the reconstruction of an event with a track.

4.3 Tracking variables

As a result of the tracking, not only the main tracking parameters but also associated variables are defined for each track. These tracking variables are used for the qualification of the track to identify muons.

- charge, momentum

The *momentum* of the track is defined at the vertex point. We use the following conventions:

$$\mathbf{p} = (p_x, p_y, p_z) = (p_x, p_y, p_z)|_{z=z_{\text{vtx}}} \quad (4.7)$$

$$p = |\mathbf{p}| = (p_x^2 + p_y^2 + p_z^2)^{1/2} \quad (4.8)$$

$$p_T = (p_x^2 + p_y^2)^{1/2} \quad (4.9)$$

and the integer charge is represented as q if needed. If we explicitly distinguish the physical (true) momentum and the reconstructed momentum, we use suffices like $p_T^{\text{reco}}, p_T^{\text{true}}$. The dimension of the momentum is in GeV/c .

- pseudorapidity (η), azimuthal angle (ϕ)

The pseudorapidity η and the azimuthal angle ϕ is defined with the track parameter at the vertex as

$$\eta = \frac{1}{2} \ln \left(\frac{p + p_z}{p - p_z} \right) \Big|_{z=z_{\text{vtx}}} \quad (4.10)$$

$$\phi = \tan^{-1} \left(\frac{p_y}{p_x} \right) \Big|_{z=z_{\text{vtx}}} . \quad (4.11)$$

- Reduced chi-square : χ_{track}^2

The reduced chi-square is the track fit quality which describes the quality of the fit to the MuTr coordinates. χ_{track}^2 is calculated in the Kalman filter based on the residuals between the measured coordinate of the cathode planes and the position of the track with taking account of the finite position resolution and error propagations related with multiple scattering and energy losses. Note that the degree of freedom of the track is 7 (3-position, 3-momentum and charge) then the number of cathode planes must be ≥ 8 . Due to the fact that the noise hits contaminating to the cluster produce non-gaussian residual distributions, the distribution of χ_{track}^2 of the given number of coordinates does not obey the corresponding statistical χ^2 distribution, and typically it has very long tail components.

- MuID road depth: lastGap

The depth of the MuID road is defined as the deepest gap ID of the associated road. By convention lastGap runs from 2 to 4, and 4 is the deepest.

- MuID matching: DG0(DG4), DDG0

The matching between the track and the road is evaluated with both the distance and the angle between the two. First the track is linearly extrapolated to the first or the last Gap of the MuID. The distance between the extrapolated track and the road at the first Gap plane (Gap-1) is called DG0. The dimension of DG0 is in cm. As well, the opening angle between the extrapolated track and the road is called DDG0. The dimension of DDG0 is in degree. We also define DG4, the same as DG0 but evaluated at the last Gap plane (Gap-5).

- Vertex matching: DCA_r , DCA_z

Distance to closest approach (DCA) is defined between two lines as the length to give the minimum distance of the two lines. We use the DCA between the extrapolated track and the beam axis to evaluate the matching of the track with the collision vertex. Here the extrapolated track is the linear extrapolation of the track from the Station-1 with keeping the direction of the track at the Station-1. DCA_r is defined as the DCA between the extrapolated track and the beam axis, as illustrated in Figure 4.7.

DCA_z is defined as the difference of the z -position of the position of the track which gives DCA_r from the collision vertex given by the BBC. As we use multiple-vertices reconstruction as described in the previous section, we would have more than one vertex candidates. For each vertex candidate j we calculate the $\text{DCA}_{z,j}$, and we *define* the DCA_z of the track as the one to give the minimum absolute value among them. Note that DCA_z in our definition has sign, i.e., it could be positive or negative. The dimensions of DCA_r , DCA_z are in cm.

- RPC3 matching: RpcDCA and RpcTime

RpcDCA is defined as the distance to closest approach of the linearly extrapolated track to the closest RPC3 strip of the associated cluster as illustrated in Figure 4.8. For each RPC hit we have the TDC value (from 0 to 43) which divides one beam clock (106 ns) into 44. The timing of the associated RPC cluster of the track is called RpcTime .

- position at the Station- i : (x_i, y_i, z_i)

The position of the track at the Station- i is defined as the intersection point of the track with the closest cathode plane of the Station- i to the origin.

- Difference of the ϕ -angle between the Stations: $d\phi_{ij}$

$$d\phi_{ij} = \phi_j - \phi_i = \tan^{-1} \left(\frac{y_j}{x_j} \right) - \tan^{-1} \left(\frac{y_i}{x_i} \right) . \quad (4.12)$$

In particular, $d\phi_{12}$ and $d\phi_{23}$ are used. Related to $d\phi_{ij}$, later in the analysis part we also use the reduced azimuthal bending dw_{ij} defined as

$$dw_{ij} \equiv p_T \cdot \sin \theta \cdot d\phi_{ij} \quad (4.13)$$

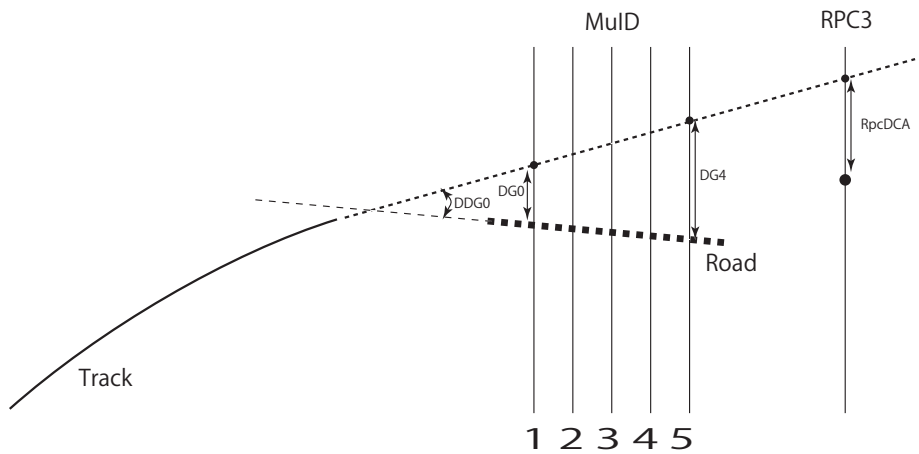


Figure 4.6: Schematic illustration of the definitions of DG0, DG4, DDG0 and RpcDCA in side view.

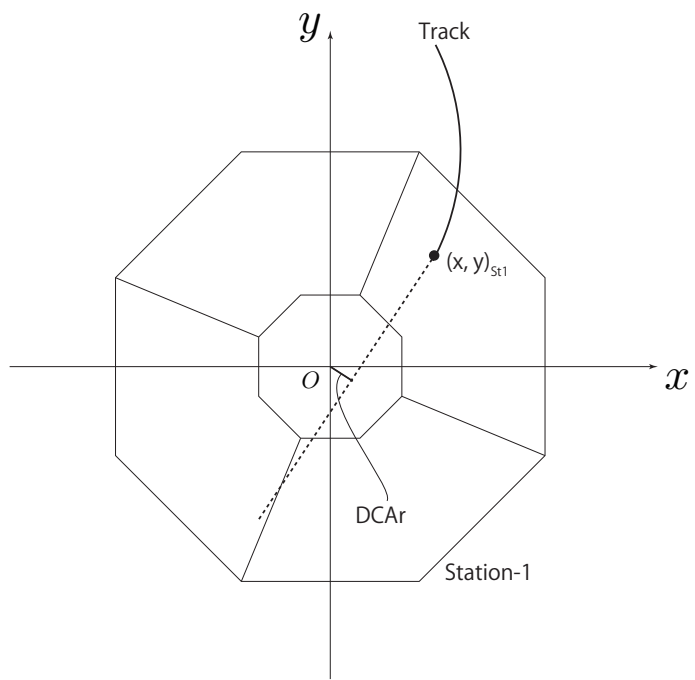


Figure 4.7: Definition of DCA_r .

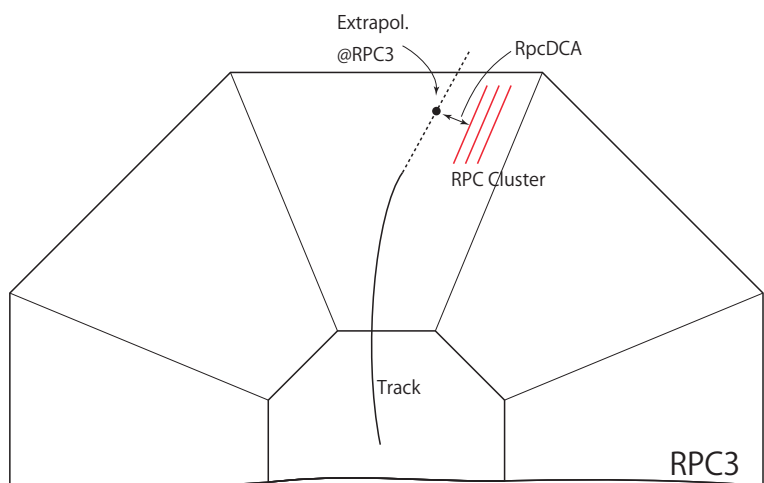


Figure 4.8: Illustration of RpcDCA in beam view.

Chapter 5

Data set

The data used in this thesis are longitudinally polarized proton-proton collisions at $\sqrt{s} = 500$ GeV, and they were taken from February 11 to April 18, 2011. During this period the PHENIX was delivered about 90 pb^{-1} of integrated luminosity by the RHIC. The PHENIX data taking has worked for about 33 pb^{-1} of the total as the physics runs. Due to the dead time of the DAQ the recorded integrated luminosity was about 30 pb^{-1} . Note that above values do not take into account of the correction for multiple collisions described in 5.1.2. At the RHIC, a stable beam fill elongates about 8 hours. The PHENIX DAQ system takes data maximally 1 hour at a time. This data taking unit is called *run*. Normally several runs are taken per fill. The accelerator group makes the numbering of the fill, while the PHENIX group makes the numbering of the run. Both the fill numbers and the run numbers are serial through the RHIC history. The runs used in this thesis is from Run 330693 to Run 340515, and the corresponding fill number is from 15154 to 15472. Among these, totally 433 runs are the physics runs used in the analysis.

Apart from the physics runs, the PHENIX takes other categories of runs for services. The zero field runs are taken every time before turning the magnets on. The zero field runs are used to calibrate the alignment of MuTr. Before the physics run duration or during beams are not filled, the cosmic runs which only the MuID trigger is turned on are taken. The calibration runs are taken normally once per day. Calibration runs are taken for each detector subsystem, by the standalone DAQ mode. The data in calibration runs are recorded to the database and referred at the time of data production.

#bunches	ions/bunch [$\times 10^9$]	β^* [m]	emittance [μm]
109	165	0.6	$24 \rightarrow 24$
$\mathcal{L}_{\text{peak}}$ [$\text{cm}^{-2}\text{s}^{-1}$]	\mathcal{L}_{avg} [$\text{cm}^{-2}\text{s}^{-1}$]	$\int_{\text{week}} \mathcal{L} dt$ [pb^{-1}]	
145×10^{30}	90×10^{30}	25	

Table 5.1: The machine parameters of the RHIC during $\sqrt{s} = 500$ GeV polarized proton-proton collisions in 2011. Values are taken from [68].

5.1 Luminosity

In the PHENIX, the luminosity of the run is monitored with the BBCs. The BBCs detect proton-proton inelastic scattering collisions with a certain fraction. This fraction is called the

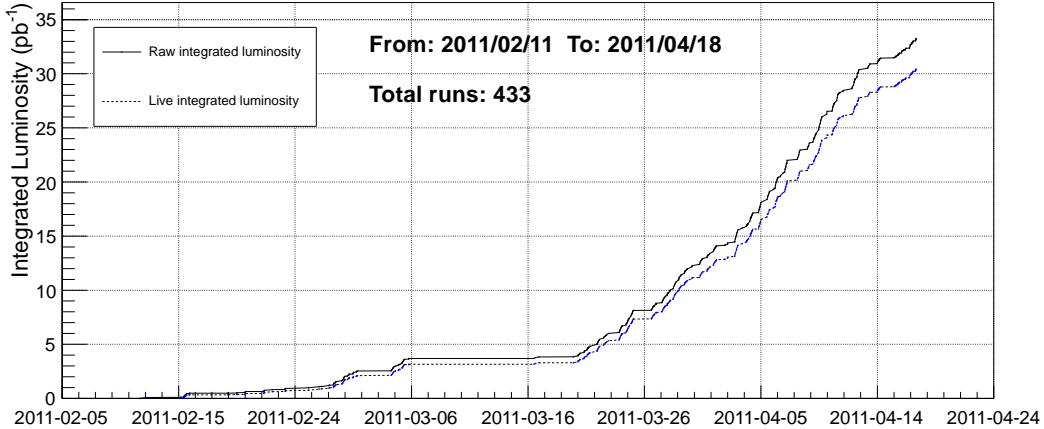


Figure 5.1: Data taking history of year 2011 runs of proton-proton collisions at $\sqrt{s} = 500$ GeV.

BBC efficiency ε_{BBC} . Alternatively the term “BBC cross section” σ_{BBC} is also used, where $\sigma_{\text{BBC}} \equiv \varepsilon_{\text{BBC}} \cdot \sigma_{pp}^{\text{tot}}$ (σ_{pp}^{tot} is the total inelastic cross section of proton-proton collisions). For the given luminosity \mathcal{L} , the BBCs have its trigger rate R_{BBC} and $\mathcal{L} = \sigma_{\text{BBC}} \cdot R_{\text{BBC}} = \sigma_{pp}^{\text{tot}} \varepsilon_{\text{BBC}} \cdot R_{\text{BBC}}$ at $\mathcal{L} \rightarrow 0$ limit. The (integrated) luminosity of the run is measured with the BBC trigger rate. The absolute calibration of the BBC efficiency or the BBC cross section is performed with a technique so-called the van der Meer scan. The BBC trigger rate is additionally needed to be corrected for the multiple collisions in one bunch crossing to obtain the accurate luminosity.

5.1.1 van der Meer scan

The van der Meer scan measures the beam-overlap size by scanning one side beam with respect to the other side beam. The luminosity determined by the van der Meer scan is especially called the *machine* luminosity, $\mathcal{L}_{\text{machine}}$. $\mathcal{L}_{\text{machine}}$ is given as

$$\mathcal{L}_{\text{machine}} = \frac{f_r n_b I_B I_Y}{2\sigma_x \sigma_y} \quad (5.1)$$

where f_r is the ring-revolution frequency of the beam, n_b is the number of collisions per revolution, $I^{(B)}(I_Y)$ is the number of ions per bunch of the Blue (Yellow) beam, and σ_x, σ_y is the beam-overlap size with respect to the x and y axis, respectively. I_B, I_Y are measured by monitoring the wall current of each ring induced by the beam-current. The van der Meer scan assumes that the number density distribution of the two beams are both Gaussian, and that no correlation exists between the x -axis and the y -axis. Let us suppose that the center of the two beams are distant by Δx in x -axis, and that the beam width in $x(y)$ -direction of the Blue (Yellow) beam is $\sigma_{B(Y),x(y)}$, and the density profile of the two beams are $\rho_B(x, y), \rho_Y(x, y)$. The overlap integral of the two beam $R(\Delta x)$ is then

$$R(\Delta x) = \int \rho_B(x, y) \rho_Y(x - \Delta x, y) dx dy \quad (5.2)$$

$$= \frac{1}{\sqrt{2\pi}\sigma_y} \cdot \left[\frac{1}{\sqrt{2\pi}\sigma_x} e^{-(\Delta x)^2/\sigma_x^2} \right] \quad (5.3)$$

where $\sigma_x^2 \equiv \sigma_{B,x}^2 + \sigma_{Y,x}^2$. By integrating $R(\Delta x)$ over Δx , we obtain

$$\int R(\Delta x) d\Delta x = \frac{1}{\sqrt{2\pi}\sigma_y} \quad (5.4)$$

then

$$\frac{\int R(\Delta x) d\Delta x}{R(\Delta x = 0)} = \sqrt{2\pi}\sigma_x . \quad (5.5)$$

Similarly for y -axis scanning, we obtain

$$\frac{\int R(\Delta y) d\Delta y}{R(\Delta y = 0)} = \sqrt{2\pi}\sigma_y . \quad (5.6)$$

$R(\Delta x), R(\Delta y)$ is proportional to the rate of luminosity monitor, e.g. the BBCs trigger rate. Hence σ_x, σ_y is obtained by scanning one beam horizontally and vertically with respect to the other beam. Once $\mathcal{L}_{\text{machine}}$ is determined, we can define the BBC cross section as

$$\sigma_{\text{BBC}} \cdot \mathcal{L}_{\text{machine}} \cdot \varepsilon_{\text{vertex}}^{\text{rel}} = R_{\text{BBC}}(\Delta x = \Delta y = 0). \quad (5.7)$$

where $\varepsilon_{\text{vertex}}^{\text{rel}}$ is the relative BBC trigger efficiency correction as a function of z . In the above derivation we assumed the beam size is static. However in the actual van der Meer scan, more complexity arises related with the focusing of the beam; at the off-focusing position in the z -axis, the size of the beam is wider than at the focusing point, then the luminosity decreases. This zt -dependence is called the *hourglass effect*. The hourglass effect is the main uncertainty of the σ_{BBC} , i.e., the main uncertainty of the luminosity measurement. Table 5.2 summarizes the uncertainties of the BBC cross section. As a result, for $\sqrt{s} = 500$ GeV proton-proton collision the BBC cross section is measured as

$$\sigma_{\text{BBC}} = 32.51 \pm 1.19_{\text{(stat)}} \pm 3.01_{\text{(sys)}} \text{ mb} \quad (5.8)$$

and the corresponding BBC trigger efficiency ε_{BBC} is 53 %.

uncertainty	value
relative trigger efficiency	2.0 %
wall current	0.4 - 1.1 %
van der Meer scan	1.5 - 3.3 %
hourglass effect, crossing angle	7.6 %
$R(\Delta x = \Delta y = 0)$, multiple collision effect	3.1 - 4.5 %
total systematic uncertainty	9.3 %
statistic uncertainty	3.6 %
total	10 %

Table 5.2: Errors on the BBC cross section.

5.1.2 Multiple collision correction

Figure 5.2 shows the distribution of data used in this thesis with respect to BBC(novtx) trigger rate. The average trigger rate is about 1.7 MHz and the maximum trigger rate is about 3.2 MHz. Thinking about the maximum rate case, 3.2 MHz is translated to that the average collision probability per bunch crossing is about 70 % from the BBC trigger efficiency of $\varepsilon_{\text{BBC}} = 0.53$. By assuming the Poisson statistics, about 30 % of the BBC-triggered events contain multiple

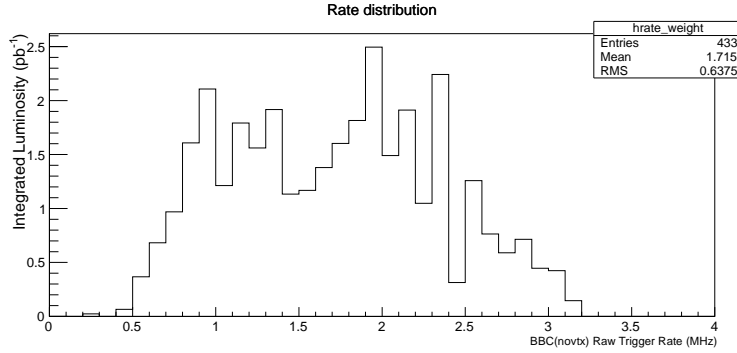


Figure 5.2: Distribution of data with respect to BBC(novtx) trigger rate.

collisions. Since the BBC trigger does not differentiate multiple collisions from single collisions, the trigger rate needs to be corrected for the multiple collisions.

The BBC trigger condition is defined, as described in 3.3.2.1, as the coincidence of the South BBC and the North BBC. Part of collisions hits only one side BBC, and these collisions are not counted by the BBC triggers. However in case of multiple collisions, we could have the case, for example, that one collision hits only the South BBC, and the other collisions hit only the North BBC then the bunch crossing is counted as a triggered event. The above situation needs us to consider not only the BBC trigger efficiency ε_{BBC} , but also the one-side BBC hit efficiencies for the South and North BBCs for correction of multiple collisions.

Let us move on the concrete calculations. Here we neglect the possible small backgrounds such as collisions between beams and remaining gas in the beam pipe. We will use the special conventions for BBC efficiencies; for n collisions in a bunch crossing, the probability to have hits in the both side BBCs is denoted as $\varepsilon_B^{(n)}$, and the probability to have only the South, North side BBC is denoted as $\varepsilon_S^{(n)}, \varepsilon_N^{(n)}$ respectively, and the probability that none of BBCs have any hit is denoted as $\varepsilon_0^{(n)}$. These efficiencies satisfy the completeness

$$\varepsilon_B^{(n)} + \varepsilon_S^{(n)} + \varepsilon_N^{(n)} + \varepsilon_0^{(n)} = 1 \quad (5.9)$$

and we simply omit (n) for $n = 1$ case, e.g. $\varepsilon_B^{(1)} = \varepsilon_B$. It is easy to find the relation

$$\varepsilon_0^{(n)} = (\varepsilon_0^{(1)})^n = (\varepsilon_0)^n. \quad (5.10)$$

The case of $\varepsilon_S^{(n)}$ occurs when $m \geq 1$ of n collisions hit only the South BBC and the other collisions hit neither sides of the BBCs. This is represented by

$$\begin{aligned} \varepsilon_S^{(n)} &= \sum_{m=1}^n {}_n C_m (\varepsilon_S)^m (\varepsilon_0)^{(n-m)} \\ &= \left(\sum_{m=0}^n {}_n C_m (\varepsilon_S)^m (\varepsilon_0)^{(n-m)} \right) - \varepsilon_0^{(n)} \\ &= (\varepsilon_S + \varepsilon_0)^n - (\varepsilon_0)^n. \end{aligned} \quad (5.11)$$

Similarly,

$$\varepsilon_N^{(n)} = (\varepsilon_N + \varepsilon_0)^n - (\varepsilon_0)^n \quad (5.12)$$

By using the completeness, we will find

$$\varepsilon_B^{(n)} = 1 - \varepsilon_S^{(n)} - \varepsilon_N^{(n)} - \varepsilon_0^{(n)} \quad (5.13)$$

$$= 1 - (\varepsilon_S + \varepsilon_0)^n - (\varepsilon_N + \varepsilon_0)^n + (\varepsilon_0)^n. \quad (5.14)$$

Next we introduce the Poisson statistics, since we are interested in the average efficiencies for the given luminosity. Let us denote that the mean number of collisions per bunch crossing as μ (also called as the multiple collision parameter) and the corresponding average efficiencies as $\varepsilon_B(\mu), \varepsilon_S(\mu), \varepsilon_N(\mu), \varepsilon_0(\mu)$. Then It is straightforward to show

$$\begin{aligned} \varepsilon_0(\mu) &= \sum_{n=0}^{\infty} \frac{e^{-\mu} \mu^n}{n!} \varepsilon_0^{(n)} \\ &= e^{-\mu} \sum_{n=0}^{\infty} \frac{(\mu \varepsilon_0)^n}{n!} \\ &= e^{-\mu} e^{\mu \varepsilon_0} = e^{-\mu(1-\varepsilon_0)} \\ &= e^{-\mu(\varepsilon_B + \varepsilon_S + \varepsilon_N)} \end{aligned} \quad (5.15)$$

and similarly,

$$\varepsilon_S(\mu) = e^{-\mu(\varepsilon_B + \varepsilon_N)} - e^{-\mu(\varepsilon_B + \varepsilon_S + \varepsilon_N)} \quad (5.16)$$

$$\varepsilon_N(\mu) = e^{-\mu(\varepsilon_B + \varepsilon_S)} - e^{-\mu(\varepsilon_B + \varepsilon_S + \varepsilon_N)} \quad (5.17)$$

$$\varepsilon_B(\mu) = 1 - e^{-\mu(\varepsilon_B + \varepsilon_S)} - e^{-\mu(\varepsilon_B + \varepsilon_N)} + e^{-\mu(\varepsilon_B + \varepsilon_S + \varepsilon_N)}. \quad (5.18)$$

Eq. (5.18) represents the BBC trigger efficiency as a function of the Poisson parameter μ . The trigger rate $R(\mu)$ is given as

$$R(\mu) = \mathcal{L}\sigma_{pp}^{\text{tot}} \varepsilon_B(\mu) = \mathcal{L}\sigma_{\text{BBC}} \frac{\varepsilon_B(\mu)}{\varepsilon_{\text{BBC}}} \quad (5.19)$$

where $\varepsilon_{\text{BBC}} = \lim_{\mu \rightarrow 0} \varepsilon_B(\mu)$. The above equation is the correction of the luminosity for multiple collisions. $\varepsilon_B(\mu)$ is determined once $\varepsilon_{S,N}$ are measured. By using the Clock trigger data, we can extract the ratios $\varepsilon_S/\varepsilon_B$ and $\varepsilon_N/\varepsilon_B$. As a result, we obtained $\varepsilon_S/\varepsilon_B = \varepsilon_N/\varepsilon_B = 0.42 \pm 0.01$. Figure 5.3 shows the relation between the multiple collision parameter μ and the BBC(novtx) trigger rate.

5.1.3 Bunch-by-bunch fluctuation

The fluctuation of luminosity bunch-by-bunch was measured with comparing bunch-by-bunch track yield for each run. The fluctuation is represented as the RMS value around the average after excluding blank bunches. Figure 5.4 shows the result of run-by-run RMS value. Through the runs, the average value of the RMS is 12.5 %. This bunch-by-bunch fluctuation causes the error to the correction of multiple collision effect at the second order level.

Bunch-by-bunch luminosity fluctuation should also be cared to calculated spin asymmetries since the pattern of the spin of the beams are different. We will return to this point in the final measurement of the spin asymmetry in Sec. 8.4.

CHAPTER 5. DATA SET

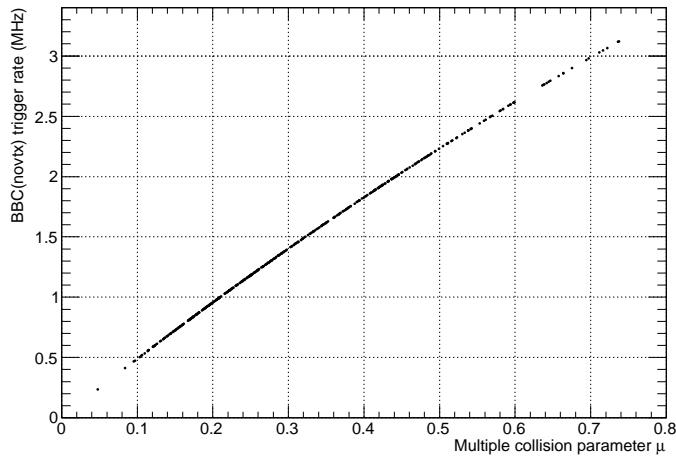


Figure 5.3: BBC(novtx) trigger rate as a function of multiple collision parameter μ .

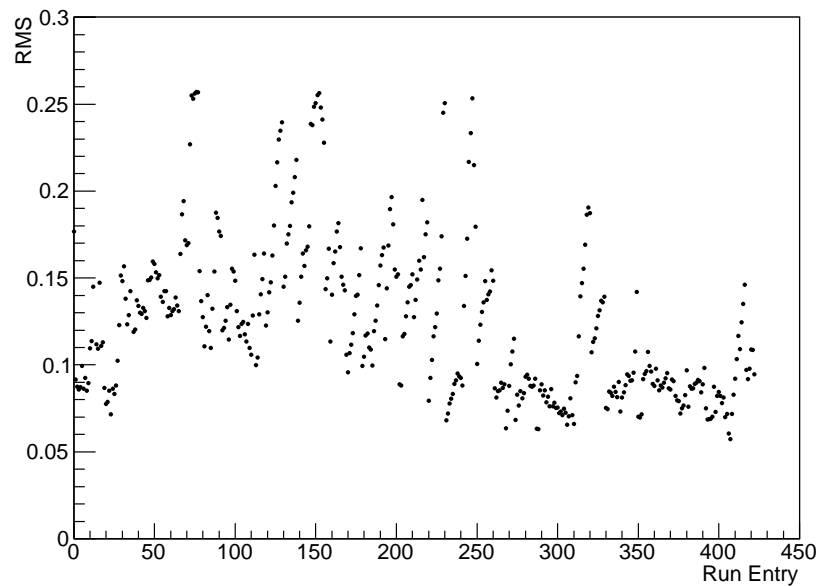


Figure 5.4: RMS of bunch-by-bunch relative luminosity for each run.

5.2 Beam polarization

5.2.1 Absolute polarization

As described in Sec. 3.1.3.2, the beam polarization is measured with the CNI polarimeter for relative profiling and the H-jet polarimeter for absolute calibration. Figure 5.5 shows the fill-by-fill beam polarization after correcting the absolute scaling in 2011 runs.

One systematic uncertainty of the H-jet measurement is the contamination of molecular hydrogen contamination in the polarized hydrogen jet. Other backgrounds to the H-jet measurement was estimated by the variation of the result by applying different cuts to the events. There is also another systematic uncertainty due to the profile of polarization in the beam; the average polarization observed by the H-jet, CNI polarimeter and the opposite colliding beam is different each other. The CNI polarimeter uses a thin carbon ribbon as the target so that it is possible to scan the profile of the beam. With the profile measured by the CNI polarimeter, the effective polarization at the collision is estimated by re-weighting the beam intensity profile. The final result of the beam polarization used in this thesis is summarized in Sec. 8.3.

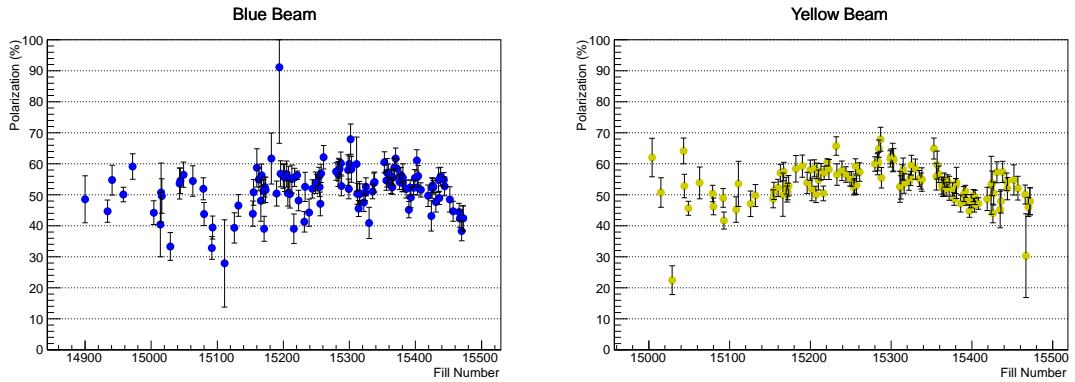


Figure 5.5: Fill-by-fill beam polarizations in year 2011 runs. The left panel is for the Blue beam and the right panel is for the Yellow beam.

5.2.2 Transverse polarization

Transverse polarization at the collision was measured with ZDC. The Shower Maximum Detector (SMD) measures the position of the neutron injection into the ZDC, and left-right, up-down asymmetries A_{LR} , A_{UD} defined as the following are evaluated:

$$A_{LR} \equiv \frac{1}{P} \frac{\sqrt{N_L^\Rightarrow N_R^\Leftarrow} - \sqrt{N_R^\Rightarrow N_L^\Leftarrow}}{\sqrt{N_L^\Rightarrow N_R^\Leftarrow} + \sqrt{N_R^\Rightarrow N_L^\Leftarrow}}, \quad (5.20)$$

$$A_{UD} \equiv \frac{1}{P} \frac{\sqrt{N_U^\Rightarrow N_D^\Leftarrow} - \sqrt{N_D^\Rightarrow N_U^\Leftarrow}}{\sqrt{N_U^\Rightarrow N_D^\Leftarrow} + \sqrt{N_D^\Rightarrow N_U^\Leftarrow}} \quad (5.21)$$

where P is the absolute beam polarization, N_L, N_R, N_U, N_D is the number of events in the four areas of the ZDC (“left”, “right”, “up”, “down”) and “ \Rightarrow ”, “ \Leftarrow ” denotes the two spin states of the beam. The transverse asymmetry A_N is defined as $A_N = \sqrt{A_{LR}^2 + A_{UD}^2}$. As the calibration, A_N is firstly measured for transverse collision runs, denoted as A_N^{trans} . The transverse

component of the beam polarization is calculated as

$$\frac{P_T}{P} = \sqrt{\left(\frac{A_{LR}}{A_N^{\text{trans}}}\right)^2 + \left(\frac{A_{UD}}{A_N^{\text{trans}}}\right)^2}. \quad (5.22)$$

The trigger used for this measurement is BBCLL1(noVtx)&(ZDCN||ZDCS). As a result, the transverse component was estimated as less than 3 % by averaging all physics runs in 2011 runs as the preliminary result. The longitudinal component of the polarization P_L is evaluated as $P_L = \sqrt{P^2 - P_T^2}$. The correction size of P_L with respect to P is then less than 0.05 % and it is negligible compared to the systematic uncertainty of the absolute polarization measurement.

5.3 Vertex distribution

The primary vertex z -distribution was measured by the BBC with the minimum-bias BBC(novtx) trigger for each run, not assuming multiple collisions. Figure 5.6 shows the distribution of a typical run. The distribution is approximated with Gaussian, and the center position and the width are extracted. The vertex z -distribution tends to expand during the fill because of growing the longitudinal emittance of the beams with time. The multiple collision effect biases to the vertex z -distribution measured by the BBC to observe slightly wider distribution than actual. The luminosity is high at the moment of the storing beams and it decreases with time, the multiple collision effect works oppositely with respect to the emittance growth, but the effect is small compared to the expansion of the beam emittance.

Figure 5.7 shows the distribution of vertex center position and the width weighted by the luminosity of the run. Most of the data has the central position within $|z_{\text{vtx}}| < 5$ cm and the width is about 40 cm. Thus the primary vertex distribution of the full detector simulation was configured as a Gaussian with the center position of $z_{\text{vtx}} = 0$ cm and the width of $\sigma_z = 40$ cm. Variation of vertex z -distribution in the central position and the width by runs create fluctuation of the acceptance of the Muon Arms. The size of the fluctuation was taken into the systematic uncertainty of the acceptance (see Sec. 6.6).

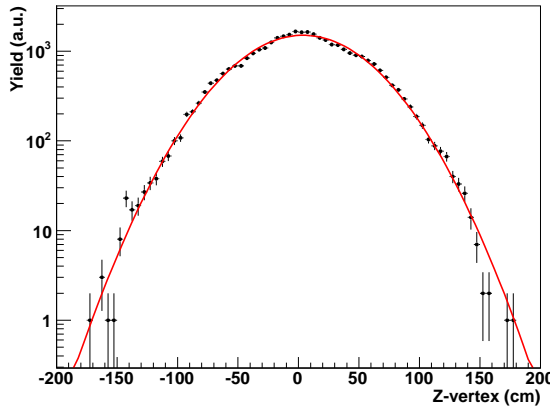


Figure 5.6: The primary vertex z -distribution of a run measured with the minimum-bias trigger. The black bullets denote data and the red line denotes the fitting of data with a Gaussian function.

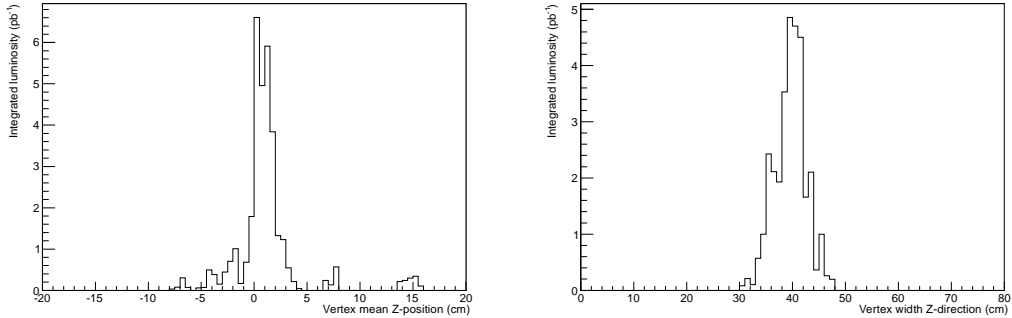


Figure 5.7: Vertex distributions of runs used in this thesis. The left figure shows the mean z -position of the vertex and the right figure shows the width of vertex z -distribution. Both plots are weighted by the integrated luminosity of the run.

5.4 Overview of the detector status and data quality

In this section a brief overview of the quality of the detector and the data used in this thesis is presented for planning the analysis of $W^\pm \rightarrow \mu^\pm$.

Dead channels Dead channels of the MuTr and the RPC3 are automatically detected in the daily calibration runs and they are stored in the database. The production software uses the database for reconstruction for the real data and the simulation data. The amount of dead channels are several-percent level for the both detectors. Also one PMT of the South BBC module was dead through the runs. Figure 5.8 shows the radiograph of reconstructed tracks in the runs. Most of the acceptance supposed to be used in the analysis was active through the runs.

Known operation issues Some operational issues are known for the data used in this thesis as follows:

- The hit efficiency of the RPC3 was low for the first ~ 50 physics runs. This is caused by configuring the gas mixture inadequately with too much quencher gas, and the issue was fixed after these runs.
- The MuID was operated without isobutane for runs in the last two days of the physics data taking.

These issues result in inefficiency of the MuID and the RPC3, but we take a run-by-run efficiency correction scheme in the analysis and these runs are included in the analysis.

Timing issue of the RPC3 electronics It turned out that the global timing offset of the RPC3 was not determined uniquely through the runs due to the non-synchronous phase between the main DAQ clock and the RPC clock, and it shifted several tens nsecs every power cycle. The offset is fixed at the beginning of the run, and shifts of the timing during the run never occur. As it is impossible to know the timing of the run *a priori*, we needed to determine the central timing of the RPC3 *in situ*. Figure 5.9 shows an example of a particular run. As clearly seen in the figure, hits from particles originated from the collision compose a peak with the timing resolution of the RPC3 and fluctuation of the TOF, while background hits like beam splash or electric noises have flat distribution. We require to runs that the RPC3 timing is

CHAPTER 5. DATA SET

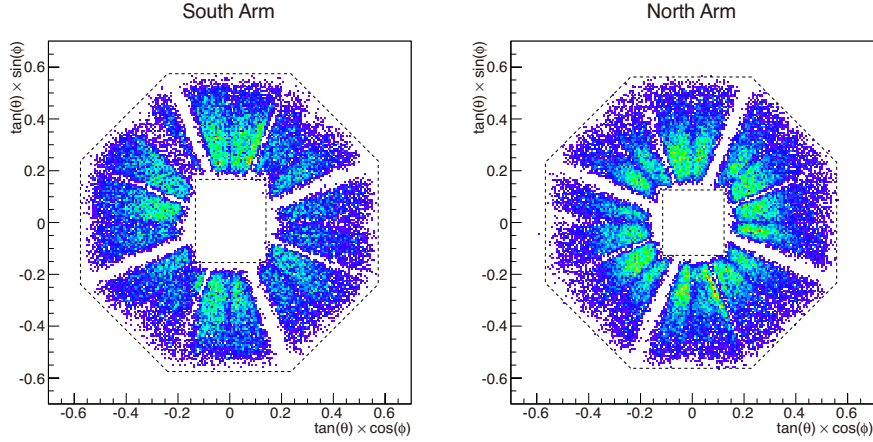


Figure 5.8: Radiograph of the South and North MuTr. Reconstructed θ and ϕ angle of tracks of real data of qualified runs with a certain quality cut are plotted. The outer edge is determined by the RPC3 acceptance and the inner edge is determined by the square beam hole of the MuID and the acceptance of the MuTr as outlined by dotted frames in the figure. The wide cross-shape radial blanks are made by boundaries of the quadrants of the Station-1 of the MuTr, and narrow radial blanks are made by boundaries of the octants of the all stations. The non-uniformity of the distribution in azimuthal direction is caused by inefficiency of detector components (MuTr, MuID, RPC3), or surplus noise hits in the MuTr.

definitively obtained in this method to use the run for the analysis. If the timing of the RPC3 was not determined, the run is rejected.

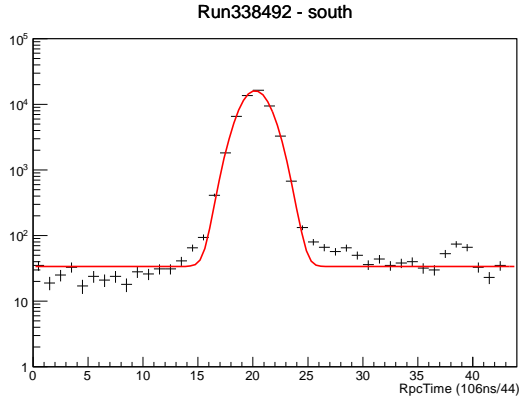


Figure 5.9: Determination of the timing of the RPC3 hits with data.

LL1 and trigger status In year 2011 runs the LL1 components of the physics trigger worked mostly stable. Both of the physics triggers WTRG(S,N) were operated without setting prescaling (scale down=0). The trigger rate of the WTRG(S,N) triggers normalized by the luminosity rapidly increased as luminosity increases as shown in Figure 5.10. BBC(novtx) trigger rate is consistent with ZDC triggers, and the luminosity measurement is considered to be accurate. Both individual MuID-1D LL1 and Mutrg-SG1 LL1 normalized trigger rates increased with

luminosity. By comparing the MuID-1D trigger and the WTRG triggers, it is the Mutrg-SG1 LL1 that issues most of extra triggers than expected from the luminosity. Several reasons are considered as the reason of increasing trigger rates:

- Increase of noise hits in the MuTr as luminosity increases.
- More than one beam clock time resolution of the MuID and the MuTr induces pile-up of hits to increase the accidental passing of the LL1 condition of the MuID-1D and Mutrg-SG1.

The increase of noise hits with luminosity was indeed confirmed in both the MuTr and the MuID as shown in Figure 5.12 and 5.13, respectively. In particular in the MuTr, hits are dominated by noises. If noise hits or pile-up hits of the MuTr make issue more of triggers, the rejection of the low momentum tracks with the Mutrg-SG1 could be bad when the luminosity is high as schematically explained in Figure 5.11.

Tracking and yields The number of reconstructed tracks normalized by the integrated luminosity of the run for various trigger conditions is compared in Figure 5.14. In the ideal detector and triggers the number of reconstructed tracks per luminosity is expected to be uniform, and the existence of non-uniformity in the plot reflects some of biases of the detector. Many of remarkable things are observed from the plot.

1. The data with the minimum-bias trigger (BBC(novtx)) show a significant decrease of the yield with luminosity. This indicates that the tracking efficiency is not stable, and the general decreasing dependence of the tracking efficiency with luminosity must be taken into account apart from run-by-run fluctuation when we evaluate the reconstruction efficiency of the Muon Arms.
2. The decreasing slope of the yield with the MuID-1D trigger (BBC(novtx)&&MuID-1D) is steeper than the BBC(novtx) trigger. This intuitively contradicts with the above discussion that the increase of noise hits would lose the rejection of low momentum tracks, hence which should lead to increase of the yield with the luminosity. Therefore we must suspect the cause of the decrease of the yield is in the trigger efficiency of the MuID-1D LL1.
3. The yield with the Mutrg-SG1(S|N)&&BBC(novtx) trigger, which is composed by finding the live trigger bit of Mutrg-SG1(S|N) in the BBC(novtx) trigger, increases with luminosity in contrast to other triggers. Since this trigger is a subset of the BBC(novtx) trigger and the yield with the mother BBC(novtx) trigger represents decreasing slope, the increasing structure should originate in the Mutrg-SG1. This is qualitatively consistent with the discussion above that the increasing of noise hits in the MuTr would relax the trigger condition to decrease the rejection power of the trigger.

Summary The status of dead channels and DAQ was generally stable through the runs. However the performance of the detector was not, in particular tracking efficiency and trigger efficiencies exhibit significant changes correlated with luminosity. These should become under control in order to obtain reliable cross section of $W^\pm \rightarrow \mu^\pm$ for measuring spin asymmetry.

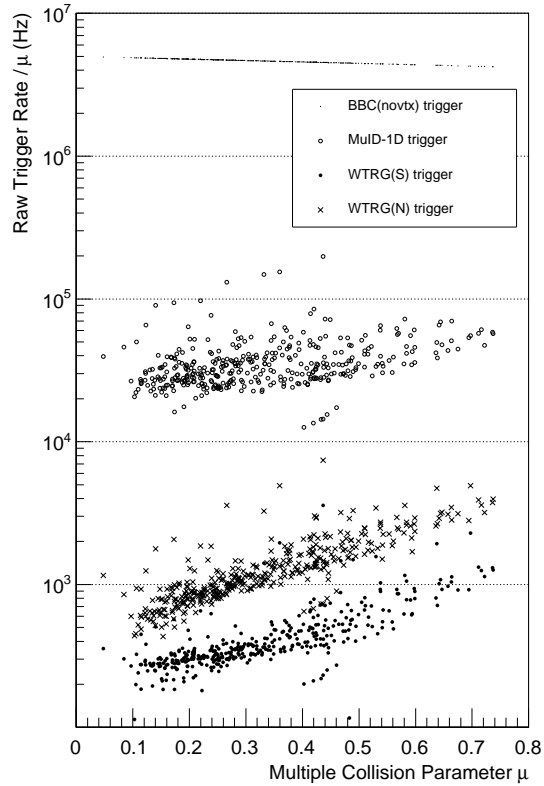


Figure 5.10: Luminosity-normalized raw trigger rate of various triggers as a function of multiple collision parameter.

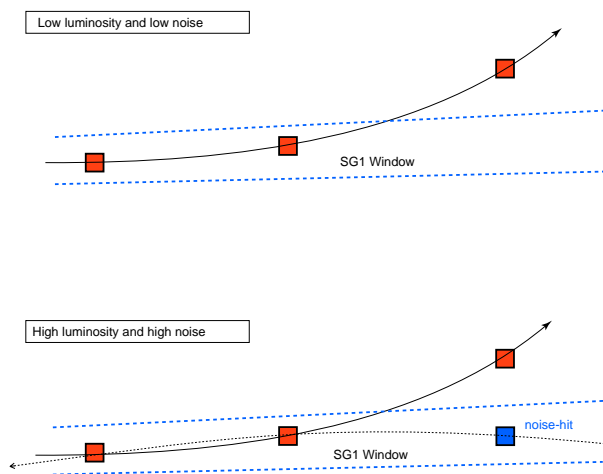


Figure 5.11: Schematic illustration of the case that the noise hits allows to trigger an event which is supposed to be rejected without noises.

5.4 Overview of the detector status and data quality

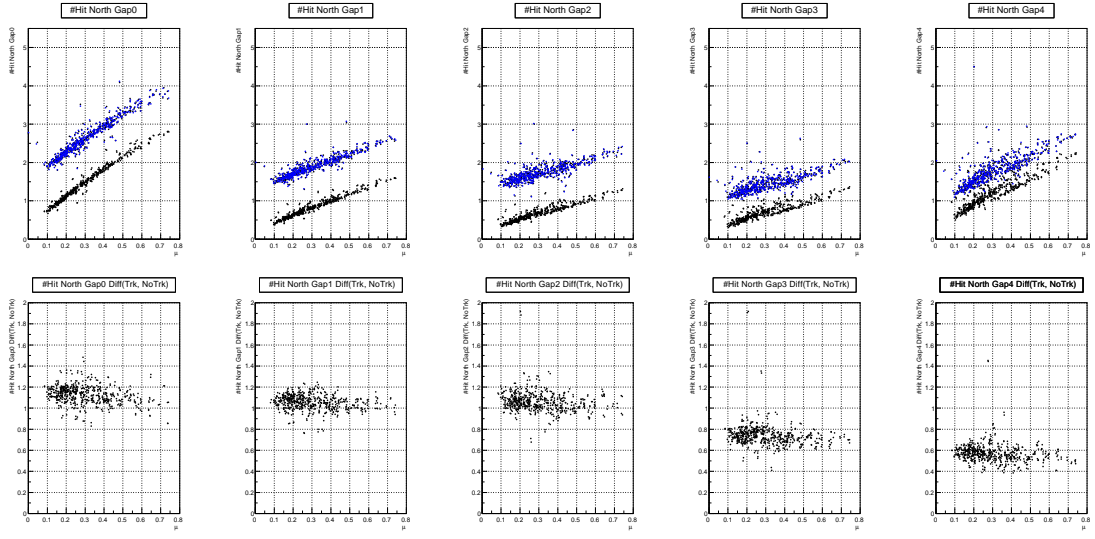


Figure 5.12: Mean number of hits per event in the North MuID of runs, sorted by the luminosity. (Above) The blue bullets are the case when tracks are reconstructed, and black bullets are all the case. (Below) The difference of the average number of hits between tracked events and all events.

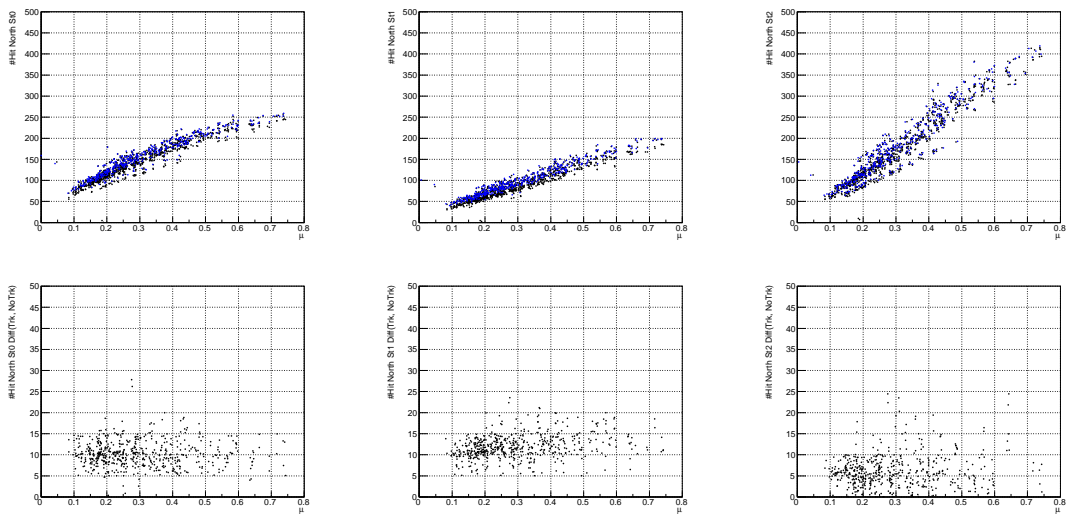


Figure 5.13: Mean number of hits per event in the North MuTr of runs, sorted by the luminosity. (Above) The blue bullets are the case when tracks are reconstructed, and black bullets are all the case. (Below) The difference of the average number of hits between tracked events and all events.

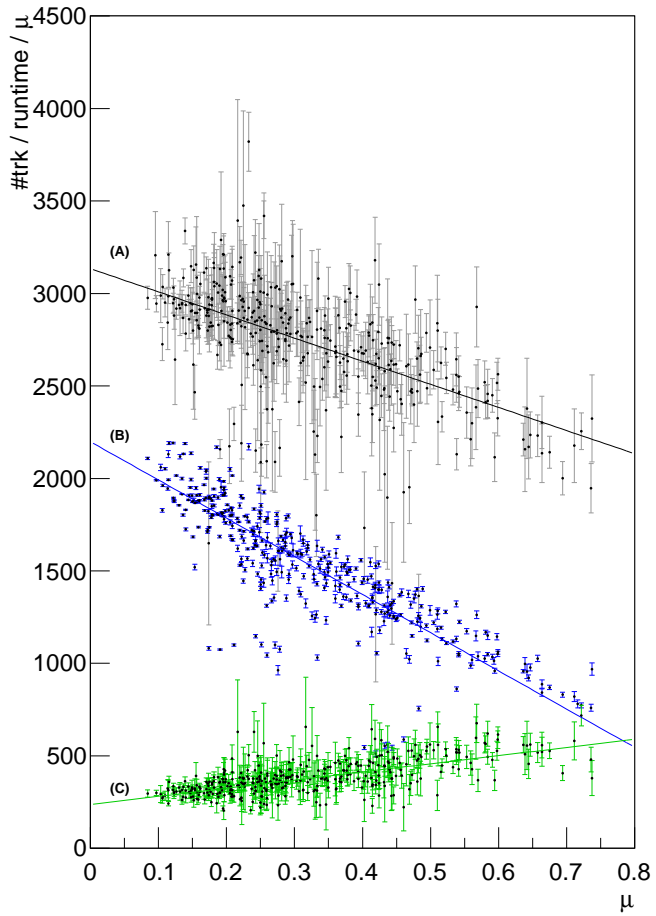


Figure 5.14: Number of reconstructed tracks normalized by luminosity with various triggers. Both the South and North Arms are combined. (A) BBC(novtx) trigger, (B) MuID-1D trigger, (C) BBC(novtx)&&Mutrg-SG1(S|N) trigger.

Chapter 6

Detector performances

In this chapter, various analyses about detector performances are presented as the preliminary for the main analysis of $W^\pm \rightarrow \mu^\pm$. The control samples used in the Muon Arms are cosmic rays without beams and $J/\psi \rightarrow \mu^+\mu^-$ or $\Upsilon \rightarrow \mu^+\mu^-$ with beams. The cosmic rays can probe to high momentum ranges, but the statistics is limited. J/ψ muons are plenty in the data, but the momentum range probed is relatively low. Υ muons cover to some extent higher p_T range compared to J/ψ muons, but statistics are limited. Thus these control samples have complementary roles. Also, tuning the simulation to reflect the real detector performances is essential to obtain reliable signal and background estimations.

6.1 Momentum resolution

The momentum resolution of a tracker for charged particles (muons) is determined by both intrinsic particle interactions and the position resolution of the tracker. The former contains both the energy loss and the multiple scattering of the particle with matters. The latter contains the intrinsic position resolution of the tracker component and the relative alignment between tracker modules. At the low momentum range which the energy loss is significant compared to the total momentum the fluctuation of the energy loss is the dominant source to limit the resolution. The size of energy loss is almost uniform for the momentum of the particle except relativistic effect, the relative fluctuation is small at high momentum range. The effect of multiple scattering is almost flat since the diffracting angle due to multiple scattering is inversely proportional to the momentum, the ratio of multiple scattering effect to the bending by the magnetic field is almost constant, which results in approximately constant effect to the momentum resolution. The position resolution is constant for all momentum, the relative size of fluctuation is proportional to the momentum. For this reason the position resolution is the dominant source to limit the resolution at large momentum. Figure 6.1 shows the simulated momentum resolution of the MuTr as a function of p_T . At the low momentum region of $p_T \lesssim 4 \text{ GeV}/c$ the relative resolution slightly improves as momentum goes up, reflecting the dominant cause of the resolution is energy loss. At the intermediate region of $4 \lesssim p_T \lesssim 10 \text{ GeV}/c$ the momentum resolution is almost flat and multiple scattering is limiting the resolution. Above $10 \text{ GeV}/c$ the momentum resolution linearly increases with p_T , reflecting that the position resolution totally dominates.

6.1.1 J/ψ and Υ mass peak

It is important that the momentum resolution of the MuTr in the simulation is well-tuned to reproduce the real data in order to obtain reliable p_T spectra for signal and background muon

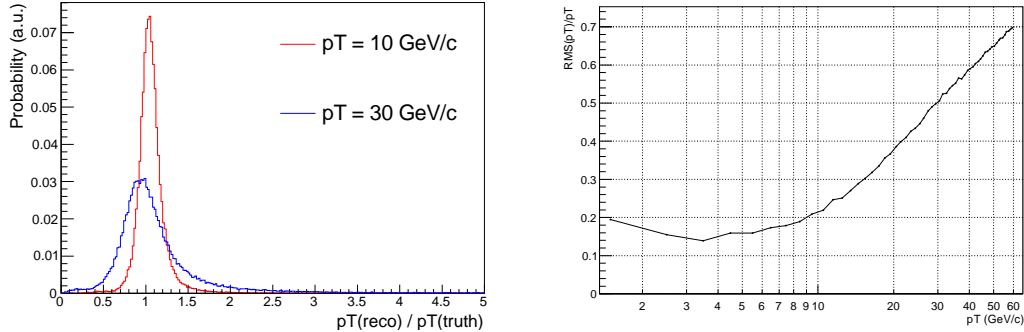


Figure 6.1: (Left) Distribution of $pT(\text{reco})/pT(\text{true})$ for $pT(\text{true}) = 10, 30 \text{ GeV}/c$. (Right) Simulated momentum resolution as a function of $pT(\text{true})$ for the North Muon Arm at $\eta = 1.5$.

processes, since we rely on the simulation for the signal and muon background events in the later extraction of signal events. The main tuning element is the position resolution of the MuTr, which is emulated in the simulation by tuning the RMS scale of the electrical noise around the ground level of the cathode strips. Figure 6.2 shows the comparison of $J/\psi \rightarrow \mu^+ \mu^-$ mass peak between the data and the simulation. Figure 6.3 shows the Υ mass peak observed in the real data. The measured mass width of J/ψ and Υ for the both Arms are listed in Table 6.1.

	South (GeV/c^2)	North (GeV/c^2)
J/ψ	0.272 ± 0.012	0.261 ± 0.012
Υ	0.713 ± 0.160	0.543 ± 0.106

Table 6.1: Mass peak width of resonant states in the real data.

We compared the above data with J/ψ and Υ mass width in the PISA simulation with changing the noise RMS scale. The result is shown in Figure 6.4 (The relation between the RMS scale and the average position resolution of MuTr (in the simulation framework) is plotted in Figure 6.5.). The default RMS scale is 1.0. From this figure, the default simulation tuning is considered as fair for the position resolution of MuTr. J/ψ or Υ mass peaks do not strongly constrain the allowed tuning of the simulation. We can regard these data as the crosscheck of the simulation tuning.

6.1.2 Estimation with cosmic rays

The cosmic ray muons have zenith angle distribution of approximately $\propto \cos^2 \vartheta$ where ϑ is the polar angle. Some cosmic muons pass through both muon arms, most of the case they are incoming to the upper half of the one Arm and outgoing from the lower half of the other Arm. The incoming-side track has opposite current direction compared to the usual collision case that the particles from beam collisions have always inside-out direction, thus regularly the incoming track is reconstructed as the opposite sign charge with respect to the true charge. As these muons are measured twice their identical momenta except the energy loss in the hadron absorbers at the Central Magnet, the momentum resolution of the Muon Arms can be estimated with these muons. We evaluate the width of the reconstructed momentum of the outgoing track with respect to the reconstructed momentum of the incoming track. Since the reconstructed momentum of the incoming track itself suffers the smearing of the momentum resolution, the

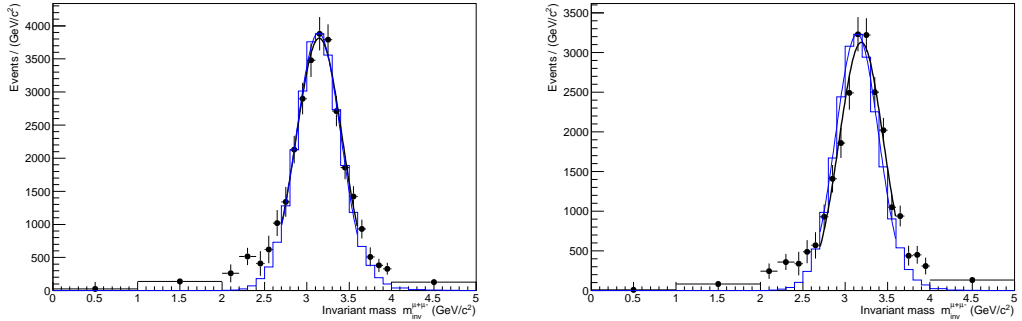


Figure 6.2: $J/\psi \rightarrow \mu^+ \mu^-$ invariant mass distribution at $\sqrt{s} = 500$ GeV. The black bullets are data and the blue histogram is the PISA simulation. The left panel is for the South Arm and the right panel is for the North Arm. The MuID-1D trigger sample data was used.

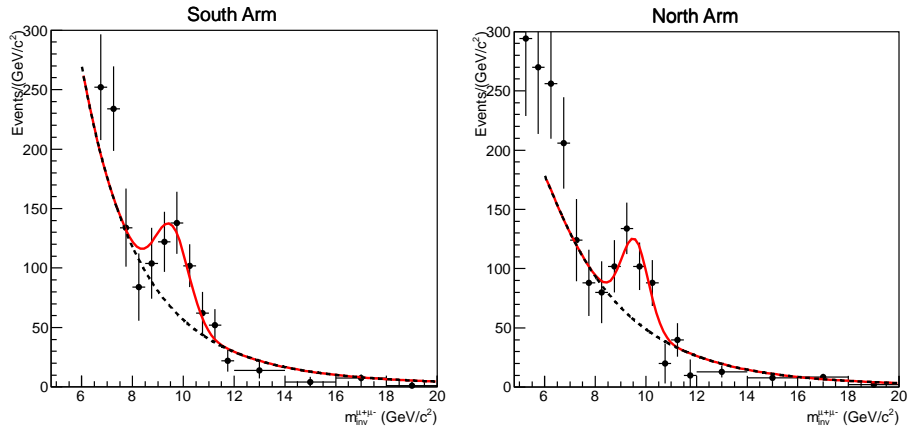


Figure 6.3: Υ mass peak observed in the real data. The data points are fitted with Drell-Yan spectrum shape was assumed as background, and Υ mass peak was fitted by gaussian. The Drell-Yan scale, the gaussian scale and the gaussian width are allowed to be free in the fitting. The used data points are the same as dimuon mass spectrum with WTRG(S,N) triggers shown in Appendix A, e.g. Figure A.7.

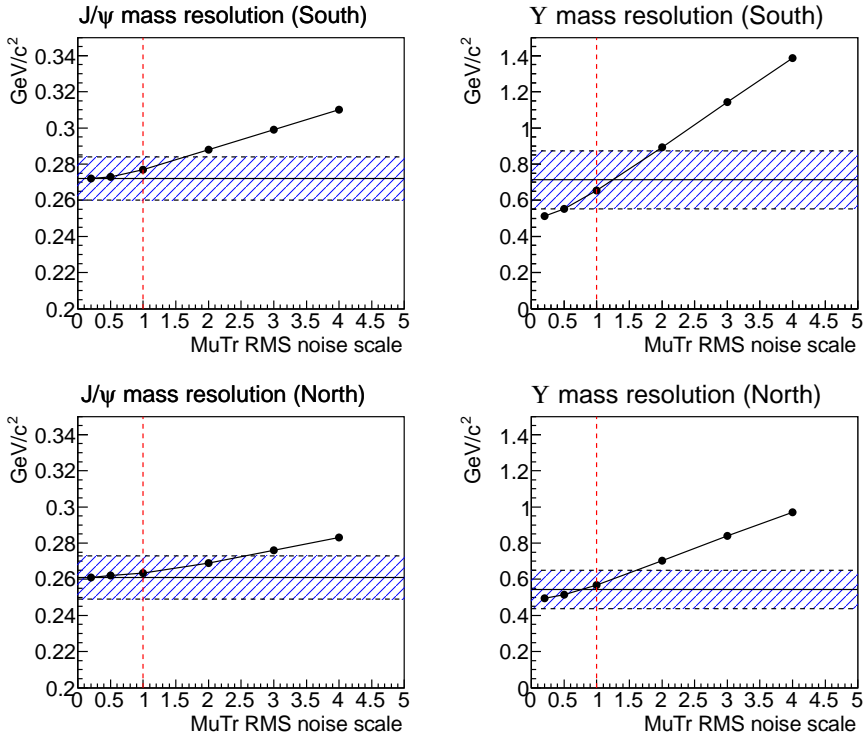


Figure 6.4: Comparison of mass peak width of resonant states ($J/\psi, \Upsilon$) between the real data and the simulation. The horizontal axis is the scale of the ground noise level of MuTr in the simulation (normalized by the default value). The bullet is the result of simulation with varying the ground noise value of MuTr, and the blue band is the result of the real data.

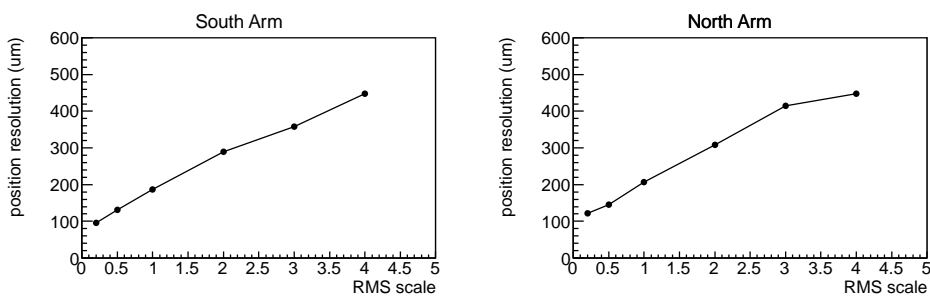


Figure 6.5: Position resolution of MuTr as a function of the ground noise level of MuTr in the simulation.

result is double-convoluted for the momentum resolution. The following cuts were applied to the di-track events:

- $\chi^2_{\text{track}} < 20.0$
- $\text{DG0} < 20.0 \text{ cm}$
- $\text{DDG0} < 9.0 \text{ deg}$
- $\text{lastGap} == 4$
- $|z_{\text{vtx}}(S) - z_{\text{vtx}}(N)| < 5.0 \text{ cm}$
- $|\phi(S) - \phi(N)| < 0.05$
- $|\eta(S) - \eta(N)| < 0.05$

The real data results were compared with the cosmic ray simulation with momentum and zenith-angle distribution based on the measurement. The result is shown in Figure 6.6. The data and simulation generally agree well. From cosmic ray studies it is suggested that the default tuning of the position resolution in the simulation is again fair for the $p_T > 10 \text{ GeV}/c$ muons as well, and the uncertainty of the position resolution is less than $\pm 30 \%$ with respect to the default value.

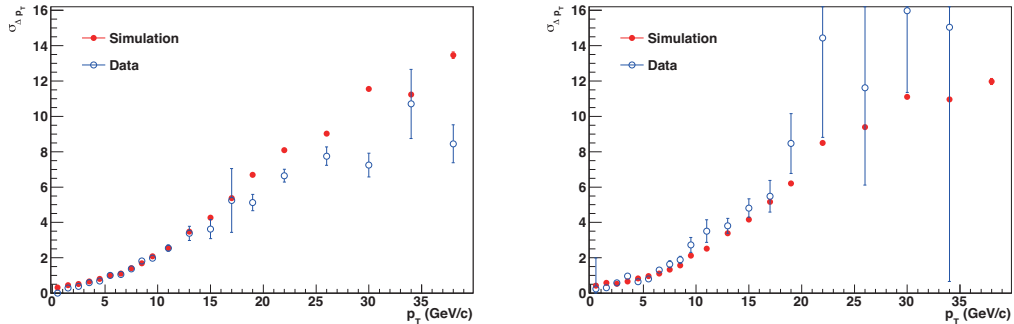


Figure 6.6: Measurement of momentum resolution with cosmic rays as a function of p_T .

6.1.3 Direct measurement of the position resolution of MuTr chambers

The position resolution of the MuTr was directly measured with a test beam experiment using the prototype[59]. With installation of the Mutrg electronics, the best achieved position resolution was about $160 \mu\text{m}$. The initial design value of the position resolution before installation of the Mutrg is $100 \mu\text{m}$ but such good resolution has never been achieved. Therefore the test beam value of $\simeq 160 \mu\text{m}$ is the possible best position resolution. By comparing this fact with the simulated position resolution in Figure 6.5, we can set the -1σ of lower side error of the position resolution as -15% compared to the default. Thus we conclude that the 1σ uncertainty of the position resolution of MuTr is $+30/-15 \%$ to the default position resolution in the simulation.

6.2 MuID and MuTr hit efficiencies

6.2.1 MuID hit efficiency

6.2.1.1 Procedure

The MuID hit efficiency was estimated using the reconstructed roads. The algorithm is summarized as follows.

1. Samples are roads of all triggers in the run.
2. Select roads which are associated with MuTr tracks.
Reject ghost tracks and some quality cuts.
3. For the plane of interest, check if both the road finder and the trigger emulator pass regardless of existing hit in the plane or not.
If it is passed, the road is counted as the denominator of the hit efficiency.
4. Check if the plane of interest has hit and count as the numerator of the hit efficiency.
5. Because of limited statistics, hit efficiency was evaluated for each HV group of the MuID. Each HV group covers about 150 cm width of MuID panel perpendicular to the direction of the tube orientation. Figure 6.7 shows the HV group mapping for horizontal and vertical planes of the MuID.

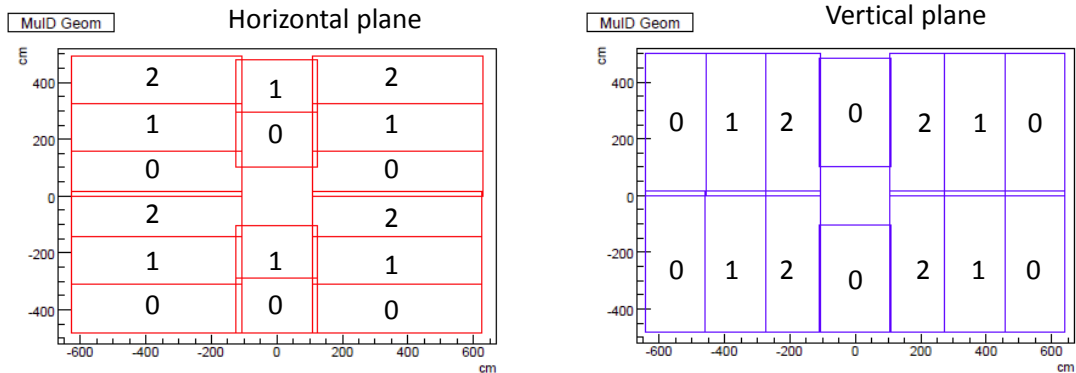


Figure 6.7: MuID HV group mapping.

6.2.1.2 Results

An example of results for one plane is shown in Figure 6.8. The MuID hit efficiency generally decreases with luminosity. It is suspected that the cause of this efficiency drop correlated with luminosity is sagging of the HV applied to MuID; with increase of particle injection to MuID tubes, the current flow through the tube protection resistor which is serially coupled to the tube would bring voltage drop.

6.2 MuID and MuTr hit efficiencies

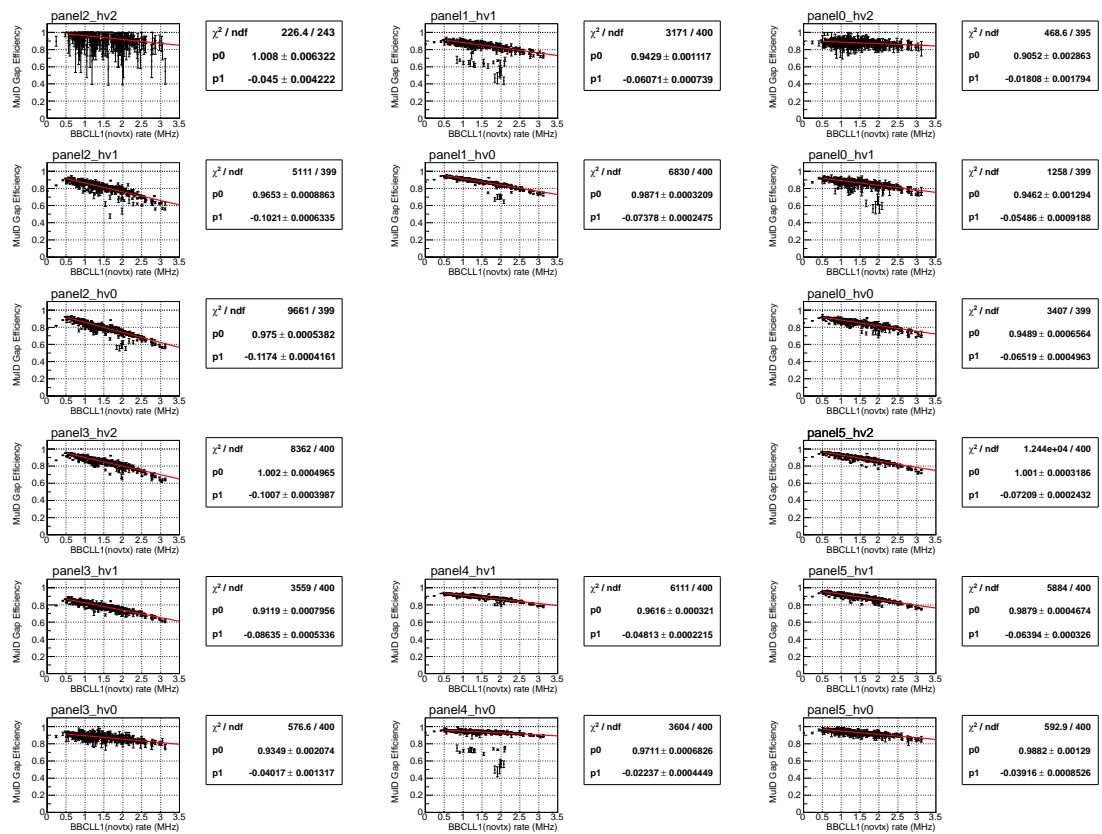


Figure 6.8: Measured run-by-run MuID hit efficiency for South Arm Gap-0 Horizontal plane sorted by multiple collision parameter.

6.2.1.3 Crosschecks

Crosscheck of MuID hit efficiency was performed by checking MuID-1D LL1 efficiencies with two different ways. One is using cosmic rays reconstructed at both South and North Arm with magnetic field on. It is expected that cosmic ray data represents the performance at luminosity zero limit. The other one is using J/ψ muons in the same Arm. The method used here is so-called “tag-and-probe method”. The crosscheck was performed by comparing the MuID-1D LL1 emulator-passing efficiency of the probe-side muon track when the tag-side muon passes MuID-1D LL1 emulator. Since the data sample is taken from triggers which include MuID-1D, one needs to rely on the simulation of LL1 for two tracks case to make the correspondence between the obtained efficiency and the MuID hit efficiency.

Cosmic ray muons The trigger of the cosmic ray is the standalone MuID-1D. The event selection criteria are the following:

- Having a track in both the South and North Arm.
- The reconstructed charge is opposite each other for the tracks.
- $p_T < 100 \text{ GeV}/c$ for both tracks
- For the track extrapolated position at $z = 0$, $r_{\text{track}} = \sqrt{x^2 + y^2} < 10 \text{ cm}$.
- Distance of the track position between the two tracks at $z = 0$ is less than 10 cm.

Then the following efficiency is defined:

$$\text{Eff(South)}_{\text{cosmic}} = \frac{N[\text{LL1(South)} \& \& \text{LL1(North)}]}{N[\text{LL1(North)}]} \quad (6.1)$$

$$\text{Eff(North)}_{\text{cosmic}} = \frac{N[\text{LL1(North)} \& \& \text{LL1(South)}]}{N[\text{LL1(South)}]} \quad (6.2)$$

where “LL1” means the MuID hit pattern of the track satisfies the LL1 condition of the MuID-1D. The requirement of the MuID LL1 in the denominator assures the MuID-1D trigger bit is issued regardless the status of the probing track. Figure 6.9 shows the result. The average efficiency in the South, North Arm was $88.5 \pm 0.3_{\text{(stat)}} \%$, $87.1 \pm 0.3_{\text{(stat)}} \%$, respectively. The calculated efficiency is interpreted as the original LL1 efficiency with the help of simulation. As a result, the MuID-1D LL1 efficiency was estimated as 93-94 %.

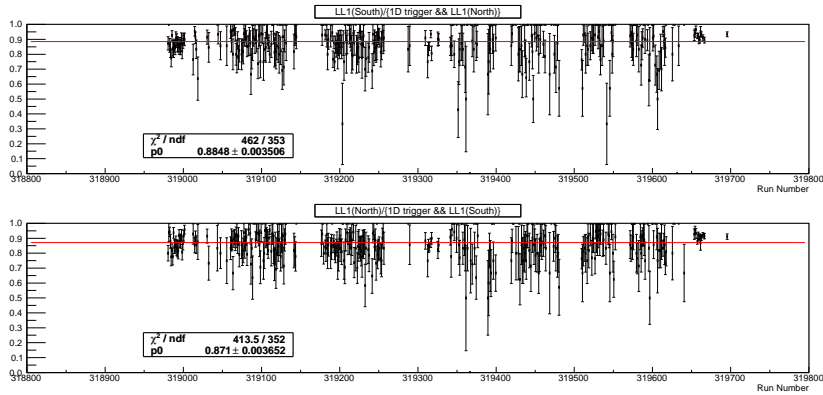


Figure 6.9: Evaluation of MuID-1D LL1 efficiency with di-track cosmic ray muons.

$J/\psi \rightarrow \mu^+ \mu^-$ events The WTRG(S,N) trigger was used to extract $J/\psi \rightarrow \mu^+ \mu^-$ events. The following cuts were applied:

- The two tracks have opposite reconstructed charge each other.
- The two tracks are in the same Arm.
- $\text{lastGap} == 4$
- $\text{DG0} < 6.5 \text{ cm}$
- $\text{DDG0} < 6.5 \text{ deg}$
- $\chi_{\text{track}}^2 < 11.0$
- $\text{DCA}_r < 12.3 \text{ cm}$
- $2.8 < m_{\text{inv}} < 3.4 \text{ GeV}/c^2$
- $p_T^{\text{probe}} > 2.0 \text{ GeV}/c$
- $1.4 < |\eta^{\text{tag}}| < 2.2 \text{ GeV}/c$

Then the following efficiency is defined:

$$\text{Eff}(\text{South})_{J/\psi} = \left. \frac{N[\text{LL1(probe)} \& \& \text{LL1(tag)}]}{N[\text{LL1(tag)}]} \right|_{\text{South}} \quad (6.3)$$

$$\text{Eff}(\text{North})_{J/\psi} = \left. \frac{N[\text{LL1(probe)} \& \& \text{LL1(tag)}]}{N[\text{LL1(tag)}]} \right|_{\text{North}} \quad (6.4)$$

The runs are segmented by luminosity. Figure 6.10 shows the result of the above efficiency for the South and North Arm as a function of multiple collision parameter μ . The data points were fitted with a linear function, and as a result the efficiencies are parameterized as a function of μ as

$$\text{Eff}(\text{South})_{J/\psi}(\mu) = (89.7_{\pm 1.5} - 13.4_{\pm 4.6} \times \mu) \% \quad (6.5)$$

$$\text{Eff}(\text{North})_{J/\psi}(\mu) = (89.6_{\pm 1.5} - 11.1_{\pm 4.6} \times \mu) \% . \quad (6.6)$$

As performed for the case of cosmic muons, the above efficiencies were interpreted as the original MuID-1D LL1 efficiencies using the simulation. The MuID-1D LL1 efficiency is estimated as $(95 \pm 1) \%$ at $\mu = 0$ and $(90 \pm 2) \%$ at $\mu = 0.7$.

Discussion The extrapolated LL1 efficiency of 95 % is consistent with the cosmic ray result. The estimated LL1 efficiency is consistent with the expectation from the average hit efficiency measured in the above method. Therefore the measurement of the MuID hit efficiency is considered to be accurate.

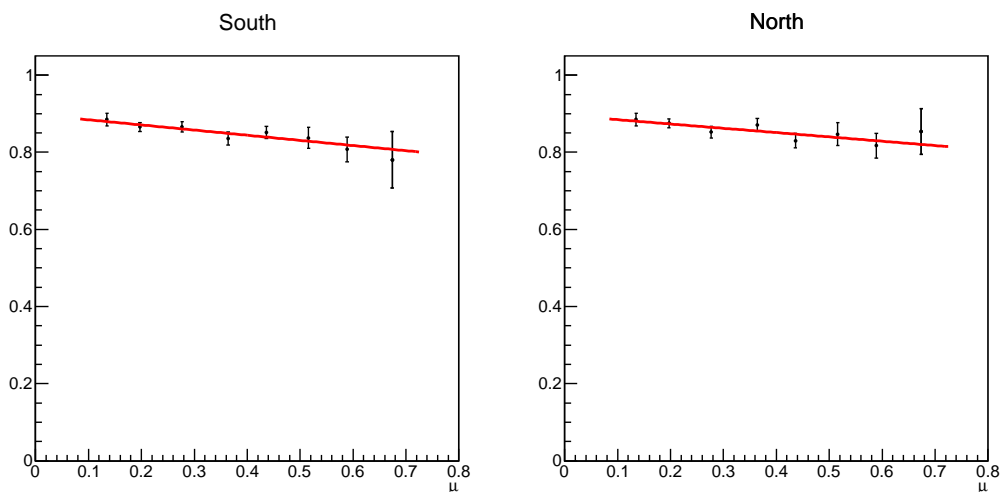


Figure 6.10: Evaluation of MuID-1D LL1 efficiency with $J/\psi \rightarrow \mu^+ \mu^-$ tag-and-probe method. $p_T > 2.0$ GeV/ c was required for the probe-side track.

6.2.2 MuTr hit efficiency

The dead channels of MuTr are automatically included into the simulation with specifying the reference run. Thus it is sufficient to correct the hit efficiency of MuTr in the simulation. For each reconstructed track there would be at maximum 16 hits in MuTr (8 gaps times 2 planes). We evaluated MuTr hit efficiency by fitting the number of hit distribution (N_{hit}) with two parameters:

- The average “OR” hit efficiency of the gaps (at least one of two planes of the gap to have hit), denoted as p_1 .
- The probability to lack one of two planes’ hits when the gap has “OR” hit, denoted as p_2 .

This parameterization considers the correlation between hits of two planes of the same gap as well as hit efficiency by introducing p_2 . It is reasonable to introduce the correlation effect into the distribution because hits of two planes of the same gap are created from the same energy deposit in the gap of the charged particle. We only evaluated these parameters for each Muon Arm, because overall MuTr performance was stable during the runs, and locality of hit efficiency variance is small compared to the luminosity dependence.

Figure 6.11 shows an example the fitting of the distribution. The model describes well the N_{hit} distribution, in particular notches between odd numbers and even numbers in the South Arm. This notch is the very reflection of correlation between two planes of the same gap. Then the result of fitting for all runs are shown in Figure 6.12.

It is possible to interpret the two parameters p_1 , p_2 with a different way. The conversions

$$\begin{aligned}\varepsilon_{\text{gap}}^{\text{AND}} &\equiv p_1(1 - p_2) \\ \varepsilon_{\text{plane}} &\equiv p_1(1 - p_2)/2\end{aligned}$$

denote the efficiency to have both hits in the same gap and the efficiency to have hit for one plane, respectively. The scattering plot of $\varepsilon_{\text{gap}}^{\text{AND}}$ and $\varepsilon_{\text{plane}}$ is shown in Figure 6.13. Here, both muon arm’s data point matches in the same line. It is clear that in low luminosity both (gap(AND) and plane) efficiencies are high, and they decrease with luminosity. The red line in the figure expresses the full correlation line of the two planes, i.e., $\varepsilon_{\text{gap}}^{\text{AND}} = \varepsilon_{\text{plane}}$, and the green line expresses the zero correlation line, i.e., $\varepsilon_{\text{gap}}^{\text{AND}} = (\varepsilon_{\text{plane}})^2$. The real data points are between the two lines. It is clear that the correlation decreases with luminosity, and at the highest luminosity the correlation of the two planes is almost zero. The cause of decreasing efficiencies and loosing the correlation between planes with luminosity is not fully understood so far, but it is considered that increase of particle injection to MuTr increases GND level fluctuation, and it affected to the performance of MuTr.

CHAPTER 6. DETECTOR PERFORMANCES

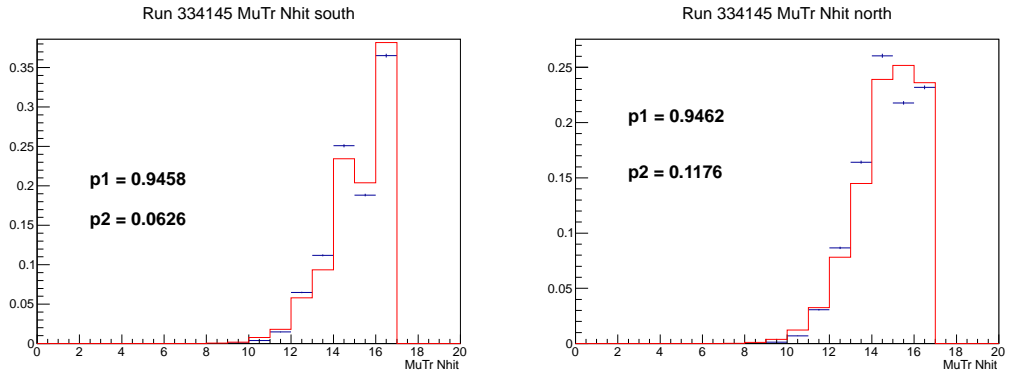


Figure 6.11: An example of fitting of N_{hit} with parameters p_1, p_2 .

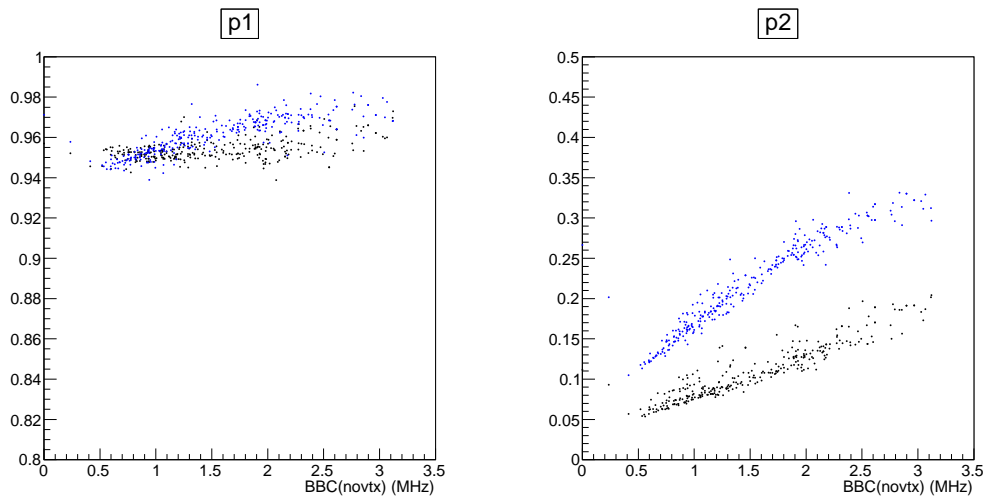


Figure 6.12: Fitting result for all runs. Each dot corresponds to each run. Black points are for South Arm and Blue points are for North Arm.

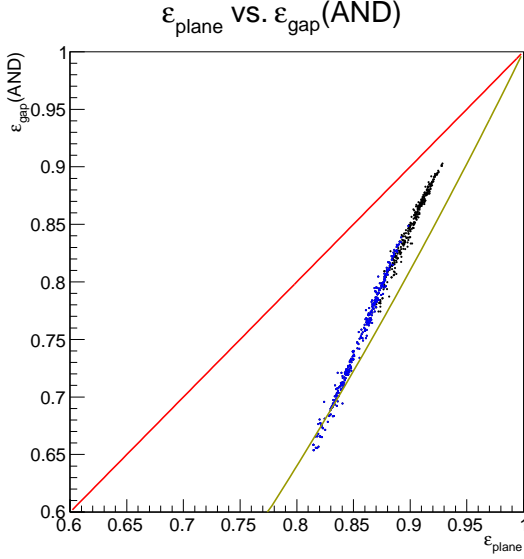


Figure 6.13: Fitting result for all runs in the space of $\{\varepsilon_{\text{plane}}, \varepsilon_{\text{gap}}^{\text{AND}}\}$. Each dot corresponds to each run. Black points are for South Arm and Blue points are for North Arm. The red line expresses the full correlation line, i.e., $\varepsilon_{\text{gap}}^{\text{AND}} = \varepsilon_{\text{plane}}$. The green line expresses the zero correlation line, i.e., $\varepsilon_{\text{gap}}^{\text{AND}} = \varepsilon_{\text{plane}}^2$.

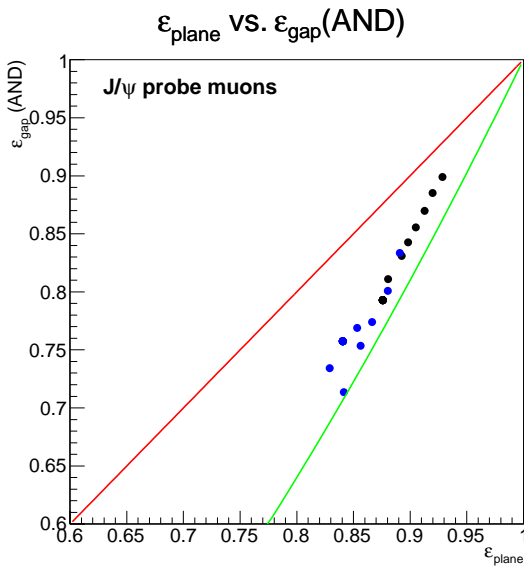


Figure 6.14: The same as Figure 6.13, but the data sample are J/ψ probe muons. Runs are bundled by luminosity groups.

6.3 Estimation of trigger efficiencies

6.3.1 BBC(novtx) trigger

The inclusion of BBC(novtx) trigger bit for the physics trigger requires us to take into account of the BBC trigger efficiency. The trigger efficiency of the BBC depends on the physics process of the collision. In this study we estimated the BBC trigger efficiency for $W^\pm \rightarrow \ell^\pm \nu$ process and dimuon process with data, and values are compared with the simulation.

6.3.1.1 Data-driven method

The BBC trigger efficiency can be measured with using triggers which do not contain BBCLL1. For $\sqrt{s} = 500$ GeV $p + p$ collision case, two BBC efficiency were measured by the collaboration so far. One is the minimum bias efficiency with van der Meer scan, and the other is efficiency for $\pi^0 \rightarrow 2\gamma$ production observing with the Central Arm. We additionally employed $W^\pm \rightarrow e^\pm$ candidates in year 2009 runs and dimuon events in year 2011 runs. Table 6.2 summarizes the results above.

$W^\pm \rightarrow \ell^\pm \nu$ process We used the data of $W^\pm \rightarrow e^\pm$ final signal selection sample in year 2009 runs[73]. The trigger of $W^\pm \rightarrow e^\pm$ in the Central Arm was ERT4x4b. With selecting events in $p_T^{e^\pm} > 30$ GeV/c, the BBC trigger efficiency was measured as $90 \pm 5_{(\text{stat})}$ %. By changing the $p_T^{e^\pm}$ threshold down to 20 GeV/c, the BBC trigger efficiency was stably around 90 % within ± 2 % error while the signal purity drastically decreases. Thus we concluded that the BBC efficiency for background is in 90 ± 2 % and this does not change the central value of BBC efficiency for $W^\pm \rightarrow e^\pm$.

Dimuon processes The BBC trigger efficiency for dimuon processes was studied using dimuon events in the Clock trigger. The same signal selection as described in Section 6.4.1 is applied here as well. Events are dominated by $J/\psi \rightarrow \mu^+ \mu^-$ process. We assumed the same combinatorial BG contamination into the foreground as the WTRG(S,N) trigger case, and concluded 91 ± 4 % BBC efficiency for dimuon process.

$\pi^0 \rightarrow 2\gamma$ process The BBC trigger efficiency for $\pi^0 \rightarrow 2\gamma$ process in the Central Arm was estimated in year 2009 runs as 91 ± 2 %[74]. The production process of π^0 and other light hadrons such as π^\pm, K^\pm is considered to be similar then the similar BBC trigger efficiency is expected.

Minimum Bias process The BBC trigger efficiency for the minimum bias process is estimated with the van der Meer scan as 53 ± 2 % as described in Sec. 5.1.1.

In summary, the BBC trigger efficiency for hard processes is consistently around 90 %. For the $W^\pm \rightarrow \mu^\pm$ cross section analysis, we employ the 2009 $W \rightarrow e^\pm$ results of 90 ± 5 %.

6.3.1.2 Simulation

Table 6.3 summarizes the BBC efficiency for each physics estimated with the PYTHIA + PISA simulation. Hard processes (other than “light”) correspond to $W^\pm \rightarrow \ell^\pm$, dimuon, and $\pi^0 \rightarrow 2\gamma$ and the light process corresponds to the Minimum Bias data. The obtained efficiencies do not

differ largely from data results. For obtaining $W^\pm \rightarrow \mu^\pm$ cross section, we correct the simulated acceptance and efficiency with the correction scale factor

$$\frac{\varepsilon_{\text{BBC}}^{\text{data}}}{\varepsilon_{\text{BBC}}^{\text{sim}}} = 0.90/0.944 \quad (6.7)$$

where the numerator is the data-driven BBC trigger efficiency for 2009 $W^\pm \rightarrow e^\pm$ candidates, and the denominator is the simulated BBC trigger efficiency for $W^\pm \rightarrow \ell^\pm \nu$ process in order to adjust the simulated BBC trigger efficiency to the data.

Process Name	BBC eff.	Method	Trigger
$W^\pm \rightarrow \ell^\pm \nu$	(90 ± 5) %	$W^\pm \rightarrow e^\pm$ (2009)	ERT4x4b
Dimuon($\approx J/\psi$)	(91 ± 4) %	dimuon in $m_{\text{inv}} > 2.5 \text{ GeV}/c^2$ (2011)	Clock
$\pi^0 \rightarrow \gamma\gamma$	(91 ± 2) %	π^0 in the Central Arm (2009)	ERT_Gamma3
Minimum Bias	(53 ± 2) %	van der Meer scan (2009)	-

Table 6.2: Summary of BBC efficiency obtained with data for different physics processes at $\sqrt{s} = 500 \text{ GeV}$ case.

Process Name	BBC eff.
$W^\pm \rightarrow \ell^\pm \nu$	(94.4 ± 0.2) %
Z/γ^*	(92.6 ± 0.2) %
open bottom	(96.5 ± 0.2) %
open charm	(93.1 ± 0.2) %
quarkonia	(95.3 ± 0.2) %
light	(49.3 ± 0.5) %

Table 6.3: Summary of BBC efficiencies estimated with the PYTHIA + PISA simulation.

6.3.1.3 Multiple collision effect

In case of multiple collisions, all collisions contribute to make hits in the BBC and the BBC trigger efficiency increases. The size of increase was estimated for $W^\pm \rightarrow \mu^\pm$ case with locally modified PYTHIA + PISA simulation which can merge collisions. The detail of event merging in the simulation is described in detail in Appendix D. For the “hard collision process” like W , the accompanying collisions in the same bunch crossing are assumed to be the light process, whose intrinsic BBC efficiency (in simulation) is 49%, and Poisson statistics are assumed for reweighting. For the MC samples single, double, and triple collision cases were produced and reweighted.

As a result, the increase of BBC efficiency is estimated to be about 2% at multiple collision parameter $\mu = 1.0$. This luminosity dependence is considered for final result of the BBC efficiency by weighting luminosities, but the correction size is 0.6 % and small compared to the error of absolute BBC efficiency.

6.3.2 MuID-1D trigger

In year 2011 runs, due to human error the timing of MuIDLL1 was misconfigured to delay by +1 BCLK relative to the proper timing. As a result, the DCM hit pattern in the recorded data and the LL1 signal were not consistent each other, and it caused significant decrease of the trigger efficiency of the MuID-1D. Since the time resolution of MuID tubes are larger than 1 BCLK width, the width of the LL1 signal is extended to 2 BCLK as described in Sec. 3.3.2.2. The consequences of the relative delay of the LL1 are as follows:

1. The 2 BCLK width of MuID hits reflecting the timing resolution of MuID tubes could make two cases of timing structure in MuID LL1: One is to have trigger bits in the 1st and the 2nd BCLKs with the probability t_{prob} , and the other is to have trigger bits in the 2nd BCLK with the probability $(1 - t_{\text{prob}})$.
2. In the nominal timing configuration the coincidence of MuID LL1 with BBC is adjusted to be at the 2nd BCLK of the MuID LL1. The delay of MuID LL1 by +1 BCLK made the coincidence with BBC at the 1st BCLK of MuID LL1. In this case a certain fraction of MuID LL1 trigger bit is lost with probability $(1 - t_{\text{prob}})$.
3. t_{prob} is not known *a priori* and is the object to be determined by measurement. There is no evidence that t_{prob} is stable through runs.
4. MuID LL1 delays by +1 BCLK with respect to the MuID hit pattern recorded as data via DCM. This timing lag between DCM data and LL1 produces 4 categories related with MuID for a given track with BBC trigger:
 - (A) a track with passing both the MuID Emulator and the MuID LL1,
 - (B) a track with passing the emulator but losing the LL1,
 - (C) a track with losing the emulator but passing the LL1,
 - (D) a track with losing both the emulator and the LL1,
5. The relative fraction of 4 categories for tracks with BBC trigger described above is considered to vary with luminosity, with reflecting the BBC rate, decrease of MuID hit efficiency, and the variation of t_{prob} .
6. Thus if we have sufficiently accurate values of the BBC efficiency and the MuID hit efficiency, it is possible to probe t_{prob} with using the fraction of 4 categories for tracks with the BBC trigger.
7. MuID-1D trigger efficiency can be measured with using data with other triggers like the ERT triggers, since the timing width of the ERT triggers is just 1 BCLK and it coincides with delayed MuID-1D trigger bit only at the BCLK timing which corresponds to the collision of producing muon.

6.3.2.1 Toy MC Simulation

A toy MC simulation to reproduce the circumstance of MuIDLL1 was developed. The concrete assumptions and procedures are as follows:

1. Assume minimum bias BBC efficiency is 53 % as given by the van der Meer scan.
2. Assume hard collision BBC efficiency is 90 % as given by various estimations in Sec. 6.3.1, and assume that a collision which has a reconstructed track is a hard collision.

6.3 Estimation of trigger efficiencies

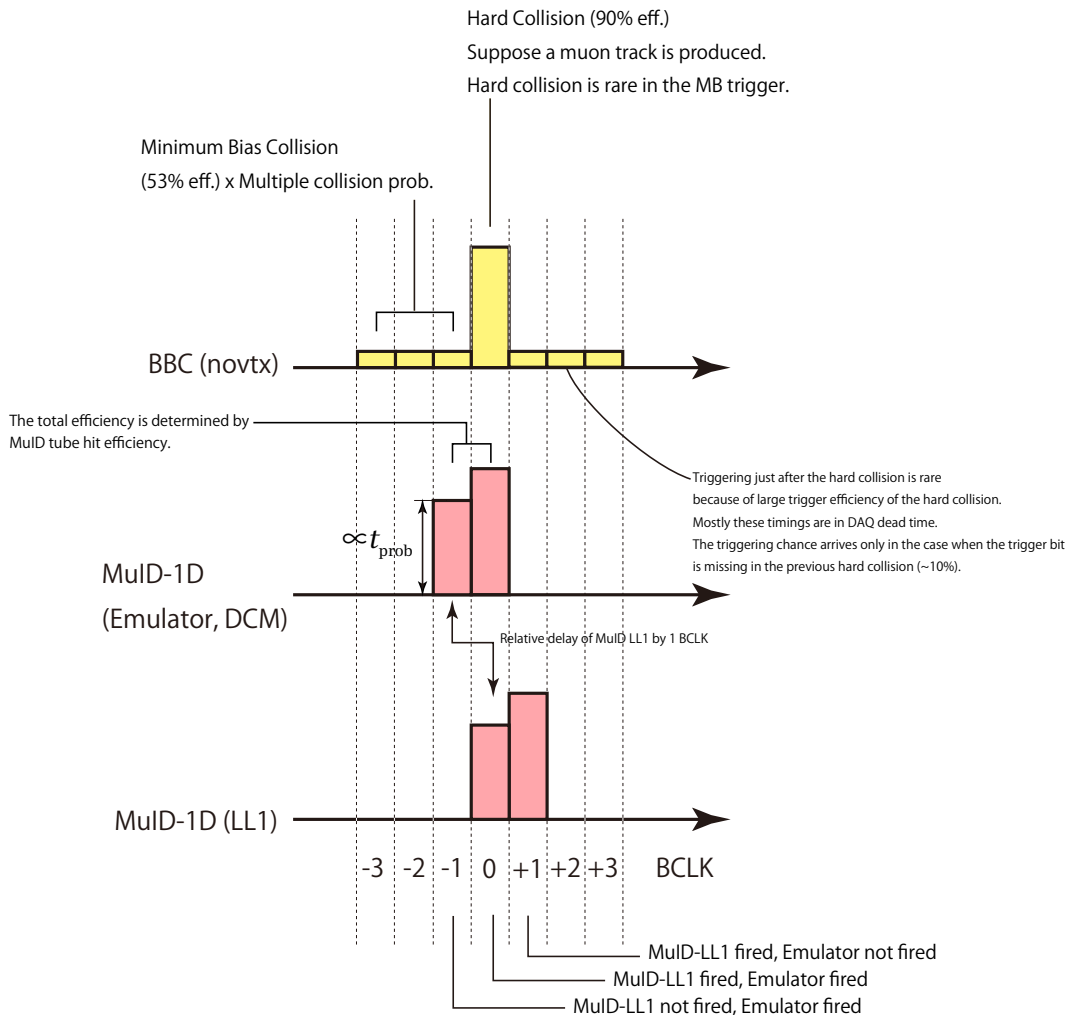


Figure 6.15: Timing chart of the MuID-1D trigger in year 2011 runs. The BCLK where a hard collision with a muon track is produced is defined as BCLK-0. The trigger efficiency of the MuID-1D should be evaluated at the BCLK-0.

3. Take into account of the increase of BBC efficiency with luminosity.
4. Assume that the MuID planes have a uniform hit efficiency, but depends on luminosity. The luminosity dependence is taken from the measurement by averaging the obtained hit efficiencies in Sec. 6.2.1.
5. Assume that all muons punch through all MuID planes.
6. Each MuID hit has 2 BCLK width.
7. The timing of the MuID LL1 is randomly chosen with the probability t_{prob} .
8. Assume that MuID-1D LL1 bit delays by +1 BCLK from the nominal timing.
9. Consider only a few BCLK timings before and after a hard collision which produces muon tracks. Randomly generate minimum bias collisions following the assumed luminosity.
10. Randomly set the BBC trigger bit for each BCLK by referring the trigger efficiency for minimum bias collisions (53 %) and that of hard collisions (90 %).
11. Set MuID-1D emulator bit based on the MuID hit pattern for each BCLK. Set MuID-1D LL1 bit based on LL1 (delayed) timing.
12. When emulating the BBC trigger mode, pick up the first BCLK whose BBC LL1 trigger bit is fired.
13. When emulating the ERT trigger mode, always pick up the hard collision timing.

The free parameter in the simulation is only t_{prob} at the given luminosity.

6.3.2.2 Adjustment of t_{prob} using BBC trigger data

Measurement of t_{prob} is possible using BBC(novtx) trigger tracks by comparing the relative yield of the four categories of tracks related with MuID-1D:

- Category (A): Tracks which have both MuID-1D trigger bit in GL1 and that DCM hit pattern recorded in DST passes the MuIDLL1 emulator.
- Category (B): Tracks which does not have MuID-1D trigger bit, but do pass the emulator.
- Category (C): Tracks which have MuID-1D trigger bit, but do not pass the emulator.
- Category (D): Tracks which have neither MuID-1D trigger bit nor passing the the emulator.

The model in the toy simulation allows that t_{prob} changes with luminosity linearly as

$$t_{\text{prob}}(\mu) = t_{\text{prob}}^0 \cdot (1 - \alpha\mu) \quad (6.8)$$

where t_{prob}^0 is the t_{prob} at $\mu \rightarrow 0$ limit, and α is the relative slope of the change of t_{prob} depending on luminosity. For a given set of parameters $\{t_{\text{prob}}^0, \alpha\}$, relative fractions of above categories A, B, C, D, was estimated with the toy simulation described in the previous section. On the other hand these fractions can be obtained from single muon tracks in BBC(novtx) trigger. We searched the parameter space of $\{t_{\text{prob}}, \alpha\}$ to find the optimal parameter sets to give the minimum deviation between the data points and the simulation. As a result, the optimal parameters are $t_{\text{prob}}^0 = 0.79$ and $\alpha = 0.30$. We found α is positive, which means t_{prob} decreases with luminosity. The decrease of t_{prob} infers that the discrimination timing of MuID tubes delays as the luminosity increases. Figure 6.16 shows the comparison of the relative fractions of four categories between simulation and the data with the optimal parameter set of t_{prob} . The calculation of simulation agrees with the data points quite very well and it supports the correctness of the picture about the circumstances about MuID-1D trigger.

6.3.2.3 Simulation of MuID-1D trigger efficiency

The simulation of MuID-1D trigger efficiency is also possible by the toy simulation with inputting the optimal parameterization of t_{prob} . Figure 6.17 shows the result of the simulated MuID-1D trigger efficiency. We assign $\pm 5\%$ uncertainty to the simulation result, taking into account of the effect of possible contamination of hadron tracks in the BBC(novtx) trigger data used to estimate t_{prob} in Figure 6.16.

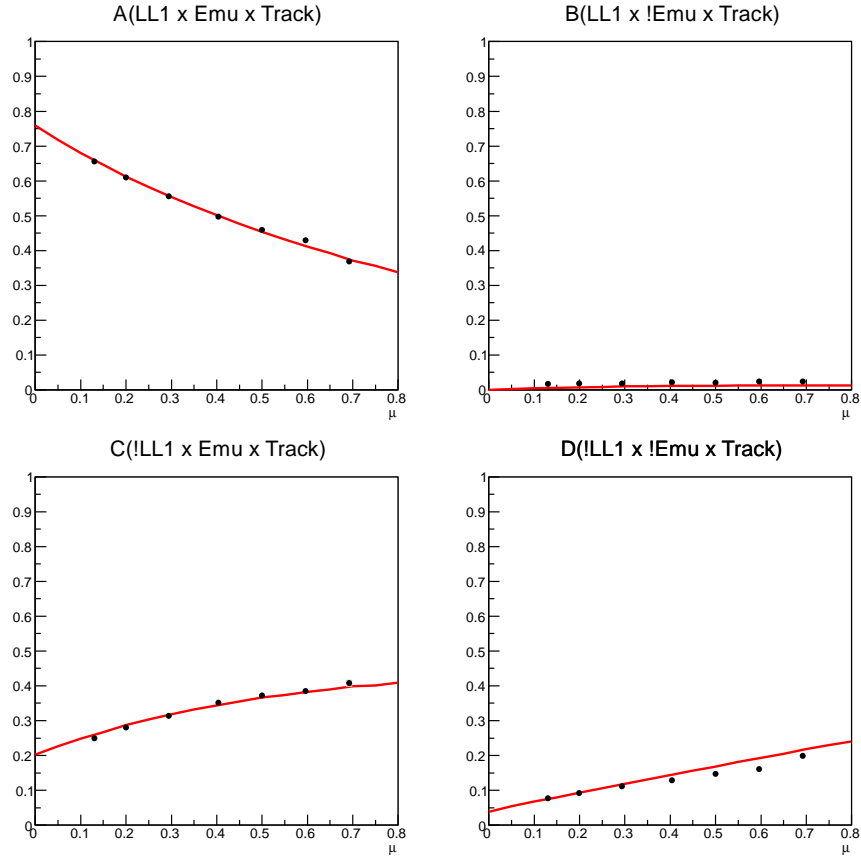


Figure 6.16: Fraction of four categories about MuID-1D trigger for reconstructed muon tracks with BBC(novtx) trigger. Black bullets are data points grouping runs by luminosity, and red lines are the result of simulation with the optimal parameterization of t_{prob} .

Average μ	(A)	(B)	(C)	(D)
Data				
0.130	0.656 ± 0.002	0.017 ± 0.001	0.249 ± 0.002	0.078 ± 0.001
0.200	0.610 ± 0.001	0.018 ± 0.000	0.280 ± 0.001	0.092 ± 0.001
0.294	0.556 ± 0.002	0.018 ± 0.001	0.314 ± 0.002	0.111 ± 0.002
0.404	0.497 ± 0.003	0.022 ± 0.001	0.352 ± 0.003	0.129 ± 0.002
0.500	0.460 ± 0.004	0.021 ± 0.001	0.373 ± 0.003	0.147 ± 0.003
0.596	0.429 ± 0.006	0.024 ± 0.002	0.385 ± 0.005	0.162 ± 0.004
0.692	0.369 ± 0.009	0.024 ± 0.003	0.408 ± 0.009	0.199 ± 0.007
Toy MC				
0.130	0.660	0.005	0.260	0.075
0.200	0.613	0.007	0.287	0.093
0.294	0.559	0.009	0.315	0.117
0.404	0.500	0.011	0.345	0.144
0.500	0.453	0.012	0.366	0.169
0.596	0.415	0.012	0.381	0.192
0.692	0.376	0.013	0.395	0.216

Table 6.4: Comparison of data points in Figure 6.16 and calculation with the toy MC.

6.3.2.4 MuID-1D trigger efficiency estimation with ERT triggers

The trigger configuration does not hold only-MuID-1D trigger bit in GL1. However we have BBC(novtx)&&MuID-1D trigger and BBC(novtx) trigger, it is possible to evaluate MuID-1D trigger efficiency by comparing the two live trigger bits using tracks in ERT triggers:

$$\varepsilon_{\text{MuID-1D}}^{\text{trg}} = \frac{N_{\text{trk}}(\text{ERT trigger} \mid \text{quality cuts} \mid \{\text{BBC(novtx)} \&\& \text{MuID-1D}\} \text{ live bit})}{N_{\text{trk}}(\text{ERT trigger} \mid \text{quality cuts} \mid \text{BBC(novtx) live bit})}$$

and this estimation gives no biasing to the trigger efficiency even taking into account of trigger timing, since substantially MuID-1D trigger had only 1 BCLK width.

The luminosity dependence of MuID-1D trigger efficiency was estimated for the ERT trigger data (the MPC trigger data was too few statistics to see the dependence clearly, especially at tighter cut levels). The runs are grouped into four by luminosity, and individually the trigger efficiency was estimated. Figure 6.17 shows the result as well as the estimation of MuID-1D trigger efficiency by the toy simulation. As a result, the measured data points exhibit clear decreasing dependence with the luminosity, and the measured data is consistent with the toy simulation within the uncertainty of both data and simulation.

6.3.2.5 Conclusion

As a conclusion, the MuID-1D LL1 trigger efficiency was estimated as a function of multiple collision parameter μ as

$$\varepsilon_{\text{trg}}^{\text{1D}} = (0.77 \pm 0.05) \times (1.0 - 0.432 \times \mu) . \quad (6.9)$$

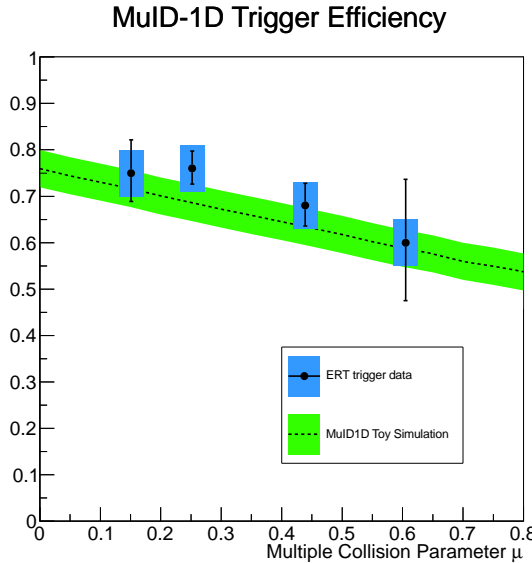


Figure 6.17: Comparison of MuID-1D trigger efficiency as a function of multiple collision parameter obtained between the ERT trigger data and the toy simulation.

Luminosity group	Average μ	Efficiency
1	0.151	$0.75^{+0.06}_{-0.07}(\text{stat}) \pm 0.05(\text{sys})$
2	0.252	$0.76^{+0.02}_{-0.04}(\text{stat}) \pm 0.05(\text{sys})$
3	0.439	$0.68^{+0.04}_{-0.05}(\text{stat}) \pm 0.05(\text{sys})$
4	0.605	$0.60^{+0.12}_{-0.14}(\text{stat}) \pm 0.05(\text{sys})$

Table 6.5: Measured MuID-1D trigger efficiency for various μ values using ERT trigger data.

6.3.3 Mutrg-SG1 trigger

6.3.3.1 Estimation with Mutrg simulator

The Mutrg-SG1 trigger efficiency for single muons were estimated with tuned Mutrg simulator described in Appendix B. We produced $10^5 \mu^+$ and μ^- for each Muon Arm per p_T and η bin, where $\Delta p_T = 1.0 \text{ GeV}/c$ and $\Delta\eta = 0.1$. An example of turn-on curves obtained in the simulator is shown in Figure 6.18. Fitting of turn-on curves with the following function is performed for each η bin in the region of $2.0 < p_T < 50.0 \text{ GeV}/c$:

$$\varepsilon_{\text{SG1}}(p_T) = A + B \exp(-Cp_T) + D \exp(-Ep_T) \quad (6.10)$$

where A , B , C , D , and E are free parameters. This function describes the obtained turn-on curves well. The plateau value and p_T to give 50 % efficiency (as a standard for turn-on p_T threshold) are extracted after fitting. The result of fitting is summarized in Figure 6.22. The plateau value decreases with η except $1.1 < \eta = 1.2$, corresponding to the edge region of the lampshade. In higher rapidity the incident angle of particles is small and the probability to have longer arrival time of ionized electrons in the chamber gap increases. This worsens time resolution of hit, which results in lower plateau efficiency. The turn-on p_T also decreases with η . The rejection of low momentum track is determined by the cathode strip width relative to the size of sagitta. At the high rapidity region the magnetic field is strong but relative strip size is also large, and both effects compete.

A remarkable point is that the turn-on point differs by the charge of the track, especially in the North Arm. We clarified this difference comes from the clustering algorithm (see Sec. 3.3.2.3). The clustering option at Mutrg LL1 is implemented to earn rejection power by reducing the continuous hits in cathode strips into one hit. Since the sweep direction of clustering reduction is the same for both positive charged tracks and negative charged tracks, the hit pattern after clustering is slightly asymmetric between opposite charges. It was confirmed that when we turn off the clustering, this asymmetry disappears. However this slight change of turn-on position because of clustering does not affect to the plateau efficiency value.

Mutrg-SG1 trigger efficiency for $W^\pm \rightarrow \mu^\pm$ The same Mutrg simulator was applied to $W^\pm \rightarrow \mu^\pm$ process for the reference run of 334145. The p_T and η distribution of W^\pm process is reflected to the averaged trigger efficiency. Table 8 summarizes the estimated Mutrg-SG1 efficiency for $16 < p_{T,\text{reco}}^{\mu^\pm} < 60 \text{ GeV}/c$ for different cut levels. Overall the Mutrg-SG1 trigger efficiency estimated with Mutrg simulator is within $91^{+4}_{-3} \%$ for μ^\pm in both South and North Arms.

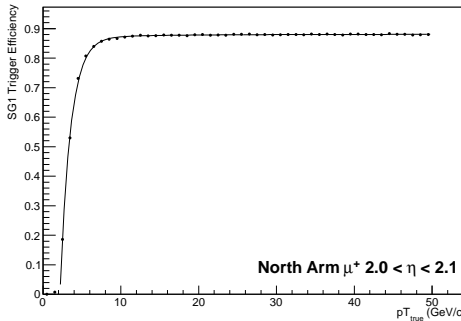


Figure 6.18: Mutrg-SG1 trigger efficiency estimation with Mutrg simulator for North Arm μ^+ , $2.0 < \eta < 2.1$ as a function of p_T .

CHAPTER 6. DETECTOR PERFORMANCES

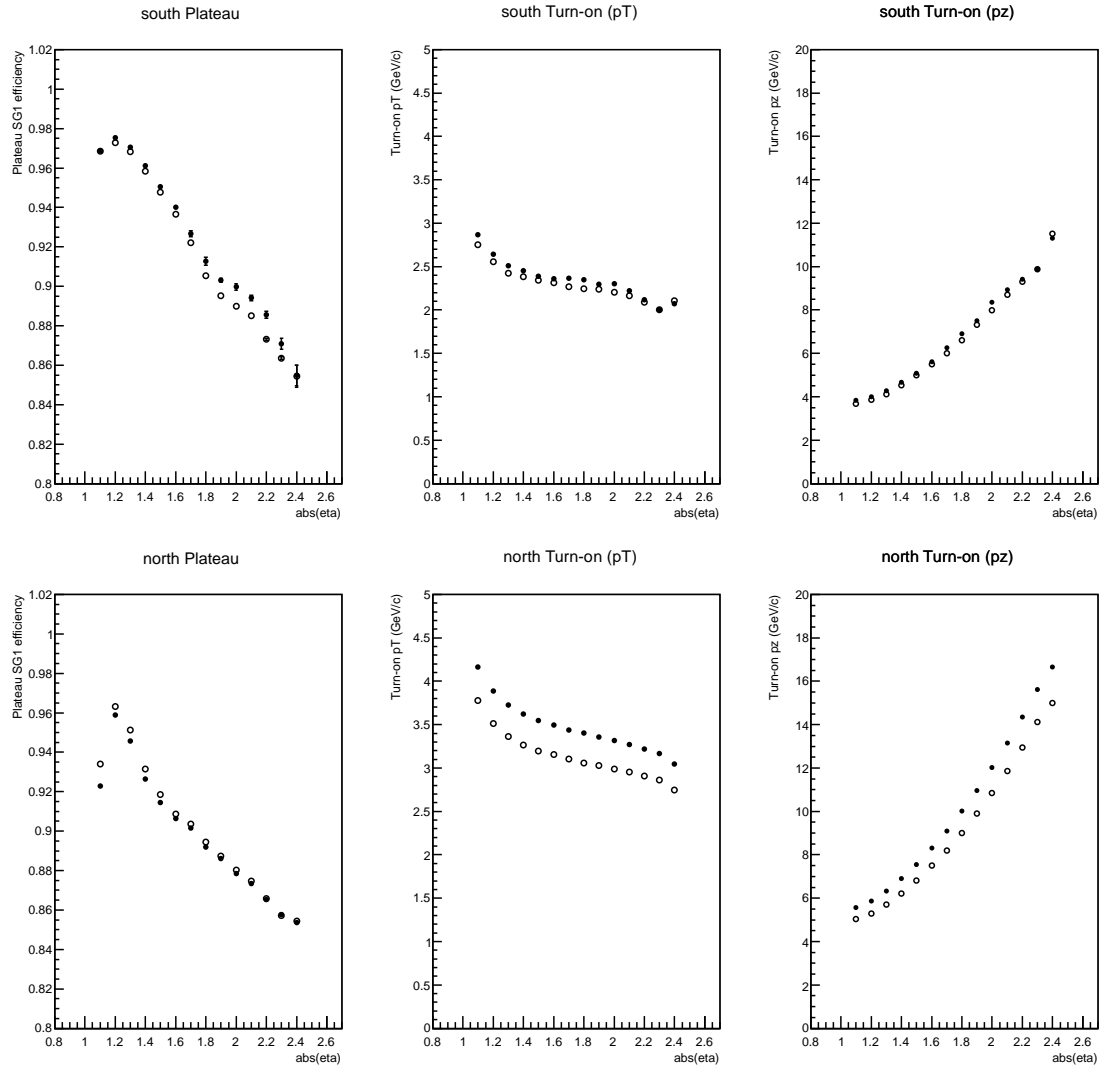


Figure 6.19: Estimated Mutrg-SG1 trigger efficiency at plateau and the turn-on p_T and p_z as a function of η for South and North Arm. Black bullets represent positive charged tracks, and white circles represent negative charged tracks.

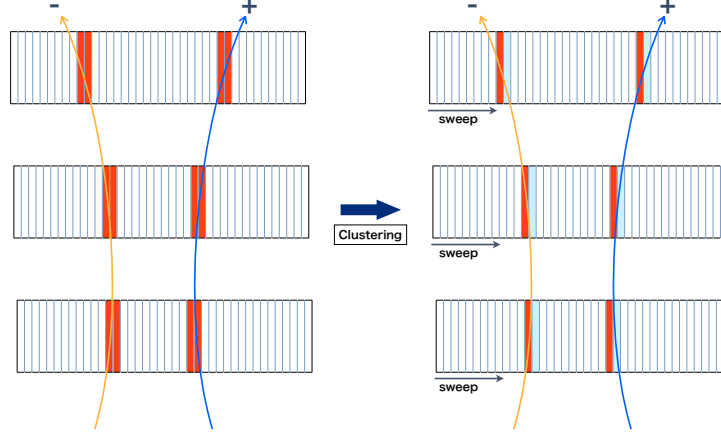


Figure 6.20: Illustration of how the clustering algorithm works for positive and negative charged tracks. The clustering algorithm thins continuous hits by sweeping strips in the same direction regardless of the charge of the track.

6.3.3.2 Mutrg-SG1 trigger efficiency estimation with data

The SG1 trigger efficiency was measured with MuID-1D trigger single muon data. The statistics is limited then the positive and negative charged tracks were combined. The following cuts were applied:

- MuID lastGap==4
- DG0 < 6.0 cm
- DDG0 < 3.1 deg
- $\chi^2_{\text{track}} < 18$
- DCA_r < 2.5 cm
- DCA_z < 5.0 cm
- $d\phi_{12} < 0.018$
- $d\phi_{12} < 0.0132$
- RpcDCA < 11.5 cm

Figure 6.21 shows an example of turn-on curve. The data points were fitted with a turn-on function

$$\varepsilon(p_T) = A + B \exp(1 - C p_T) \quad (6.11)$$

where A , B , C are the free parameters of the fitting. The plateau value were extracted from the fitting result for each rapidity section of $1.2 < |\eta| < 1.6$, $1.6 < |\eta| < 2.0$, $|\eta| > 2.0$. Figure 6.21 is the result of Mutrg-SG1 plateau efficiency obtained from MuID-1D trigger data and the prediction from the simulation. All data points are within $(90 \pm 5) \%$ and they support the accuracy of the prediction with simulation within the error. Moreover, the obtained data points shows decreasing tendency as the absolute rapidity increases, and the tendency is also consistent with the simulation. However the statistics of data at the plateau region is quite few and most

CHAPTER 6. DETECTOR PERFORMANCES

of plateau value estimation relies on the shape of rising region of the turn-on curve, thus we conservatively conclude that the Mutrg simulator can calculate Mutrg-SG1 trigger efficiency within $\pm 5.5\%$ uncertainty. Still this study assures the general validity of the Mutrg simulator under the uncertainty.

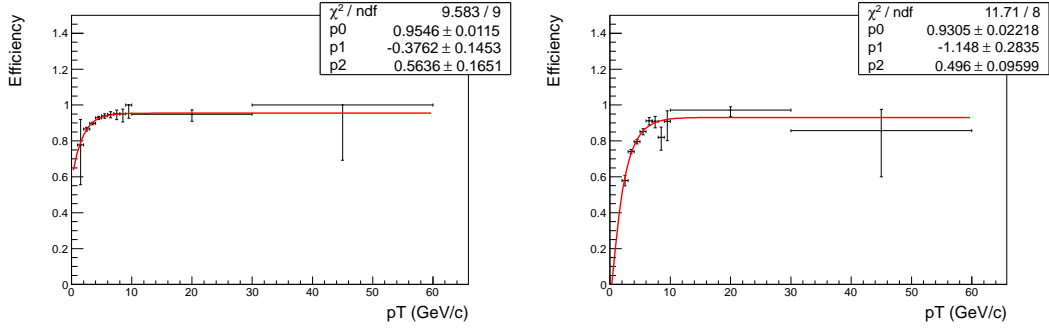


Figure 6.21: Examples of Mutrg-SG1 trigger efficiency turn-on curve, for South (Left) and North (Right) Arm $1.2 < |\eta| < 1.6$ obtained with MuID-1D trigger data and the fitting result to the data points.

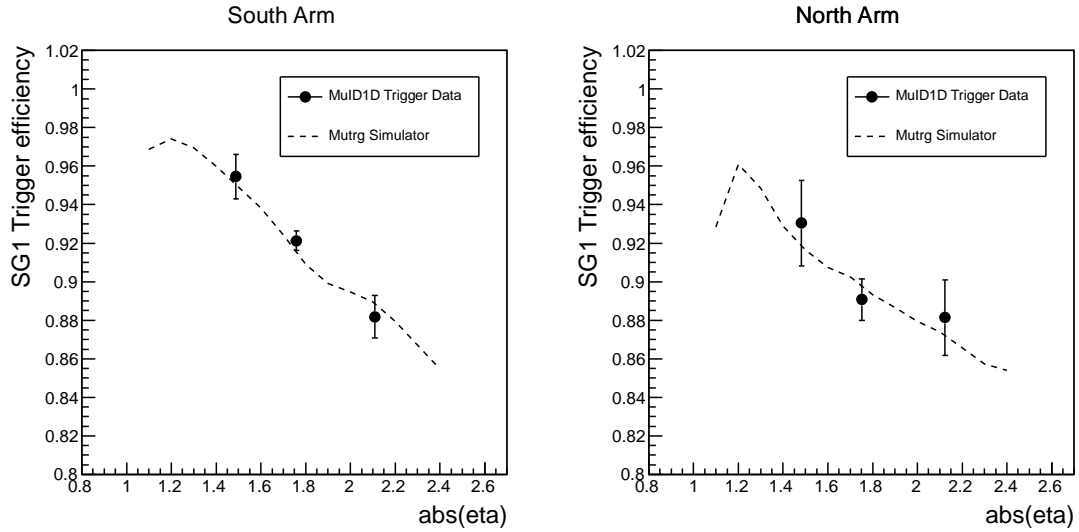


Figure 6.22: Rapidity dependence of Mutrg-SG1 trigger measured with MuID-1D trigger data and the prediction of Mutrg simulator for South and North Arms.

6.3.3.3 Luminosity dependence

The luminosity dependence of Mutrg-SG1 trigger was checked with the Mutrg simulator with tuning the PISA simulation for $W^\pm \rightarrow \mu^\pm$ (the tuning of the PISA simulation will be discussed in Sec.6.5.1.) As a result, the relative slope of the Mutrg-SG1 efficiency was $-0.1 \pm 0.3\%$ for the South Arm and $-4.3 \pm 0.3\%$ for the North Arm. The worse degradation of the trigger efficiency of the North Arm than the South Arm is because of lower hit efficiency of the MuTr.

6.4 RPC aefficiency

The RPC efficiency was low at the former period of the runs due to the misconfiguration of the gas mixture, but it was almost stable in the latter period of the runs. Thus the absolute RPC acceptance and efficiency is calculated with dimuons for runs in RunNumber > 338000 where the RPC efficiency was stable, and the relative RPC efficiency is calculated using single muons for all fills.

6.4.1 Absolute RPC efficiency estimation with dimuon data

Absolute RPC acceptance and efficiency is estimated with so-called “tag-and-probe method” using dimuon data in WTRG(S,N) trigger, and comparing unlike-sign efficiency and like-sign efficiency to subtract the effect of combinatorial background events.

- Event selection
 - $m_{\text{inv}} > 2.5 \text{ GeV}/c^2$
 - $|\phi_1 - \phi_2| > 1.2$: jet rejection cut
- Cuts applied to tag-side track
 - MuID lastGap == 4
 - DG0 < 4.0 cm
 - DDG0 < 2.2 deg
 - $\chi^2_{\text{track}} < 7.0$
 - DCA_r < 12.0 cm
- Fiducial cuts for probe-side track
 - $1.4 < |\eta| < 2.2$
- Numerator
 - Require to have associated RPC hits for probe-side muon

Results Figure 6.23 is the RPC efficiency turn-on curves for South Arm and North Arm as a function of probe-side muon’s p_T^{reco} for unlike-sign dimuons. The turn-on curve is fitted with Erf-based turn-on function, and the fitted result of plateau value are used for the efficiency at plateau.

The same procedure is performed for like-sign dimuons, and efficiency values are extracted as well. According to the fitting result, plateau approximation is valid at $p_T^{\text{reco}} > 2.5 \text{ GeV}/c$, then the denominator events in this region are counted. The fraction of combinatorial backgrounds in unlike-sign events are estimated to be

$$N_{\text{comb}} = 2\sqrt{N_{++} \times N_{--}},$$

and suppose unlike-sign efficiency is expressed as:

$$\varepsilon_{(+)} = p \varepsilon_{(\mu^+ \mu^-)} + (1 - p) \varepsilon_{\text{comb}} \quad (6.12)$$

where p denotes the purity of true dimuons in unlike-sign events defined as

$$p \equiv \frac{N_{(+)} - N_{\text{comb}}}{N_{(+)}} \quad (6.13)$$

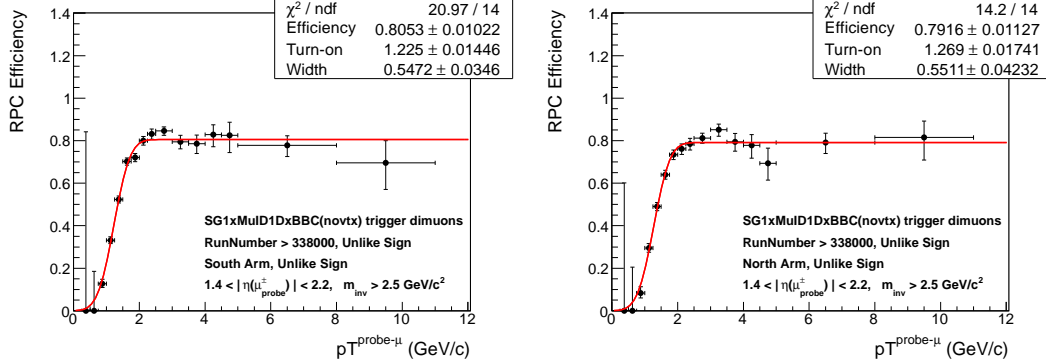


Figure 6.23: RPC efficiency for unlike sign dimuons in RunNumber > 338000.

and $\varepsilon_{(\mu^+\mu^-)}$, $\varepsilon_{\text{comb}}$ efficiency for true muons, efficiency for combinatorial backgrounds, respectively. $\varepsilon_{\text{comb}}$ was calculated by combining both (++) and (--) combinatorial backgrounds. Under this assumption, the absolute RPC acceptance and efficiency was calculated as

$$\varepsilon_{(\mu^+\mu^-)} = \frac{\varepsilon_{(+-)} - (1-p)\varepsilon_{\text{comb}}}{p}. \quad (6.14)$$

To calculate $\varepsilon_{\text{comb}}$, we combined both (++) and (--) combinatorial background events to earn statistics; within the statistical uncertainty, the plateau efficiency for (++) and (--) combinatorial background events does not differ. The obtained efficiency was 87.0 ± 6.0 % (South Arm) and 86.6 % (North Arm). The dead area in the fiducial area of $1.4 < |\eta| < 2.2$ was estimated as 2 %.

Event type	South Arm		North Arm	
	Events	Plateau eff (%)	Events	Plateau eff (%)
Unlike sign	918	80.5 ± 1.0	881	79.2 ± 1.1
Like sign (++)	103	60.8 ± 3.8	111	66.3 ± 5.0
Like sign (--)	86	63.3 ± 3.4	99	64.4 ± 3.8
Combinatorial Subtracted	730 ± 36	87.0 ± 6.0	671 ± 36	86.6 ± 7.2

Table 6.6: The number of events of the denominator of efficiency and the plateau value for unlike-sign, like-sign, and unlike-sign after subtracting combinatorial backgrounds for South and North Arm.

6.4.2 Relative RPC efficiency correction using single track data

The RPC efficiency differs by runs reflecting dead channels or gas conditions or other electronics errors. By using single muon data, these fluctuations were measured relative to the average absolute efficiency $\langle \varepsilon_{\text{abs}} \rangle$ obtained in the previous subsection. The same cuts as Sec.6.3.3.2 except RpcDCA was applied for WTRG(S,N) trigger single muons, then it was calculated that the efficiency $\varepsilon_{\text{single}}$ of events which satisfies $\text{RpcDCA} > 0$ for $p_T^{\text{reco}} > 3 \text{ GeV}/c$ muons for each run. Note that $\varepsilon_{\text{single}}$ could be lower than the absolute efficiency reflecting contamination of hadrons. However the intrinsic hadron inefficiency of RPC because of absorption in MuID absorbers does not contribute to biasing of relative efficiency correction, because once hadrons

injected to RPC then the response of RPC is the same as that for muons. The relative efficiency correction for RunNumber j is calculated as

$$\varepsilon_{\text{abs}}^j = \frac{\varepsilon_{\text{single}}^j}{\langle \varepsilon_{\text{single}} \rangle} \cdot \langle \varepsilon_{\text{abs}} \rangle \quad (6.15)$$

where $\langle \varepsilon_{\text{single}} \rangle$ is the averaged $\varepsilon_{\text{single}}$ for runs in $\text{RunNumber} > 338000$. Figure 6.24 shows the result of the relative corrections. The statistics error of $\varepsilon_{\text{single}}^j / \langle \varepsilon_{\text{single}} \rangle$ is included as the systematic uncertainty of RPC efficiency for each run.

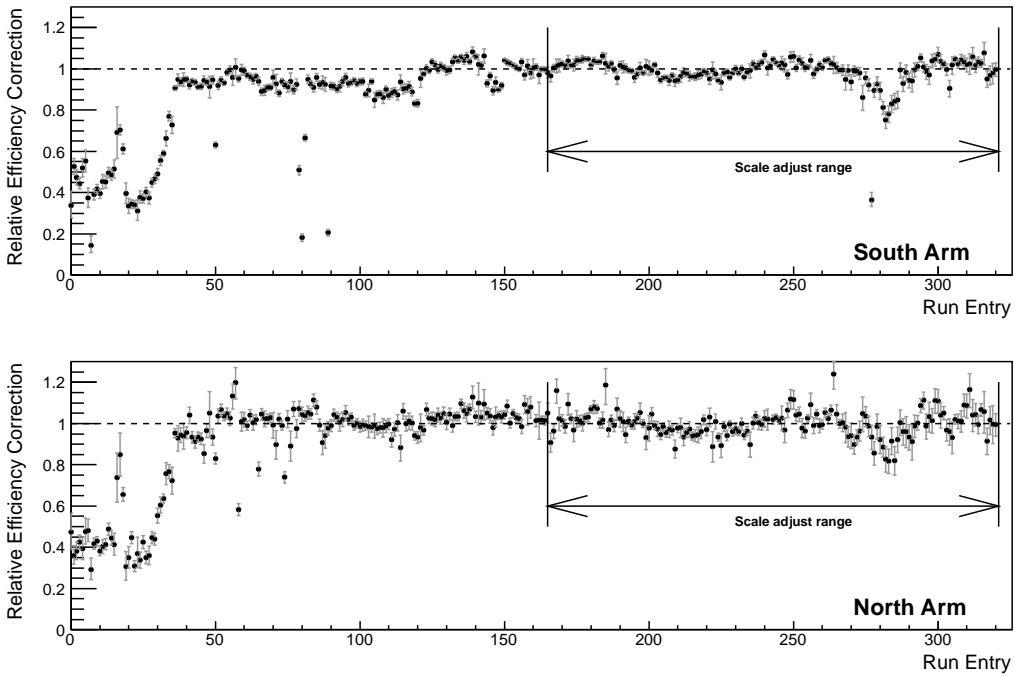


Figure 6.24: Run-by-run relative RPC efficiency correction for South and North Arms.

6.5 Tracking efficiency

6.5.1 Tuning of the PISA simulation

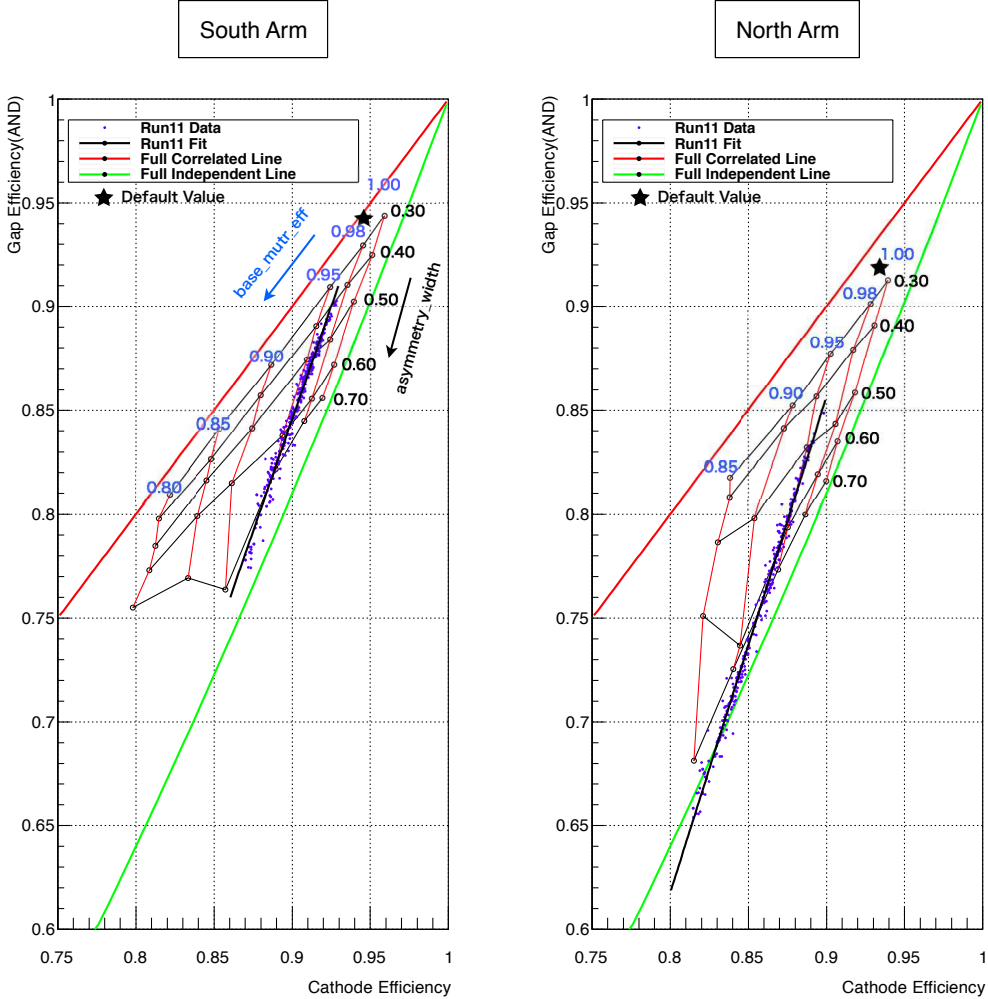


Figure 6.25: Mapping of the result of simulation for different efficiency parameterizations. The data points are overlaid.

We performed tuning of the PISA simulation for each reference run to evaluate the tracking efficiency and the change of variable distributions for each reference run. The RPC efficiency was not implemented, and the RPC efficiency in the simulation was set 100 %. The measured MuID hit efficiency for each HV group was input to the PISA simulation. The measured MuTr hit efficiency showed some non-coherence between the stereo and the non-stereo plane of the same gap. To reproduce the observed MuTr efficiency on the simulation, we need to adjust both the efficiency of the gap and the correlation between the two planes of the same gap. We emulated the observed situation by changing the hit efficiency with the following two parameters in the simulation:

- The total hit efficiency : `base_mutr_eff`
- Charge asymmetry between the two planes : `asymmetry_width`

Since the correspondence between the two measured efficiencies of $\{\varepsilon_{\text{gap}}^{\text{AND}}, \varepsilon_{\text{plane}}\}$ and the two simulation parameters of $\{\text{base_mutr_eff}, \text{asymmetry_width}\}$ was not known, this mapping is searched by varying simulation parameters as shown in Figure 6.25. As we observed a clear luminosity dependence of $\{\varepsilon_{\text{gap}}^{\text{AND}}, \varepsilon_{\text{plane}}\}$ with small fluctuation, it is possible to approximate these efficiencies as a function of multiple collision parameter μ :

$$\begin{aligned}\varepsilon_{\text{gap}}^{\text{AND}} &= \varepsilon_{\text{gap}}^{\text{AND}}(\mu) \\ \varepsilon_{\text{plane}} &= \varepsilon_{\text{plane}}(\mu)\end{aligned}$$

By combining these relations with the measured-efficiency-to-simulation mapping, finally the following correspondence was obtained as a function of μ :

$$\begin{aligned}(\text{SouthArm}) &: \begin{cases} \text{base_mutr_eff} = 0.9725 - 0.0526\mu + 0.0275\mu^2 \\ \text{asym_width} = 0.3472 + 1.070\mu - 2.181\mu^2 - 3.214\mu^3 \end{cases} \\ (\text{NorthArm}) &: \begin{cases} \text{base_mutr_eff} = 0.9534 - 0.0084\mu - 0.1307\mu^2 \\ \text{asym_width} = 0.4322 + 0.0355\mu - 3.763\mu^2 - 1.425\mu^3 \end{cases}\end{aligned}$$

and these mappings are used to estimate the tracking and cut efficiencies for given luminosity of the specified reference run.

6.5.2 Crosscheck: Relative yield of $J/\psi \rightarrow \mu^+\mu^-$

The validity of the tuning of the simulation was verified with $J/\psi \rightarrow \mu^+\mu^-$ events. The simulation includes the degradation effect of the MuID-1D trigger efficiency. Since the dimuon events has two tracks, the MuID-1D trigger is issued if either of the two tracks satisfies the trigger condition. We simply estimated the MuID-1D trigger efficiency for $J/\psi \rightarrow \mu^+\mu^-$ in the acceptance as

$$\varepsilon_{\text{1D}}^{J/\psi} = 1 - \left(1 - \varepsilon_{\text{1D}}^{\text{single}}\right)^2 \quad (6.16)$$

Figure 6.26 shows the result of the relative J/ψ yield in the simulation for each reference run. Aside from the fluctuation, the reconstructed J/ψ yield shows clear luminosity dependence. Note that the fluctuation larger than the statistical error of each simulation comes from run-by-run MuID and MuTr efficiency inputs into the simulation. The relative slope of luminosity dependence was measured as -0.76 for the South Arm and -0.77 for the North Arm. Note that the fluctuation of run points greater than the statistical error of the simulation comes from the tuning of MuID and MuTr hit efficiencies by runs. These relative slopes were compared with the real data. Figure 6.27 shows the dimuon events in $2.5 < m_{\text{inv}} < 4.0 \text{ GeV}/c^2$ with WTRG(S,N) triggers in the real data¹. The relative slope was measured as -0.76 ± 0.02 for the South Arm and -0.71 ± 0.04 for the North Arm. The measured and simulated relative slopes agreed well, and that manifests the validity of the tuning of the PISA simulation with measured MuID and MuTr hit efficiencies, as well as the validity of the MuID-1D trigger efficiency estimation.

¹For the event selection of $J/\psi \rightarrow \mu^+\mu^-$, see Appendix A.

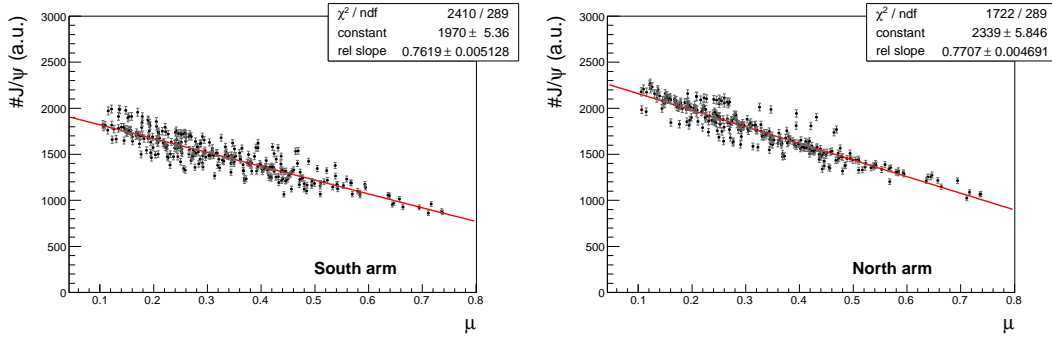


Figure 6.26: Reconstructed yield of $J/\psi \rightarrow \mu^+ \mu^-$ for each reference run in the PYTHIA + PISA simulation sorted by multiple collision parameter μ after taking account of the degradation of MuID-1D trigger efficiency with luminosity.

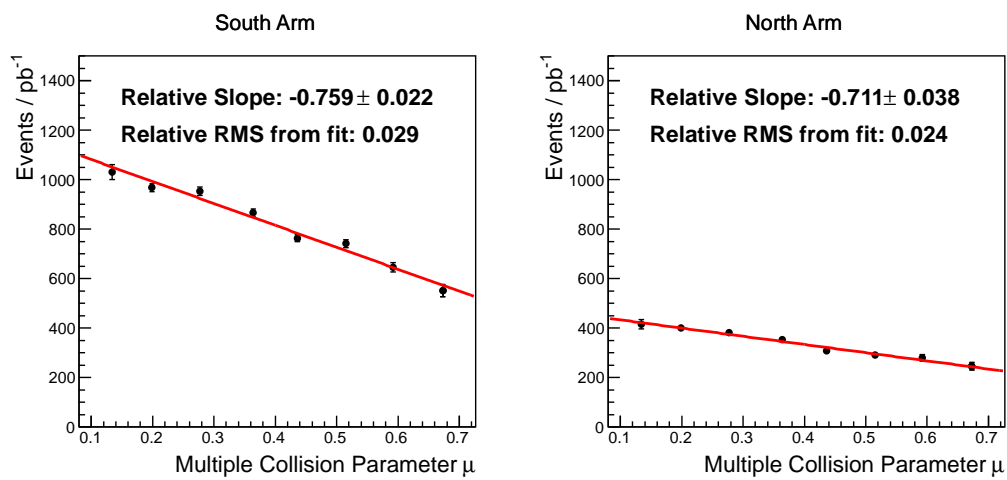


Figure 6.27: Luminosity dependence of dimuon yield in real data in $2.5 < m_{\text{inv}} < 4.0 \text{ GeV}/c^2$ with WTRG(S,N) triggers, after subtracting combinatorial backgrounds.

6.5.3 Uncertainty of the absolute tracking efficiency

The acceptance and the tracking efficiency for the specific physics process is evaluated with using the PISA simulation in this thesis. However the tuning of the simulation did not cover the following points:

- We evaluated the MuTr hit efficiency with assuming the gap efficiency is uniform in the same Arm, and the MuID hit efficiency was estimated with bundling tubes in HV group. The locality of detector inefficiencies could be the cause of the uncertainty of the acceptance and tracking efficiency.
- Increase of noise hits in the detector shown in Sec.5.4 was not implemented in the simulation. We would have unexpected increase of tracking efficiency because of noise hits.

While the relative tracking efficiency was validated with $J/\psi \rightarrow \mu^+ \mu^-$ data, data-driven evaluation of the absolute tracking efficiency is not available. Therefore we assign 10 % uncertainty for the absolute tracking efficiency as the conserved value.

6.6 Effect of vertex distribution on acceptance

The width of the collision vertex distribution and the center position of the distribution fluctuate run by run, and it produces fluctuation of acceptance of reconstruction with Muon Arms. The size of fluctuation was estimated by re-weighting the vertex distribution in the simulation of $W^\pm \rightarrow \mu^\pm$ process. Figure 6.28 shows the contour line of relative fluctuation of yield to the reference vertex configuration (center: $z_{\text{vtx}} = 0$ cm, width: $\sigma_{\text{vtx}} = 40$ cm). The black dots are run-by-run the measured vertex distributions using BBC(novtx) trigger. The Gaussian distribution is assumed for all runs for both measurement and simulation.

As a result, we found the relative systematic uncertainty of acceptance caused by the fluctuation of vertex width was 3.5 %.

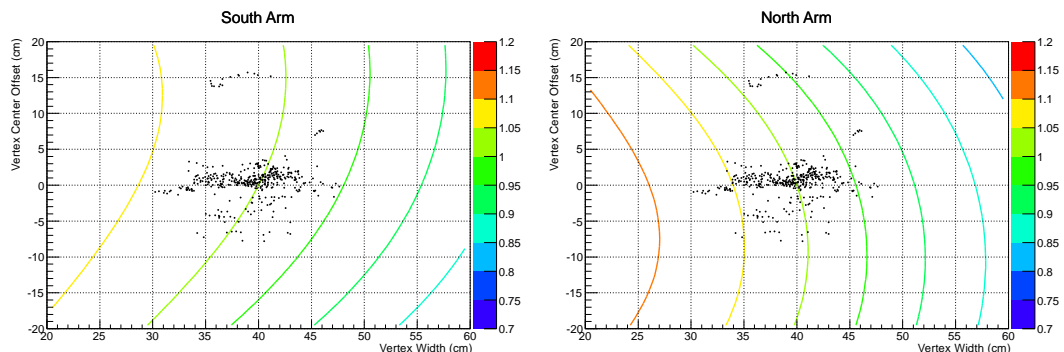


Figure 6.28: Contour plot of the relative fluctuation of acceptance to the reference configuration for South Arm and North Arm. The dots are the measured data points.

CHAPTER 6. DETECTOR PERFORMANCES

Chapter 7

Extraction of $W^\pm/Z \rightarrow \mu^\pm$

7.1 Introduction

The signal of $W^\pm \rightarrow \mu^\pm$ in this analysis is to have a single high- p_T muon in the event. The $W^\pm \rightarrow \mu^\pm$ events compose broad p_T distributions in $10 \lesssim p_T^{\text{true}} \lesssim 50$ GeV/c at the rapidity region we measure. The sizable momentum resolution of the MuTr the p_T -distribution is even smeared to have the continuum up to $p_T^{\text{reco}} \simeq 100$ GeV/c.

Muons are naively identified by requiring associated hits in the last gap in the MuID, since hadrons are absorbed by the absorbers at the Central Magnet and at the MuID steel walls. As we will see later in Sec. 7.3.2, however, hadrons which decay in flight to produce muons in the MuTr could be reconstructed as “fake-high- p_T ” tracks - even though it occurs in very rare case - and due to the huge cross sections of charged hadron productions these events are the dominant backgrounds for $W^\pm \rightarrow \mu^\pm$. In addition to hadronic backgrounds, muon production events which were explained in Sec. 2.6.4.2 also remain as a certain amount of irreducible backgrounds because of smearing. Some analysis techniques which are often employed to identify W bosons in collider experiments - missing transverse energy and transverse mass, track isolation - are not available in the PHENIX Muon Arms. Thus we are involved in serious event selection analysis to identify $W^\pm \rightarrow \mu^\pm$ events and to measure the single spin asymmetry $A_L^{\mu\pm}$.

The first key of the event selection is to require the consistency between the reconstructed momentum and the size of multiple scattering through the absorbers. As the angle of multiple scattering ϑ is inversely proportional to the momentum

$$\vartheta \propto \frac{1}{p},$$

and true high momentum tracks make approximately straight lines from the collision vertex to the deepest detector (RPC3). Large multiple scatterings take place at both the Central Magnet and the MuID walls, variables which are sensitive to see the difference of the track between before and after passing these materials are usable to require the condition which the true high momentum tracks satisfy.

Second, W^\pm bosons decay to muons immediately. The decay position is exactly on the beam axis, and at the interaction point. Thus the track must be put back very closely to the beam axis and the collision vertex. DCA_r and DCA_z are the variables to require these conditions.

Third, the bending size (sagitta) of the track in the magnetic field must be consistent with the reconstructed momentum. The MuTr has the most precise position resolution in the Muon Arm. Hadrons which decay in flight have kinks inside the MuTr, and mostly the sagitta do not match with the size which is expected for the true high momentum muons.

Fourth and finally, muons from W^\pm decays should be consistent with the kinematics of the production and decay of $W^\pm \rightarrow \mu^\pm$ expected from the theory. As a matter of fact the η distribution is different between the signal and the backgrounds. Moreover η is measured precisely and robustly while the momentum measurement for the region of interest is fairly tough. Both the signal and the background distribute broadly in η but we can expect signal-dense regions and background-dense regions in η -axis.

The number of events of $W^\pm \rightarrow \mu^\pm$ is expected to be a few tens for each charge in each Muon Arm with the integrated luminosity of $\simeq 25 \text{ pb}^{-1}$. One suitable technique to differentiate $W^\pm \rightarrow \mu^\pm$ events from the backgrounds in these low statistics is the unbinned maximum likelihood method. Specifically we employed the maximum likelihood method which considers the low number of events with the Poisson statistics.

Terms used in the analysis

Tracking variables Tracking variables used in this analysis were introduced in Sec. 4.3.

Basic cut The muons are naively identified by requiring associated hits in the last gap in the MuID, by utilizing the fact that the hadrons (K^\pm, π^\pm) are rare to survive to the last gap through hadron absorbers at the Central Magnet and the MuID steel walls. Also some track qualities are required. For rough identification of muons we typically require

- Number of reconstructed track == 1
- MuID lastGap == 4
- $\chi_{\text{track}}^2 < 20$
- $\text{DG0} < 20 \text{ cm}$
- $\text{DDG0} < 9 \text{ deg}$
- Has associated RPC3 hits for the track

The above set of requirements are called the *basic cut* in this analysis.

Tight cut The tight cut is only used to investigate the characteristic of hadronic backgrounds. The requirements are the following:

- the Basic cut
- $\text{DG0} < 4.8 \text{ cm}$
- $\text{DDG0} < 2.5 \text{ deg}$
- $\chi_{\text{track}}^2 < 8.0$
- $\text{DCA}_r < 5.0 \text{ cm}$
- $\text{DCA}_z < 10.0 \text{ cm}$
- $\text{RpcDCA} < 7.0 \text{ cm}$
- $-0.05 < dw_{23} < 0.10$ (positive charge), $-0.10 < dw_{23} < 0.05$ (negative charge)

7.2 Topology of $W^\pm \rightarrow \mu^\pm$ signal

- Generally DG0, DDG0, DCA_r, RpcDCA reflect the effect of multiple scattering in the hadron absorber and the MuID absorbers. At low p_T region all of these have wider distributions. The width of the distribution obeys $\propto 1/p$ at low p_T then saturates to a constant at high p_T .
- One cause of the saturation of the width of the above variables is the position resolution of the detector. For example, the position resolution of the MuID is limited by its readout segment of about 8 cm in X and Y direction. The parameters of MuTr-MuID matching, i.e. DG0, DDG0 do not see finer structure than the MuID resolution. Therefore the DG0, DDG0 converge to constant distributions at high p_T (typically saturated at $p_T > 10$ GeV/c).
- The χ^2_{track} distribution has almost flat distribution as a function of p_T . The non-uniformity comes from the p_T distribution of the $W^\pm \rightarrow \mu^\pm$ signal. For example, there are few events with the true p_T greater than 50 GeV/c. The reconstructed p_T could be smeared to this region from lower true p_T , but in this case χ^2_{track} value tends to be large.

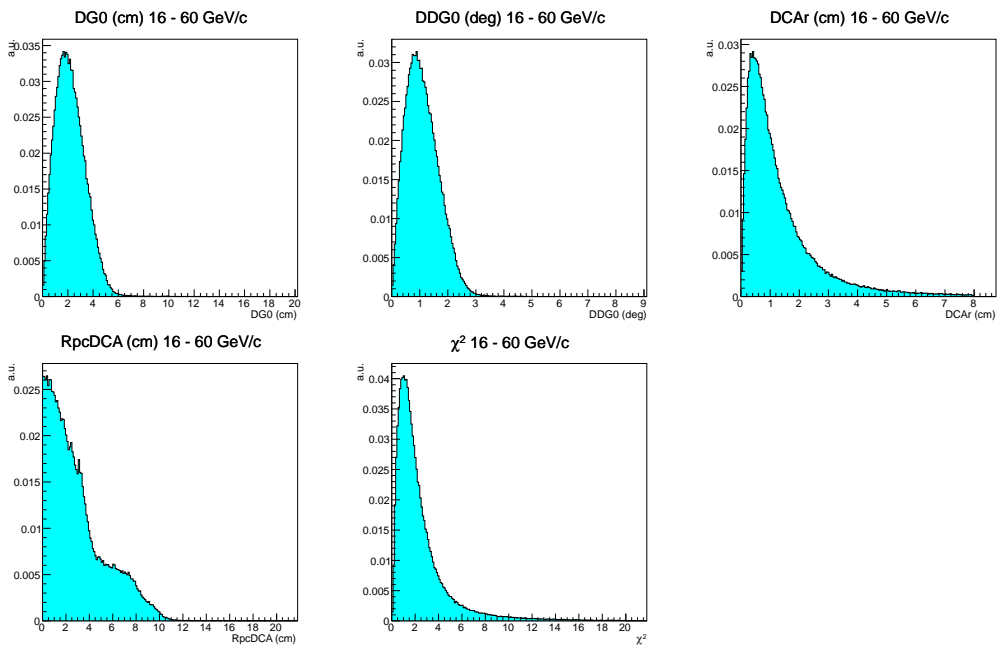


Figure 7.1: Distribution of variables for $W^+ \rightarrow \mu^+$ at $16 < p_T^{\text{reco}} < 60$ GeV/c in the North Arm acceptance.

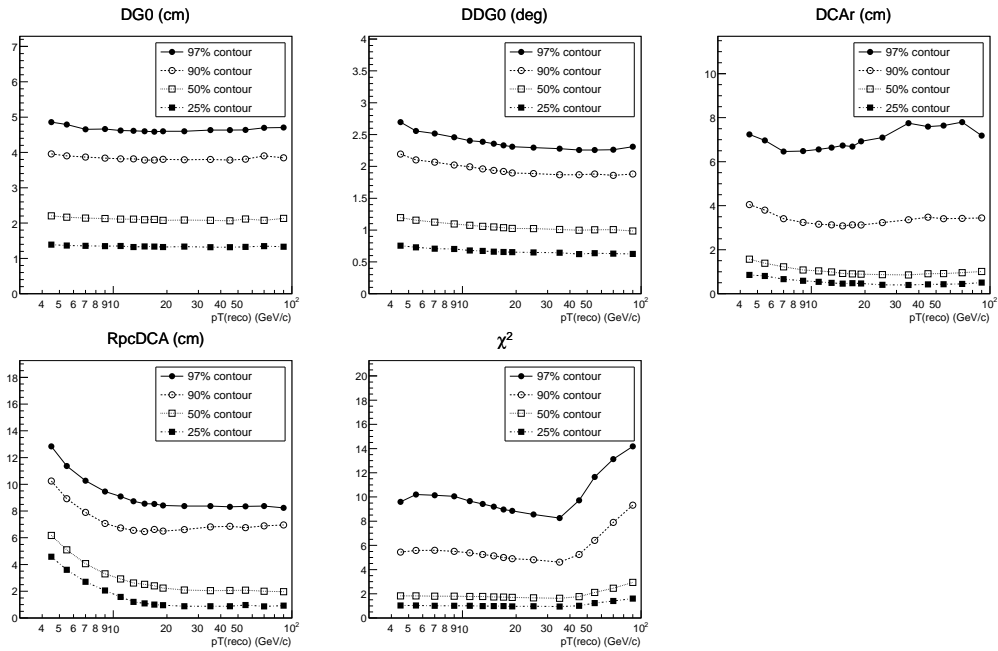


Figure 7.2: Contour lines of the distribution of variables for $W^+ \rightarrow \mu^+$ in the North Arm acceptance as a function of p_T^{reco} .

7.3 Backgrounds

7.3.1 Muon backgrounds

The subprocesses to produce muons were presented in Sec 7.3. To summarize, in the momentum region above 20 GeV/c is dominated by $W^\pm \rightarrow \mu^\pm$ and small fraction of $Z \rightarrow \mu^\pm$. However due to the finite momentum resolution of the MuTr low p_T muon events from QCD background processes such as open heavy flavor contaminate to the region of interest. In the later analysis we attempt to reject these background events as much as possible though primarily these events are irreducible. The major processes of the irreducible muon background events are

- open heavy flavor (open charm, open bottom)
- quarkonia
- Drell-Yan

and we estimated single muon yield from these processes with the PYTHIA + PISA simulation. The cross section of the above processes is estimated with the dimuon mass spectrum in Appendix A, and we employ the result from the dimuon analysis.

7.3.2 Hadronic backgrounds

Inclusive production cross section of charged hadrons The total production cross section of charged hadrons (π^\pm, K^\pm) is further immense than muon production in proton-proton collisions. The inclusive cross section of charged hadron production was measured in the UA1 experiment in which protons and anti-protons were collided at $\sqrt{s} = 500$ GeV as shown in Figure 7.3[70]. The measured differential cross section with respect to the transverse momentum averaged in $|\eta| < 2.5$ is parameterized as

$$E \frac{d^3\sigma}{dp_T^3} \left[\frac{h^+ + h^-}{2} \right] = 408(\text{mb}/\text{GeV}^2) \left(1 + \frac{p_T}{1.61} \right)^{-10.64} \quad (7.1)$$

which is translated to

$$\frac{d^2\sigma}{dp_T d\eta} [h^+ + h^-] = 5.13(\text{b}/\text{GeV}^2) p_T \left(1 + \frac{p_T}{1.61} \right)^{-10.64} \quad (7.2)$$

for a given p_T and η bin. The composition of hadrons in the inclusive cross section is not given in the UA1 reference. In the ISR collaboration the exclusive K^\pm and π^\pm cross sections are given at $\sqrt{s} = 53$ GeV[71]. According to the result, we roughly estimated the fraction of K^\pm and π^\pm are 12 % and 32 %, respectively for each charge. Another estimation of cross section of hadrons at NLO level was performed based on CTEQ6M PDFs[76] and DSS fragmentation functions[77] for the rapidity range of $1.2 < |\eta| < 2.4$ for π^\pm and K^\pm . As shown in the Figure 7.4, the UA1-ISR based cross section and the NLO calculation agrees well in $p_T \lesssim 5$ GeV/c. In $p_T \gtrsim 5$ GeV/c the NLO calculation exceeds the UA1-ISR cross section.

Reconstruction of charged hadrons with the Muon Arms As mentioned above most of charged hadrons produced in collisions are absorbed first at the Central Magnet and second at the MuID walls, it is rare for hadrons to be reconstructed as tracks then reach to the MuID last gap. Hadrons might decay to produce muons in flight, and the muons from hadron decays do not have hadronic interaction in the absorbers then easily reach to the MuID last gap. The decay in flight of hadrons are classified into two topologies. One is called *early decay* which hadrons decay to muons before reaching to the Central Magnet, and the other is called *late decay* which hadrons decay to muons inside the MuTr. In the former case the charge deposits on the tracker

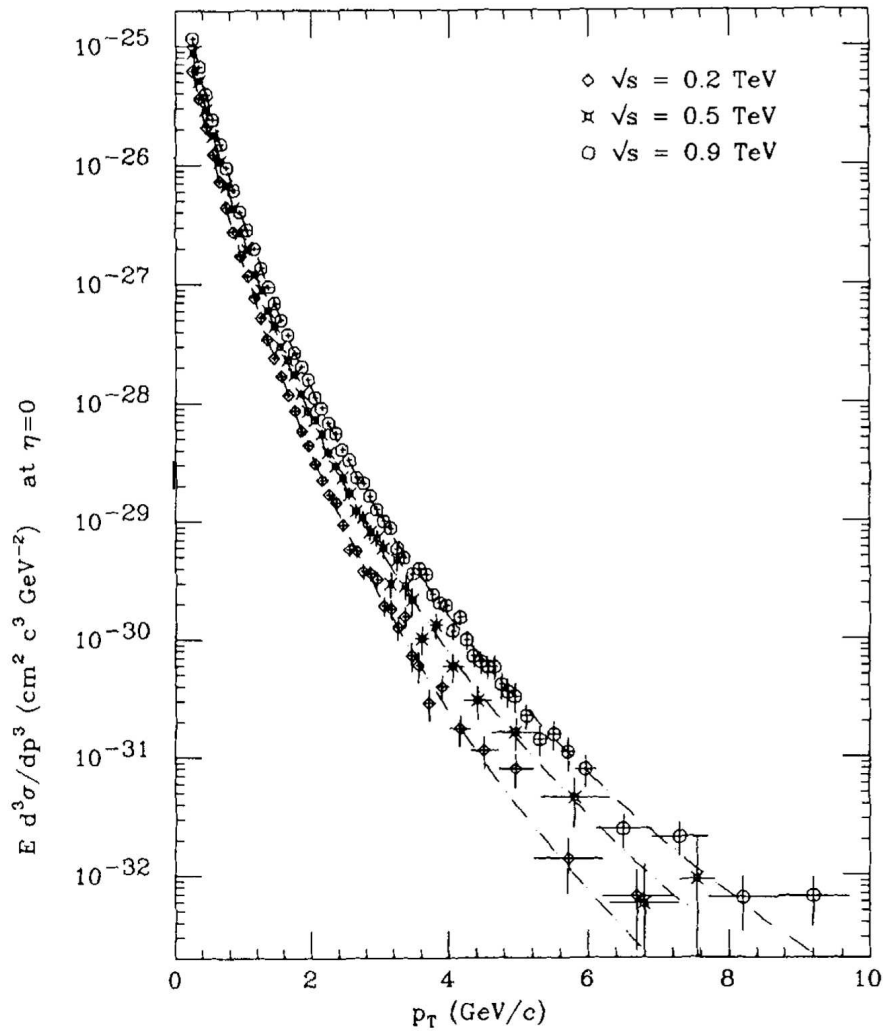


Figure 7.3: Inclusive Differential cross section of hadron production as a function of transverse momentum p_T in proton-antiproton collisions at $\sqrt{s} = 200, 500, 900 \text{ GeV}$ measured by the UA1 experiment[70].

are all created by muons, we expect to reconstruct consistent muon tracks but having relatively large DCA_r and DCA_z . In the latter case we have decay point in the middle of the tracker and the tracking algorithm attempts to fit the trajectory with kinks with a single momentum track, then the χ^2_{track} of the track is generally large and the reconstructed momentum does not have physical meaning. In both cases the reconstructed momentum could be $p_T > 15 \text{ GeV}/c$ either because of momentum smearing or regarding kink tracks as smooth tracks. The probability to have large reconstructed momenta is relatively rare case, nevertheless the number of events of these events are significant and even dominant events at the basic cut level at high reconstructed momentum region, due to the huge cross section of hadron productions.

To investigate the characters of the hadronic backgrounds, a single charged hadron MC was generated in PISA from $1 < p_T < 9 \text{ GeV}/c$ according to the differential production cross section. Figure 7.4 shows the differential cross section of charged hadrons as a function of p_T^{true} , and yield of reconstructed track in $15 < p_T^{\text{reco}} < 60 \text{ GeV}/c$. Both the basic cut and the tight cut are applied. As can be seen from the Figure, at both the basic cut and the tight cut the high p_T^{reco} yield is dominated by $p_T^{\text{true}} \lesssim 3 \text{ GeV}/c$ events, reflecting the initial differential cross section. The rejection effect of the tight cut is large for lower p_T^{true} events. Figure 7.7 is projecting the same simulated events to p_T^{recp} . It is clear that K^\pm yield is much larger than π^\pm , despite the initial production cross section is much larger for π^\pm than K^\pm . Primarily this is because of longer lifetime and larger boost of π^\pm than K^\pm . Applying the tight cut greatly suppresses π^\pm events in $p_T^{\text{reco}} > 15 \text{ GeV}/c$, while some of K^\pm events persistently remain even after the tight cut. Next Figure 7.6 shows the decay z -position of producing muons for K^+ events in the North Arm which are reconstructed with $15 < p_T^{\text{reco}} < 60 \text{ GeV}/c$. The decay z -position concentrates on two regions, one is before the hadron absorber of the Central Magnet, and the other is inside the MuTr lampshade. In particular the latter case is dominant. These events are schematically illustrated in Figure 7.7.

We classified charged hadron events whose p_T^{reco} is in $15 < p_T^{\text{reco}} < 60 \text{ GeV}/c$ as follows:

- Late muonic decay: decay to produce muons inside the MuTr.
- Early muonic decay: decay to produce muons before reaching to the MuTr.
- Punch-through hadrons:
- Others

Figure 7.4 and 7.5 show the fraction of the above categories as a function of initial p_T^{true} of the charged hadrons. For kaons, at the basic cut level the majority is late muonic decay for lower p_T^{reco} , but the fraction decreases as p_T^{true} increases. With applying the tight cut, most of the events are universally late muonic decays. For π^+ on the other hand, the dominant category is early muonic decay at the tight cut level. As the dominant component of hadronic backgrounds is K^+ with $p_T^{\text{true}} \lesssim 3 \text{ GeV}/c$, we estimate the dominant hadronic background events are late muonic decays which has decay point inside the MuTr.

Summary The yield of charged hadron backgrounds are about two orders of magnitude larger than real muon yields at $15 < p_T^{\text{reco}} < 60 \text{ GeV}/c$ at the basic cut level. Even applying the tight cut, the hadronic yield dominates. Therefore we need to select signals much more carefully. In particular we employ likelihood-based signal selection in Sec.7.4.4. As hadronic backgrounds are dominant at $15 < p_T^{\text{reco}} < 60 \text{ GeV}/c$ region, we have large samples of background events around the signal region in the variable space. This indicates we have practicality to estimate hadronic backgrounds with data-driven way.

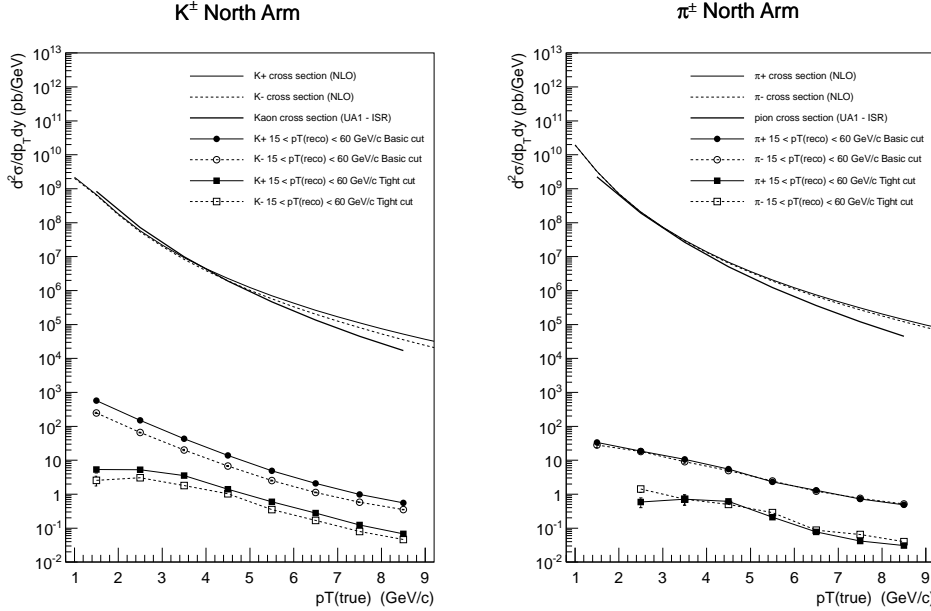


Figure 7.4: Differential cross section of K^\pm and π^\pm as a function of p_T^{true} for the North Muon Arm acceptance in the simulation. The left panel is for K^\pm and the right panel is for π^\pm . The bold solid line denotes the parameterization of UA1 cross section measurement with assuming ISR's measurement of particle fractions. The thin solid and dotted lines represent the calculation of NLO for positive and negative charge, respectively. The filled and open circle plots represent the yield which has a reconstructed track with passing the basic cut in the Muon Arm. The filled and open square plots represent the yield which has a reconstructed track with passing the tight cut.

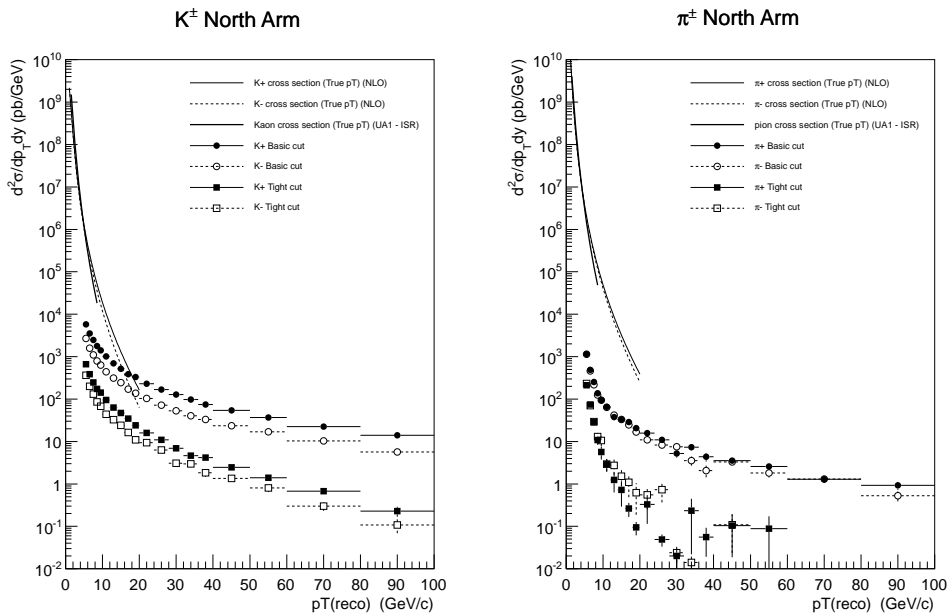


Figure 7.5: Yield of hadronic backgrounds as a function of p_T^{reco} in the simulation where the original p_T^{true} range of the hadrons is $1 - 9 \text{ GeV}/c$. The filled and open circle plots represent the yield which has a reconstructed track with passing the basic cut in the Muon Arm. The filled and open square plots represent the yield which has a reconstructed track with passing the tight cut. The original hadronic cross sections which are identical to Figure 7.4 are superimposed as a function of p_T^{true} .

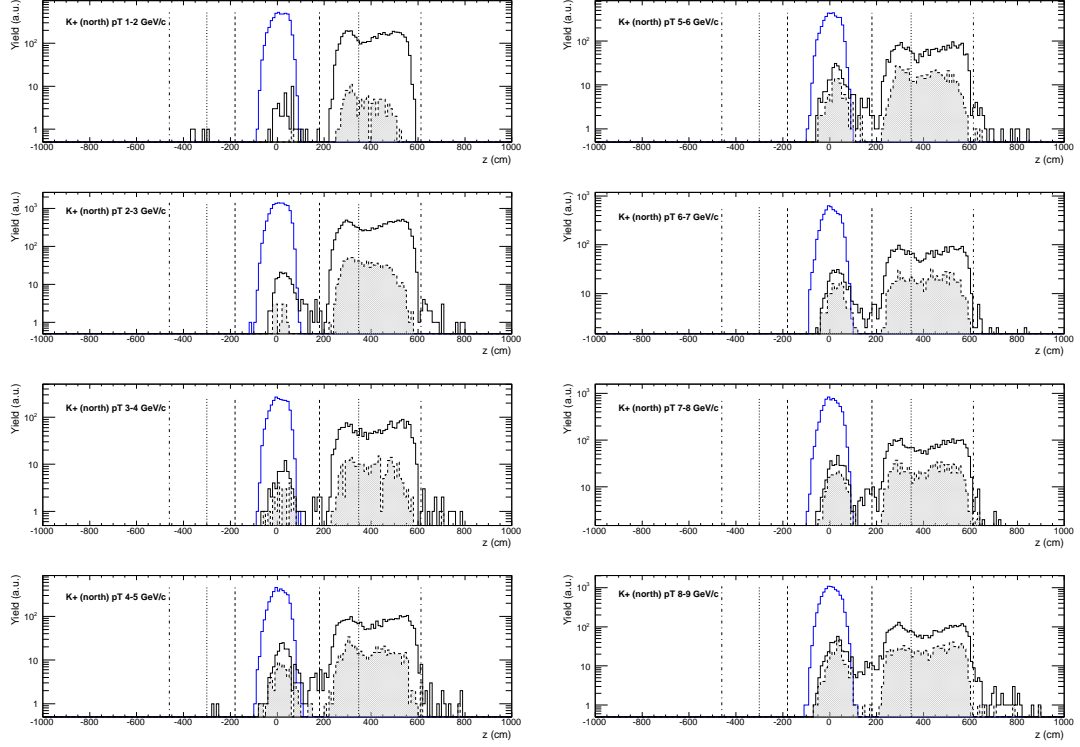


Figure 7.6: Distribution of decay z -position of producing muons (μ^+ or μ^-) from K^+ flying to the North Arm for various initial p_T , whose reconstructed momentum of the track is in $15 < p_T^{\text{reco}} < 60 \text{ GeV}/c$. The solid histogram is at the basic cut level, and the hatched histogram is at the tight cut level. The blue histogram is the distribution of the primary vertex for the basic cut tracks. The vertical lines represent the z -position of the Station-1,2,3 of the MuTr.

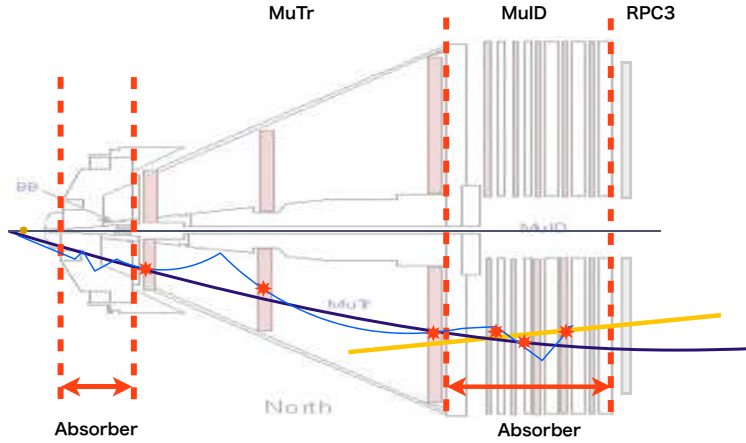


Figure 7.7: Schematic illustration of charged hadrons' muonic decay in flight to be reconstructed as a high p_T track.

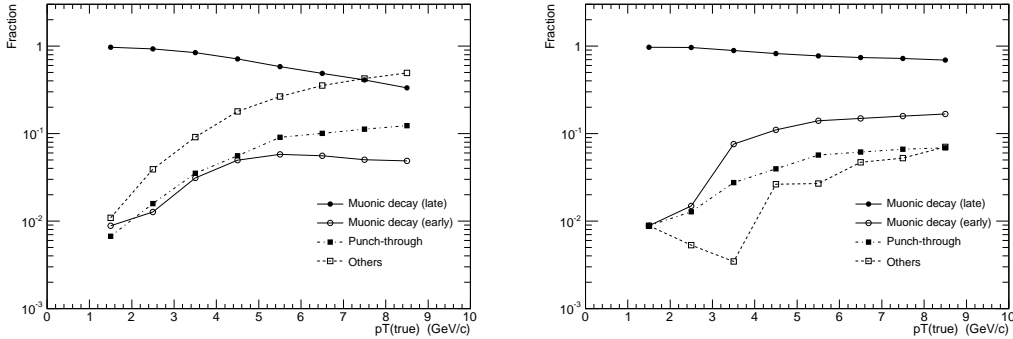


Figure 7.8: Fraction of topologies of events whose reconstructed momentum is in $15 < p_T^{\text{reco}} < 60 \text{ GeV}/c$ for K^+ flying to the North Arm as a function of various initial p_T . The left panel is for the basic cut and the right panel is for the tight cut. The late in-flight muonic decay is the dominant topology.

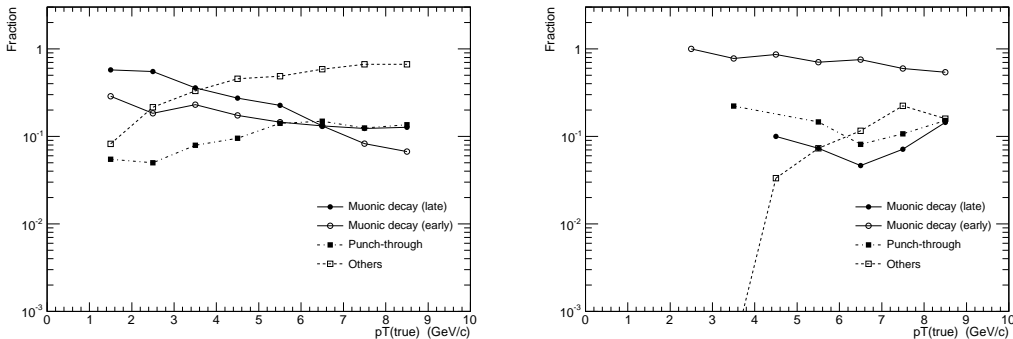


Figure 7.9: Fraction of topologies of events whose reconstructed momentum is in $15 < p_T^{\text{reco}} < 60 \text{ GeV}/c$ for π^+ flying to the North Arm as a function of various initial p_T . The left panel is for the basic cut and the right panel is for the tight cut. For the tight cut level the early in-flight muonic decay is the dominant topology.

7.4 Preselection of $W^\pm/Z \rightarrow \mu^\pm$ candidates

7.4.1 Run selection

Table 7.1 summarizes the quality cut conditions used to select runs. In total 321 runs were used for the analysis. The total integrated luminosity is 24.84 pb^{-1} for the South Arm and 24.80 pb^{-1} for the North Arm.

#	filter	surviving runs
0	Physics run	433
1	BBC(novtx) trigger rate > 10 kHz	432
2	Data production	423
3	WTRG(S,N) worked	388
4	RpcTime well-defined in both Arm	321

Table 7.1: Run filtering cuts used in this analysis.

7.4.2 Quality cut

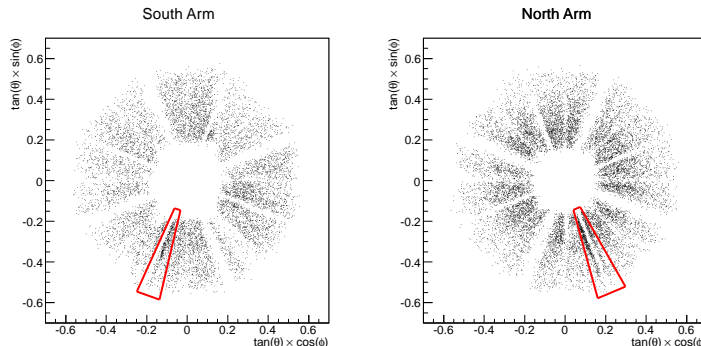


Figure 7.10: Radiograph of reconstructed tracks at $10 < p_T < 60 \text{ GeV}/c$ with some quality cuts.

Detector acceptance where unclear behaviors are seen was rejected from analysis for both data and simulation. As a quality check the only high p_T tracks with passing the following cuts are plotted in Figure 7.10:

- the Basic cut
- $10 < p_T^{\text{reco}} < 60 \text{ GeV}/c$
- $\chi_{\text{track}}^2 < 8.0$
- having associated hit in the RPC and RpcDCA < 7.0
- $\text{DCA}_r < 5.0$

Then the following acceptance regions exhibit abnormal excess of events:

- $-2.0 < \phi < -1.8$ in the South Arm
- $-1.3 < \phi < -1.05$ in the North Arm

These regions are both edges of octants. Remarkably these excesses of events are not significant in low p_T region and they are significant with high p_T selection. The possible cause of the excesses is to have very frequent electrical noises around the edge strips of the octant, and that produces non-physical reconstructed tracks. We applied fiducial cuts to the above ϕ regions.

7.4.3 Selection of p_T range

The selection of the p_T range of muons has some arbitrariness. Clearly in low- p_T region muon events are dominated by muon backgrounds, we should exclude low- p_T region to earn signal-to-background ratio. On the other hand, if we raise up minimum p_T threshold too high, the statistical power for $W^\pm \rightarrow \mu^\pm$ signal decreases. We adopted to maximize the sensitivity of $W^\pm \rightarrow \mu^\pm$ signal against muon background processes. We regarded open heavy flavor, quarkonia, Drell-Yan, and $Z \rightarrow \mu^\pm$ processes as background¹. The basic cut is applied to both signal and background simulations, and single muon p_T^{reco} distribution was compared between the signal and the background. For a reconstructed momentum range of $[p_T^{\min}, p_T^{\max}]$, we define the signal and background yield as

$$n_S(p_T^{\min}, p_T^{\max})_{\text{arm}} = L_{\text{int}} \cdot \int_{p_T^{\min}}^{p_T^{\max}} dp_T^{\text{reco}} \int_{\text{arm}} d\Omega \frac{d^2\sigma_S}{dp_T^{\text{reco}} d\Omega} (A \cdot \varepsilon), \quad (7.3)$$

$$n_B(p_T^{\min}, p_T^{\max})_{\text{arm}} = L_{\text{int}} \cdot \int_{p_T^{\min}}^{p_T^{\max}} dp_T^{\text{reco}} \int_{\text{arm}} d\Omega \frac{d^2\sigma_B}{dp_T^{\text{reco}} d\Omega} (A \cdot \varepsilon), \quad (7.4)$$

respectively, where L_{int} denotes integrated luminosity used in the analysis, $d\Omega$ denotes integration over solid angle enough to cover whole South or North Arm, and $(A \cdot \varepsilon)$ denotes acceptance and efficiency at the basic cut level. The figure of merit was defined as follows:

$$\text{FOM}(p_T^{\min}, p_T^{\max})_{\text{arm}} = \sqrt{\frac{n_S}{1 + 2(n_B/n_S)}}. \quad (7.5)$$

For p_T^{\max} , we tried 40, 50, 60, 80, 100 GeV/c and we scanned p_T^{\min} for each p_T^{\max} as shown in Figure 7.11. For all p_T^{\min} the FOM was maximized when p_T^{\max} was set to 60 GeV/c, although the effect of selecting p_T^{\max} is small compared to that of p_T^{\min} . The optimal p_T^{\min} was 18 GeV/c and 16 GeV/c for $W^+ \rightarrow \mu^+$ and $W^- \rightarrow \mu^-$, respectively for both Arms. Note that the maximum signal-to-background ratio (n_S/n_B) is achieved at $p_T^{\min} \simeq 28$ GeV/c. We also tried to use the tight cut in place of the basic cut. With the tight cut the signal-to-background ratio was improved, however the optimal p_T^{\min} was kept at the above values. The difference of FOM by changing p_T^{\min} from 16 GeV/c to 18 GeV/c was not large. Thus we decided to use a single momentum range of

$$16 < p_T^{\text{reco}} < 60 \text{ GeV}/c$$

regardless of charge and Arm for simplicity.

¹Regarding $Z \rightarrow \mu^\pm$ process as background for momentum range selection is appropriate because it is preferable to have less $Z \rightarrow \mu^\pm$ events in signal candidates.

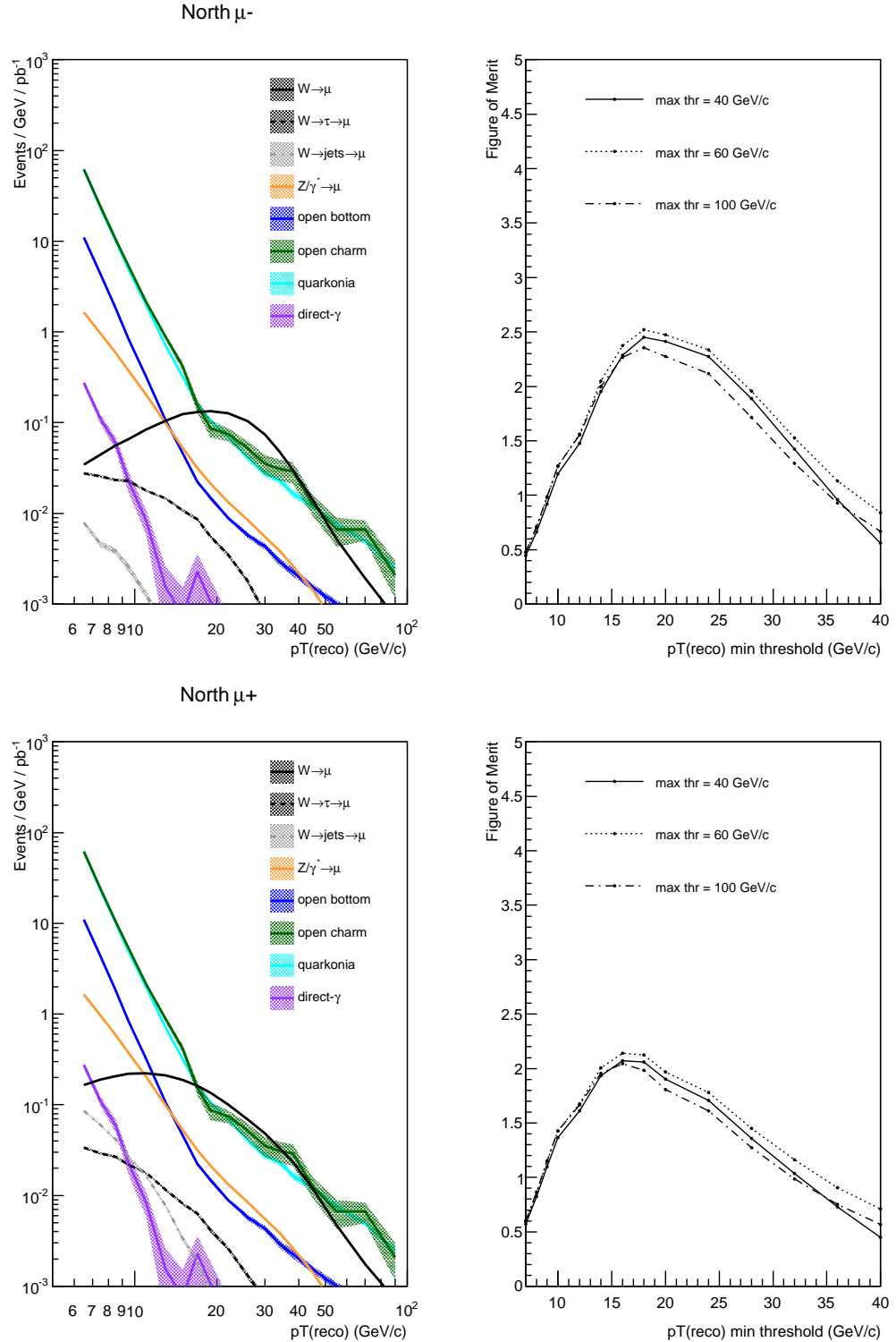


Figure 7.11: Reconstructed Yield of $W^\pm \rightarrow \mu^\pm$ and muon background events (left panel), and figure of merit of $W^\pm \rightarrow \mu^\pm$ by changing the momentum selection ranges (right panel) for North Arm μ^\pm .

7.4.4 Likelihood-based preselection

We used the likelihood method to select signal. The following variables were used to make preselection of $W^\pm/Z \rightarrow \mu^\pm$ candidates: DG0, DDG0, DCA_r , RpcDCA, χ^2_{track} . Then the likelihood was composed as

$$\lambda = p(\text{DG0}, \text{DDG0}) \cdot p(\text{DCA}_r) \cdot p(\text{RpcDCA}) \cdot p(\chi^2_{\text{track}}). \quad (7.6)$$

The mother distributions of the signal for the likelihood λ_{sig} were taken from the PYTHIA + PISA simulation with passing the basic cut. The distributions of individual variables were not parameterized, and the histogram of each variable was directly applied to obtain the probability. The likelihood of the background λ_{BG} was composed similarly, and the distributions were taken from the data with passing the basic cut. The fraction of the signal in data at the basic cut level is two orders of magnitude less than the data, and that small contamination of the signal do not change the background distribution significantly. Then the cut parameter f is defined for each event as

$$f \equiv \frac{\lambda_{\text{sig}}}{\lambda_{\text{sig}} + \lambda_{\text{BG}}}. \quad (7.7)$$

Then the same criteria of defining f was assigned to both real data and MC simulations. Figure 7.14 shows the distribution of $W^\pm \rightarrow \mu^\pm$ in the simulation as a function of f as well as the cumulative signal efficiency distribution with cut threshold at the given $f = f_{\text{cut}}$ value. Figure 7.15 shows the distribution of data as a function of f . Figure 7.16 shows the cumulative efficiency of signal and muon backgrounds.

7.4 Preselection of $W^\pm/Z \rightarrow \mu^\pm$ candidates

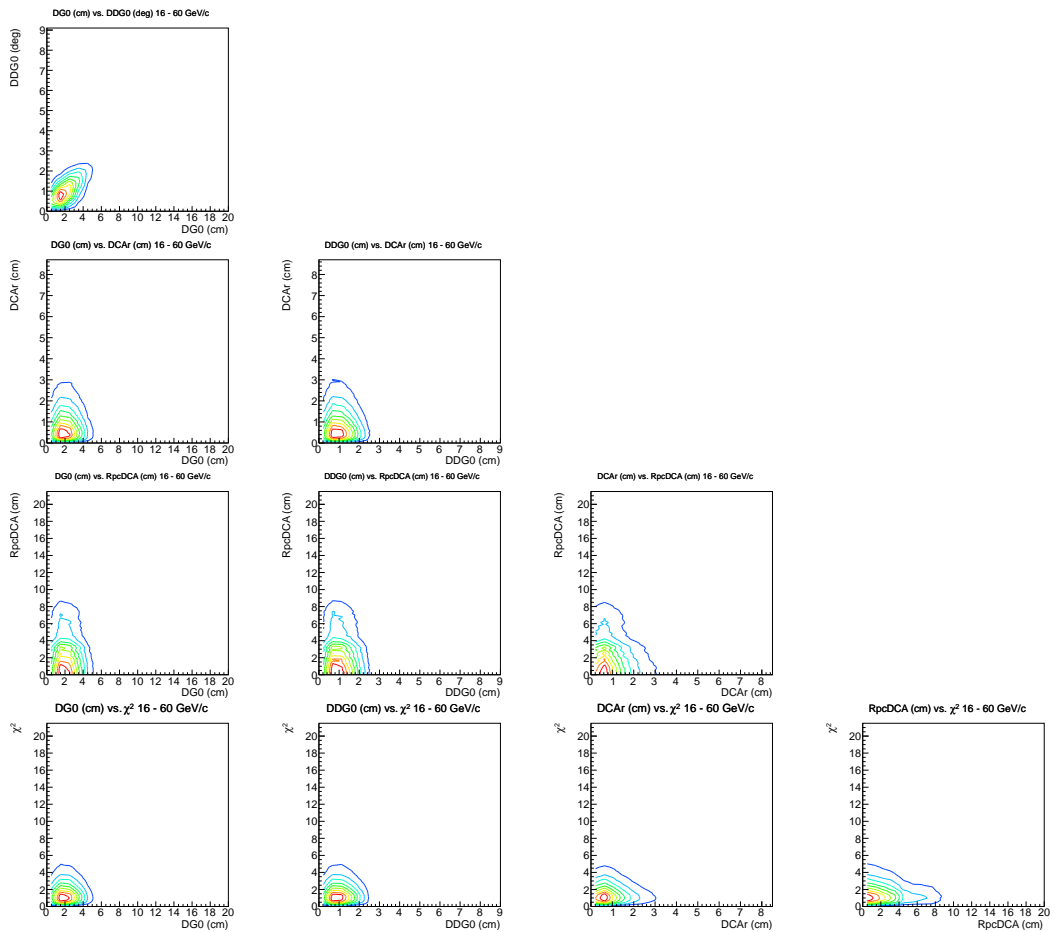


Figure 7.12: Contour lines of the 2D distribution of variables for $W^+ \rightarrow \mu^+$ at $16 < p_T^{\text{reco}} < 60$ GeV/c in the North Arm acceptance.

CHAPTER 7. EXTRACTION OF $W^\pm/Z \rightarrow \mu^\pm$

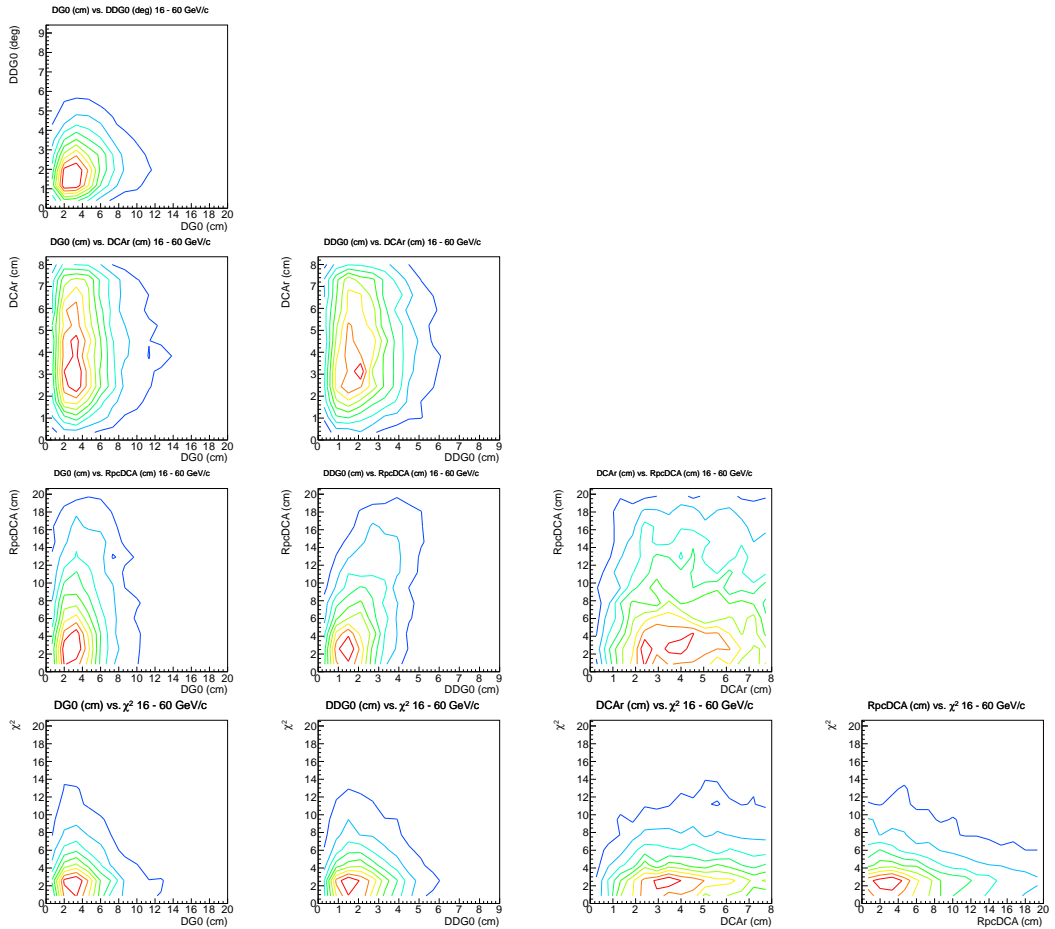


Figure 7.13: Contour lines of the 2D distribution of variables for real data at $16 < p_T^{\text{reco}} < 60 \text{ GeV}/c$ in the North Arm acceptance.

7.4 Preselection of $W^\pm/Z \rightarrow \mu^\pm$ candidates

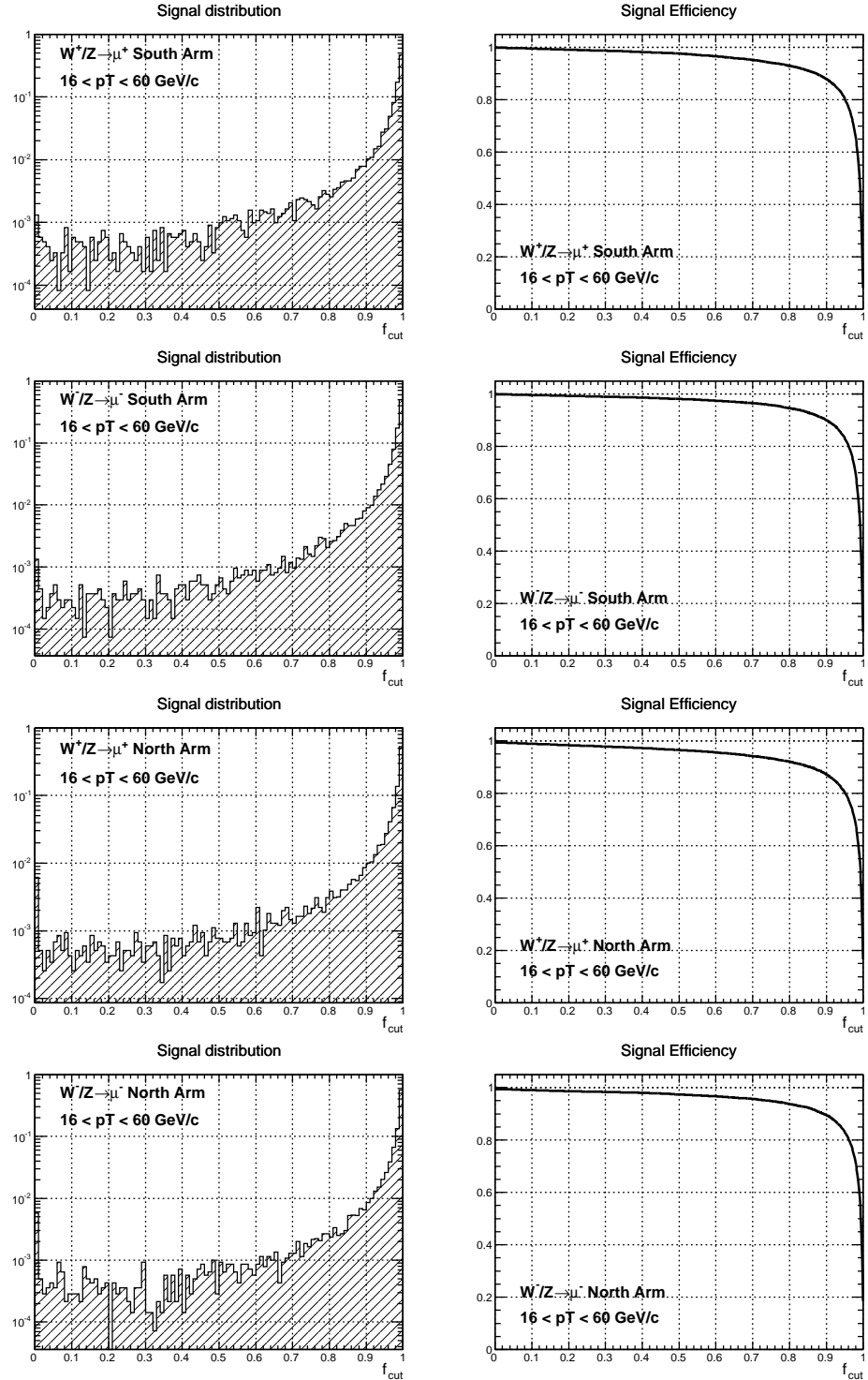


Figure 7.14: Distribution of $W^\pm/Z \rightarrow \mu^\pm$ signal at $16 < p_T^{\text{reco}} < 60 \text{ GeV}/c$ as a function of f_{cut} , and the cumulative signal efficiency at the given f_{cut} threshold.

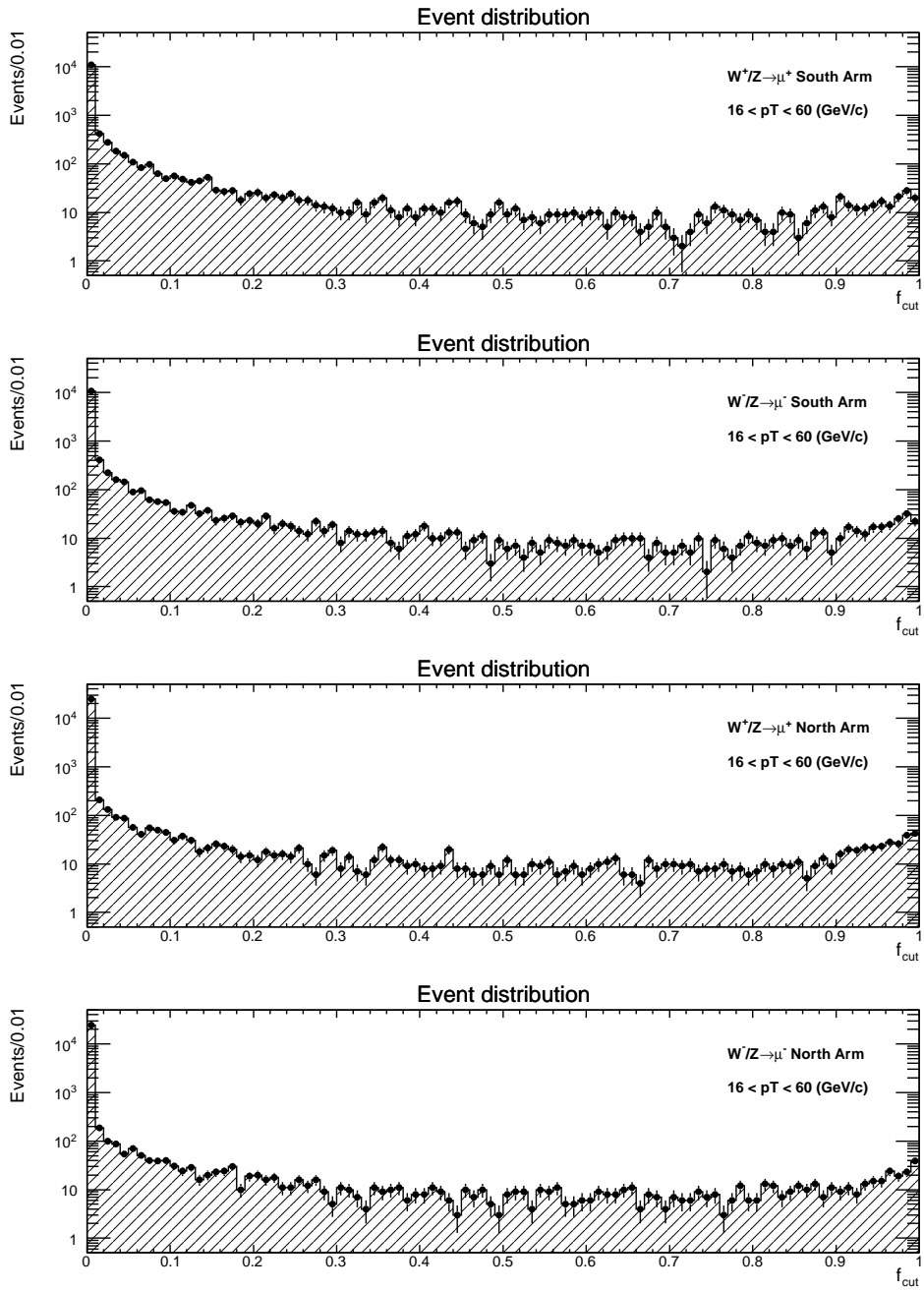


Figure 7.15: Distribution of real data at reconstructed at $16 < p_T^{\text{reco}} < 60$ GeV/c as a function of cut threshold f_{cut} .

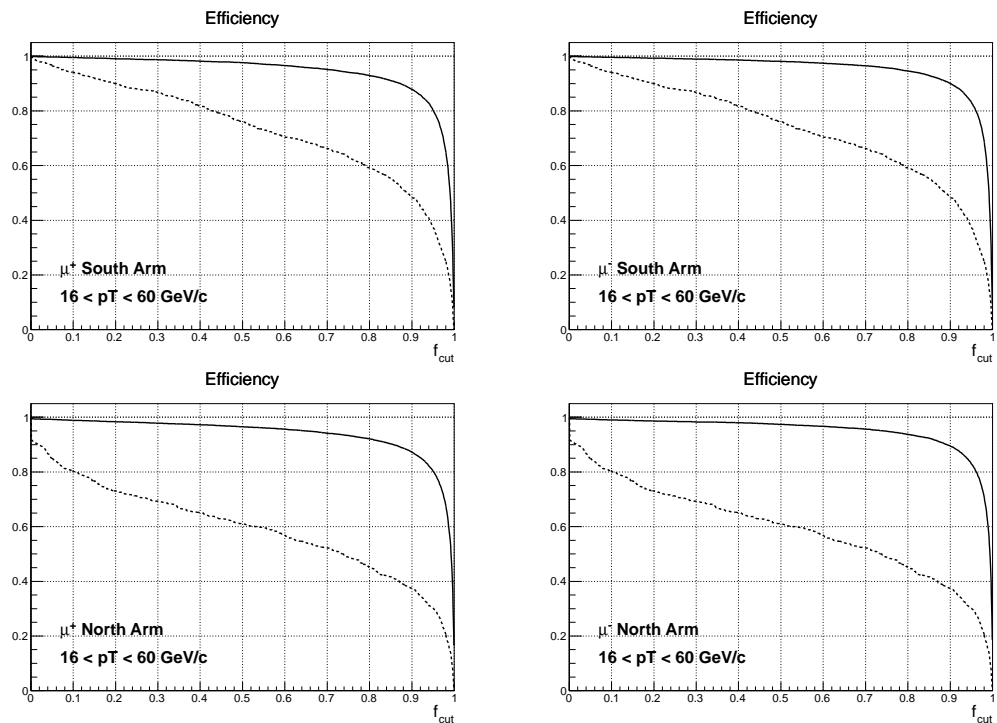


Figure 7.16: $W^\pm/Z \rightarrow \mu^\pm$ signal and muon background efficiency as a function of cut threshold f_{cut} . The solid line denotes $W^\pm/Z \rightarrow \mu^\pm$ and the dashed line denotes the sum of other muon backgrounds.

7.5 Signal extraction

7.5.1 Fitting variables

The remaining background fraction after the preselection was estimated with likelihood method. Here we used the following variables:

- pseudorapidity: η
- reduced azimuthal bending between the Station-2 and Station-3 in the MuTr: dw_{23}

Figure 7.17 shows the distribution of $W^\pm \rightarrow \mu^\pm$ signals in $16 < p_T^{\text{reco}} < 60 \text{ GeV}/c$ in $f_{\text{cut}} > 0.95$ with respect to η and dw_{23} . The distribution is approximately orthogonal between the two variables. The lower edge of the η -distribution is determined by the acceptance of the RPC3. The η -distribution is different between W^+ and W^- as described in Sec. 2.6.4.1. The physical explanation of dw_{23} is as follows. The bending direction of the particle is azimuthal as the magnetic field is radial. The size of bending is proportional to $p_T \sin(\theta)$. If the momentum reconstruction is accurate and at the limit where the multiple scattering is small, the reduced azimuthal bending should concentrate on a particular constant value. In other words, the magnitude of the reduced azimuthal bending corresponds to the electric charge of the particle. Reduced azimuthal bending is used to require the consistency of the reconstructed p_T and the true p_T . For the $W^\pm \rightarrow \mu^\pm$ signal, the relative deviation of the reconstructed p_T from the true p_T ($|p_T^{\text{reco}} - p_T^{\text{true}}|/p_T^{\text{true}}$) is small in the region of interest of the momentum range. For the hadronic background case where the dominant events are muonic decay in flight, the reconstructed momentum does not relate to the true momentum then the consistency is bad. For the muon background, most of the time the true momentum of the reconstructed track at the ROI is smeared from lower momentum region since the p_T^{true} is well suppressed in $p_T > 20 \text{ GeV}/c$, thus the consistency in dw_{23} is worse than truly high-momentum tracks.

7.5.2 Composing PDFs

1. $W^\pm/Z \rightarrow \mu^\pm$ signal

The PDF of $W^\pm/Z \rightarrow \mu^\pm$ signal was taken from the PYTHIA + PISA simulation with weighting the predicted production cross section of W^\pm and Z . The 2D histogram of (η, dw_{23}) for signals of $f > f_{\text{cut}}$ was directly used for the PDF.

2. Muon backgrounds

The PDF of muon background processes was taken from the PYTHIA + PISA simulation. Due to the small statistics of the MC samples the η -distribution and dw_{23} -distribution were individually calculated, and the 2D distribution was composed as the orthogonal product of the two distributions. To help the low statistics of the MC, both positive and negative charged tracks are combined to produce the PDF. The polarity of the dw_{23} was flipped by reconstructed charge. As the γ^*/Z process contains the contribution of Z , the exclusive Z process was subtracted from γ^*/Z . The correlation of the error of the dimuon mass spectrum fitting was propagated, and the uncertainty of muon background yield from the uncertainty of the cross sections was estimated as 7 %. Table 7.2 summarizes the cross section and the yield in the ROI of muon background processes.

3. Hadronic backgrounds

A data-driven method was employed to compose the PDF of hadronic backgrounds for the following reasons:

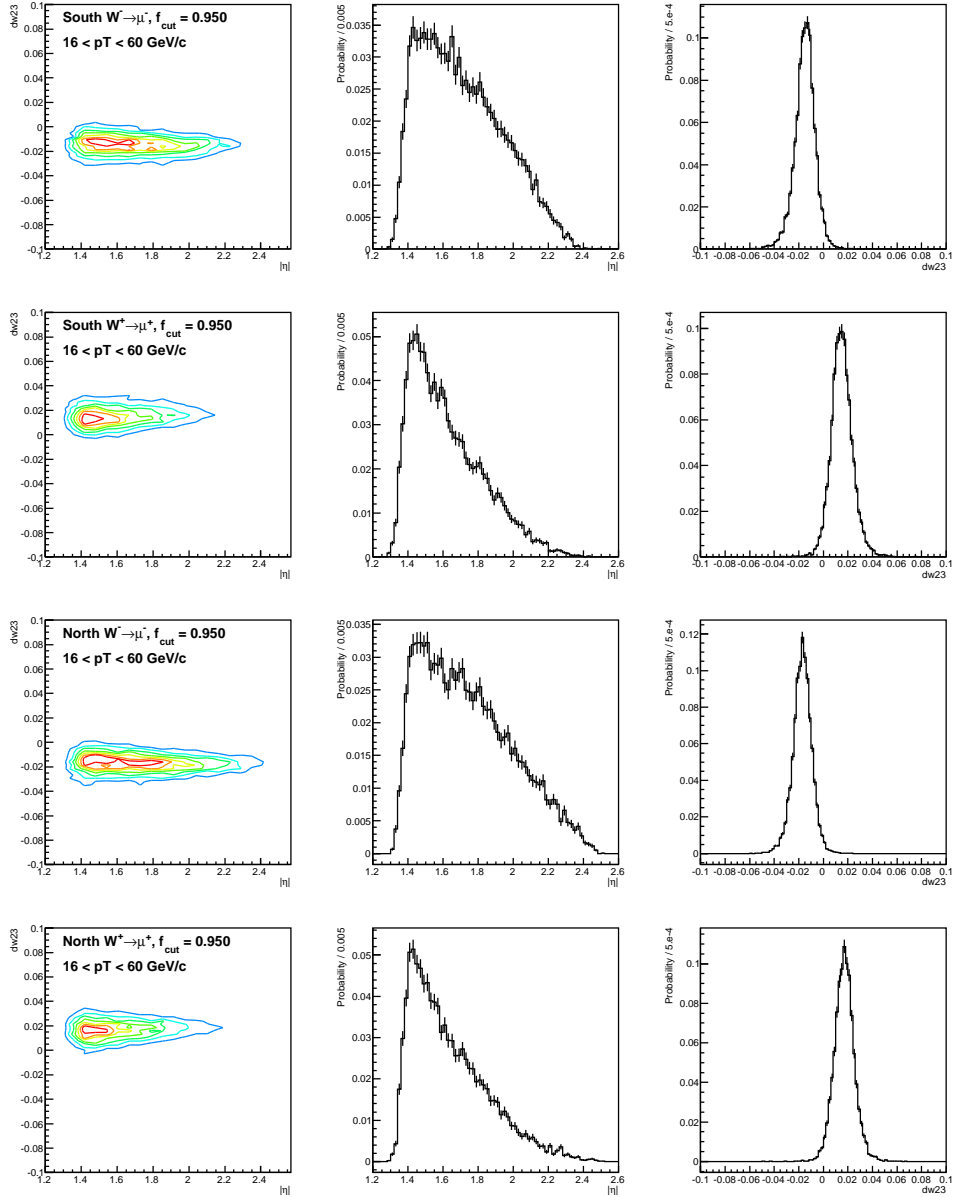


Figure 7.17: Distribution of $W^\pm \rightarrow \mu^\pm$ in $16 < p_T^{\text{reco}} < 60 \text{ GeV}/c$ in $f_{\text{cut}} > 0.95$.

process	cross section (PYTHIA)	correction factor	yield in the ROI
open charm	4.08×10^8 pb	3.4 ± 1.0	3.99
open bottom	5.21×10^6 pb	0.77 ± 0.39	0.44
quarkonia	9.64×10^7 pb	1.3 ± 0.23	3.34
γ^*/Z	1.13×10^4 pb	2.2 ± 0.31	1.40
exclusive Z	2.41×10^2 pb	1.4	1.31
γ^*	1.11×10^4 pb	2.2 ± 0.31	0.09
direct photon	3.80×10^6 pb	1.4	< 0.01
total			7.87
		cross section uncertainty	12 %
		MC simulation statistics	7 %
		efficiency uncertainty	17 %
		luminosity correction	10 %
		total uncertainty	24 %

Table 7.2: Cross section of muon backgrounds with PYTHIA simulation and muon yields in $16 < p_T^{\text{reco}} < 60$ GeV/ c per charge at $f > 0.95$ in the North Arm for the integrated luminosity of 24.8 pb^{-1} .

- The single hadron MC simulation assumed uniform rapidity distribution. It is necessary to re-weight η -distribution of hadronic backgrounds to fit with data, and in any case we need the help of data.
- As the main component of the hadronic backgrounds is muonic decay in-flight, the true momentum of the original hadron is mostly less than $p_T \lesssim 3$ GeV/ c and large multiple scattering is expected for both parent hadrons and their daughter muons. We do not expect significant change of η -distribution for events in $f > f_{\text{cut}}$ and for those in $f_{\text{low_cut}} < f < f_{\text{cut}}$ if $f_{\text{low_cut}}$ is sufficiently close. Thus events in the range $f_{\text{low_cut}} < f < f_{\text{cut}}$ are used as the sideband data to estimate the η -distribution of hadronic backgrounds if the contamination of the signal and muon backgrounds are small.

Figure 7.18 shows 2D distribution of η , dw_{23} and f .

- η -distribution

The η -distribution of the hadronic backgrounds were taken from events whose f -value is small. Figure 7.20 shows the η distribution of data in $0.1 < f < 0.5$ and $0.5 < f < 0.95$, and the difference of the two. As can be seen in the figure, the distribution does not change drastically by the selection of the range of f . Therefore in this analysis, we selected the region $0.1 < f < 0.90$.

- dw_{23} -distribution

As seen in Figure 7.18, the dw_{23} -distribution of data is wide at lower f and it narrows as f increases. One cause of narrowing down the width of dw_{23} -distribution as f increases comes from the geometrical limitation with the constraint of DCA_r (see Figure 7.19). The f -distribution of data in $0.10 < f < 0.95$ $p(f)$ was approximated with 4th degree polynomial function. Note that $p(f)$ is determined and fixed by 1-dimensional fitting before looking at dw_{23} distribution. The dw_{23} -distribution at the given f is modeled by coaxial double gaussian:

$$p(dw_{23}|f) \propto \text{Gaus}(dw_{23}, \mu_f, \sigma_{1,f}) + c_f \cdot \text{Gaus}(dw_{23}, \mu_f, \sigma_{2,f}) \quad (7.8)$$

where

$$\int p(dw_{23}|f)d(dw_{23}) = 1 \text{ for any } f \quad (7.9)$$

and the total PDF $p(f, dw_{23})$ is

$$p(f, dw_{23}) = p(f) \cdot p(dw_{23}|f), \quad (7.10)$$

$$\int p(f, dw_{23}) df d(dw_{23}) = \int p(f) \left[\int p(dw_{23}|f)d(dw_{23}) \right] df = 1. \quad (7.11)$$

We assumed all conditional parameters of $p(dw_{23}|f)$ of $\mu_f, \sigma_{1,f}, \sigma_{2,f}, c_f$ changes with f linearly. The distribution was filled in the 2D histogram then fitted with the above function. The contour in the center plot of Figure 7.18 is the fit result of the PDF to the data. The intersection of dw_{23} distribution for various f ranges is also shown in Figure 7.21. With these parameterization, the conditional PDF $p(dw_{23}|f)$ can be extrapolated to $f > 0.95$ region up to $f \rightarrow 1$ to give the distribution at the signal region $[f_{\text{cut}}, 1.00]$ as the conditional PDF $p(dw_{23}|f_{\text{ext}})$ where $f_{\text{ext}} = (f_{\text{cut}} + 1.00)/2$.

		$\mu_f (\times 10^{-2})$		$\sigma_{1,f} (\times 10^{-1})$		$\sigma_{2,f} (\times 10^{-2})$		c_f	
		const.	slope	const.	slope	const.	slope	const.	slope
South μ^-	value	-2.96	0.66	1.12	-0.59	5.69	-3.48	-1.53	18.4
	(error)	.37	.54	.10	.14	.65	.80	.98	8.0
South μ^+	value	2.42	-0.35	1.02	-0.72	3.28	-0.225	-0.36	6.47
	(error)	.39	.58	.05	.11	.85	1.1	.53	2.94
North μ^-	value	-2.64	0.36	1.05	-0.75	5.94	-4.10	7.34	-6.00
	(error)	.33	.50	.18	.22	.49	.69	5.88	6.33
North μ^+	value	2.84	-0.37	0.91	-0.53	5.27	-3.30	4.95	-0.62
	(error)	.30	.45	.15	.19	.59	.77	5.74	8.26

Table 7.3: Coefficients of the fitting of hadronic background dw_{23} distribution.

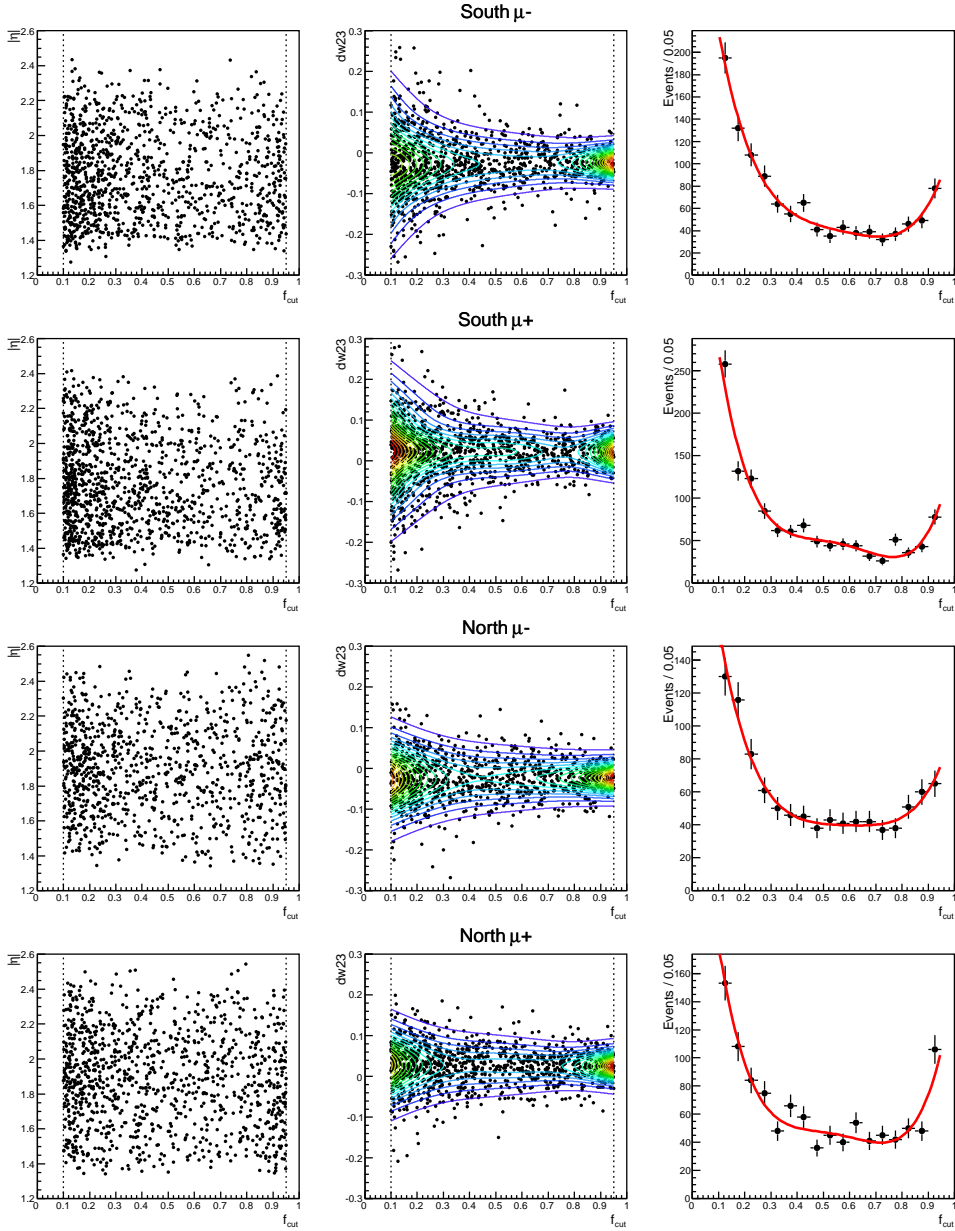


Figure 7.18: Distribution of data in $0.10 < f < 0.95$. Left: 2D distribution of η and f , Center: 2D distribution of dw_{23} and f , Right: f -distribution with fitting the distribution with 4th degree polynomial. The contour plot in the center (dw_{23}, f) distribution is the 2D fitting with a product of 4th degree polynomial and conditional double gaussian (see text).

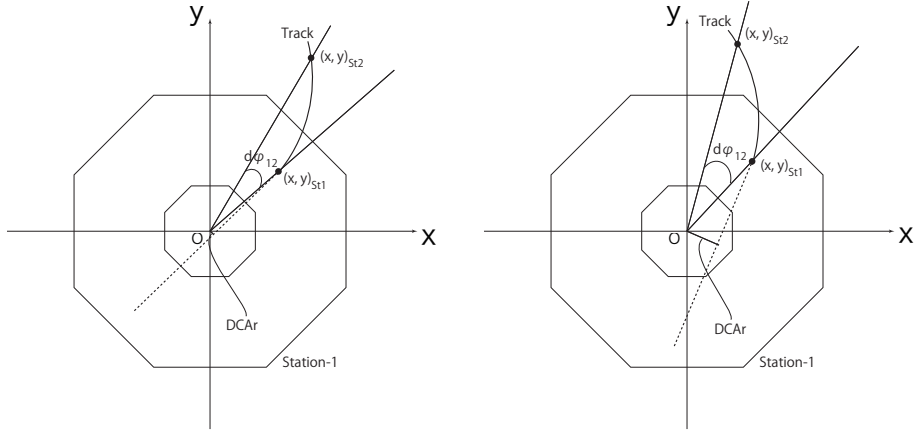


Figure 7.19: Illustration of geometrical limitation of $d\phi_{ij}$ with requirement of DCA_r . Left: the case which DCA_r is small, Right: the case which DCA_r is large. The allowed $d\phi_{12}$ angle for the given p_T is large when DCA_r is large.

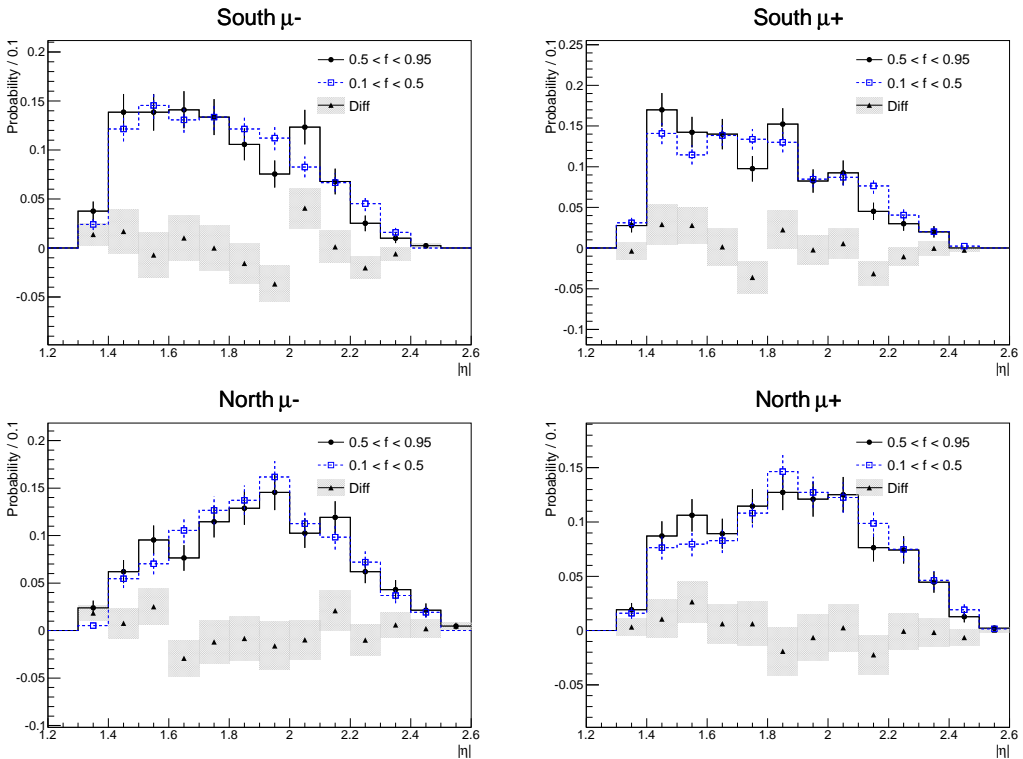


Figure 7.20: η -distribution of hadronic backgrounds.

CHAPTER 7. EXTRACTION OF $W^\pm/Z \rightarrow \mu^\pm$

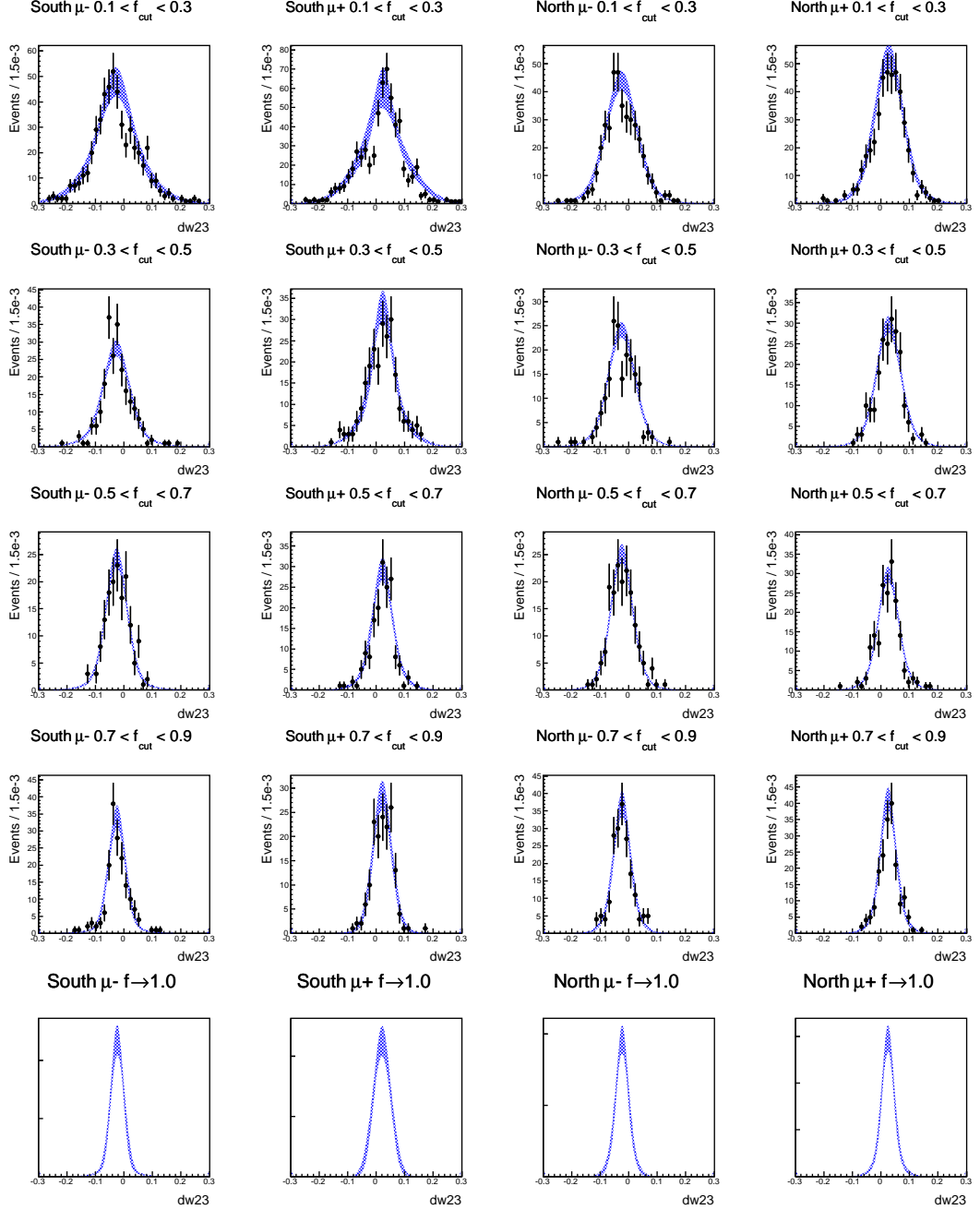


Figure 7.21: dw_{23} -distribution of hadronic backgrounds at various range of f and extrapolation to the signal region ($f \rightarrow 1$).

7.5.3 Extended unbinned maximum likelihood fitting

The extended unbinned maximum likelihood method was used to fit the PDFs to data. We denote the event set of the object of the fitting as X . Suppose X has totally N events, and denote i -th event of the object of the fitting as x_i ($i = 1, 2, \dots, N$). Each x_i in the set X satisfies the cut condition $f_i > f_{\text{cut}}$. Each event x_i is a set of variables used in the fitting. In this analysis $x_i = (\eta_i, dw_{23}^i)$. Let us denote the PDF of the process c as $p_c(x|f_{\text{cut}})$, where the argument f_{cut} explicitly denotes that the PDF for each process is determined at the specified cut threshold f_{cut} . We normalize the PDF as

$$\int p_c(x|f_{\text{cut}}) dx = \int \int p_c(x|f_{\text{cut}}) d\eta d(dw_{23}) = 1. \quad (7.12)$$

Once PDFs are determined, the unknown parameters are the number of events for each process n_c . The extended unbinned maximum likelihood method is a maximum likelihood method which takes into account of the Poisson statistics of the number of events. Then the extended unbinned likelihood function is defined as

$$\mathcal{L}(\theta|X) \equiv \frac{n^N e^{-n}}{N!} \prod_{x_i \in X}^N \left[\sum_c \frac{n_c}{n} p_c(x_i) \right], \quad n = \sum_c n_c \quad (7.13)$$

where $\theta = \{n_c\}$ is the parameter set to be fitted. Technically negative log likelihood (NLL)

$$\text{NLL} \equiv -\log(\mathcal{L}(\theta|X)) \quad (7.14)$$

is minimized to find the best estimation of the parameter set.

Specifically we consider three processes for the fitting: $W^\pm/Z \rightarrow \mu^\pm$, muon backgrounds, and hadronic backgrounds. We denote the corresponding number of events and PDF as

$$\{n_{\text{sig}}, n_\mu, n_{\text{had}}\}, \quad \{p_{\text{sig}}(x|f_{\text{cut}}), p_\mu(x|f_{\text{cut}}), p_{\text{had}}(x|f_{\text{cut}})\},$$

respectively.

In the fitting procedure we fixed n_μ to the expected yield from the cross section of muon background processes and efficiency corrections. The uncertainties of n_μ and $p_\mu(x|f_{\text{cut}})$ is systematic uncertainties for n_{sig} , and they were estimated by repeating the fitting with changing n_μ and p_μ . We used RooFit toolkits[78] and Minuit package[79] for the likelihood fitting and minimizing.

7.5.4 Results

We set the cut point at $f_{\text{cut}} = 0.92$. Table 7.4 summarizes the condition of the fitting. Under the condition, The extended unbinned maximum likelihood fitting was performed for data. The result was shown in Table 7.5 and Figure 7.22,7.23 shows the result of the extended unbinned maximum likelihood fitting.

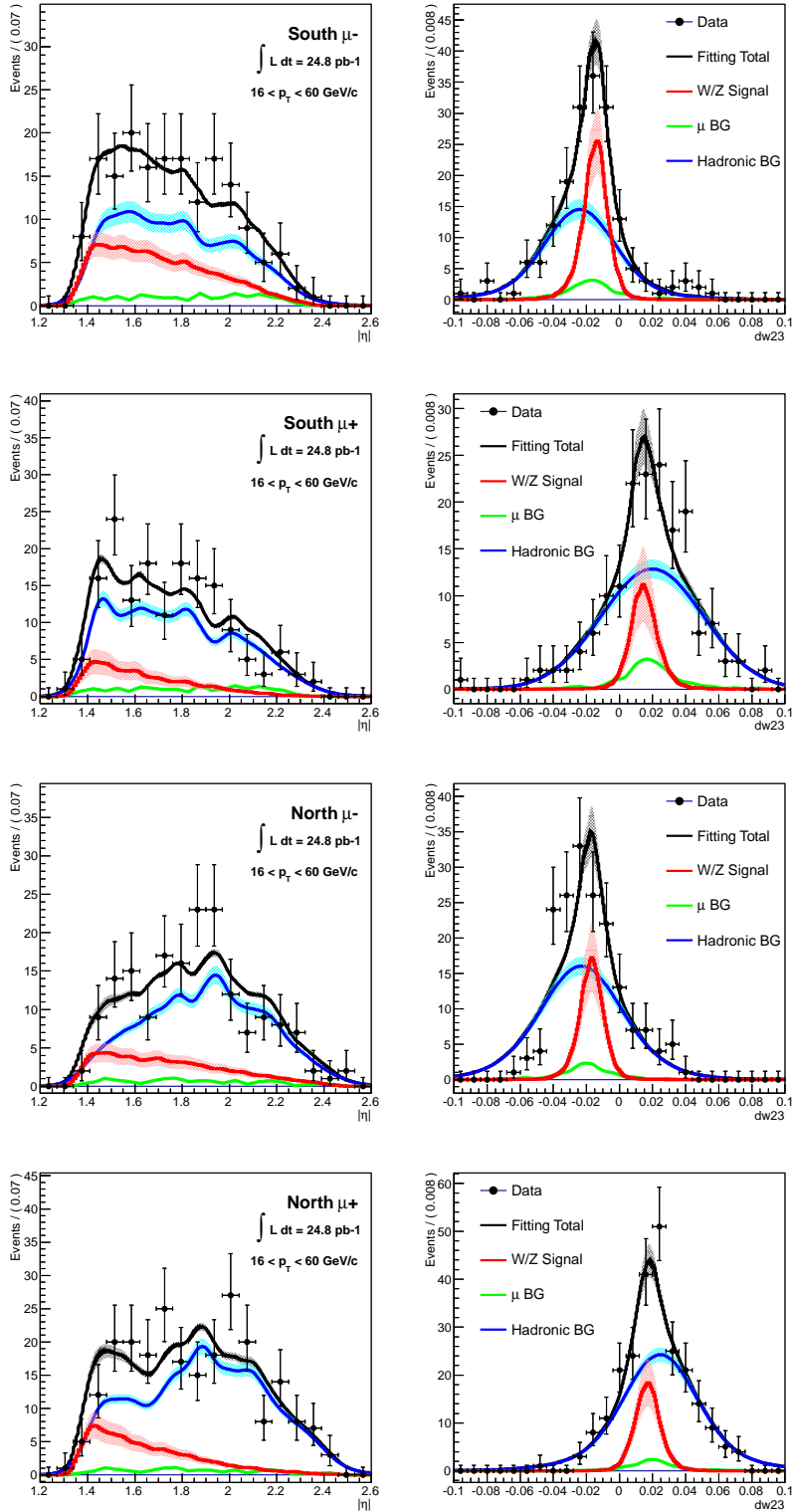


Figure 7.22: Result of the unbinned maximum likelihood fitting.

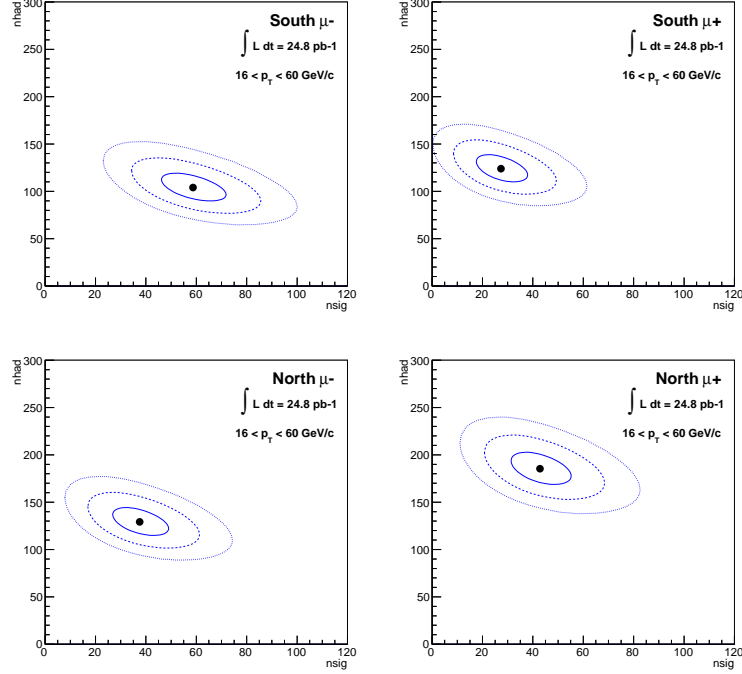


Figure 7.23: NLL contour plot of the likelihood fitting. The black bullet denotes the minimized point, and the solid, dashed, dotted line represents 1, 2, 3-sigma contour lines, respectively.

item	condition
Total runs	321
Integrated luminosity	24.8 pb ⁻¹
p_T^{reco} range	$16.0 < p_T^{\text{reco}} < 60.0 \text{ GeV}/c$
cut	$f > 0.92$
n_μ	fixed

Table 7.4: Condition of the fitting.

channel	Total data events	n_{sig} (fit)	n_{had} (fit)	n_μ (fixed)
South μ^-	176	$58.7^{+13.1}_{-12.5}$	$104.0^{+15.1}_{-14.1}$	13.4
South μ^+	165	$27.4^{+10.6}_{-9.8}$	$123.9^{+14.8}_{-13.9}$	13.6
North μ^-	176	$37.5^{+11.5}_{-10.7}$	$129.2^{+15.1}_{-14.3}$	8.9
North μ^+	238	$42.8^{+12.4}_{-11.5}$	$185.4^{+17.4}_{-16.6}$	9.1

Table 7.5: Result of the unbinned maximum likelihood fitting.

7.5.5 Acceptance and efficiency

For the given run j used to extract $W^\pm \rightarrow \mu^\pm$ candidates, we considered the following factors to calculate the acceptance and efficiency of the run:

- Geometrical acceptance, dead channels (A)
- Tracking efficiency based on MuTr and MuID hit efficiencies ($\varepsilon_{\text{track}}$)
- Plateau Mutrg-SG1 trigger efficiency ($\varepsilon_{\text{Mutrg}}$)
- MuID-1D trigger efficiency ($\varepsilon_{\text{MuID}}$)
- BBC trigger efficiency (ε_{BBC})
- RPC3 hit efficiency (ε_{RPC})
- Analysis efficiency: Basic cut, momentum selection, and preselection efficiency (ε_f) .

Then the acceptance and efficiency of the run $(A\varepsilon)_j$ was calculated by the following equation:

$$(A\varepsilon)_j \equiv \frac{\int \frac{d\sigma}{d\Omega'} (A_j \cdot \varepsilon_j) d\Omega'}{\int \frac{d\sigma}{d\Omega'} d\Omega'}, \quad (7.15)$$

$$\varepsilon_j = \varepsilon_{\text{track}}^j \cdot \left[\frac{\varepsilon_{\text{BBC}}^{\text{data}}}{\varepsilon_{\text{BBC}}^{\text{sim}}} \cdot \varepsilon_{\text{MuID}}^j \cdot \varepsilon_{\text{Mutrg}}^j \right] \cdot \varepsilon_{\text{RPC}}^j \cdot \varepsilon_f^j, \quad (7.16)$$

where $d\Omega'$ denotes phase space of the reconstructed track in p_T, η, ϕ for the reconstruction space, and $d\sigma/d\Omega'$ is the differential cross section of $W^\pm \rightarrow \mu^\pm$. We evaluated run-by-run efficiency values for $A, \varepsilon_{\text{track}}, \varepsilon_{\text{MuID}}, \varepsilon_{\text{RPC}}$, and ε_f , and we used the common efficiency values for ε_{BBC} and $\varepsilon_{\text{Mutrg}}$. The BBC trigger efficiency in the simulation was collected by the amount of the difference between the data-driven $W^\pm \rightarrow e^\pm$ efficiency and the simulated efficiency ($= \varepsilon_{\text{BBC}}^{\text{data}}/\varepsilon_{\text{BBC}}^{\text{sim}} = 0.90/0.94$). Figure 7.24 shows the scattering plot of each run in the calculated acceptance and efficiency for $W^\pm \rightarrow \mu^\pm$, and the multiple collision parameter μ .

The average acceptance and efficiency $\langle A \cdot \varepsilon \rangle$ was calculated by weighting the collected luminosity of the run by the following equation:

$$\sum_j [\mathcal{L}_j \Delta t_j (A\varepsilon)_j] = \left(\sum_j \mathcal{L}_j \Delta t_j \right) \cdot \langle A \cdot \varepsilon \rangle = L_{\text{int}} \cdot \langle A \cdot \varepsilon \rangle \quad (7.17)$$

The relative uncertainties for each item were added quadratically to calculate the uncertainty of net efficiency. Table 7.6 summarizes the average acceptance and efficiency $\langle A \cdot \varepsilon \rangle$ for each $W^\pm \rightarrow \mu^\pm$ channel. Note that these values do not contain the systematic uncertainty uncertainty of ε_f related with the MuTr position resolution, and that will be discussed in the next section.

channel	$\langle A \cdot \varepsilon \rangle$
South $W^- \rightarrow \mu^-$	$(2.48 \pm 0.41) \times 10^{-2}$
South $W^+ \rightarrow \mu^+$	$(7.56 \pm 1.26) \times 10^{-3}$
North $W^- \rightarrow \mu^-$	$(2.54 \pm 0.43) \times 10^{-2}$
North $W^+ \rightarrow \mu^+$	$(8.22 \pm 1.37) \times 10^{-3}$

Table 7.6: Summary of the average acceptance and efficiency $\langle A \cdot \varepsilon \rangle$ for runs used in this study. PYTHIA simulation was used as $W^\pm \rightarrow \mu^\pm$ process generator.

item	relative uncertainty
Acceptance fluctuation (primary vertex dist.) (A)	3.5 %
Track reconstruction efficiency ($\varepsilon_{\text{track}}$)	10 %
Trigger efficiency	
BBC trigger efficiency ($\varepsilon_{\text{BBC}}^{\text{data}}$)	5.5 %
MuID-1D trigger efficiency (ε_{1D})	6.5 %
Mutrg-SG1 trigger efficiency ($\varepsilon_{\text{Mutrg}}$)	5.5 %
RPC effieicny (ε_{RPC})	8.3 %
Total	17 %

Table 7.7: List of uncertainties of acceptance and efficiency.

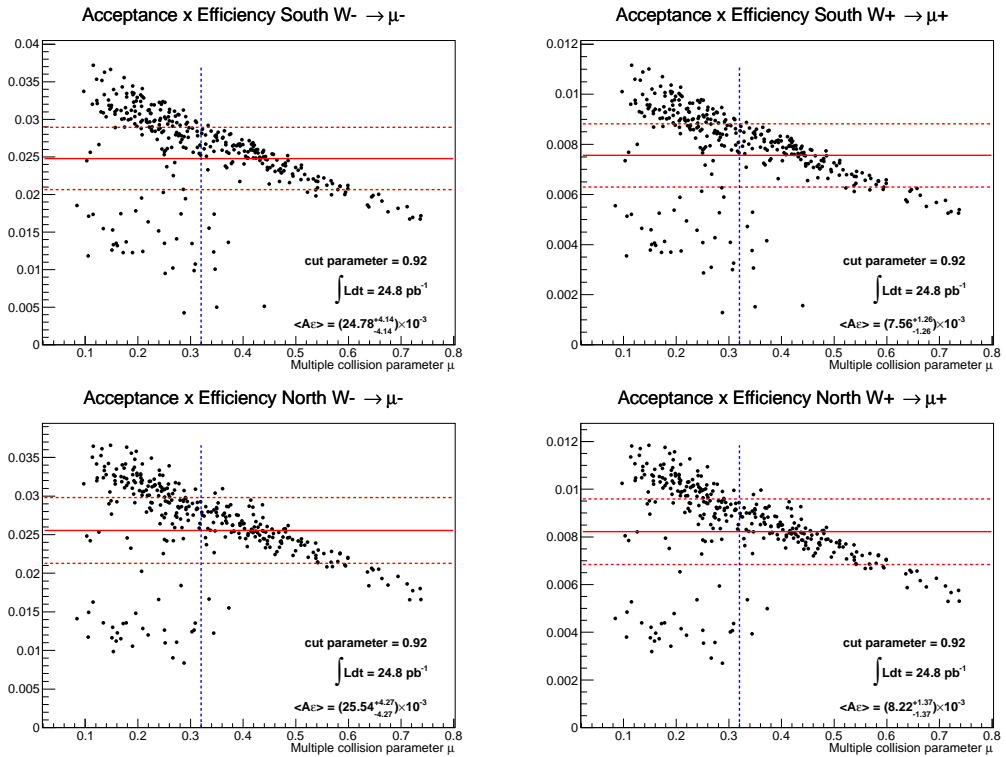


Figure 7.24: Scattering plot of run-by-run acceptance and efficiency, and multiple collision parameter. The blue dotted line indicates the average luminosity. The solid red line indicates the average acceptance, and the dashed red lines indicate the uncertainty range.

7.5.6 Systematic uncertainties

7.5.6.1 Position resolution of MuTr

The uncertainty of the position resolution of MuTr was already discussed in Sec. 6.1. Here we discuss about the systematic uncertainty of $W^\pm \rightarrow \mu^\pm$ due to this.

In our signal extraction scheme, it is considered that the uncertainty of the MuTr position resolution is propagated to the following elements:

- the preselection efficiency of the signal (ε_f),
- the PDF for the signal,
- and the muon background yield ($n_{\mu\text{BG}}$) as well as the PDF for the muon background .

Note that we need to take into account of simultaneous propagation of the MuTr position resolution uncertainty to the above elements. To evaluate the effect, we additionally created simulation samples for various tunings of the MuTr position resolution. For W^\pm and Z processes, we directly produced the full simulation with changing the noise RMS scales in the PISA simulation. Figure 7.25 illustrates the fluctuation of p_T spectrum as well as $|\eta|$ and dw_{23} distribution for $W^\pm \rightarrow \mu^\pm$ signal. For muon background processes, we produced re-smeared samples from the original background simulation samples with using the following equation:

$$\left(\frac{1}{p_T^{\text{reco}}} \right)'_\alpha = \left(\frac{1}{p_T^{\text{true}}} \right) + \alpha \left[\left(\frac{1}{p_T^{\text{reco}}} \right) - \left(\frac{1}{p_T^{\text{true}}} \right) \right] \quad (7.18)$$

where α is the ratio of the MuTr position resolution of the re-tuned RMS scale to the default in the PISA simulation. The relation between α and the RMS scale r is approximated as follows:

$$\text{South : } \alpha = 0.492 + 0.507 \times r, \quad \text{North : } \alpha = 0.482 + 0.517 \times r .$$

Table 7.8 lists the relative variation of the cross section estimation with various configurations of the noise RMS scale of the MuTr in the simulation compared to the default setting. The likelihood fitting result becomes larger for larger RMS scale, while the preselection efficiency becomes smaller. Thus these two factors work to magnify the total cross section uncertainty.

Figure 7.26 show the same estimation as a function of the simulated position resolution of the MuTr. The tendency can be approximated with a quadratic function. As discussed in Sec. 6.1, we employ asymmetric gaussian weighting with (+30, -15) % relative position resolution for the systematic uncertainty of the position resolution of MuTr. The weighting is also shown in Figure 7.26. The propagated relative cross section uncertainty distribution is shown in Figure 7.26, and the corresponding 68 % error interval is listed in Table 7.10.

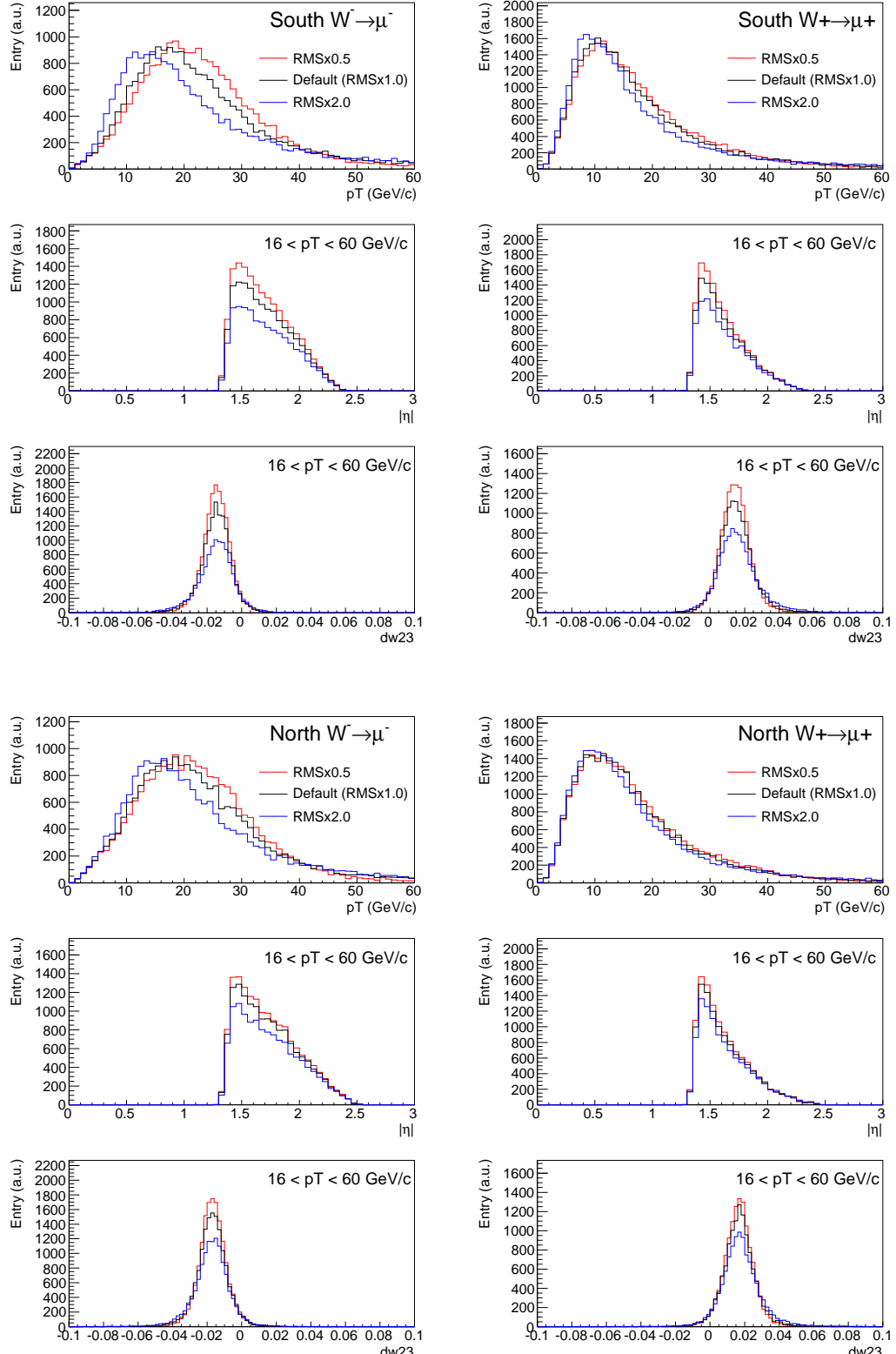


Figure 7.25: Simulated p_T , $| \eta |$, and dw_{23} distribution of $W^\pm \rightarrow \mu^\pm$ at the basic cut with different tunes of MuTr noise scale.

CHAPTER 7. EXTRACTION OF $W^\pm/Z \rightarrow \mu^\pm$

RMS scale	South μ^-			South μ^+			North μ^-			North μ^+		
	fit	ε_f	total									
0.5	0.94	1.17	0.80	0.92	1.14	0.80	0.96	1.11	0.87	0.97	1.10	0.88
0.6	0.94	1.14	0.82	0.92	1.15	0.81	0.96	1.10	0.99	0.96	1.11	0.86
0.8	0.94	1.08	0.87	0.90	1.09	0.83	0.94	1.05	0.90	0.96	1.07	0.89
1.0	1.00	1.00	1.00	1.00	1.00	1.00	1.00	1.00	1.00	1.00	1.00	1.00
1.2	1.02	0.94	1.09	1.07	0.97	1.10	1.04	0.97	1.07	1.04	0.98	1.07
1.4	1.10	0.87	1.26	1.16	0.91	1.28	1.09	0.92	1.19	1.10	0.94	1.18
1.6	1.16	0.82	1.42	1.24	0.86	1.44	1.12	0.85	1.30	1.13	0.90	1.26
1.8	1.19	0.76	1.57	1.29	0.81	1.60	1.13	0.82	1.38	1.13	0.85	1.32
2.0	1.22	0.72	1.70	1.38	0.76	1.81	1.13	0.77	1.47	1.15	0.82	1.40

Table 7.8: Estimation of relative cross section deviation for various configuration of the simulated position resolution of MuTr compared to the default. The total value is defined as the fitting value divided by preselection efficiency ε_f .

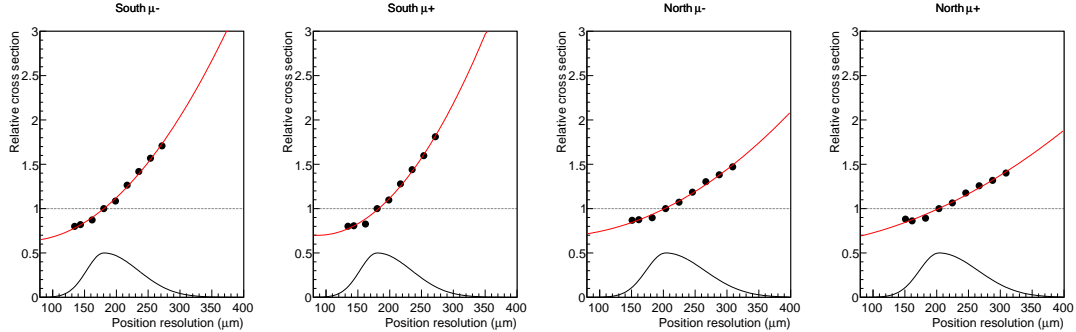


Figure 7.26: Relative cross section measurement deviation as a function of the simulated position resolution of the MuTr. The red line is the fitting of plotted values with a quadratic function. The black line is the weighting of the systematic uncertainty of the position resolution of the MuTr with arbitrary scale.

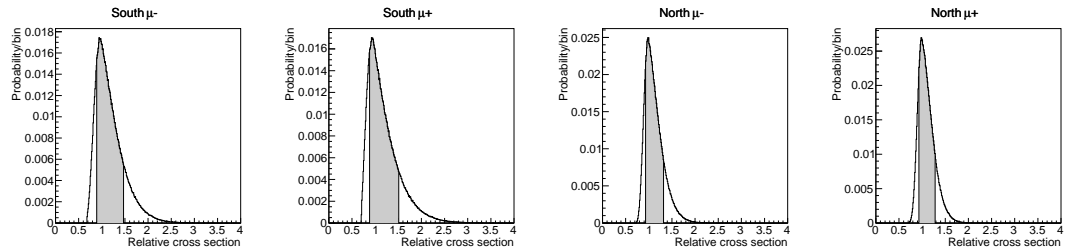


Figure 7.27: Distribution of relative cross section uncertainty due to the position resolution uncertainty of the MuTr. The gray band shows the range of 68 % interval listed in Table 7.10.

South μ^-	South μ^+	North μ^-	North μ^+
+46 %	+50 %	+31 %	27 %
-11	-12	-7	-7

Table 7.9: Relative systematic cross section error (68 %) due to the uncertainty of the MuTr position resolution.

7.5.6.2 PDF of hadronic backgrounds

dw_{23} -distribution As described in Sec. 7.5.2, we set the target f -value of the extrapolation of dw_{23} -distribution of hadronic backgrounds at $f_{\text{ext}} = (f_{\text{cut}} + 1.00)/2 = 0.96$ (where $f_{\text{cut}} = 0.92$). We assumed that the parameters of dw_{23} distribution of the hadronic background change linearly as a function of f . At least this assumption is fair for low- f region. However, there is no assurances that this is also valid for the signal region. For this issue we refer the single hadron simulation result. Figure 7.28 shows the RMS value of dw_{23} distribution for the hadronic background as a function of f in the simulation. The hatched region is the signal region used in this analysis. The blue level is the RMS value of dw_{23} in the signal region. The RMS value decreases almost linearly below the signal region, but it drastically decreases in the signal region. If we rely on the simulation, the data-driven estimation of dw_{23} distribution we employed would overestimate the width of dw_{23} distribution. In this case, we would overestimate signal yield. For this reason we also take larger f_{ext} values than 1.00 into the range of systematic uncertainty of the estimation of dw_{23} distribution. On the other hand, the possibility to have too-sharp dw_{23} distribution than the actual at $f_{\text{ext}} = 0.96$ would be small. Therefore we take asymmetric gaussian systematic weighting of $f_{\text{ext}} = 0.96^{+0.10}_{-0.02}$ for estimating the systematic uncertainty. Figure 7.29 shows the relative difference of the cross section by changing f_{ext} for the hadronic background's dw_{23} distribution. The relation between the cross section deviation and the choice of f_{ext} was approximated with a linear function, and the uncertainty of f_{ext} was propagated to the cross section error. Figure 7.30 shows the result.

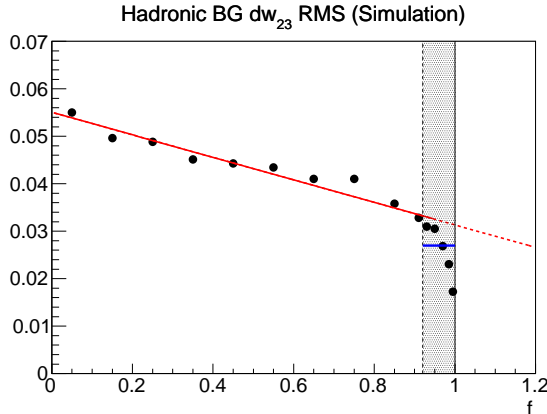


Figure 7.28: The RMS value of dw_{23} distribution for the hadronic background as a function of f in the simulation. The black bullets are data points in the simulation.

South μ^-	South μ^+	North μ^-	North μ^+
+0.0 % -31 %	+0.0 % -13 %	+0.0 % -39 %	0.0 % -31 %

Table 7.10: Relative systematic cross section error (68 %) due to the estimation of dw_{23} distribution of hadronic backgrounds.

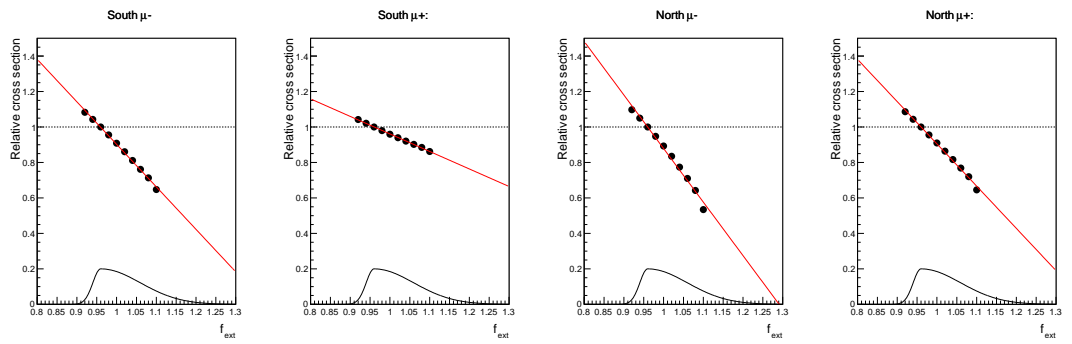


Figure 7.29: Relative cross section measurement deviation as a function of the assumed f_{ext} value for estimating the dw_{23} distribution of hadronic backgrounds. The red line is the fitting of plotted values with a linear function. The black line is the weighting of the systematic uncertainty with asymmetric gaussian of $f_{\text{ext}} = 0.96^{+0.10}_{-0.02}$.

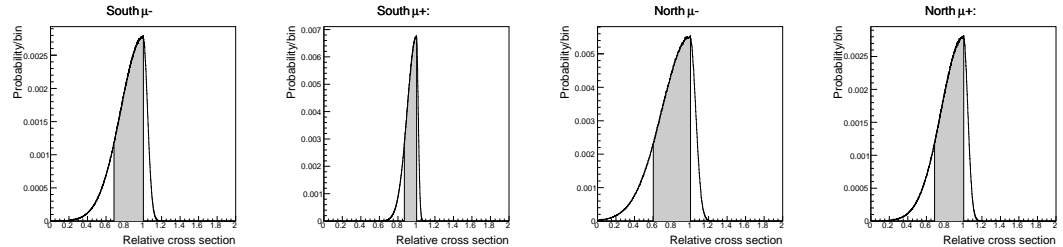


Figure 7.30: Distribution of relative cross section uncertainty due to the estimation of dw_{23} distribution of hadronic backgrounds. The gray band shows the range of 68 % interval.

η -distribution The similar arguments as dw_{23} -distribution is possible also for η -distribution. As discussed in Sec 7.5.2, we do not expect the η -distribution of hadronic background depends on the selection of the sideband range, but contamination of signal and muon backgrounds would affect to the estimation of the distribution. Table 7.11 summarizes the fitting result for changing the range of the sample. The absolute maximum deviation from the original fitting was assigned as systematic uncertainty.

7.5.6.3 Signal shape uncertainty

The signal PDF was estimated using the PYTHIA6 leading order event generator with the CTEQ5L PDF set. We also tried to use CHE next-to-leading order event generator with MRST02 PDF set for $W^\pm \rightarrow \mu^\pm$ process, and we took the difference of the cross section measurement as the systematic uncertainty of the signal shape due to theoretical uncertainty. Table 7.12 shows the relative cross section difference between the calculation with CHE and the default (PYTHIA). We regard this difference is minor, and we concluded the theoretical uncertainty does not affect the final cross section measurement.

7.5.6.4 Muon background uncertainties

We assumed the fixed muon background yield at the expected number of events in the fitting. The following uncertainties of muon backgrounds is taken as systematics. As the uncertainty of the muon background yield due to the uncertainty of the MuTr was already discussed in Sec. 7.5.6.1, here we discuss about the remaining uncertainties. Table 7.13 summarizes the list of systematic uncertainties about muon backgrounds.

Statistics We randomly changed the fixed yield around the expected value assuming Poisson statistics and set the error.

Cross section error (relative) We reflected the error of cross section measurement to the weighting of muon backgrounds with taking account of the correlation of the fitting error of the dimuon mass spectrum in Appendix A. Note that this error is associated to the relative determination of muon background processes in dimuon data, and this does not contain the uncertainty of efficiencies.

Cross section error (normalization) The error of acceptance & efficiency in measuring dimuon cross sections is propagated to the error of the yield of muon backgrounds. Note that the luminosity error is not considered as it is fully correlated for both dimuon analysis and this analysis. Note that for the final cross section measurement of $W^\pm \rightarrow \mu^\pm$, only the error for the product of (single) MuID-1D trigger efficiency, the (single) track reconstruction efficiency, and RPC efficiency is considered. The reason that the acceptance & efficiency error does not fully compensate is that the dimuon events have two reconstructed tracks, while this study uses single muon events.

Statistics of MC samples Statistics of MC samples would change the shape of PDF. The number of events in the bin of the histogram was randomly changed by the size of the statistic error of the bin for each muon background process.

channel	f_{\min}	f_{\max}	n_{sig}	n_{had}	n_μ (fixed)	comment
South μ^-	0.10	0.98	$58.2^{+13.1}_{-12.5}$	$104.5^{+15.2}_{-14.1}$		
	0.10	0.90	$62.7^{+13.0}_{-12.4}$	$99.9^{+14.7}_{-13.7}$		default
	0.10	0.80	$58.6^{+13.1}_{-12.4}$	$104.1^{+15.1}_{-14.1}$		
	0.10	0.60	$59.1^{+13.1}_{-12.4}$	$103.6^{+15.0}_{-14.3}$		
South μ^+	0.10	0.98	$26.7^{+10.6}_{-9.8}$	$124.6^{+14.8}_{-14.0}$		
	0.10	0.90	$28.0^{+10.6}_{-9.8}$	$123.3^{+14.7}_{-13.8}$		default
	0.10	0.80	$27.7^{+10.6}_{-9.8}$	$123.6^{+14.7}_{-13.8}$		
	0.10	0.60	$28.1^{+10.6}_{-9.8}$	$123.2^{+14.7}_{-13.8}$		
North μ^-	0.10	0.98	$36.4^{+11.5}_{-10.7}$	$130.4^{+15.2}_{-14.3}$		
	0.10	0.90	$35.3^{+11.5}_{-10.7}$	$131.5^{+15.3}_{-14.4}$		default
	0.10	0.80	$37.4^{+11.5}_{-10.7}$	$129.3^{+15.2}_{-15.1}$		
	0.10	0.60	$37.9^{+11.4}_{-10.6}$	$128.9^{+15.0}_{-14.2}$		
North μ^+	0.10	0.98	$41.3^{+12.3}_{-11.5}$	$186.9^{+17.5}_{-16.7}$		
	0.10	0.90	$43.0^{+12.3}_{-11.4}$	$185.3^{+17.3}_{-16.5}$		default
	0.10	0.80	$44.6^{+12.3}_{-11.4}$	$183.6^{+17.2}_{-16.4}$		
	0.10	0.60	$45.7^{+12.3}_{-11.5}$	$182.4^{+17.2}_{-16.4}$		
Summary	error					
South μ^-	$\pm 7\%$					
South μ^+	$\pm 5\%$					
North μ^-	$\pm 4\%$					
North μ^+	$\pm 6\%$					

Table 7.11: Variation of fitting result with changing the selection of sideband data for determining η -distribution of hadronic background.

South W^-	South W^+	North W^-	North W^+
3 %	3 %	1 %	5 %

Table 7.12: Relative difference of the cross section estimation of the CHE NLO event generator with the MRT02 PDF set compared to the default PYTHIA LO event generator.

uncertainty	South μ^-	South μ^+	North μ^-	North μ^+
Statistics	$\pm 3\%$	$\pm 6\%$	$\pm 5\%$	$\pm 3\%$
MC sample stat.	$\pm 1\%$	$\pm 2.2\%$	$\pm 1.6\%$	$\pm 1\%$
Relative cross section	$\pm 1\%$	$\pm 1.7\%$	$\pm 1.2\%$	$\pm 1\%$
Acceptance & eff. for muon backgrounds	$\pm 3\%$	$\pm 5\%$	$\pm 4\%$	$\pm 3\%$

Table 7.13: Summary of relative systematic uncertainties related with muon backgrounds.

7.6 Cross section of $W^\pm \rightarrow \mu^\pm$

The total cross section of $W^\pm \rightarrow \mu^\pm$ was calculated with the following equation:

$$\sigma(pp \rightarrow W) \times \mathcal{BR}(W \rightarrow \mu) = \frac{1}{L_{\text{int}}} \frac{n_{\text{sig}}(1 - f_Z)}{\langle A \cdot \varepsilon \rangle} \quad (7.19)$$

where f_Z is the fraction of $Z \rightarrow \mu^\pm$ in the signal ($f_Z \equiv n_Z/(n_W + n_Z)$). The estimation of f_Z with the PYTHIA + PISA simulation is shown in Table 7.14.

The total uncertainty of the cross section after including the statistical uncertainty and the all systematic uncertainties considered was estimated with composing a MC sampling for randomly varying values by the amount of their uncertainties. We employ the combined result of both South and North Arm cross section measurements as the final result. Therefore we need to take into account of the correlation of systematic uncertainties between the South and North Arms. Table 7.15 lists the degree of freedom allowed to be varied to estimate the total cross section uncertainty. With these conditions, the MC generates a set of cross sections (σ_S, σ_N) simultaneously for each try where $\sigma_S(\sigma_N)$ denotes the South (North) Arm cross section. We generated 10^7 samples for both W^+ and W^- cross sections. By projecting the 2D distribution to σ_S or σ_N axis, we obtain the likelihood for the individual Arm's measurement, $\lambda_S(\sigma)$ and $\lambda_N(\sigma)$. The combined likelihood $\lambda(\sigma)$ is defined as follows:

$$\lambda(\sigma) = \lambda_S(\sigma) \cdot \lambda_N(\sigma | \sigma_S = \sigma) \quad (7.20)$$

where the second factor means the likelihood of the North Arm cross section under the condition that $\sigma_S = \sigma$. We quote the 68 % confidence interval with excluding both side 16 % of the likelihood distribution of the total integral as the measurement result.

South μ^-	South μ^+	North μ^-	North μ^+
7.6 %	7.2 %	7.8 %	7.8 %

Table 7.14: Expected fraction of $Z \rightarrow \mu^\pm$ events (f_Z) in the signal.

Category	Item	Arm corr.	Error dist.
A	Statistical uncertainties	No	asymmetric gaussian
B	MuTr position resolution	Yes	special (see Sec. 7.5.6.1)
	Hadronic BG PDF (dw_{23})	No	special (see Sec. 7.5.6.2)
	Hadronic BG PDF (η)	No	gaussian
	Muon BG statistics	No	gaussian
	Muon BG cross section error (relative)	Yes	gaussian
	Muon BG cross section error (norm.)	Yes	gaussian
	Muon BG MC statistics	No	gaussian
C	Acceptance and efficiency ($\langle A\varepsilon \rangle$)	Yes	gaussian (for denominator)
D	Integrated luminosity (L_{int})	Yes	gaussian (for denominator)

Table 7.15: List of statistic and systematic uncertainties which are varied independently in estimating the total cross section uncertainty in the MC sampling.

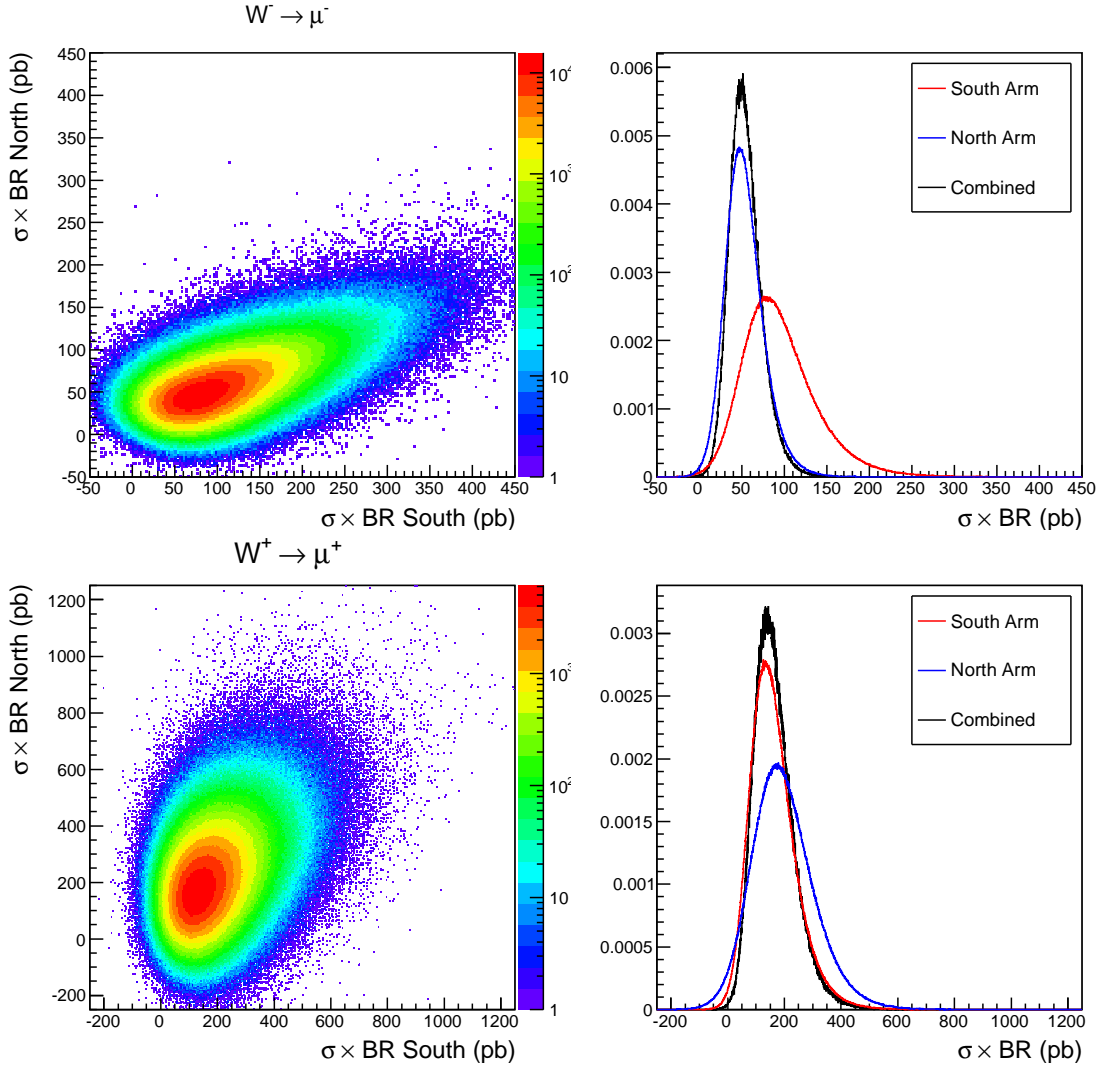


Figure 7.31: Likelihood distribution of $W^\pm \rightarrow \mu^\pm$ cross section measurement. All statistical and systematic uncertainties (category A,B,C,D in Table 7.15) are taken into account. The 2D histogram (the left panel) shows the correlation of likelihood between the South and North Arms. The 1D plot (the right panel) shows the projection of the 2D likelihood to the South or North axis for individual measurements (the red and blue histograms) as well as the combined likelihood (the black histogram).

Result

Table 7.16 summarizes the result of total cross section measurement for each Arm individually. Also, Table 7.17 summarizes the result of the combined cross section measurement. The values with taking all statistic and systematic uncertainties (A+B+C+D) are the final result. As the final result of the combined measurement, we obtained $47.8^{+25.0}_{-11.8}$ pb for $\sigma(pp \rightarrow W^-) \times \mathcal{BR}(W^- \rightarrow \mu^-)$ and $129.5^{+102.0}_{-33.5}$ pb for $\sigma(pp \rightarrow W^+) \times \mathcal{BR}(W^+ \rightarrow \mu^+)$, where the central values are the most probable values of the combined likelihood distribution. In case of combined measurements, the integral of likelihood distribution below zero to the total likelihood integral was 2.9×10^{-4} for $W^- \rightarrow \mu^-$ and 1.3×10^{-3} for $W^+ \rightarrow \mu^+$, respectively. If we regard these numbers in manner of standard deviation, these numbers correspond to 3.6σ and 3.2σ , respectively. We discuss about the significance of the $W^\pm \rightarrow \mu^\pm$ signal a little more in detail in Chapter 9. Table 7.18 summarizes the final result of the cross section measurement.

Taken uncertainties	South W^-	South W^+	North W^-	North W^+
A (stats only)	$88.2^{+19.8}_{-18.7}$	$54.6^{+10.9}_{-9.9}$	$136.3^{+52.2}_{-48.8}$	$196.8^{+86.2}_{-82.8}$
A+B	[55.5, 126.2] (mpv: 83.6)	[32.5, 69.8] (mpv: 51.1)	[86.5, 223.0] (mpv: 139.2)	[91.5, 285.0] (mpv: 189.8)
A+B+C	[54.2, 133.0] (mpv: 77.3)	[31.8, 73.5] (mpv: 47.5)	[85.0, 234.0] (mpv: 129.9)	[90.5, 297.0] (mpv: 168.4)
A+B+C+D	[54.0, 135.2] (mpv: 75.3)	[31.5, 75.0] (mpv: 46.7)	[84.5, 237.5] (mpv: 126.3)	[90.0, 301.5] (mpv: 165.0)

Table 7.16: Result of cross section of $W^\pm \rightarrow \mu^\pm$ for each Arm individually with various inclusions of uncertainty categories in Table 7.15. Units are in (pb). The 68 % confidence interval as well as the most probable value is listed other than statistics only values. The 68 % confidence interval was determined to exclude both side 16 % regions.

Taken uncertainties	W^-	W^+
A (stats only)	$67.2^{+9.3}_{-9.2}$	$152.1^{+44.9}_{-42.1}$
A+B	[29.0, 69.8] (mpv: 53.9)	[102.5, 225.5] (mpv: 144.5)
A+B+C	[36.8, 71.8] (mpv: 49.3)	[97.5, 230.0] (mpv: 132.8)
A+B+C+D	[36.0, 72.8] (mpv: 47.8)	[96.0, 231.5] (mpv: 129.5)

Table 7.17: Result of cross section of $W^\pm \rightarrow \mu^\pm$ for combining both Arm measurements with various inclusions of uncertainty categories in Table 7.15.

channel	$\sigma(pp \rightarrow W) \times \mathcal{BR}(W \rightarrow \mu)$ (pb)
$W^- \rightarrow \mu^-$ combined	$47.8^{+25.0}_{-11.8}$ (68 % C.L.)
South Arm	$75.3^{+59.9}_{-21.3}$ (68 % C.L.)
North Arm	$46.7^{+28.3}_{-15.2}$ (68 % C.L.)
$W^+ \rightarrow \mu^+$ combined	$129.5^{+102.0}_{-33.5}$ (68 % C.L.)
South Arm	$126.3^{+111.2}_{-41.8}$ (68 % C.L.)
North Arm	$165.0^{+136.5}_{-75.0}$ (68 % C.L.)

Table 7.18: Result of total cross section measurement and of $W^\pm \rightarrow \mu^\pm$ in this study. The central value is the most probable value after taking account of both statistical and systematic uncertainties, and the uncertainty range was determined to exclude 16 % of the likelihood distribution of both sides to the total integral.

Chapter 8

Measurement of longitudinal single spin asymmetry of $W^\pm/Z \rightarrow \mu^\pm$

8.1 Introduction

In this chapter we measure the longitudinal spin asymmetry of $W^\pm/Z \rightarrow \mu^\pm$. We call the beam which the spin asymmetry is measured as “probe”, and the other side beam as “target”. The longitudinal single spin asymmetry is defined as

$$A_L(\eta_\mu) = \frac{d\sigma^{\Rightarrow} - d\sigma^{\Leftarrow}}{d\sigma^{\Rightarrow} + d\sigma^{\Leftarrow}} \Big|_{\eta_\mu} \quad (8.1)$$

where the arrow denotes the helicity of the polarized proton (“ \Rightarrow ” denotes positive helicity and “ \Leftarrow ” denotes negative helicity), and pseudorapidity of muon η_μ is defined with taking the z -axis to the direction of the momentum of the probe-side beam. Namely in case of focusing on the polarization of the Blue beam η_μ is taken as the same as the PHENIX coordinate system, but in case of the Yellow beam the sign of η_μ is opposite. We attempt to combine the measurement of the two Arms with assuming the biasing of the measurement in two Arms to the η -distribution of the signal does not differ largely. Let us denote the spin asymmetry in forward ($\eta_\mu > 0$) and backward ($\eta_\mu < 0$) pseudorapidity as $A_L^{\eta_\mu > 0}, A_L^{\eta_\mu < 0}$, respectively. We also define longitudinal double spin asymmetry A_{LL} as

$$A_{LL}(\eta_\mu) = \frac{d\sigma^{\Rightarrow\Rightarrow} - d\sigma^{\Leftarrow\Leftarrow}}{d\sigma^{\Rightarrow\Rightarrow} + d\sigma^{\Leftarrow\Leftarrow}} \Big|_{\eta_\mu} \quad (8.2)$$

where the first arrow denotes the polarization of the probe-side beam and the second denotes that of the target-side beam. Again the rapidity η_μ is defined with respect to the probe-side beam, however due to the symmetry we have $A_{LL}(\eta_\mu) = A_{LL}(-\eta_\mu)$ and the sign of η_μ does not matter. Hereafter we alternatively use “+” as positive helicity state and “-” for negative.

We have four spin combinations in beam collisions as $(s_B, s_Y) = \{++, +-, -+, --\}$ where the first sign denotes the helicity of the Blue beam and the second denotes that of the Yellow beam. We denote the number of signal candidates after signal selection for each spin combination for each arm as

$$\left\{ n_{(++)}^S, n_{(+-)}^S, n_{(-+)}^S, n_{(--)}^S \right\}, \left\{ n_{(++)}^N, n_{(+-)}^N, n_{(-+)}^N, n_{(--)}^N \right\}$$

CHAPTER 8. MEASUREMENT OF LONGITUDINAL SINGLE SPIN ASYMMETRY OF $W^\pm/Z \rightarrow \mu^\pm$

where the index S, N denotes the South and North Arm, respectively. We call these numbers as *observables* in this chapter. We denote the total number of signals and backgrounds summing up all spin patterns as $n_{\text{sig}}^{S,N}$, $n_{\text{BG}}^{S,N}$, respectively, and denote the polarization of the Blue and Yellow beam as P_B, P_Y , respectively. As the background events do not have spin asymmetries, the relation between spin asymmetries and the observables are expressed as

$$n_{(++)}^N = [(1 + A_L^{\eta>0} P_B + A_L^{\eta<0} P_Y + A_{LL} P_B P_Y) n_{\text{sig}}^N + n_{\text{BG}}^N] \cdot L_{(++)}/L_0 \quad (8.3)$$

$$n_{(+ -)}^N = [(1 + A_L^{\eta>0} P_B - A_L^{\eta<0} P_Y - A_{LL} P_B P_Y) n_{\text{sig}}^N + n_{\text{BG}}^N] \cdot L_{(+ -)}/L_0 \quad (8.4)$$

$$n_{(- +)}^N = [(1 - A_L^{\eta>0} P_B + A_L^{\eta<0} P_Y - A_{LL} P_B P_Y) n_{\text{sig}}^N + n_{\text{BG}}^N] \cdot L_{(- +)}/L_0 \quad (8.5)$$

$$n_{(--)}^N = [(1 - A_L^{\eta>0} P_B - A_L^{\eta<0} P_Y + A_{LL} P_B P_Y) n_{\text{sig}}^N + n_{\text{BG}}^N] \cdot L_{(--)}/L_0 \quad (8.6)$$

and

$$n_{(++)}^S = [(1 + A_L^{\eta<0} P_B + A_L^{\eta>0} P_Y + A_{LL} P_B P_Y) n_{\text{sig}}^S + n_{\text{BG}}^S] \cdot L_{(++)}/L_0 \quad (8.7)$$

$$n_{(+ -)}^S = [(1 + A_L^{\eta<0} P_B - A_L^{\eta>0} P_Y - A_{LL} P_B P_Y) n_{\text{sig}}^S + n_{\text{BG}}^S] \cdot L_{(+ -)}/L_0 \quad (8.8)$$

$$n_{(- +)}^S = [(1 - A_L^{\eta<0} P_B + A_L^{\eta>0} P_Y - A_{LL} P_B P_Y) n_{\text{sig}}^S + n_{\text{BG}}^S] \cdot L_{(- +)}/L_0 \quad (8.9)$$

$$n_{(--)}^S = [(1 - A_L^{\eta<0} P_B - A_L^{\eta>0} P_Y + A_{LL} P_B P_Y) n_{\text{sig}}^S + n_{\text{BG}}^S] \cdot L_{(--)}/L_0 \quad (8.10)$$

where $L_{(\pm\pm)}$ denotes the integrated luminosity of the corresponding spin combination and L_0 is the total integrated luminosity. Note that the single spin asymmetry which couples to the beam polarization is replaced each other between the South and the North Arm. We define the ratio $r_{(\pm\pm)} \equiv L_{(\pm\pm)}/L_0$ as the *relative luminosity* of the corresponding spin combination. Trivially the following relation holds:

$$\sum_{s_B=\pm} \sum_{s_Y=\pm} r_{(s_B s_Y)} = 1. \quad (8.11)$$

We define corrected yield as $\tilde{n}_{(\pm\pm)}^{S,N} \equiv n_{(\pm\pm)}^{S,N}/r_{(\pm\pm)}$.

The *observed* or *raw* spin asymmetries are defined as follows:

$$\epsilon_{L,S}^{\eta>0} \equiv \left[\frac{\tilde{n}_{(++)}^S - \tilde{n}_{(+ -)}^S + \tilde{n}_{(- +)}^S - \tilde{n}_{(--)}^S}{\tilde{n}_{(++)}^S + \tilde{n}_{(+ -)}^S + \tilde{n}_{(- +)}^S + \tilde{n}_{(--)}^S} \right] \quad (8.12)$$

$$\epsilon_{L,S}^{\eta<0} \equiv \left[\frac{\tilde{n}_{(++)}^S + \tilde{n}_{(+ -)}^S - \tilde{n}_{(- +)}^S - \tilde{n}_{(--)}^S}{\tilde{n}_{(++)}^S + \tilde{n}_{(+ -)}^S + \tilde{n}_{(- +)}^S + \tilde{n}_{(--)}^S} \right] \quad (8.13)$$

$$\epsilon_{LL,S} \equiv \left[\frac{\tilde{n}_{(++)}^S - \tilde{n}_{(+ -)}^S - \tilde{n}_{(- +)}^S + \tilde{n}_{(--)}^S}{\tilde{n}_{(++)}^S + \tilde{n}_{(+ -)}^S + \tilde{n}_{(- +)}^S + \tilde{n}_{(--)}^S} \right] \quad (8.14)$$

$$\epsilon_{L,N}^{\eta>0} \equiv \left[\frac{\tilde{n}_{(++)}^N + \tilde{n}_{(+ -)}^N - \tilde{n}_{(- +)}^N - \tilde{n}_{(--)}^N}{\tilde{n}_{(++)}^N + \tilde{n}_{(+ -)}^N + \tilde{n}_{(- +)}^N + \tilde{n}_{(--)}^N} \right] \quad (8.15)$$

$$\epsilon_{L,N}^{\eta<0} \equiv \left[\frac{\tilde{n}_{(++)}^N - \tilde{n}_{(+ -)}^N + \tilde{n}_{(- +)}^N - \tilde{n}_{(--)}^N}{\tilde{n}_{(++)}^N + \tilde{n}_{(+ -)}^N + \tilde{n}_{(- +)}^N + \tilde{n}_{(--)}^N} \right] \quad (8.16)$$

$$\epsilon_{LL,N} \equiv \left[\frac{\tilde{n}_{(++)}^N - \tilde{n}_{(+ -)}^N - \tilde{n}_{(- +)}^N + \tilde{n}_{(--)}^N}{\tilde{n}_{(++)}^N + \tilde{n}_{(+ -)}^N + \tilde{n}_{(- +)}^N + \tilde{n}_{(--)}^N} \right] \quad (8.17)$$

These observed spin asymmetries are related with $A_L^{\eta>0}, A_L^{\eta<0}, A_{LL}$ as

$$A_L^{\eta>0} = \frac{D^N}{P_B} \epsilon_{L,N}^{\eta>0} = \frac{D^S}{P_Y} \epsilon_{L,S}^{\eta>0} \quad (8.18)$$

$$A_L^{\eta<0} = \frac{D^N}{P_B} \epsilon_{L,N}^{\eta<0} = \frac{D^S}{P_Y} \epsilon_{L,S}^{\eta<0} \quad (8.19)$$

$$A_{LL} = \frac{D^N}{P_B P_Y} \epsilon_{LL,N} = \frac{D^S}{P_B P_Y} \epsilon_{LL,S} \quad (8.20)$$

where

$$D^{S,N} \equiv \frac{n_{\text{sig}}^{S,N} + n_{\text{BG}}^{S,N}}{n_{\text{sig}}^{S,N}} \quad (8.21)$$

is called *dilution factor* by means of diluting the *observed* or *raw* spin asymmetries. Therefore we can calculate these spin asymmetries with knowing the following parameters:

- Dilution factor D^S, S^N
- Beam polarization P_B, P_Y
- Relative luminosity $r_{(\pm\pm)}$

We start with the combined measurement result of the cross section of $W^\pm/Z \rightarrow \mu^\pm$ given in the previous chapter.

8.2 Dilution factor

The dilution factor is preferable to be as small as possible to gain the sensitivity to the spin asymmetries, while the statistical uncertainty increases if we impose too tight signal selection. Therefore we search the optimal point of the signal selection for the given integrated luminosity, and evaluate the dilution factor for the optimized signal selection. Here we omit the Arm label S, N for simplicity.

8.2.1 Signal selection and signal efficiency

We attempt to increase the purity of the signal using the (η, dw_{23}) PDFs. We define the likelihood ratio of the event x_i as

$$\lambda'(x_i) \equiv \frac{p_{\text{sig}}(x_i)}{p_{\text{sig}}(x_i) + p_\mu(x_i) + p_{\text{had}}(x_i)} \quad (8.22)$$

where PDFs are given at the preselection $f > f_{\text{cut}} = 0.92$, and we compose the second cut parameter

$$f'(x_i) \equiv f(x_i) \cdot \lambda'(x_i) \quad (8.23)$$

to select event candidates. Here we define four signal numbers:

- n_{sig}^0 : Total expected number of signals produced
- $n_{\text{sig}}^{\text{reco}}$: Total reconstructed number of signals
- $n_{\text{sig}}^{\text{pre}}$: Number of signals remaining after the preselection using f

CHAPTER 8. MEASUREMENT OF LONGITUDINAL SINGLE SPIN ASYMMETRY OF $W^\pm/Z \rightarrow \mu^\pm$

- $n_{\text{sig}}^{\text{sel}} \equiv n_{\text{sig}}$: Number of signals remaining after the selection using f'

and the relative relations between these signal numbers are expressed as follows:

$$n_{\text{sig}}^0 = \sigma_{\text{sig}} \cdot L, \quad (8.24)$$

$$n_{\text{sig}}^{\text{reco}} = (A\varepsilon)_{\text{det}} \cdot n_{\text{sig}}^0, \quad (8.25)$$

$$n_{\text{sig}}^{\text{pre}} = \epsilon_f(f_{\text{cut}}) \cdot n_{\text{sig}}^{\text{reco}}, \quad (8.26)$$

$$n_{\text{sig}}^{\text{sel}} = \epsilon_{f'}(f'_{\text{cut}}) \cdot n_{\text{sig}}^{\text{pre}}. \quad (8.27)$$

The number of signal estimated by the extended unbinned maximum likelihood corresponds to $n_{\text{sig}}^{\text{pre}}$. We use the term “signal efficiency” in this chapter to express $\epsilon_{f'}(f'_{\text{cut}})$. To determine the dilution factor $D^{S,N}$, we calculate $n_{\text{sig}}^{\text{sel}}$ and total remaining number of events with that signal selection $n_{\text{tot}}^{\text{sel}}$. The latter is directly obtained by calculating the f' -value for each event in data. The former is estimated using the signal MC simulation with assuming the measured cross section. The figure of merit (FOM) is defined as

$$\text{FOM}(f'_{\text{cut}}) \equiv \left. \frac{\sqrt{n_{\text{tot}}}}{D} \right|_{f'=f'_{\text{cut}}} . \quad (8.28)$$

for the given value of f'_{cut} . The optimal f'_{cut} was selected to give the maximum FOM.

Figure 8.1 shows the result of the determination of signal selection. In Table 8.1 the expected number of signal and for each channel is summarized.

channel	f'_{cut}	#events	Max. FOM	D	$\epsilon_{f'}(f'_{\text{cut}})$	$n_{\text{sig}}^{\text{sel}}$
South $W^-/Z \rightarrow \mu^-$	0.30	91	3.9	2.45	0.85	37.1
North $W^-/Z \rightarrow \mu^-$	0.24	86	4.5	2.07	0.92	41.5
South $W^+/Z \rightarrow \mu^+$	0.31	61	3.6	2.18	0.85	28.0
North $W^+/Z \rightarrow \mu^+$	0.46	44	3.6	1.86	0.66	23.7

Table 8.1: f'_{cut} value to give the maximum FOM, and the remaining number of events and the dilution factor using the central value of the cross section measurement. The central value dilution factor, signal efficiency and number are also listed.

8.2.2 Final signal candidates

With using the determined f'_{cut} -value, the number of signal candidates for each spin pattern was obtained as listed in Table 8.2.

channel	$n_{(++)}^S$	$n_{(+-)}^S$	$n_{(-+)}^S$	$n_{(--)}^S$	$n_{(++)}^N$	$n_{(+-)}^N$	$n_{(-+)}^N$	$n_{(--)}^N$
$W^-/Z \rightarrow \mu^-$	21	25	28	17	26	21	20	18
$W^+/Z \rightarrow \mu^+$	21	16	8	16	15	9	9	11

Table 8.2: Number of events for each spin combination with f'_{cut} -value given in the Table 8.1.

8.2.3 Error propagation

Here we discuss the error propagation in calculating the dilution factor D and $n_{\text{sig}}^{\text{sel}}$ using the method described above. As the major source of the systematic uncertainty comes from the choice of PDF, here we suppose the difference of the result by using different PDF compositions.

8.2 Dilution factor

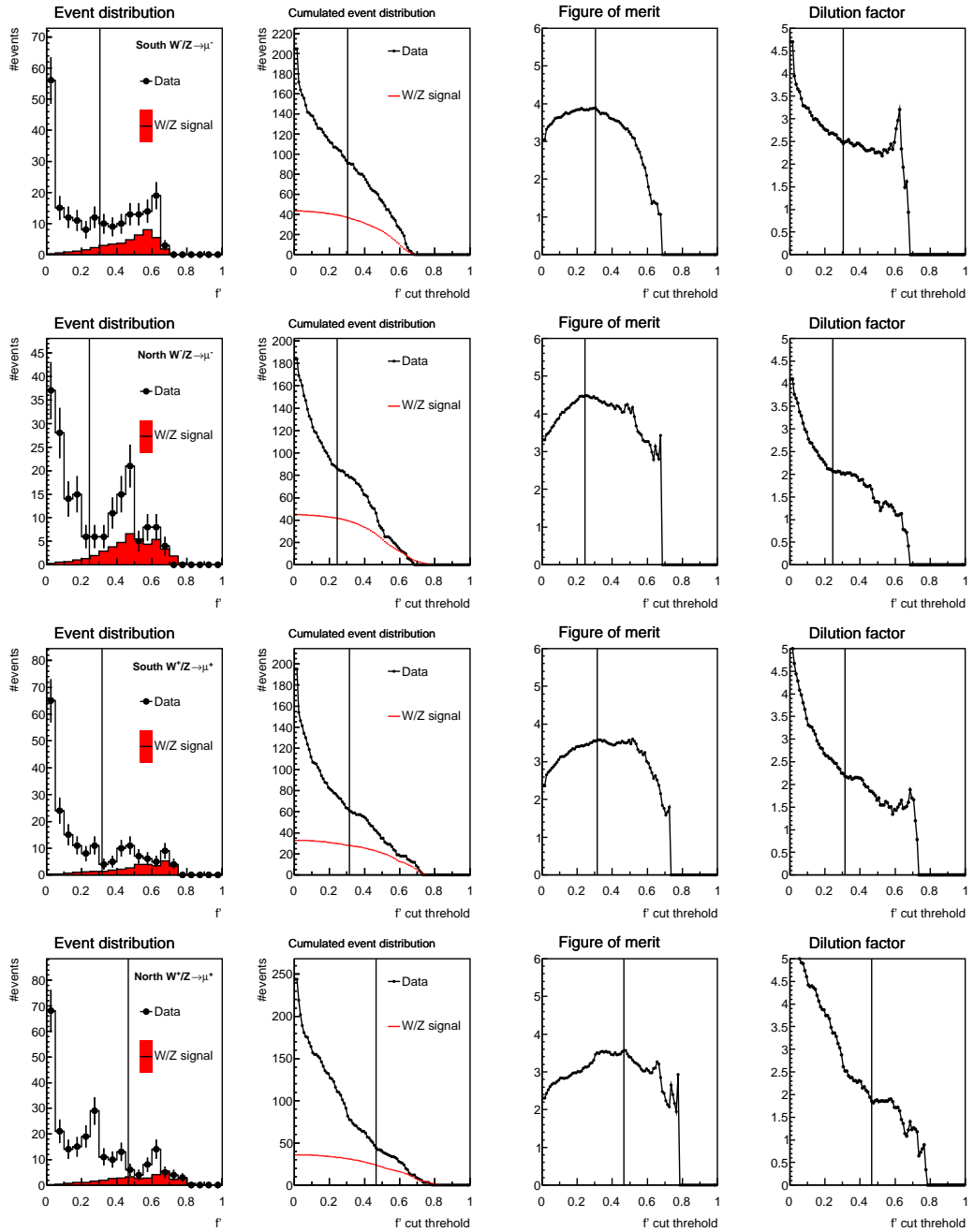


Figure 8.1: Determination of the signal selection. The first panel shows the event distribution for signal and data where the signal yield is scaled to the central value of the measured cross section. The second panel shows the cumulated distribution of the both as a function of f'_{cut} . The third panel shows the FOM as a function of f'_{cut} , and the cut threshold is determined to give the maximum FOM. The last panel shows the dilution factor as a function of f'_{cut} .

CHAPTER 8. MEASUREMENT OF LONGITUDINAL SINGLE SPIN ASYMMETRY OF $W^\pm/Z \rightarrow \mu^\pm$

Let us denote the PDF composition employed for the central value as S_0 , and a particular other PDF composition as S_1 . We have signal and background f' -distributions for each composition. We use the following conventions to express the f' -distribution of the signal and background:

- Signal: $s(f'_{S_k}; S_k)$ ($k = 0, 1$)
- Background: $b(f'_{S_k}; S_k)$ ($k = 0, 1$),

where we employ the following normalizations:

$$\int_0^1 s(f'_{S_k}; S_k) df' = n_{\text{sig}, S_k}^{\text{pre}}, \quad (8.29)$$

$$\int_0^1 b(f'_{S_k}; S_k) df' = n_{\text{bg}, S_k}^{\text{pre}} \quad (k = 0, 1). \quad (8.30)$$

$n_{\text{sig}, S_k}^{\text{pre}}, n_{\text{bg}, S_k}^{\text{pre}}$ are the number of signal (W^\pm/Z) and background (remaining) events at the preselection estimated with the PDF composition S_k . Obviously $n_{\text{sig}, S_k}^{\text{pre}}, n_{\text{bg}, S_k}^{\text{pre}}$ do not uniquely determined for a particular S_k , these values have statistical uncertainty as well as other source of systematic uncertainties than PDF determination. The S_k -index of f' explicitly denotes that the f' -value is defined under S_k , but we omit this label unless confusing.

For the case of S_0 , $n_{\text{sig}}^{\text{sel}}$ is

$$n_{\text{sig}}^{\text{sel}}(f'_{\text{cut}}; S_0) = \int_{f'_{\text{cut}}}^1 s(f'; S_0) df'. \quad (8.31)$$

The dilution factor is expressed as

$$D(f'_{\text{cut}}; S_0) = \frac{\int_{f'_{\text{cut}}}^1 [s(f'; S_0) + b(f'; S_0)] df'}{\int_{f'_{\text{cut}}}^1 [s(f'; S_0)] df'}. \quad (8.32)$$

Let us denote the event set in $f' > f'_{\text{cut}}$ for S_0 as X_{S_0} . The number of events in X_{S_0} is $n_{\text{tot}}^{\text{sel}} \equiv n_{\text{sig}}^{\text{sel}} + n_{\text{BG}}^{\text{sel}}$. The dilution factor is expressed as

$$D(f'_{\text{cut}}; S_0) = \frac{n_{\text{tot}}^{\text{sel}}}{n_{\text{sig}}^{\text{sel}}}, \quad (8.33)$$

which trivially shows that the dilution factor is a bound variable.

Now we consider the composition S_1 . Each event in X_{S_0} is mapped to different f' -value in S_1 . We can define the fraction of events in X_{S_0} at the given f' of S_1 , and let us denote them as $r(f'; S_1, f'^{S_0}_{\text{cut}})$. We have the following equation:

$$\begin{aligned} n_{\text{tot}}^{\text{sel}} &= \int_{f'_{\text{cut}}}^1 [s(f'; S_0) + b(f'; S_0)] df' \\ &= \int_0^1 [s(f'; S_1) + b(f'; S_1)] \cdot r(f'; S_1, f'^{S_0}_{\text{cut}}) df'. \end{aligned} \quad (8.34)$$

One should note that

$$\int_0^1 [s(f'; S_0)] df' \neq \int_0^1 [s(f'; S_1)] df' \quad (\text{or } n_{\text{sig}, S_0}^{\text{pre}} \neq n_{\text{sig}, S_1}^{\text{pre}}) \quad (8.35)$$

$$\int_0^1 [b(f'; S_0)] df' \neq \int_0^1 [b(f'; S_1)] df' \quad (\text{or } n_{\text{BG}, S_0}^{\text{pre}} \neq n_{\text{BG}, S_1}^{\text{pre}}) \quad (8.36)$$

$$(8.37)$$

but

$$\int_0^1 [s(f'; S_0) + b(f'; S_0)] df' = \int_0^1 [s(f'; S_1) + b(f'; S_1)] df' \\ (\text{or } n_{\text{sig}, S_0}^{\text{pre}} + n_{\text{bg}, S_0}^{\text{pre}} = n_{\text{sig}, S_1}^{\text{pre}} + n_{\text{bg}, S_1}^{\text{pre}}) \quad (8.38)$$

since the likelihood fitting result for the cross section measurement is different between S_0 and S_1 . Then $n_{\text{sig}}^{\text{sel}}$, and the dilution factor for the event set X_{S_0} is evaluated with using the composition S_1 as

$$n_{\text{sig}}^{\text{sel}}(f'^{S_0}_{\text{cut}}; S_0) \Big|_{S_1} = \int_0^1 s(f'_{S_1}; S_1) \cdot r(f'_{S_1}; S_1, f'^{S_0}_{\text{cut}}) df'_{S_1}, \quad (8.39)$$

$$D(f'^{S_0}_{\text{cut}}; S_0) \Big|_{S_1} = \frac{\int_0^1 [s(f'_{S_1}; S_1) + b(f'_{S_1}; S_1)] \cdot r(f'_{S_1}; S_1, f'^{S_0}_{\text{cut}}) df'_{S_1}}{\int_0^1 [s(f'_{S_1}; S_1) \cdot r(f'_{S_1}; S_1, f'^{S_0}_{\text{cut}})] df'_{S_1}} \\ = \frac{n_{\text{tot}}^{\text{sel}}}{n_{\text{sig}}^{\text{sel}}(f'^{S_0}_{\text{cut}}; S_0) \Big|_{S_1}}, \quad (8.40)$$

respectively. The second equation only expresses again the dilution factor is a bound variable. The difference between $n_{\text{sig}}^{\text{sel}}(f'_{\text{cut}}; S_0)$ and $n_{\text{sig}}^{\text{sel}}(f'^{S_0}_{\text{cut}}; S_0) \Big|_{S_1}$ is the error of evaluating the number of signals in X_{S_0} reflecting the uncertainty of the cross section measurement depending on the composition of PDF. In this manner the systematic uncertainty of the dilution factor and number of signals are correctly evaluated. Figure 8.2 shows an example of evaluating $n_{\text{sig}}^{\text{sel}}(f'^{S_0}_{\text{cut}}; S_0) \Big|_{S_1}$, $D(f'^{S_0}_{\text{cut}}; S_0) \Big|_{S_1}$ with changing the composition of PDF from S_0 . The method is extended to include other systematic uncertainties.

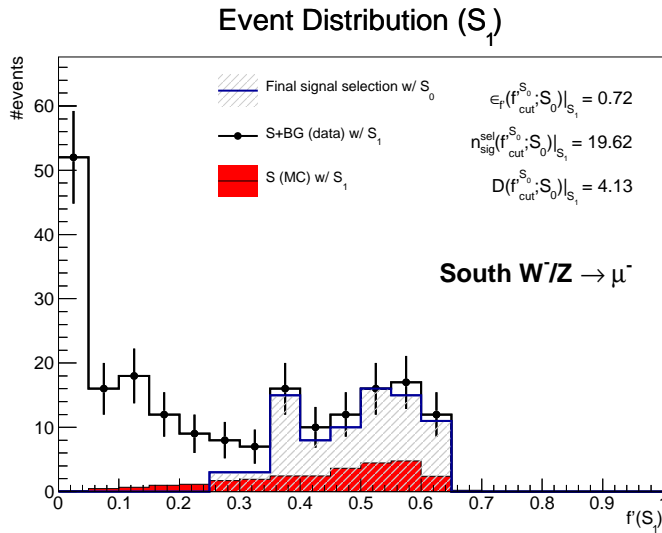


Figure 8.2: An example of event distribution in f'_{S_1} .

channel	$n_{\text{sig}}^{\text{sel}}$
South $W^-/Z \rightarrow \mu^-$	$37.1^{+9.5}_{-19}$
North $W^-/Z \rightarrow \mu^-$	41.5^{+10}_{-18}
South $W^+/Z \rightarrow \mu^+$	$28.0^{+11}_{-9.4}$
North $W^+/Z \rightarrow \mu^+$	$23.7^{+9.3}_{-11}$

Table 8.3: Uncertainty of $n_{\text{sig}}^{\text{sel}}$ in the data set of the final signal selection.

8.3 Beam polarization

Table 8.4 summarizes the relative systematic uncertainties for beam polarization. The average polarization of the Blue, Yellow beam for the used runs was $(51.3 \pm 4.4) \%$, $(51.1 \pm 4.1) \%$, respectively. For the product of the two beam polarizations was $(26.2 \pm 3.3) \%$. Note the error propagation must be taken into account to calculate uncertainties. In particular, the “H-jet (molecular)” and “H-jet (background)” uncertainties are considered to be correlated between the Blue and the Yellow beams.

uncertainty	P_B	P_Y	$P_B P_Y$	Correlated
H-jet (statistics)	7.4 %	7.0 %	10.2 %	
H-jet (molecular)	2.0 %	2.0 %	4.0 %	×
H-jet (background)	3.0 %	3.0 %	6.0 %	×
pC (profile)	2.0 %	1.9 %	2.7 %	
Total	8.5 %	8.1 %	12.8 %	

Table 8.4: Systematic uncertainties of beam polarization.

8.4 Relative luminosity

The relative luminosity was measured using low reconstructed p_T tracks. The following cuts were applied for samples.

- the Basic cut
- Fiducial cut in Sec. 7.4.2.
- $6 < p_T^{\text{reco}} < 10.0$
- Having associated RPC3 hit and RpcDCA < 7.0
- $\chi^2_{\text{track}} < 20.0$
- $\text{DCA}_r < 7.0 \text{ cm}$
- $|dw_{23}| < 0.05$

Figure 8.3 shows the accumulated events for four spin combinations and events by bunch ID, and Table 8.5 summarizes the result. The effect of relative luminosity to the final spin asymmetry result is negligibly small.

combination	++	+−	−+	−−	total
number of events	18964	19267	19193	19212	76646
relative luminosity (%)	24.76 ± 0.16	25.14 ± 0.16	25.04 ± 0.16	25.07 ± 0.16	100 %

Table 8.5: Summary of relative efficiency measurement.

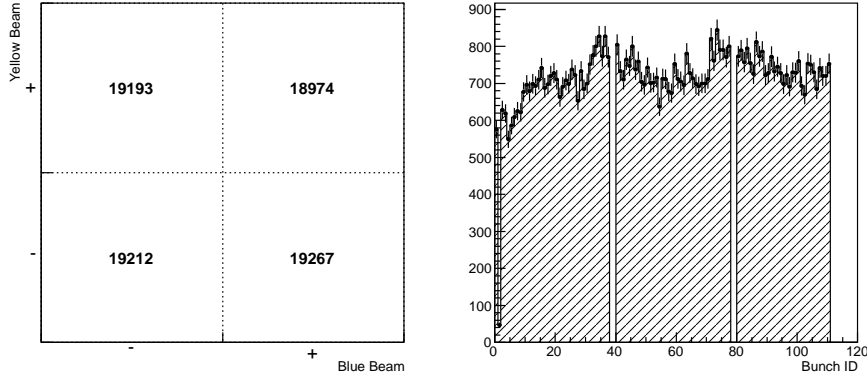


Figure 8.3: Result of relative luminosity measurement using low momentum track events. (Left) Number of events per spin combination, (Right) Number of events by Bunch ID.

8.5 Maximum likelihood fitting for spin asymmetry

As the statistics is limited, we employed maximum likelihood fitting to evaluate spin asymmetries. We define the expectation value of each observable as

$$\hat{n}_{(s_B s_Y)}^S = n_{\text{sig},S}^{\text{sel}} \cdot r_{(s_B s_Y)} \left[(1 + (-1)^{s_B} A_L^{\eta < 0} P_B + (-1)^{s_Y} A_L^{\eta > 0} P_Y + (-1)^{s_B+s_Y} A_{LL} P_B P_Y + (D^S - 1)) \right] \quad (8.41)$$

$$\hat{n}_{(s_B s_Y)}^N = n_{\text{sig},N}^{\text{sel}} \cdot r_{(s_B s_Y)} \left[(1 + (-1)^{s_B} A_L^{\eta > 0} P_B + (-1)^{s_Y} A_L^{\eta < 0} P_Y + (-1)^{s_B+s_Y} A_{LL} P_B P_Y + (D^N - 1)) \right] \quad (8.42)$$

where $s_B, s_Y = \pm 1$. Then the likelihood is composed as

$$\mathcal{L}_{\text{spin}} \equiv \prod_{a \in S, N} \prod_{s_B, s_Y} P_o \left(n_{(s_B s_Y)}^a; \hat{n}_{(s_B s_Y)}^a (A_L^{\eta < 0}, A_L^{\eta > 0}, A_{LL}; [n_{\text{sig},a}^{\text{sel}}, D^a], r_{(s_B s_Y)}, P_B, P_Y) \right) \quad (8.43)$$

where $P_o(n; \hat{n})$ is Poisson's distribution. The free parameters are only spin asymmetries ($A_L^{\eta > 0}$, $A_L^{\eta < 0}$, A_{LL}), and the other parameters are fixed for each time of the fitting. (The bracket $[n_{\text{sig},a}^{\text{sel}}, D^a]$ expresses that these are bound via the total number of selected events $n_{\text{tot},a}^{\text{sel}} = \sum_{s_B, s_Y} n_{(s_B s_Y)}^a$). The estimation for the set of spin asymmetry ($A_L^{\eta > 0}$, $A_L^{\eta < 0}$, A_{LL}) is obtained with maximizing the likelihood. Figure 8.4 shows the result of the maximum likelihood fitting with the central value of the parameter set.

The same fitting was repeated with changing PDF compositions (reflecting the different set of position resolution and hadronic background estimation with correct weighting) as well as beam polarizations by the size of its systematic uncertainties, and the systematic uncertainty for the central value of the spin asymmetries was determined. Figure 8.5 shows the distribution of the systematic uncertainty. Note that the correlations of polarization uncertainties described in

CHAPTER 8. MEASUREMENT OF LONGITUDINAL SINGLE SPIN ASYMMETRY OF $W^\pm/Z \rightarrow \mu^\pm$

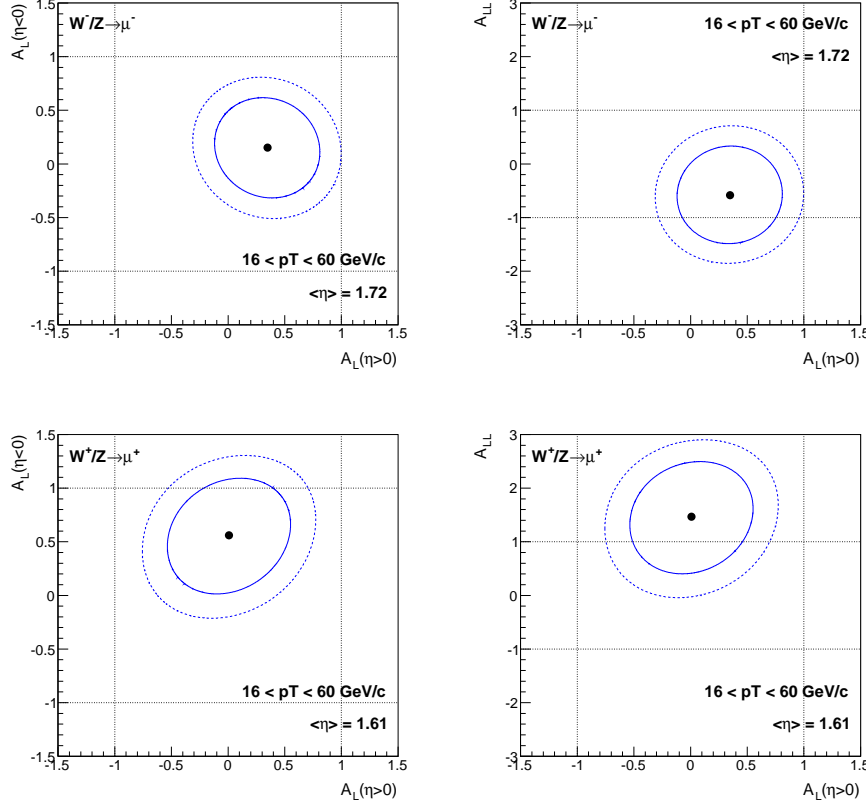


Figure 8.4: Result of the maximum likelihood fitting for measuring spin asymmetries. The black bullet shows the most probable value, and the solid and dotted line shows 1-sigma and 2-sigma contour of the fitting, respectively.

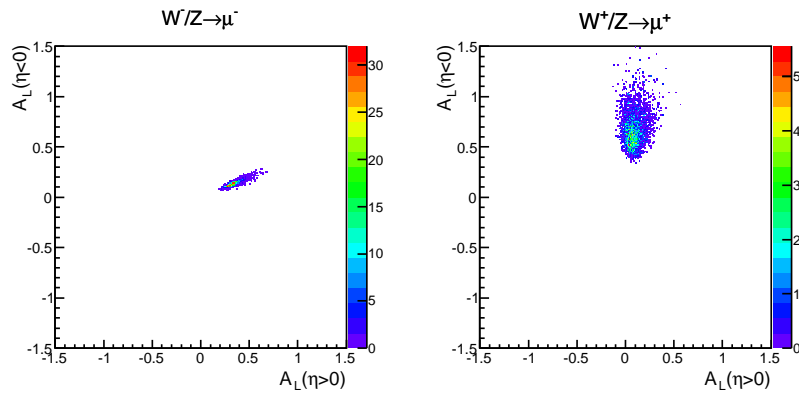


Figure 8.5: Systematic uncertainty of the central value of spin asymmetries.

8.5 Maximum likelihood fitting for spin asymmetry

Sec. 8.3 was correctly implemented. Relative luminosity is ignored since the effect is negligible. The obtained systematic error band due to the dilution factors and polarizations has asymmetric width for the central value.

channel	$\epsilon_L^{\eta>0}$	(num./denom.)	$\epsilon_L^{\eta<0}$	(num./denom.)	ϵ_{LL}	(num./denom.)
South $W^-/Z \rightarrow \mu^-$	0.077	7/91	0.011	1/91	-0.165	-15/91
North $W^-/Z \rightarrow \mu^-$	0.106	9/85	0.082	7/85	0.035	3/85
South $W^+/Z \rightarrow \mu^+$	-0.049	-3/61	0.213	13/61	0.213	13/61
North $W^+/Z \rightarrow \mu^+$	0.091	4/44	0.091	4/44	0.182	8/44

Table 8.6: Raw asymmetries for the final signal selection. The correction for the relative luminosity is ignored.

channel	$\langle \eta_\mu \rangle$	$A_L^{\eta>0}$	$A_L^{\eta<0}$	A_{LL}
$W^-/Z \rightarrow \mu^-$	1.72	$0.35^{+0.46}_{-0.47}(\text{stat})$	$0.15^{+0.47}_{-0.47}(\text{stat})$	$-0.58^{+0.92}_{-0.90}(\text{stat})$
(syst. range)		[0.23, 0.51]	[0.09, 0.21]	[-1.09, -0.30]
$W^+/Z \rightarrow \mu^+$	1.61	$0.07^{+0.55}_{-0.54}(\text{stat})$	$0.56^{+0.53}_{-0.55}(\text{stat})$	$1.47^{+1.03}_{-1.07}(\text{stat})$
(syst. range)		[-0.04, 0.29]	[0.42, 1.13]	[0.99, 2.0]

Table 8.7: Result of the measurement of spin asymmetries. The systematic range shows the uncertainty range of the central value.

**CHAPTER 8. MEASUREMENT OF LONGITUDINAL SINGLE SPIN
ASYMMETRY OF $W^\pm/Z \rightarrow \mu^\pm$**

Chapter 9

Discussion and conclusion

9.1 Cross section of $W^\pm \rightarrow \mu^\pm$

The obtained total production cross section of W^\pm bosons for μ^\pm decays in $p + p$ collisions at $\sqrt{s} = 500$ GeV in this analysis are

$$\begin{aligned}\sigma(pp \rightarrow W^-) \times \mathcal{BR}(W^- \rightarrow \mu^-) &= 47.8^{+25.0}_{-11.8} \text{ (pb)} \text{ (68 \% C.L.)}, \\ \sigma(pp \rightarrow W^+) \times \mathcal{BR}(W^+ \rightarrow \mu^+) &= 129.5^{+102.0}_{-33.5} \text{ (pb)} \text{ (68 \% C.L.)}.\end{aligned}$$

by combining both South and North Muon Arms' results. Here a likelihood analysis was performed for combining both Arms' results with both statistical and systematic uncertainties. Here the central value is the most probable value of the likelihood function, and the 68 % confidence interval is defined to reject 16 % of the total integral of both sides of the likelihood function. Under our assumption of systematic uncertainties, the result represented that the likelihood that the cross section is zero was 2.9×10^{-4} and 1.3×10^{-3} for W^- and W^+ , respectively. If we regard these numbers in manner of standard deviation, these numbers correspond to 3.6σ and 3.2σ , respectively. Although the systematic uncertainty does not have statistical rigidness, these numbers indicate that it is quite likely here we observed $W^\pm \rightarrow \mu^\pm$ signal in event candidates.

Both the cross section of W^+ and W^- were already measured at mid-rapidity region at the same center of mass energy of $\sqrt{s} = 500$ GeV in $p + p$ collisions by the PHENIX and the STAR experiments for e^\pm decays, and these results agree well with theoretical calculations in NLO and NNLO levels[31, 43]. Hence we can highly rely on theoretical calculation of $W^\pm \rightarrow \mu^\pm$ cross section. Table 9.1 shows several theoretical calculations of $W^\pm \rightarrow \mu^\pm$ production cross sections[31]. Figure 9.1 shows comparison of total cross section of $W^\pm \rightarrow \ell^\pm$ between the result of this analysis and other measurements as well as theoretical calculations. The obtained cross sections (both W^+ and W^-) are consistent with the existing measurements as well as theoretical calculations. Therefore we conclude that we obtained $W^\pm \rightarrow \mu^\pm$ events in the collected data sample which are consistent with our current knowledge of W^\pm production cross section. The above cross section results assures the validity of the following measurement of longitudinal single spin asymmetry $A_L^{\mu\pm}$.

Discussion about systematic uncertainty

Even the statistics of this measurement is limited, the obtained cross sections has large systematic uncertainty due to the momentum resolution of the MuTr and estimation of the PDF of hadronic backgrounds for likelihood fitting.

CHAPTER 9. DISCUSSION AND CONCLUSION

PDF	Generator	σ_{W^+} (pb)	σ_{W^-} (pb)
NLO MSTW08	FEWZ	132.4 ± 9.0	45.7 ± 3.6
NNLO MSTW08	FEWZ	136.7 ± 9.5	48.1 ± 3.0
NLO CTEQ 6.6	FEWZ	121.8 ± 8.8	41.1 ± 4.3
Resummation CTEQ 6.6	RHICBOS	121.1	39.9

Table 9.1: Theoretical calculations of total cross section of total cross section times branching ratio [31, 75, 80, 81, 85]. The error in the table comes from uncertainty of PDFs.

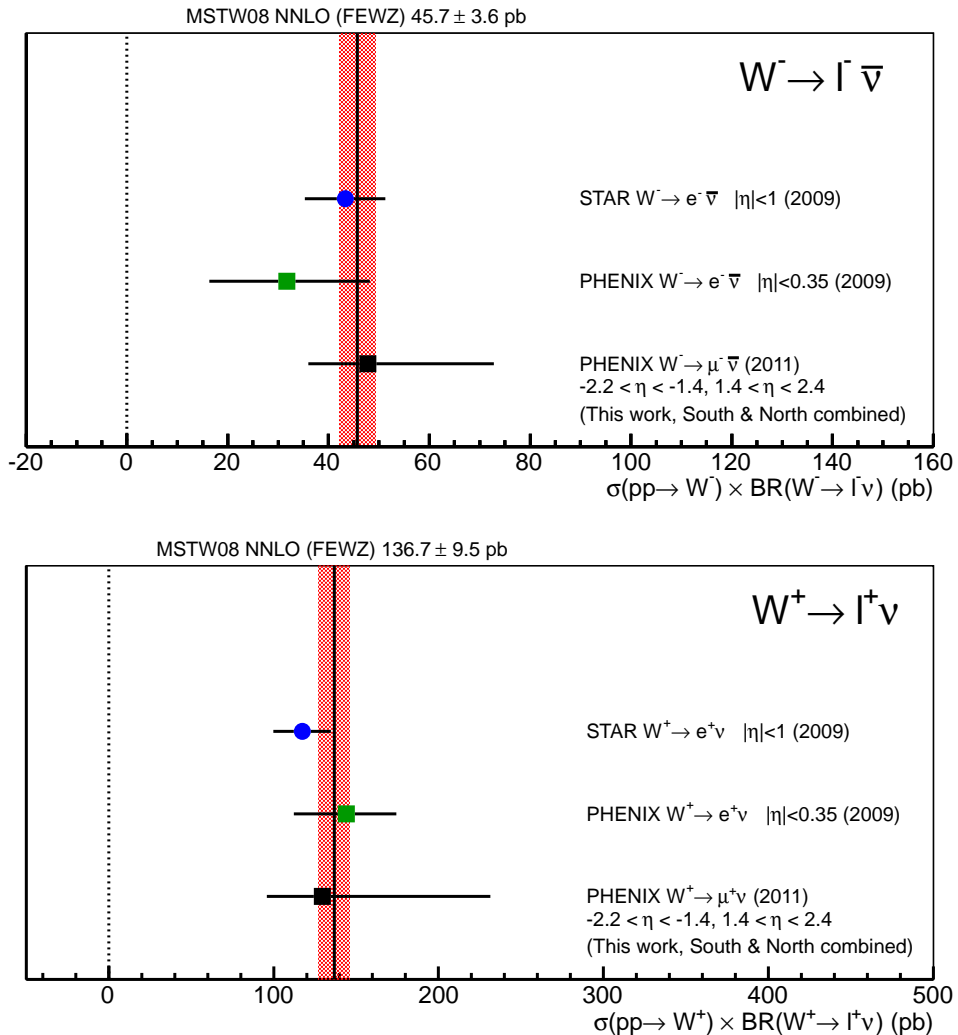


Figure 9.1: Comparison of the obtained cross section in this analysis and other measurements and theoretical calculation. For the theoretical calculation, only MSTW08 NNLO calculation with FEWZ in Table 9.1 is plotted as a representative calculation.

MuTr position resolution

The momentum resolution of the MuTr is determined by the strength of the magnetic field and the position resolution of the MuTr. It is essential to improve the position resolution of the MuTr. The achieved position resolution of the MuTr is worse than its initial design value of 100 μm . With installation of the Mutrg electronics, it was studied that the position resolution was degraded by about 30 %. Even though we would have room to improve the position resolution up to $\simeq 150 \mu\text{m}$. Several attempts to improve the position resolution is ongoing. One is to improve the position measurement procedure. As described in Sec. 4.2.2, the position measurement of the MuTr is performed by fitting the charge distribution in cathode strips with the Mathieson function. The parameter of the Mathieson function is defined by the geometry of the cell structure of the cathode strip chamber, and a study shows that calibrating this geometrical parameter to give the optimized position measurement could give position resolution which is by 30 % better than the current performance. At the same time, the relative alignment of the MuTr chambers needs to be improved. Improvement of position resolution contributes not only to reduce the systematic uncertainty of cross section measurement of $W^\pm \rightarrow \mu^\pm$ in terms of determination of signal spectrum, but also to reduce the irreducible muon backgrounds in the signal region due to reducing the smearing of low- p_T muon events to high- p_T regions. For evaluation of data-driven estimation of the position resolution and its uncertainty, Inclusive evaluation of position resolution with J/ψ or Υ mass peak widths will be improved when we obtain higher statistics. For analysis side, we would have room of improvement of momentum range selection not to suffer the effect of the uncertainty of momentum resolution.

PDF of hadronic background

Identification of muons in high- p_T region is a serious task in this analysis due to large hadronic background contamination. We employed a data-driven background shape estimation using the side-band data. With increase of statistics, the precision of data-driven shape estimation will be improved in both η and dw_{23} distributions. However, the shape of hadronic background distribution in the signal region is not reliably known. With the current detector configuration it is not possible to obtain the trajectory of charged particles between the interaction point and the hadron absorber before the MuTr. After 2011 runs a new silicon tracking detector called FVTX was installed inside the hadron absorber (Figure 9.2). Association of FVTX hits with MuTr tracks will be an effective analysis tool for observing the amount of multiple scattering at the hadron absorber, which will be useful to reject hadronic background events or clarify the shape of hadronic background overlapping in the signal region. Another possibility to utilize the FVTX detector hits is to use it for track isolation analysis, or to see the matching of MuTr+FVTX tracks with collision vertex.

9.2 $A_L^{\mu\pm}$ measurement

We measured the first longitudinal single spin asymmetry of μ^\pm in $16 < p_T^{\text{reco}} < 60 \text{ GeV}/c$ from W^\pm/Z bosons $A_L^{\mu\pm}$ at forward and backward rapidity regions as

$$\begin{aligned} A_L^{\mu-} &= 0.15^{+0.47}_{-0.47}(\text{stat})^{+0.06}_{-0.06}(\text{sys}) \quad (\eta = -1.72) , \\ A_L^{\mu-} &= 0.35^{+0.46}_{-0.47}(\text{stat})^{+0.16}_{-0.12}(\text{sys}) \quad (\eta = 1.72) , \\ A_L^{\mu+} &= 0.56^{+0.53}_{-0.55}(\text{stat})^{+0.57}_{-0.14}(\text{sys}) \quad (\eta = -1.61) , \\ A_L^{\mu+} &= 0.07^{+0.55}_{-0.54}(\text{stat})^{+0.22}_{-0.11}(\text{sys}) \quad (\eta = 1.61) . \end{aligned}$$

The results of $A_L^{\mu\pm}$ are plotted in Figure 9.3 with predictions of $A_L^{\mu\pm}$ as a function of η of various global analyses. Among four measurement data points, $A_L^{\mu-}$ at $\langle\eta\rangle = -1.72$ is sensitive

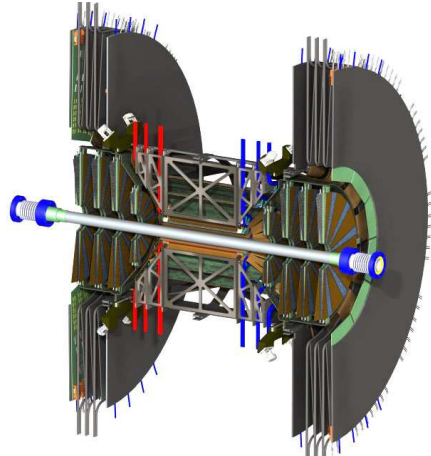


Figure 9.2: 3D layout of the FVTX detector.

to $\Delta\bar{u}(x)$ at $x \sim 0.05$. The difference of global analyses is large for $A_L^{\mu^-}$ at negative η_μ . This is mainly because of the difference of $\Delta\bar{u}(x)$ in different polarized PDF sets. Currently the statistical error dominates the uncertainty, and the impact on constraining polarized PDFs is still peripheral. On the other hand, the obtained asymmetry values are consistent with the predictions with polarized PDFs. The importance of the result of this analysis is that this is the first result of measuring the $A_L^{\mu^\pm}$ at forward rapidity regions, and this analysis is the proof of concept for the PHENIX experiment that it is possible to measure $A_L^{\mu^\pm}$ of muons from W^\pm/Z at forward rapidity regions.

9.3 Future prospect

Recalling that the statistical uncertainty is magnified by the dilution factor D , reduction of background in final signal selection is essentially important for this measurement. The major background events in this analysis were hadronic backgrounds mainly from low-momentum K^\pm decaying to muons in the MuTr volume which are reconstructed as high momentum tracks. Reduction of hadronic background will be possible in future improvements. As mentioned in the previous section, the newly installed FVTX silicon detector since 2012 can trace the trajectory of charged particles in front of the hadron absorber, and it will be useful to reduce the dilution factor for spin asymmetry measurement. Also, the systematic uncertainty of the dilution factor was sizable in this analysis. This is the reflection of the uncertainty of cross section measurement, and the major uncertainties are the position resolution of MuTr and the hadronic background PDF shape in dw_{23} distribution. Future improvements for these systematic uncertainties are already described in the previous section.

The new RPC1 detector was installed in 2012 between the hadron absorber and the MuTr Station-1. The RPC1 covers the lower rapidity range than the acceptance of RPC3 of $1.2 < |\eta| < 1.4$. By comparing the η distribution of $W^\pm \rightarrow \mu^\pm$ signal, we can expect that the background fraction of this rapidity region in signal candidates is not severer than the acceptance in this analysis, and relatively large differential cross section of the signal. Therefore the cross section of $W^\pm \rightarrow \mu^\pm$ can be measured more precisely with including RPC1 acceptance. In context of data taking, the RPC1 and RPC3 started to provide Level-1 trigger along with Mutrg-SG1 trigger, which will reserve further trigger bandwidth for upcoming high luminosity runs.

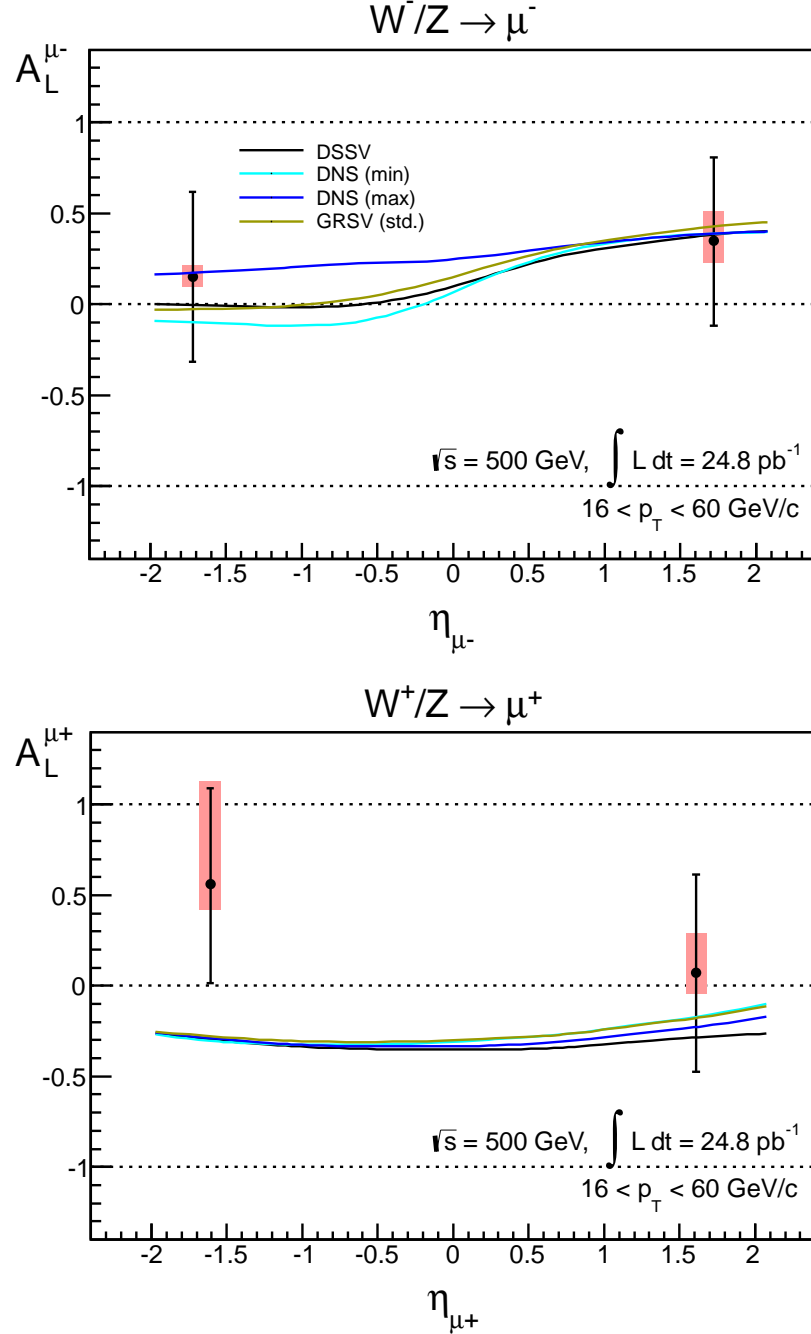


Figure 9.3: $A_L^{\mu\pm}$ measured in this study. The black bullets denote the central value, and the black bar shows the statistical error at the central value. The blue band at the data point shows the systematic uncertainty range of the central value. The continuous lines represent the theoretical predictions generated by CHE NLO generator[10] with using DSSV[8], DNS(minimum), DNS(maximum)[84], GRSV (standard)[83] polarized PDFs and MRST02[7] unpolarized PDFs.

The average beam polarization was $\sim 34\%$ in 2009 run, and it improved to $\sim 48\%$ and 52% in 2011 and 2012 runs, respectively. Improvement of beam polarization is also essential upgrade for spin physics as well as luminosity. Since 2012, RHIC has started to collide longitudinally polarized protons at $\sqrt{s} = 510$ GeV. The detector upgrades program of the PHENIX Muon Arms dedicated for $W^\pm \rightarrow \mu^\pm$ measurement was done, and it is expected that we will collect more than 300 pb^{-1} in total. In RHIC experiment, both PHENIX and STAR is committing for W measurement program. The STAR detector was also upgraded to cover forward rapidity region up to $|\eta| < 2$ in addition to existing coverage of $|\eta| < 1$. With combining both PHENIX and STAR results, RHIC W measurement will definitely give new constraints on sea quark polarization, and it will lead us to new and deeper understanding of the spin structure of the nucleon and of the confinement of the quarks in the nucleon.

9.4 Conclusion

In this thesis, longitudinal single spin asymmetry of production of muons from W^\pm/Z boson decays, $A_L^{\mu\pm}$ at forward/backward rapidity regions in longitudinally polarized p+p collisions at $\sqrt{s} = 500$ GeV with integrated luminosity of 25 pb^{-1} was measured. The result is the world fist measurement of parity-violating spin asymmetry A_L from W^\pm/Z bosons with muons. We obtained the results of $A_L^{\mu\pm}$ at $\langle\eta\rangle = \pm 1.61$ for $W^+/Z \rightarrow \mu^+$ and $\langle\eta\rangle = \pm 1.72$ for $W^-/Z \rightarrow \mu^-$. These rapidities were unexplored kinematic regions before this study including all other W^\pm/Z decay channels. The above rapidity regions are crucial for determining quark and antiquark polarized PDFs, especially in $W^- \rightarrow \mu^-$ case, as $A_L^{\mu-}$ at large $|\eta|$ regions directly constrains $\Delta\bar{u}(x)$ and $\Delta d(x)$.

The presented data were taken with the PHENIX detector at RHIC in 2011, and the Muon Arm detectors (MuTr, MuID, RPC3, BBC) were used for the analysis. The presented data is the first-year data with the Mutrg trigger and the RPC3, which were installed into the PHENIX detector dedicatedly for achieving $W \rightarrow \mu^\pm$ measurements. The detector performances were carefully inspected to evaluate efficiencies correctly. In particular, the measurement in this thesis is the first physics result with using newly installed Mutrg and RPC3. $W^\pm/Z \rightarrow \mu^\pm$ signal at large $|\eta|$ regions encounters immense background events from charged hadrons with having high- p_T reconstructed tracks in addition to irreducible muon backgrounds, and this was the major challenge in the analysis. A likelihood-based signal selection was used for the preselection procedure which utilized multiple scattering in the hadron absorbers and in the MuID walls, and other track qualities. We developed a signal extraction procedure using unbinned maximum likelihood fitting. As a result, with using single muon events in $16 < p_T^{\text{reco}} < 60$ GeV/c the cross section of $W^\pm \rightarrow \mu^\pm$ was obtained as

$$\begin{aligned}\sigma(pp \rightarrow W^-) \times \mathcal{BR}(W^- \rightarrow \mu^-) &= 47.8^{+25.0}_{-11.8} \text{ (pb)} \quad (68\% \text{ C.L.}), \\ \sigma(pp \rightarrow W^+) \times \mathcal{BR}(W^+ \rightarrow \mu^+) &= 129.5^{+102.0}_{-33.5} \text{ (pb)} \quad (68\% \text{ C.L.}).\end{aligned}$$

The major systematic uncertainty comes from MuTr position resolution and the estimation of the PDF of hadronic background events at the signal region, and the size of systematic these uncertainties were larger than statistical uncertainty. Still, we conclude that we observed $W^\pm \rightarrow \mu^\pm$ events in the data sample used in this thesis. The above statement is also supported by the result that the obtained cross section was consistent with NLO or higher-order theoretical calculations for both W^+ and W^- . In future, improvement of MuTr position resolution and new analyses using newly-installed FVTX and RPC1 detector with larger acceptance will lead better understanding of background events and systematic uncertainties to reduce the systematic uncertainty of the cross section measurement as well as reducing background events for spin asymmetry measurement.

Based on the observed numbers of $W^\pm/Z \rightarrow \mu^\pm$ events, $A_L^{\mu\pm}$ for muons in $16 < p_T^{\text{reco}} < 60$ GeV/ c were measured as

$$\begin{aligned} A_L^{\mu-} &= 0.15^{+0.47}_{-0.47}(\text{stat})^{+0.06}_{-0.06}(\text{sys}) \quad (\eta = -1.72) , \\ A_L^{\mu-} &= 0.35^{+0.46}_{-0.47}(\text{stat})^{+0.16}_{-0.12}(\text{sys}) \quad (\eta = 1.72) , \\ A_L^{\mu+} &= 0.56^{+0.53}_{-0.55}(\text{stat})^{+0.57}_{-0.14}(\text{sys}) \quad (\eta = -1.61) , \\ A_L^{\mu+} &= 0.07^{+0.55}_{-0.54}(\text{stat})^{+0.22}_{-0.11}(\text{sys}) \quad (\eta = 1.61), \end{aligned}$$

which are still consistent with the prediction of various global analyses of polarized PDFs. The current uncertainty on $A_L^{\mu\pm}$ is highly dominated by statistics and we need more of data to constrain polarized sea quark PDFs. Future runs at $\sqrt{s} = 510$ GeV will collect one order of magnitude higher statistics in total, and with such high statistics, quark and antiquark polarized PDFs will be significantly constrained altogether with $A_L^{\ell\pm}$ measurements in other η regions with PHENIX and STAR in RHIC. The work in this thesis is a pioneering proof of concept toward that quest.

CHAPTER 9. DISCUSSION AND CONCLUSION

Appendix A

Muon background estimation with dimuon events

In this appendix, we estimate the cross section of muon background processes for $W^\pm \rightarrow \mu^\pm$ using dimuon event sample. The foregrounds are unlike-sign dimuons which both muons go to the same side (South or North) Muon Arm. Basic cuts and jet cleaning cuts are applied to dimuon pairs. Next, the yield of combinatorial backgrounds are estimated using like-sign dimuons and it is subtracted from the foreground. Then a simultaneous fitting of the mass spectrum of the two different triggers of MuID-1D and WTRG(S,N) is performed and scale factors of each physics process is extracted.

A.1 Data analysis

A.1.1 Triggers

In this analysis we used both MuID-1D trigger data and WTRG(S,N) trigger data. The trigger efficiency for these triggers were studied in detail in Sec. 6.3.

A.1.2 Integrated luminosity

We used totally 380 runs for this study. The number of runs employed in this study is larger than the main $W^\pm \rightarrow \mu^\pm$ analysis, since we do not use the RPC in this study, and the quality of the RPC status is not cared. The integrated luminosity is calculated based on DAQ database and corrected for multiple collision. For MuID-1D and WTRG(S,N) trigger the total integrated luminosity is 1.52 pb^{-1} and 28.6 pb^{-1} , respectively. The systematic uncertainty of the integrated luminosity is $\pm 10\%$.

A.1.3 Cuts

We applied the following cuts for the both tracks of dimuon events.

- MuID lastGap == 4
- DG0 < 20.0 cm
- DDG0 < 9.0 deg
- $\chi^2_{\text{track}} < 23.0$

APPENDIX A. MUON BACKGROUND ESTIMATION WITH DIMUON EVENTS

- $\text{DCA}_r < 30.0 \text{ cm}$

- $1.2 < |\eta| < 2.0$

The last rapidity selection is slightly narrower than the rapidity acceptance of Muon Arms at higher rapidity side, but this is effective for rejecting hadron jet events. We also applied for the kinematic cuts for the relation between two tracks to reject jets:

- $1.2 < |\phi_0 - \phi_1| < 5.8$, where $\phi_j \equiv \text{atan}2(p_y^j, p_x^j)$.

This cut is effective because di-tracks in jets have correlation in the opening angle between the tracks.

All these cuts are applied to South and North dimuon pairs of like-sign and unlike-sign, respectively.

A.1.4 Subtraction of combinatorial backgrounds

The “combinatorial background” events which accidentally emits plural tracks in a event consists a background to dimuon events and this is the object of subtraction. The combinatorial background events in unlike-sign dimuon events were estimated using the like-sign events as:

$$N_{(+-)}^{\text{comb}} = 2 \times \sqrt{N_{(++)} \times N_{(--)}} . \quad (\text{A.1})$$

A.1.5 Acceptance and efficiency

A.1.5.1 Relative efficiency correction

Figure A.1 shows the dimuon yield in South and North Arm in $2.5 < m_{\text{inv}}^{\mu+\mu-} < 4.0 \text{ GeV}/c^2$ after subtracting combinatorial backgrounds for each luminosity group of runs and fitting of data points with a linear function. The relative slope with respect to the extrapolated yield at $\mu \rightarrow 0$ was -0.759 ± 0.022 and -0.711 ± 0.024 for South and North Arm, respectively. The relative RMS of data points around the fit is calculated as 2.9 % and 2.4 % for South and North Arm, respectively, and this relative deviation from the fit line is taken as the systematic uncertainty of efficiency estimation. The relative efficiency for each run is determined by referring the μ parameter of each run, and weighted by the integrated luminosity of each run. Table A.1 summarizes the total relative efficiency of whole runs.

Trigger	South Arm	North Arm
MuID-1D	0.93 ± 0.07	0.94 ± 0.06
WTRG(S,N)	0.82 ± 0.06	0.84 ± 0.05

Table A.1: Total relative efficiency of dimuon process to the reference run for MuID-1D and WTRG(S,N) trigger.

A.2 Simulation

The dimuon spectrum of each physics process is simulated with PYTHIA + PISA. In this section we describe about the detail of the configuration of the simulation.

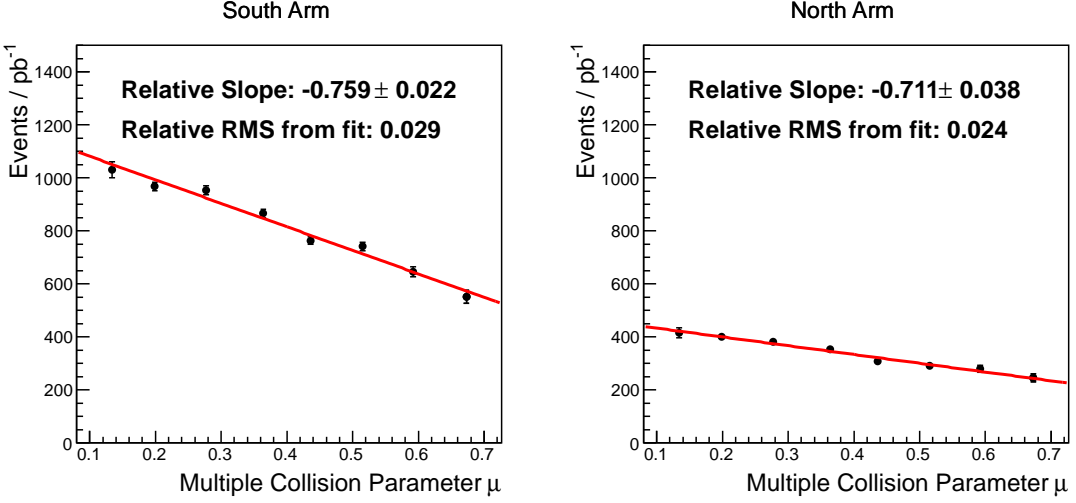


Figure A.1: Relative dimuon yield in $2.5 < m_{\text{inv}} < 4.0 \text{ GeV}/c^2$ with WTRG(S,N) trigger for different luminosity groups.

A.2.1 General framework

- For z_{vtx} distribution a gaussian with sigma of 40 cm was applied and fed to PYTHIA simulation.
- We applied the same cuts as applied to the data.

A.2.2 Parameterization of mass spectra and notes

To perform fitting of data, we parameterized the invariant mass spectrum with empirical analytic functions for each process. At first the fitting was performed for each Muon Arm (South, North) and for each trigger (MuID-1D, WTRG(S,N)) to obtain the shape, then constraints on the common scale factors is considered at the step of fitting data. In the following equations in this section, m denotes the invariant mass, variables expressed with the character “ p ” denote free parameters, and the other characters denote constants.

A.2.2.1 Open charm

$$Q_{cc}(m) = p_0^{Qcc} \times \left[\exp \left(1 + p_1^{Qcc} m + p_2^{Qcc} m^2 \right) \times \frac{1}{2} \left(1 + \text{Erf} \left(\frac{m - p_4^{Qcc}}{p_5^{Qcc}} \right) \right) \right] \quad (\text{A.2})$$

A.2.2.2 Open bottom

$$\begin{aligned} Q_{bb}(m) = & p_0^{Qbb} \times \left[\exp \left(1 + p_1^{Qbb} m + p_2^{Qbb} m^2 \right) \times \frac{1}{2} \left(1 + \text{Erf} \left(\frac{m - p_4^{Qbb}}{p_5^{Qbb}} \right) \right) \right] \\ & + p_0^{Qbb} p_6^{Qbb} \times \text{Gaus}(m, p_7^{Qbb}, p_8^{Qbb}) \end{aligned} \quad (\text{A.3})$$

Note that open bottom process includes the decay chain of $B \rightarrow J/\psi + X \rightarrow \mu^+ \mu^- + X$, thus J/ψ mass peak is seen in the open bottom dimuon simulation. At the step of data fitting, the parameters of J/ψ part is constrained so that it should be consistent with J/ψ peak.

APPENDIX A. MUON BACKGROUND ESTIMATION WITH DIMUON EVENTS

A.2.2.3 Drell-Yan + Z^0

$$\gamma_*(m) = p_0^{\gamma*} \times \left[\exp(1 + p_1^{\gamma*}m + p_2^{\gamma*}m^2 + p_3^{\gamma*}m^3) \times \frac{1}{2} \left(1 + \text{Erf} \left(\frac{m - p_4^{\gamma*}}{p_5^{\gamma*}} \right) \right) \right] \quad (\text{A.4})$$

A.2.2.4 J/ψ , ψ' (Charmonia)

Combination of J/ψ and ψ' peaks are fitted with the following function:

$$\psi(m) = p_0^\psi \times [F_\psi(m, m_{J/\psi}) + p_3^\psi \times F_\psi(m, m_{\psi'})] W(m) \quad (\text{A.5})$$

where $F_\psi(m, m_{J/\psi})$ or $F_\psi(m, m_{\psi'})$ are the convolution of Gaussian and asymmetric Lorentzian

$$F(m, m_{J/\psi}) \equiv \int \text{Gaus}(m', m_{J/\psi} \cdot p_1^\psi, p_2^\psi) \cdot L(m' - m) dm' ,$$

$$L(m) \equiv \begin{cases} 1/(1 + (p_3^\psi m)^2) & (m < 0) \\ 1/(1 + (p_4^\psi m)^2) & (m > 0) \end{cases} ,$$

and $W(m)$ is

$$W(m) \equiv \frac{1}{2} \left(1 + \text{Erf} \left(\frac{m - p_5^\psi}{p_6^\psi} \right) \right) \times \frac{1}{2} \left(1 - \text{Erf} \left(\frac{m - p_7^\psi}{p_8^\psi} \right) \right) , \quad (\text{A.6})$$

Note that ψ' process includes the decay chain of $\psi' \rightarrow J/\psi + X \rightarrow \mu^+ \mu^- + X$. The scaling of mass peak position is allowed in the fitting. The same mass width is assumed for both J/ψ and ψ' since the difference of the mass is small.

A.2.2.5 Upsilon states

For Upsilon states we consider $\Upsilon(1S)$, $\Upsilon(2S)$, $\Upsilon(3S)$. Upsilon states are fitted with the following function:

$$\Upsilon(m) = p_0^\Upsilon \times [f_{1S} \times F(m, m_{\Upsilon(1S)}) + f_{2S} \times F(m, m_{\Upsilon(2S)}) + f_{3S} \times F(m, m_{\Upsilon(3S)})] \times W(m) \quad (\text{A.7})$$

where $F(m, m_\Upsilon)$ is the convolution of Gaussian and asymmetric Lorentzian

$$F(m, m_\Upsilon) \equiv \int \text{Gaus}(m', m_\Upsilon \cdot p_1^\Upsilon, p_2^\Upsilon) \cdot L(m' - m) dm' ,$$

$$L(m) \equiv \begin{cases} 1/(1 + (p_3^\Upsilon m)^2) & (m < 0) \\ 1/(1 + (p_4^\Upsilon m)^2) & (m > 0) \end{cases} ,$$

and $W(m)$ is

$$W(m) \equiv \frac{1}{2} \left(1 + \text{Erf} \left(\frac{m - p_5^\Upsilon}{p_6^\Upsilon} \right) \right) \times \frac{1}{2} \left(1 - \text{Erf} \left(\frac{m - p_7^\Upsilon}{p_8^\Upsilon} \right) \right) , \quad (\text{A.8})$$

respectively, and relative fractions of $\Upsilon(1S)$, $\Upsilon(2S)$, $\Upsilon(3S)$ (f_{1S} , f_{2S} , f_{3S}) are fixed. $F(m, m_\Upsilon)$ is basically the convolution of Gaussian and asymmetric Lorentzian, and additional window function $W(m)$ is applied. The asymmetric structure of Upsilon mass peak (represented by the asymmetric Lorentzian) would be explained by the asymmetric momentum smearing at high momentum region.

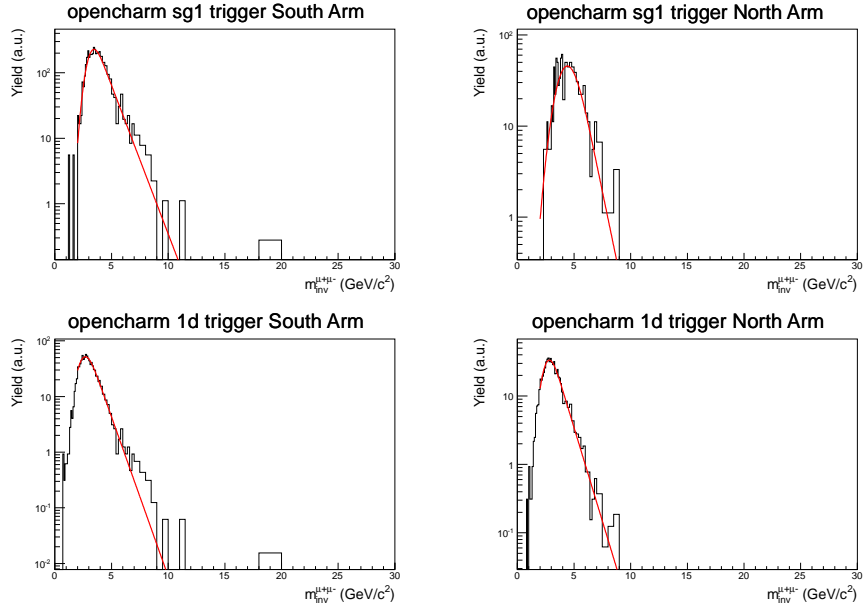


Figure A.2: Simulated mass spectrum of open charm process and fit results for South and North Arms.

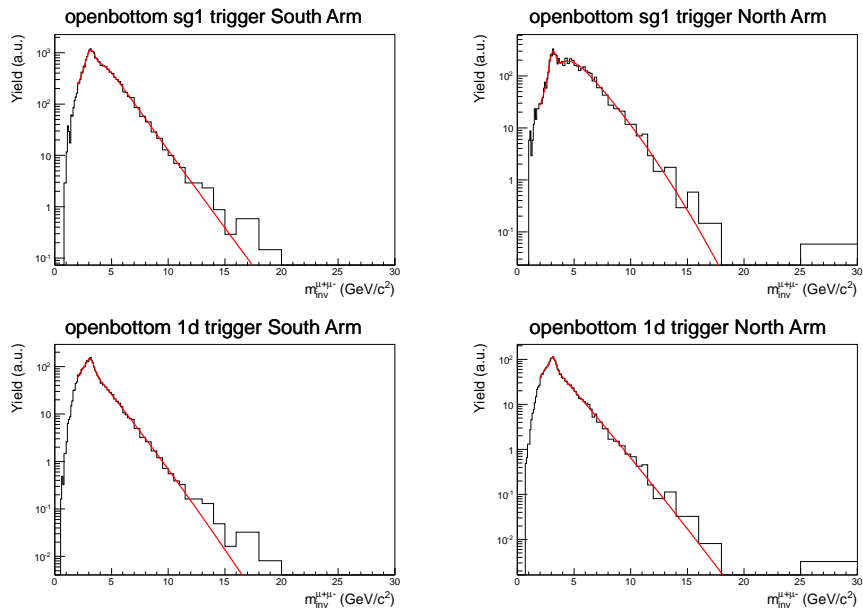


Figure A.3: Simulated mass spectrum of open bottom process and fit results for South and North Arms.

APPENDIX A. MUON BACKGROUND ESTIMATION WITH DIMUON EVENTS

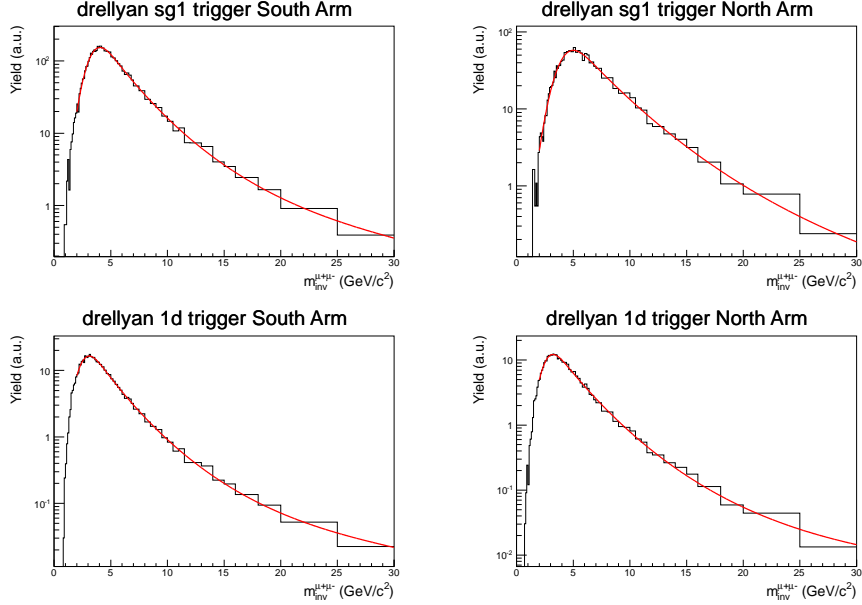


Figure A.4: Simulated mass spectrum of Drell-Yan+ Z^0 process and fit results for South and North Arms after applying SG1 trigger efficiency.

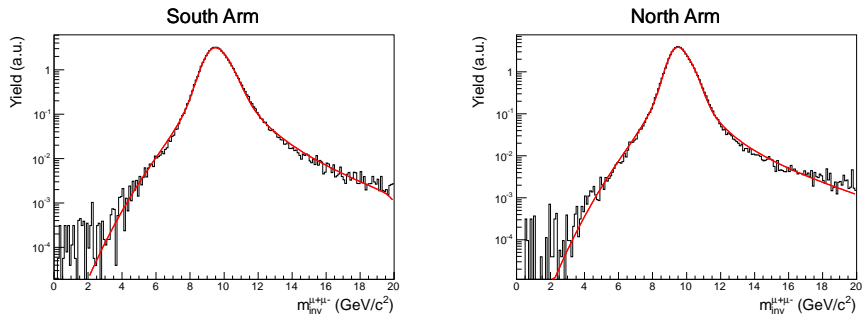


Figure A.5: Simulated mass spectrum of the sum of Υ family and fit results for South and North Arms.

A.2.3 Effect of Mutrg-SG1 trigger to different physics processes

Figure A.6 shows the dimuon yield spectrum for South and North Arm with MuID-1D and SG1 triggers normalized by the integrated luminosity of each trigger. At high mass region such as $m_{\text{inv}}^{\mu+\mu-} > 8 \text{ GeV}/c^2$ the yield of the two triggers roughly match despite the very low statistics of MuID-1D trigger, however, the yield of WTRG(S,N) trigger is suppressed significantly in the lower mass region. This suppression is considered to be the effect of WTRG(S,N) trigger.

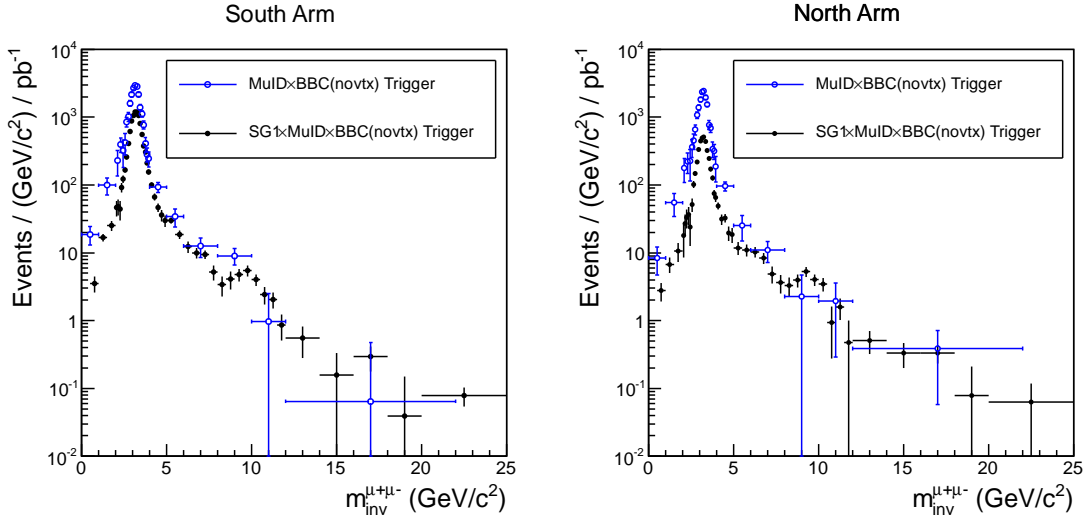


Figure A.6: Dimuon yield comparison between MuID-1D and WTRG(S,N) trigger after normalized with the integrated luminosity of each trigger.

To check how Mutrg-SG1 trigger works for different physics process, Mutrg simulator was used. According to the simulation, The degree of suppression is quite different between processes. The Drell-Yan process keeps flat value of about 78 % above $10 \text{ GeV}/c^2$. The Upsilon states almost suffers the efficiency of Mutrg-SG1 trigger flatly, reflecting the fact of having sufficiently high momenta of both muons decayed from the resonances.

Open bottom and open charm processes exhibit flat efficiency value for $m_{\text{inv}}^{\mu+\mu-} > 10 \text{ GeV}/c^2$, since muons from these processes are decay products. The efficiency value is lower in open charm process than in open bottom process, reflecting relatively lower momenta of muons in open charm process. Remarkably the WTRG(S,N) trigger efficiency is different between South and North Muon Arms by more than factor of 2 for J/ψ process. Qualitatively these characteristics are consistent with the difference of the yield between the two triggers that is seen in Figure A.6.

For charmonia and open heavy flavor processes, it is considered that the Mutrg-SG1 trigger efficiency is sensitive to the shape of the turn-on curve of SG1 trigger in the real case, thus a possible slight difference of SG1 trigger efficiency between the real data and simulation could reflect to the yield. In particular, it was found that the relative J/ψ yield between South and North Arm in Mutrg-SG1 trigger in the actual data deviated about 20 % from the expectation in the simulation, and this deviation is considered to be the precision of SG1 trigger simulation around the turn-on region of the muon momentum. The estimation of open heavy flavor processes relies on the mass spectrum shape under the J/ψ mass peak, thus using WTRG(S,N) trigger data for estimating cross section of these processes would make large systematic biases. Moreover, according to the simulation the yield of open charm and open bottom is largely

APPENDIX A. MUON BACKGROUND ESTIMATION WITH DIMUON EVENTS

suppressed by Mutrg-SG1 trigger, which would result in reducing the sensitivity to these processes under the J/ψ mass peak. On the other hand, the plateau value of Mutrg-SG1 efficiency turn-on curve is well-described with the simulation. Considering these circumstances, we will perform a simultaneous fitting of both WTRG(S,N) and MuID-1D trigger data with using the common scale factor of each physics process.

A.3 Fitting of dimuon mass spectrum

A.3.1 Procedure

We set the fitting range of mass spectrum as follows:

- $2.0 < m_{\text{inv}}^{\mu+\mu^-} < 22.0 \text{ GeV}/c^2$ for MuID-1D trigger in both Arms
- $5.0 < m_{\text{inv}}^{\mu+\mu^-} < 25.0 \text{ GeV}/c^2$ for SG1 trigger in South Arm
- $7.0 < m_{\text{inv}}^{\mu+\mu^-} < 25.0 \text{ GeV}/c^2$ for SG1 trigger in North Arm .

The mass range for SG1 trigger was chosen so that the SG1 trigger efficiency is larger than 80 %. With the mass range above, Drell-Yan and Upsilon states are mainly determined by the SG1 trigger data points, and open heavy flavors and J/ψ are mainly determined by the MuID-1D trigger data points. We assumed the same k -factor for J/ψ and ψ' processes. The simulated mass spectrum for MuID-1D trigger is corrected by the difference of relative efficiency between SG1 trigger and MuID-1D trigger listed in Table A.1. The error of relative efficiency is added to the error of MuID-1D data points in calculation of chi-square. We treated all data points are statistically independent and composed a chi-square by combining the two triggers for both Arms. Strictly speaking the data points between the two triggers are NOT statistically independent, and the correlation between the two trigger data should be considered. However we can approximate that all data points are statistically independent, because the sensitivity to individual process owes to mostly either of the two triggers. For example, J/ψ yield is only estimated with MuID-1D trigger data points, and Drell-Yan process is determined with SG1 trigger data points. In the fitting process, the following parameters are allowed to be free:

- Scale of Drell-Yan, Υ family, open bottom, open charm, $J/\psi(\psi')$. All these scales are common for both Arms and the two triggers.
- Scale of J/ψ mass scale for each Arm individually. ψ' mass is forced to scale together with J/ψ mass scale.
- Scale of Υ family mass scale for each Arm individually.

Figure A.7 shows the result of fitting.

process	Raw scaling	(Error percentage)
Drell-Yan	1.75 ± 0.24	15 %
Υ states	3.10 ± 0.46	15 %
open bottom	0.61 ± 0.28	39 %
open charm	2.71 ± 0.72	27 %
charmonia	1.32 ± 0.03	2 %

Table A.2: Results of the fitting.

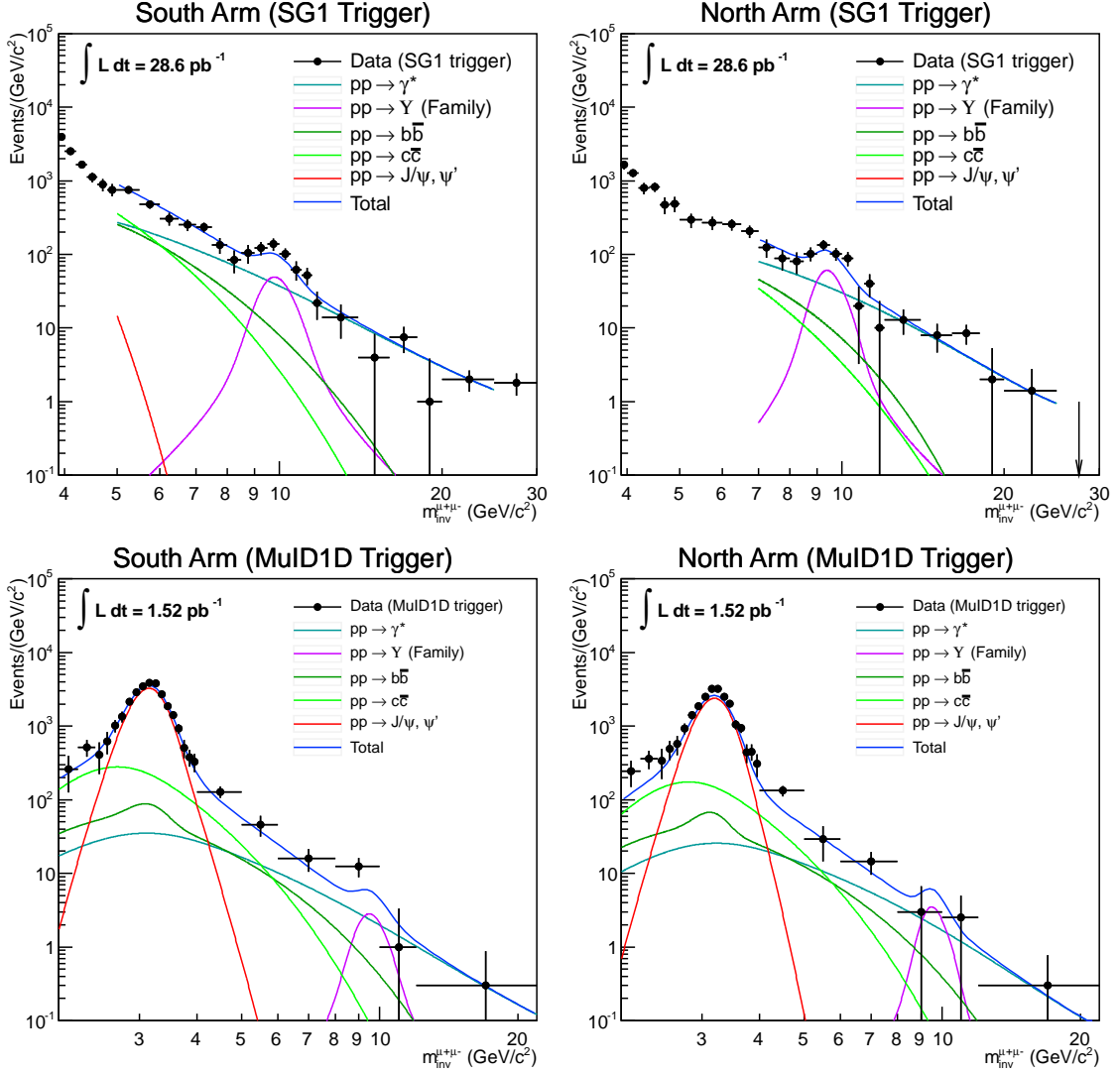


Figure A.7: Result of fitting dimuon data with combining the South and North Arms for the WTRG(S,N) and MuID-1D triggers.

Item	Uncertainty
Absolute acceptance × efficiency	14 %
Relative efficiency correction (SG1 trigger)	7 %
SG1 Trigger efficiency	5.5 %
MuID-1D Trigger efficiency	3 %
BBC(novtx) Trigger efficiency	5.5 %
Luminosity	10 %
Total	17 % _(efficiency) ⊕ 10 % _(luminosity) = 20 %

Table A.3: Table of systematic errors about efficiencies and luminosity

APPENDIX A. MUON BACKGROUND ESTIMATION WITH DIMUON EVENTS

A.3.2 Results

After the efficiency correction, the final correction scales to the PYTHIA cross section are obtained as listed in Table A.4.

process	correction scale factor	Error
Drell-Yan	2.20	$0.31_{\text{(stat)}} \oplus 0.38_{\text{(eff)}} \oplus 0.22_{\text{(lumi)}} = 0.54$
Υ states	3.90	$0.61_{\text{(stat)}} \oplus 0.66_{\text{(eff)}} \oplus 0.39_{\text{(lumi)}} = 0.98$
open bottom	0.77	$0.39_{\text{(stat)}} \oplus 0.13_{\text{(eff)}} \oplus 0.08_{\text{(lumi)}} = 0.42$
open charm	3.41	$1.00_{\text{(stat)}} \oplus 0.58_{\text{(eff)}} \oplus 0.04_{\text{(lumi)}} = 1.16$
charmonia	1.66	$0.29_{\text{(stat)}} \oplus 0.28_{\text{(eff)}} \oplus 0.17_{\text{(lumi)}} = 0.44$

Table A.4: Final results of cross section correction factors in this study.

Appendix B

Development of Mutrg simulator

Mutrg simulator was developed to study SG1 trigger efficiency. The structure of the simulator will be described in this section.

B.1 Drift of ionized electrons in the gap

The reproduction of discrimination timing of pulses is essential for simulating Mutrg, because the timing resolution of the MuTr is wider than one beam-clock with reflecting the drift velocity of ionized electron in the gas in the MuTr gaps. Thus a Garfield simulation[72] was performed.

The arrival timing of ionized electron to the anode wires for a injected charged particle depends on the injection position and direction. Since the MuTr wires are approximately stretched perpendicular to the radial direction, the dependence is approximately reduced to the offset of the injection point closest to the nearest anode wire in the injection-side cathode plane (d_r), and the injection angle with respect to the beam axis (θ). It is assumed that the injection point is statistically randomized and the correlation of injection points between gaps are ignored. Then d_r dependence is averaged and only θ dependence is considered.

Figure B.1 shows the simulated arrival time distribution for different injection angle. When the injection angle is smaller the tail part of the distribution is large, which consists of particle injections whose d_r is relatively larger. The arrival time distributions by injection angles are fed to the Mutrg simulator.

B.1.1 Selection of arrival time of ionized electrons

The Mutrg simulator employs PISA tracking simulation for creation of hits in MuTr and tracking. After the reconstruction process with MuonDeV, in the Mutrg simulator each hit in `TMutHit` the algorithm finds the associated track in `TMutTrk` and calculate the incident angle θ . If no associated track is found, it finds the associated `coord` in `TMutCoord` then estimates the incident angle by calculating the angle of the line between the origin and the `coord`. If no associated `coord` is found, the incident angle is assumed to be 15 deg. This calculation is performed only once for a track and all hits in the track share the same incident angle.

After determining the incident angle, the simulator looks up the corresponding timing probability distribution described in the previous section and randomly choose an arrival time. The arrival time is shared among hits in the same `coord`, but independent selection is performed for different gaps.

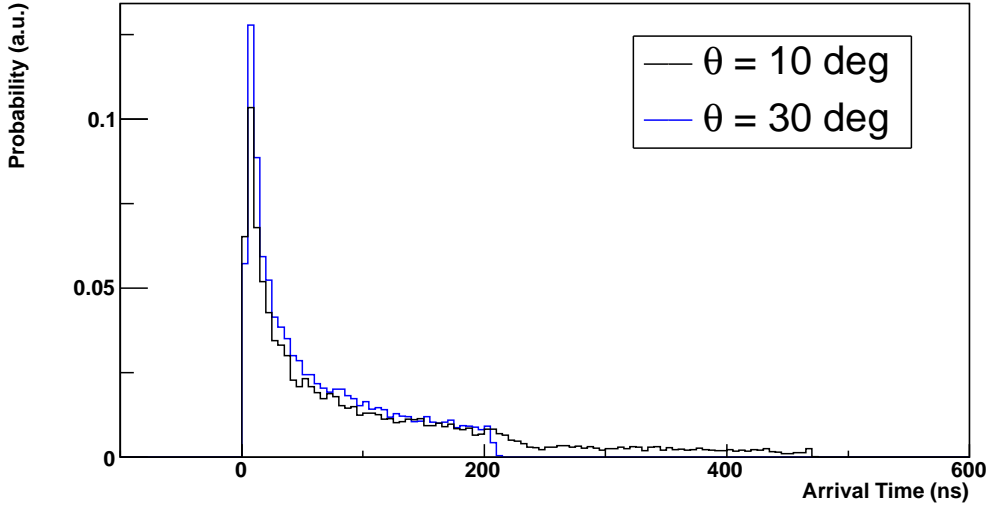


Figure B.1: The arrival time distribution for different incident angles into MuTr based on Garfield simulation.

B.1.2 Time walk, jitter

The arrival time is smeared considering the so-called time walk and the jitter. The time walk is calculated when we turn on the LED (Leading Edge Discriminator) flag. The time walk is determined by referring the charge of the hit. In the CFD (Constant Fraction Discriminator) mode, the time walk is not concerned¹.

After calculating the time walk the simulator calculates the jitter. The size of jitter is pulse-height dependent, i.e.

$$\sigma_{\text{jitter}} = \sigma_0 \oplus \frac{\sigma_1}{q} . \quad (\text{B.1})$$

B.2 Hit efficiency

Mutrg ADTX shares only $\sim 5\%$ of the charge of total charge on the strip, and the Mutrg hit efficiency is different from MuTr hit efficiency. A turn-on curve using Gaussian error function is assumed.

B.2.1 GTM tuning

Mutrg has a system of fine timing tuning within 1BCLK by tweaking the phase of GTM into the Mutrg logic boards to realize the maximum trigger efficiency. The emulation of GTM tuning is performed in the simulator by setting an arbitrary global offset to the arrival time.

¹However in the actual runs Mutrg is always operated in LED mode because the pipeline length is too short to use CFD mode.

B.2.2 LL1 width, AND/OR logic, clustering

The functions of Mutrg and LL1 logics, in particular LL1 width, AND2/AND3/OR logic selection and Clustering option are directly implemented in the simulator. For the detail of these functions, see the reference.

B.2.3 Trigger Map

After these processes, a set of hit patterns to be compared with the trigger map is created. For each event, there are 7 hit patterns corresponding to the 7BCLK (-3BCLK, -2BCLK, ..., ± 0 BCLK, ..., +3BCLK) around the collision, and the pattern differs for each BCLK. The hit pattern is compared with the trigger map, and once the pattern matches with the trigger map the SG1 triggerbit is issued in the simulator. Note that currently the triggerbit is issued for the event and not issued for the track (i.e. the triggerbit is not associated to tracks), it might need further improvements when we study multi-track events.

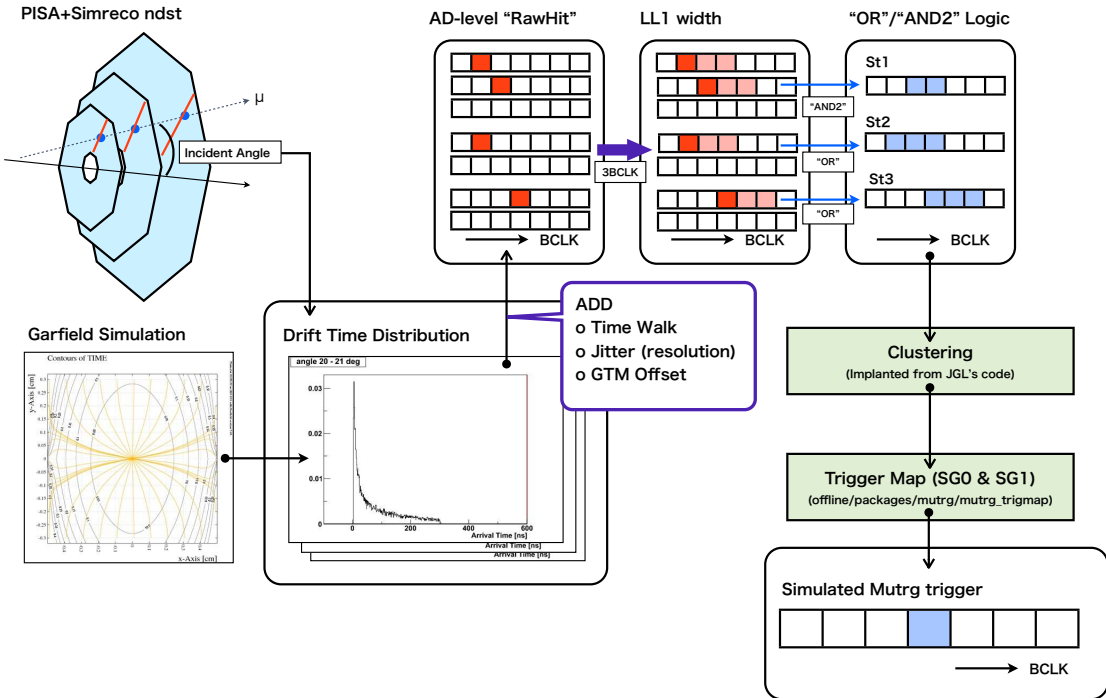


Figure B.2: Schematic drawing of the Mutrg simulator

APPENDIX B. DEVELOPMENT OF MUTRG SIMULATOR

Appendix C

Variable distributions for $J/\psi \rightarrow \mu^+\mu^-$ events

As a check of the validation of the simulation, the distributions of variables for J/ψ muons were compared between real data and the simulation of the reference run. The following requirements were applied for both the data and the simulation.

- Trigger: WTRG(S,N)
- Kinematic cuts
 - $2.5 < m_{\text{inv}} < 4.0 \text{ GeV}/c^2$
 - opposite charge pairs
 - $1.2 < |\phi_0 - \phi_1| < 5.8$
- Tag-side track requirements
 - MuID lastGap==4
 - DG0 < 7.0
 - DDG0 < 4.0
 - $\chi^2_{\text{track}} < 7.0$
 - DCA_r < 5.0
- Probe-side track requirements
 - $|\eta| > 1.4$
 - $p_T^{\text{reco}} > 3.0 \text{ GeV}/c$

Figure C.1 shows the results.

APPENDIX C. VARIABLE DISTRIBUTIONS FOR $J/\psi \rightarrow \mu^+ \mu^-$ EVENTS

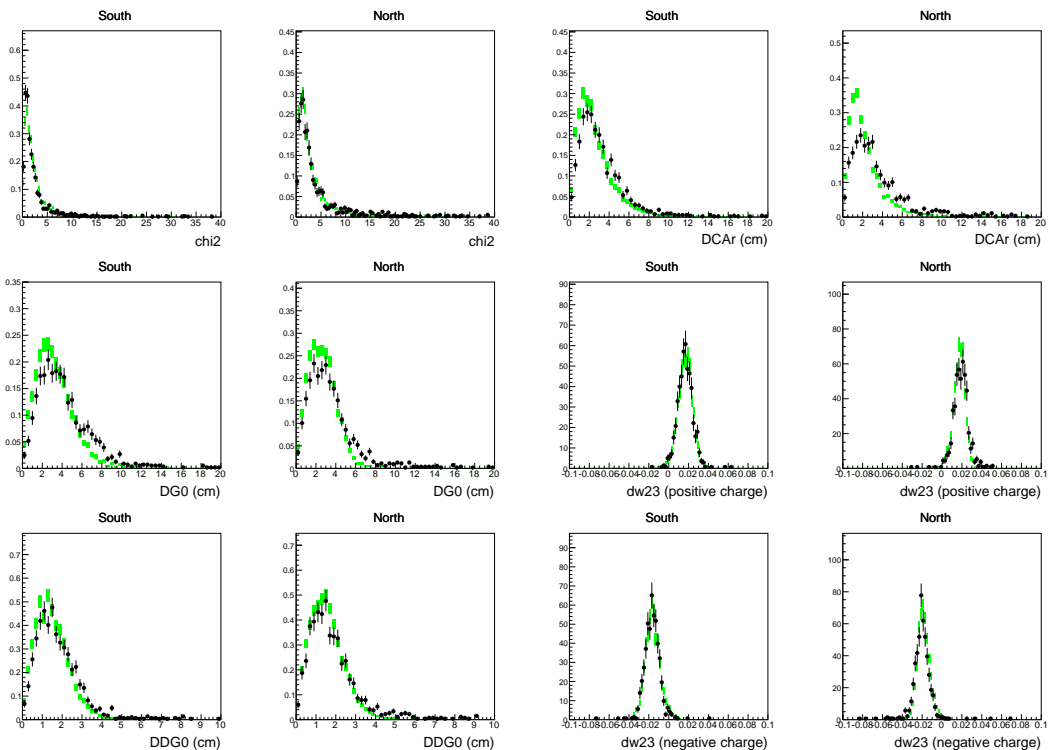


Figure C.1: Kinematic variable distributions for J/ψ probe-muons in the data and the simulation. The black bullets are the data, and the green bands are the simulation.

Appendix D

Pseudo multiple vertex simulation and DCA_z

D.1 Simulation of multiple collision events

For the evaluation of the performance of multiple vertex reconstruction algorithm with the BBC called `BbcMultipleVtx` as described in Sec. 4.1.2, we need to simulate multiple collision events. However, the standard PISA simulation does not have a function to reproduce multiple collisions with independent t_0 . Thus we developed an event merging tool. For simulating multiple collision events, one has to distribute each collision so that it obeys observed z_{vtx} and t_0 distribution. The practical diagram of event merging in the simulation is shown in Figure D.1.

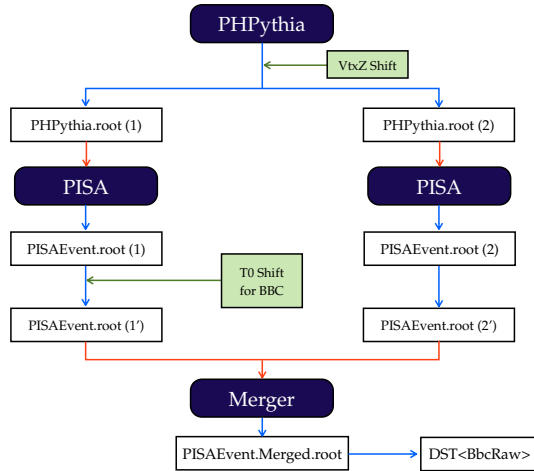


Figure D.1: Diagram of merging two collisions in simulation.

Then we performed event simulations with multiple collisions for $p + p \rightarrow W^\pm$ process with Pythia. We are interested in how accurate the vertex candidates we reconstruct are in case of multiple collision events and how they vary with the multiple collision parameter μ^1 . First we prepare two sets of simulation data:

¹ μ is the average number of collisions per bunch crossing, as the main part of the thesis.

APPENDIX D. PSEUDO MULTIPLE VERTEX SIMULATION AND DCA_Z

1. Pythia simulation of $p + p \rightarrow W^\pm$ with z_{vtx} distribution of gaussian with the mean position of $z = 0$ cm and the width of $\sigma_z = 35$ cm, and with t_0 distribution of gaussian with $\sigma_t = 1.5$ ns. We call this simulation set as S_W .
2. Different two sets of Pythia $p + p$ general process simulation, with the same z_{vtx} and t_0 distribution. We call these two simulation sets as $S_L^{(a)}, S_L^{(b)}$, respectively.

We generated 10,000 events for each process. Then we merged S_W and $S_L^{(a)}$ and created double collision data sets of W^\pm and light process, denoted as S_{W+L} . Similarly, by merging $S_W, S_L^{(a)}$, and $S_L^{(b)}$ we created triple collision data sets of W^\pm and another two light processes, denoted as S_{W+L+L} . If we consider the case of $\mu < 1.0$, it is substantially sufficient to consider up to three collisions.

Figure D.2 shows the result of this simulation for conventional BBC reconstruction and BbcMultipleVtx (binsize= 0.5 ns) for $\mu = 0.6$, where we took the collision vertex of $p + p \rightarrow W^\pm$ process as the true vertex. Since BbcMultipleVtx reconstruction could have more than one vertex candidates, we chose the most closest candidate to the true vertex of $p + p \rightarrow W^\pm$ for evaluation. The result shows that BbcMultipleVtx has more probability to have a z_{vtx} candidate which is closer than the conventional reconstruction.

Next we compared the μ -dependence of the width of this distribution. Here we used 66.7% integration full width range of the distribution as the measure of this comparison. Figure D.3 shows the μ -dependence of the width for the conventional reconstruction (Sec. 4.1.1) and BbcMultipleVtx. As shown in Figure D.3, BbcMultipleVtx has better tolerance to μ than the conventional reconstruction. Moreover, it is remarkable that BbcMultipleVtx has sharper width even at $\mu \rightarrow 0$ limit. The possible reason is that the clustering algorithm of the BbcMultipleVtx sets narrower scope to hits used to calculate the arrival time of the particles, and that will automatically reject outlier hits such like backscattering particles.

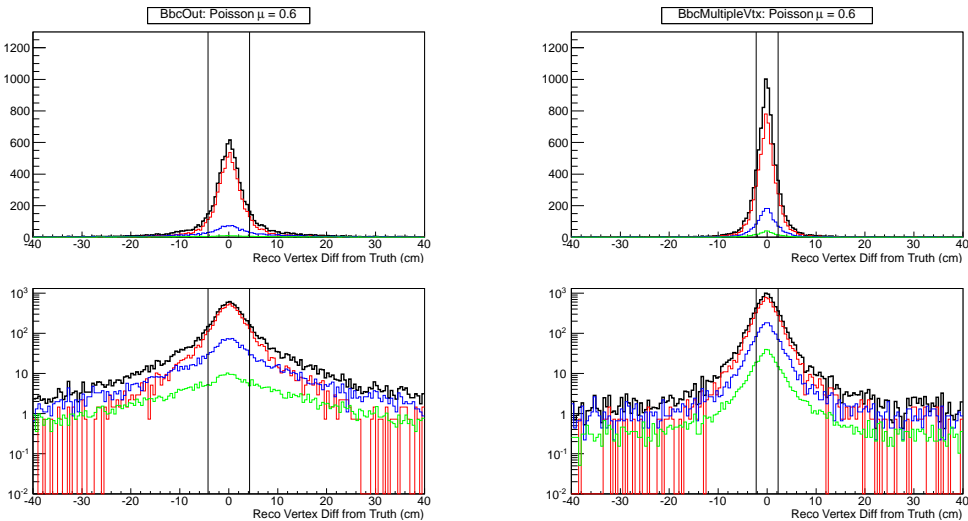


Figure D.2: (Left) Difference between reconstructed vertex and true vertex for $p + p \rightarrow W^\pm$ process with conventional BBC reconstruction in $\mu = 0.6$ case (simulation). Red: single collision, Blue: double collision, Green: triple collision, Black: total in $\mu = 0.6$. Vertical lines show 66.7% region. (Right) For BbcMultipleVtx algorithm with binsize = 0.5 ns.

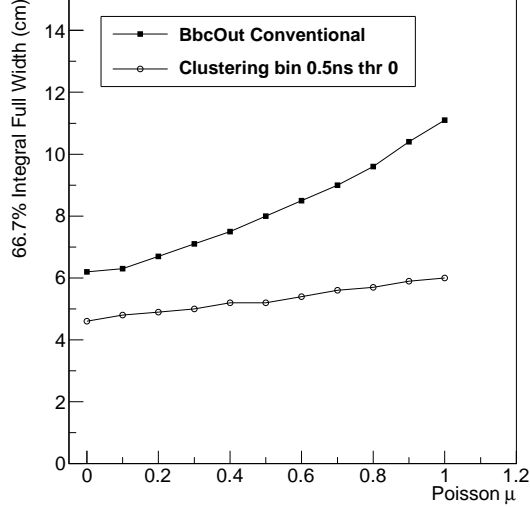


Figure D.3: Comparison of accuracy of reconstructed vertex between the conventional BBC reconstruction and BbcMultipleVtx for different multiple collision parameters.

D.2 DCA_{*z*} with multiple vertices

Next we evaluate the performance of obtaining DCA_{*z*} with the BbcMultipleVtx reconstruction. In case of multiple collisions, the algorithm does not necessarily find the accurate vertex, and even it is possible to indicate ghost vertices. Thus we define the DCA_{*z*} of the track with the BbcMultipleVtx reconstruction as the DCA_{*z*} which gives the smallest absolute value. This definition is justified by the following reasons:

1. We are interested in $p_T > 15$ GeV/*c* muons of which the multiple scattering effect inside the absorber is small. For these high p_T true muons, tracking back to the vertex will reach to the true collision point within a few cm and this is comparable to the intrinsic z_{vtx} position resolution of BBC for p + p collision.
2. As presented in Sec.6.3.1 for “hard” collision events such like W^\pm production or π^0 production, the trigger efficiency of BBC is about 90 %. This means that most of cases $W^\pm \rightarrow \mu^\pm$ events have hits in both BBC. Then we can expect we have accurate vertex candidates among which are reconstructed by the BbcMultipleVtx algorithm with about 90 % probability. Thus for true high- p_T muons, selecting the smallest DCA_{*z*} is a good guess for the DCA_{*z*} to the true vertex.

D.3 DCA_{*z*} afterburner

The above merging simulation is possible to simulate only for the BBC, and is not compatible with the Muon Arm simulations. Then we developed a tool called “DCA_{*z*} afterburner” to calculate DCA_{*z*} for multiple collisions with BbcMultipleVtx in the simulation. The key of this afterburner is to prepare a data bank of BBC multiple vertex reconstruction results for each physics process in advance, then to provide the BBC reconstruction results to simulated pDSTs randomly. The schematic diagram of this afterburner is shown in Figure D.4. The flow of the process is as follows:

APPENDIX D. PSEUDO MULTIPLE VERTEX SIMULATION AND DCA_z

1. Define a multiple collision parameter μ arbitrarily.
2. Extract the true z_{vtx} of track of the specified process.
3. Determine the number of collisions of the event according to the Poisson distribution with μ .
4. Ask the data bank of the specified physics process to randomly extract one BBC reconstruction event for the z_{vtx} of the event.
5. Calculate the smallest DCA_z for each vertex candidate reconstructed by `BbcMultipleVtx`, as well as DCA_z of the conventional BBC reconstruction.

Note that this simulation decouples the correlation between particles which pass through muon arms and particles hitting the BBC. If we have large correlation between the BBC reconstruction and the Muon Arm reconstruction, we would have significant systematic uncertainty in simulation. Figure D.5 shows the result of simulated DCA_z distributions for $p + p \rightarrow W^\pm$ process with using different vertex reconstruction algorithms. The same reconstruction procedure was applied to all the signal and background simulations with the average μ value in year 2011 runs ($\mu \simeq 0.30$).

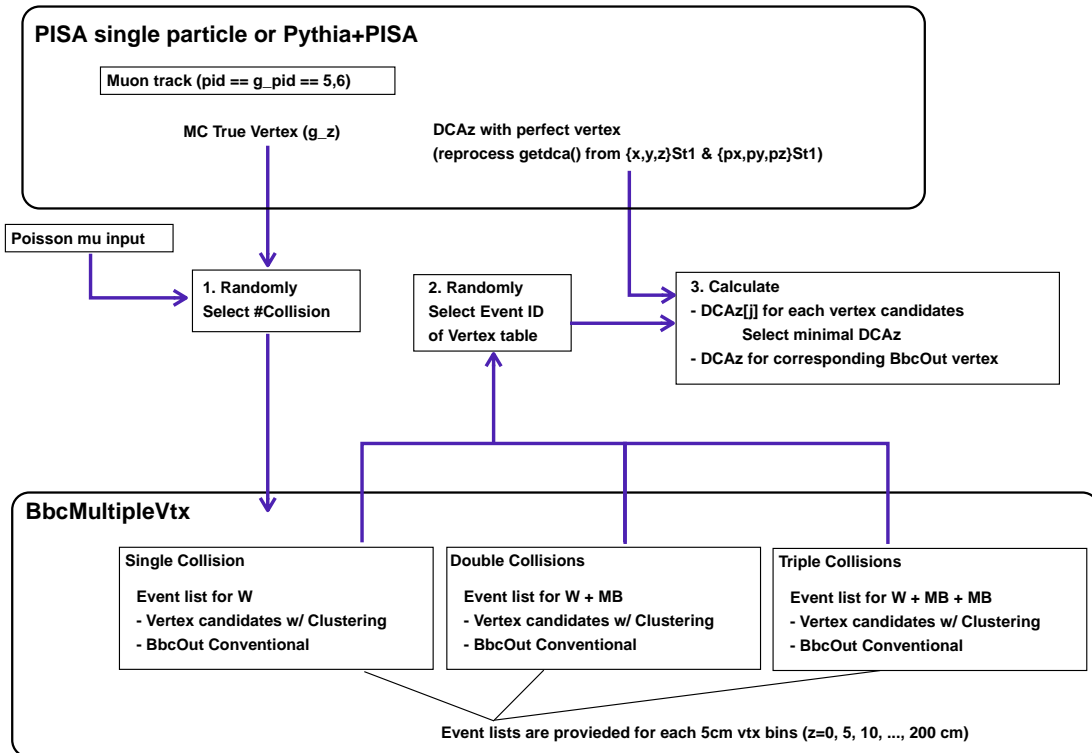


Figure D.4: The process diagram of DCA_z afterburner

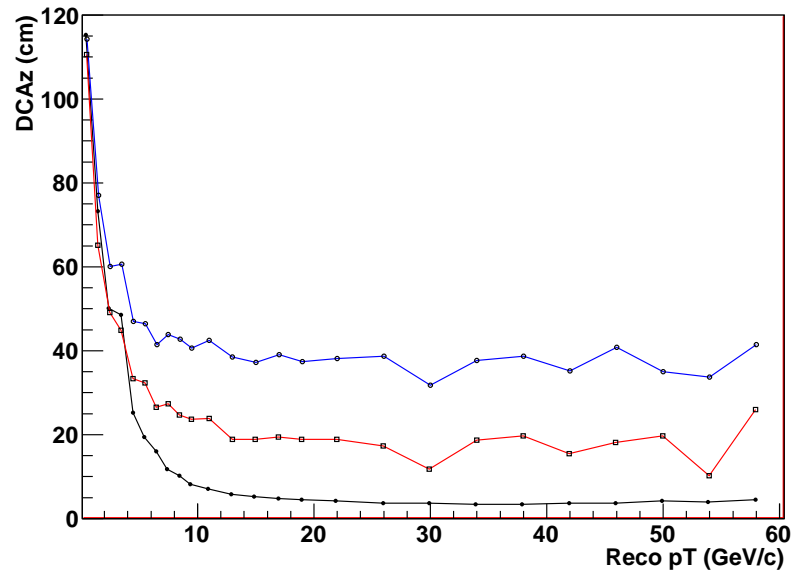


Figure D.5: DCA_z 97% contour line for $p + p \rightarrow W^\pm$ process as a function of reconstructed p_T with multiple collision parameter $\mu = 0.3$. Blue: using the conventional BBC reconstruction, Red: using the `BbcMultipleVtx` reconstruction, Black: using the true vertex of the MC.

APPENDIX D. PSEUDO MULTIPLE VERTEX SIMULATION AND DCA_Z

Appendix E

Determination of unpolarized PDFs

In this section, let us review experimental determinations of unpolarized PDFs as an introduction to techniques of constraining PDFs. The Q^2 -dependence of PDFs are described with DGLAP evolution equations, but x -dependence is not known from the pQCD. Thanks to the factorization theorem, if we stick with a particular scheme we can apply PDFs universally to different types of interactions. The most precise way to obtain PDFs is to gather as much data as possible from different type experiments to probe wide x and Q^2 range and find the best single set of PDFs that fits to all available experimental data. These kinds of analyses are called “global analysis”. In global analyses the DGLAP evolution is used as a constraint of PDFs.

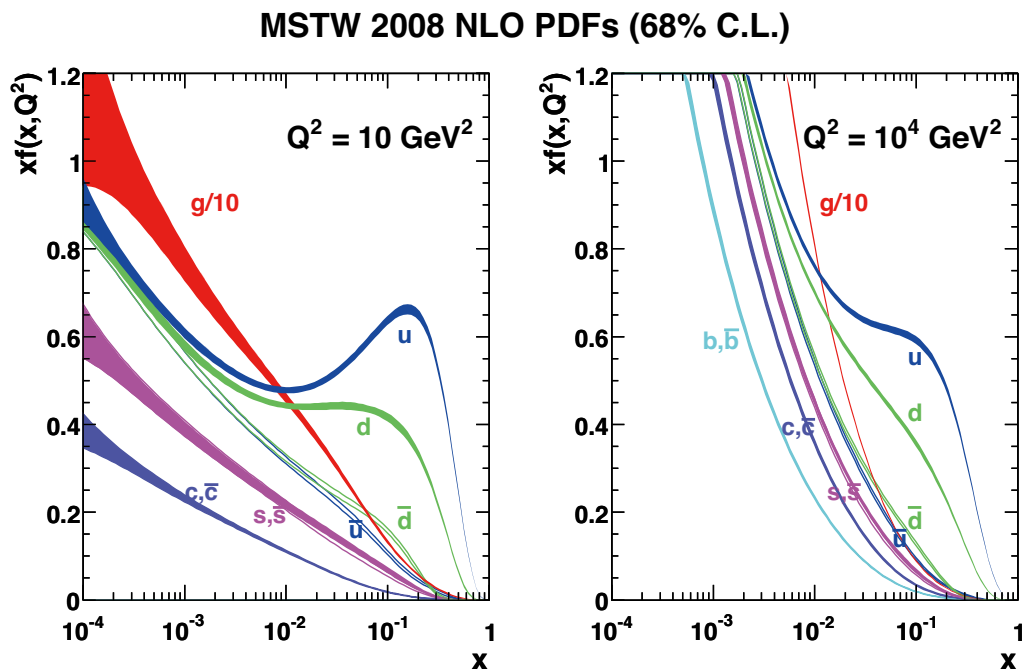


Figure E.1: MSTW08 unpolarized PDFs[85].

E.1 Sum rules

The measurement of hadron structure functions $F_{1,2}$ gives the sum of PDFs, but it does not decompose the components. However we have several constraints. First of all the momentum conservation requires Eq. (2.11). More specifically the momentum sum rule (2.11) is written as

$$\int_0^1 dx x \left[\sum_{u,d,s} q(x, Q^2) + \sum_{u,d,s,c,b} \bar{q}(x, Q^2) + g(x, Q^2) \right] = 1 \quad (\text{E.1})$$

for the proton, where $g(x, Q^2)$ is the gluon PDF.

Next, by thinking of the constituent quarks of the proton is two u -quarks and one d -quark, the net number of these quarks must be conserved, thus for u and d -quarks we obtain

$$\int_0^1 [u_p(x) - \bar{u}_p(x)] dx = 2, \quad \int_0^1 [d_p(x) - \bar{d}_p(x)] dx = 1, \quad (\text{E.2})$$

and for other quarks (s, c, b, t),

$$\int_0^1 [q_p(x) - \bar{q}_p(x)] dx = 0 \quad (q = s, c, b, t). \quad (\text{E.3})$$

Here we dropped Q^2 -dependence for the simplicity of notation, and the index p denotes the PDF is of the proton¹. The contributions of t -quarks are mostly negligible. Contributions of c, b -quarks are relatively small, but at very large Q^2 of $\mathcal{O}(10^4 \text{ GeV}^2)$ their contributions are comparable with s -quarks.

E.2 Valence quarks and sea quarks

In the above notation we discriminated quark distributions and antiquark distributions. Thinking about the proton is a bound state of (uud), antiquarks do not stably exist, and they should be continuously produced and annihilated by QCD interaction. In the terminology of the parton picture these antiquarks are called “sea quarks.” As antiquarks are produced with pairs of ($\bar{q}q$), not only antiquark-sea but quark-sea should exist. Thus conceptually the quark PDF is separated into two, one is from the original quarks and the other is from sea quarks. The former is called “valence quarks.” Often we discriminate valence quark PDFs and sea quark PDFs. In this case the quark PDFs are written as

$$q_p(x) = q_p^V(x) + q_p^S(x), \quad \bar{q}_p(x) = \bar{q}_p^S(x) \quad (\text{E.4})$$

where index V, S means valence quark and sea quark, respectively. Note that $q_p^S(x)$ is not necessarily identical to $\bar{q}_p^S(x)$, but it is often to assume these are the same. In the latest work of MSTW08 $s_p^S(x)$ and $\bar{s}_p^S(x)$ are discriminated, but for the other flavors $q_p^S(x) = \bar{q}_p^S(x)$ is assumed. The antiquark PDFs are also just called “sea-quark PDFs” in the literature, since no valence quarks contribute to antiquark PDFs.

¹If there is no index to express of which particle it is, the PDF is of the proton, implicitly.

E.3 Electromagnetic DIS

Experimentally we can probe protons and neutrons. Similar to the proton, we can think of PDFs of the neutron, and let us write them with index n . If we neglect electromagnetic interaction and think about the massless limit of constituent quarks, we can think the proton and the neutron is symmetric under $u \leftrightarrow d$ quark exchange, known as SU(2) *isospin* symmetry. Then we can assume

$$u_p(x) = d_n(x), \quad d_p(x) = u_n(x), \quad \bar{u}_p(x) = \bar{d}_n(x), \quad \bar{d}_p(x) = \bar{u}_n(x) , \quad (\text{E.5})$$

$$s_p(x) = \bar{s}_p(x) = s_n(x) = \bar{s}_n(x) . \quad (\text{E.6})$$

If we compare photon-exchange $F_2(x)$ for the proton and the neutron, at the leading order

$$F_2^{\gamma p}(x) = \left(\frac{2}{3}\right)^2 (u_p(x) + \bar{u}_p(x)) + \left(\frac{1}{3}\right)^2 (d_p(x) + \bar{d}_p(x)) \quad (\text{E.7})$$

$$\begin{aligned} F_2^{\gamma n}(x) &= \left(\frac{2}{3}\right)^2 (u_n(x) + \bar{u}_n(x)) + \left(\frac{1}{3}\right)^2 (d_n(x) + \bar{d}_n(x)) \\ &= \left(\frac{2}{3}\right)^2 (d_p(x) + \bar{d}_p(x)) + \left(\frac{1}{3}\right)^2 (u_p(x) + \bar{u}_p(x)) . \end{aligned} \quad (\text{E.8})$$

Thus

$$F_2^{\gamma p}(x) - \frac{1}{4}F_2^{\gamma n}(x) = \frac{7}{36}(u_p(x) + \bar{u}_p(x)) \quad (\text{E.9})$$

$$F_2^{\gamma p}(x) - 4F_2^{\gamma n}(x) = -\frac{31}{9}(d_p(x) + \bar{d}_p(x)) \quad (\text{E.10})$$

then we can separate $(u_p + \bar{u}_p)$ from $(d_p + \bar{d}_p)$. Or, we can also extract

$$F_2^{\gamma p}(x) - F_2^{\gamma n}(x) = \frac{1}{3}(u_p(x) - d_p(x)) \simeq \frac{1}{3}(u_p^V(x) - d_p^V(x)) \quad (\text{E.11})$$

which is almost free from antiquark PDFs in the approximation of $u_p^S(x) \approx d_p^S(x)$. If we subtract all quark contributions from momentum conservation (2.11), we obtain the neutral parton distribution, which is identified as gluon distribution. Note that it is known the gluon PDF is sizable; almost half of the total momentum of the proton is carried by gluons.

E.4 Neutrino DIS

Neutrino DIS is another approach to constrain PDFs (Figure E.2). Neutrino DIS is effective especially to determine $s(x)$ or $\bar{s}(x)$, since W^* boson couples with $s(\bar{s})$ -quark and mainly produces charm mesons, and charm boson production is suppressed for $d \rightarrow c$ channel because of CKM matrix element. Note that neutrino DIS is a parity-violating process, then we need to introduce another hadron structure function called F_3^{Wp} in addition to F_1^{Wp} and F_2^{Wp} for analyzing the data.

E.5 Drell-Yan process

According to the factorization theorem, the parton picture is valid not only lepton-hadron scattering but also hadron-hadron scattering. One representative interaction is lepton-pair

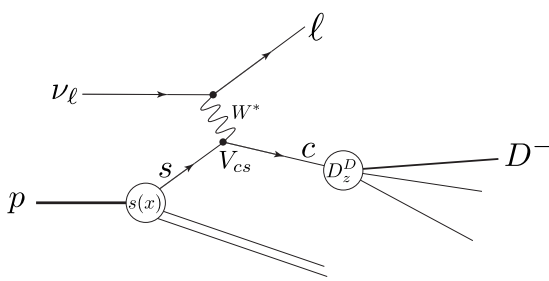


Figure E.2: A diagram of neutrino DIS which accesses to $s(x)$.

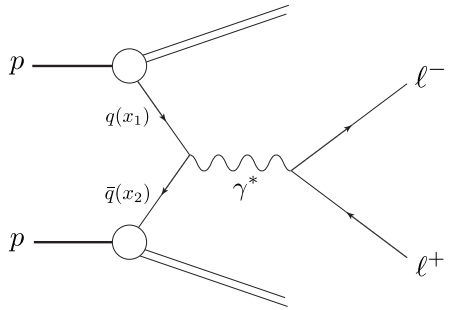


Figure E.3: A Drell-Yan diagram to produce a lepton pair in proton-proton collisions.

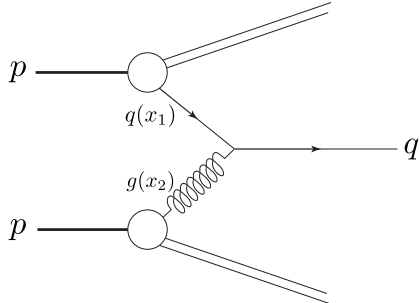


Figure E.4: A single jet production diagram in proton-proton collisions.

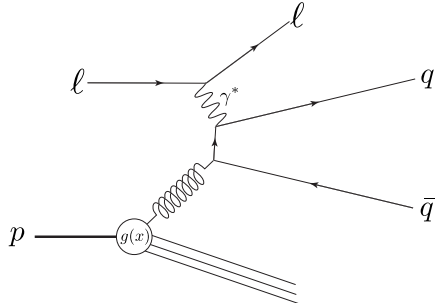


Figure E.5: A di-jet production diagram in DIS.

production in hadron-hadron collisions, called Drell-Yan process (Figure E.3). In this case two PDFs relate with the pair production. In case of proton-proton or proton-neutron collisions, the Drell-Yan process is sensitive to antiquark PDFs as a quark and an antiquark couple to produce a lepton pair. W/Z boson productions are very similar to Drell-Yan process and they are also sensitive to antiquark PDFs.

E.6 Jet productions

Jet productions in hadron-hadron collisions are also used for direct probing of gluon PDFs (Figure E.4). Also, in DIS at next-to-leading order (NLO) jet production has some sensitivity to gluon PDFs (Figure E.5).

E.7 Summary of unpolarized PDFs

In summary, the characteristics of unpolarized PDFs are the following:

- Valence quark PDFs $u(x), d(x)$ dominate at large x region, reflecting the existence of the valence quarks.
- $u(x)$ is larger than $d(x)$, reflecting that the proton consists of two u -quarks and one d -quark.
- $\int dx x g(x) \sim 0.5$. Gluons are the main conveyer of the momentum of the proton.
- $u(x)$ ($d(x)$) gets close to $\bar{u}(x)$ ($\bar{d}(x)$) at small x region, where sea quarks are dominant.

E.7 Summary of unpolarized PDFs

- The heavier the flavor of the sea quark the smaller the PDF. However at large Q^2 the difference of the mass of the quarks becomes less significant.

APPENDIX E. DETERMINATION OF UNPOLARIZED PDFS

References

- [1] L.W. Alvarez, F.Bloch, Phys. Rev. 57, 111 [1](#)
- [2] M. Gell-Mann, Phys. Lett. 8, 214 (1964) [1](#)
- [3] K. Nishijima, Prog. Theor. Phys. Vol. 13 No. 3 (1955) pp. 285-304 [1](#)
- [4] J.D. Bjorken, Phys. Rev. 148, 1467 (1966) [16](#)
- [5] E155 Collaboration, Phys. Lett. B493, 19 (2000). [16](#)
- [6] HERMES Collaboration, Phys. Rev. D75, 012007 (2007). [16](#)
- [7] **(MRST02)** A.D. Martin, et al. (MRST02), Eur.Phys.J.C28:455-473,2003 [30](#), [193](#)
- [8] **(DSSV)** D. de Florian, et al. (DSSV), Phys.Rev.D80:034030,2009 [18](#), [29](#), [30](#), [33](#), [193](#), [229](#)
- [9] **(PDG2012)** J. Beringer et al., Phys. Rev. D86, 010001 (2012) [14](#), [17](#), [20](#), [229](#), [235](#)
- [10] **(DSSV)** D. de Florian and W. Vogelsang, Phys. Rev. D81, 094020 (2010), hep-ph/1003.4533 [29](#), [30](#), [193](#), [229](#)
- [11] M. J. Alguard et al., Phys. Rev. Lett. 37, 1261 (1976) [16](#)
- [12] M. J. Alguard et al., Phys. Rev. Lett. 41, 70 (1978)
- [13] G. Baum et al., Phys. Rev. Lett. 45, 2000 (1980)
- [14] G. Baum et al., Phys. Rev. Lett. 51, 1135 (1983). [16](#)
- [15] **(EMC)** J. Ashman et al., Phys. Lett. B 206 (2) 364 (1988) [2](#), [16](#)
- [16] **(EMC)** J. Ashman et al., Nucl. Phy. B 328 (1989) 1-35 [2](#), [16](#)
- [17] **(E142)** P.L. Anthony et al., Phys. Rev. D54, 6620 (1996) [16](#)
- [18] **(E143)** K. Abe et al., Phys. Rev. D58, 112003 (1998)
- [19] **(SMC)** B. Adeva et al., Phys. Rev. D58, 112001 (1998)
- [20] **(SMC)** B. Adeva et al., Phys. Rev. D60, 072004 (1999) and Erratum-Phys. Rev. D62, 079902 (2000)
- [21] **(HERMES)** A. Airapetian et al., Phys. Rev. D75, 012007 (2007)
- [22] **(HERMES)** K. Ackerstaff et al., Phys. Lett. B404, 383 (1997)
- [23] **(E154)** K. Abe et al., Phys. Rev. Lett. 79, 26 (1997)
- [24] **(E154)** P.L. Anthony et al., Phys. Lett. B493, 19 (2000)
- [25] **(E155)** P.L. Anthony et al., Phys. Lett. B463, 339 (1999)

REFERENCES

- [26] (**Jlab-E99-117**) X. Zheng et al., Phys. Rev. C70, 065207 (2004)
- [27] (**COMPASS**) V.Yu. Alexakhin et al., Phys. Lett. B647, 8 (2007)
- [28] (**COMPASS**) E.S. Ageev et al., Phys. Lett. B647, 330 (2007)
- [29] (**COMPASS**) M.G. Alekseev et al., Phys. Lett. B690, 466 (2010)
- [30] (**CLAS**) K.V. Dharmawardane et al., Phys. Lett. B641, 11 (2006) [16](#)
- [31] (**STAR**) G. Agakishiev et al., Phys. Rev. D 85 (2012) 92010, hep-ex/1112.2980v1 [23](#), [189](#), [190](#), [229](#), [236](#)
- [32] (**UA1**) C. Albajar et al., Phys. Lett. B198, 271 (1987).
- [33] (**UA1**) C. Albajar et al., Z. Phys. C44, 15 (1989).
- [34] (**UA1**) J. Alitti et al., Z. Phys. C47, 11 (1990).
- [35] (**UA1**) J. Alitti et al., Phys. Lett. B276, 365 (1992).
- [36] (**CDF**) F. Abe et al., Phys. Rev. Lett. 76, 3070 arXiv:hep-ex/9509010
- [37] (**CDF**) A. Abulencia et al., J. Phys. G34, 2457 arXiv:hep-ex/0508029
- [38] (**D0**) S. Abachi et al., Phys. Rev. Lett. 75, 1456 arXiv:hep-ex/9505013
- [39] (**D0**) B. Abbott et al., Phys. Rev. D61, 072001 arXiv:hep-ex/9906025
- [40] (**ATLAS**) G. Aad et al., JHEP 12, 060 arXiv:1010.2130
- [41] (**CMS**) V. Khachatryan et al., JHEP 01, 080 (2011), arXiv:1012.2466
- [42] (**CMS**) S. Chatrchyan et al., JHEP 10, 132 (2011), arXiv:1107.4789 [23](#), [229](#)
- [43] (**PHENIX**) A. Adare et al. PHENIX Collaboration, Phys.Rev.Lett.106:062001,2011 [31](#), [189](#), [229](#), [235](#)
- [44] (**STAR**) M. Aggarwal et al., Phys. Rev. Lett. 106 (2011) 062002. [31](#), [32](#), [229](#), [235](#)
- [45] A. Zelenski et al., Hyperfine Interactions 127, 475 (2000), 10.1023/A:1012682104479. [37](#), [38](#), [229](#)
- [46] P. Sona, Energia Nucleare 14, 295 (1967) [37](#)
- [47] Y. S. Derbenev et al., Part. Accel. 8, 115 (1978) [39](#)
- [48] S.R. Mane, et al., J. Phys. G: Nucl. Part. Phys. 31 (2005) R151-R209 [39](#), [40](#), [230](#)
- [49] I. Alekseev, et al., “RHIC Polarized Proton Manual”
<http://www.bnl.gov/cad/accelerator/docs/pdf/RHICPPCMan.pdf> [41](#)
- [50] O. Jinnouchi et al., RHIC/CAD Accelerator Physics Note 171 (2004) [40](#)
- [51] H. Okada et al., Phys. Lett. B638, 450 (2006), nucl-ex/0502022 [40](#)
- [52] A. Zelenski et al., Nucl. Instrum. Meth., vol. A536, pp. 248?254, 2005. [40](#), [42](#), [230](#)
- [53] A. Bazilevsky et al., Phys. Lett. B650, 325 (2007), hep-ex/0610030 [40](#)
- [54] (**PHENIX**) K. Adcox et al., NIM A499 489-507 (2003) [45](#)
- [55] (**PHENIX**) M. Aizawa et al., NIM A499 508-520 (2003)
- [56] (**PHENIX**) L. Aphecetche et al., NIM A499 521-536 (2003) [45](#)
- [57] (**PHENIX**) H. Akikawa et al., NIM A499 537-548 (2003) [45](#)

REFERENCES

- [58] T. Mibe, et al., “Technical Design Report on Amplifier-Discriminator board and Data Transfer board for the MuTr FEE upgrade ver.3.3” (2007) [57](#)
- [59] S. Adachi, et. al., Nuclear Inst. and Methods in Physics Research, A (2013), pp. 114-132 [57](#), [105](#)
- [60] A. Basye, et al., “Conceptual Design Report for a Fast Muon Trigger at PHENIX”, 2007 [58](#)
- [61] R. Towell, Nucl. Instr. Meth. A 602 (2009) 705-708 [59](#)
- [62] (**PHENIX**) M. Allen et al., NIM A499 549-559 (2003) [61](#)
- [63] (**PHENIX**) C. Adler, et al., NIM A 470 (2001) 488-499 [62](#)
- [64] E. Mathieson, “Cathode charge distributions in multiwire chambers”, Nuclear Instruments and Methods in Physics Research A270 (1988) 602-603 [78](#)
- [65] (**PHENIX**) S.S. Adler et al., NIM A499 560-592 (2003) [63](#), [64](#), [230](#)
- [66] (**PHENIX**) S.S. Adler et al., NIMA499 593-602 (2003) [71](#)
- [67] P. Chand et al., “A Primer Manual for the PHENIX Simulation Code PISA”,
http://www.phenix.bnl.gov/phenix/WWW/simulation/primer4/seq_primer.html [71](#)
- [68] “RUN OVERVIEW OF THE RELATIVISTIC HEAVY ION COLLIDER”,
<http://www.rhicome.bnl.gov/RHIC/Runs/> [87](#), [235](#)
- [69] (**PYTHIA6**) Torbjörn Sjöstrand, et al., JHEP05 (2006) 026 [35](#), [71](#)
- [70] (**UA1**) UA1 Collaboration (C. Albajar et al.), CERN-EP-89-85, Jul 1989. 30pp., Nucl. Phys. B335:261,1990 [139](#), [140](#), [232](#)
- [71] (**ISR**) Alper et al. Nucl. Phys. B100, 237 (1975) [139](#)
- [72] (**Garfield**) Rob Veenhof, Garfield - simulation of gaseous detectors,
<http://garfield.web.cern.ch/garfield/> [207](#)
- [73] (**PHENIX**) K.Okada, et al., “Central Arm W Analysis”, the PHENIX collaboration analysis note No. 923 [114](#)
- [74] (**PHENIX**) A.Bazilevsky, “ π^0 cross section analysis at mid-rapidity from pp Run9 $\sqrt{s} = 500$ GeV”, the PHENIX collaboration analysis note No. 884 [114](#)
- [75] (**CTEQ6.6**) P. M. Nadolsky, H.-L. Lai, Q.-H. Cao, J. Huston, J. Pumplin, D. Stump, W.-K. Tung, C.-P. Yuan, Phys.Rev.D78:013004,2008, hep-ph/0802.0007 [190](#), [236](#)
- [76] (**CTEQ6M**) J. Pumplin, D.R. Stump, J. Huston, H.L. Lai, P. Nadolsky, W.K. Tung, arXiv:hep-ph/0201195 [139](#)
- [77] (**DSS**) D. de Florian, R. Sassot and M. Stratmann, Phys. Rev. D75 (2007) 114010 hep-ph/0703242; Phys. Rev. D76 (2007) 074033 0707.1506; [139](#)
- [78] W. Verkerke and D. Kirby, “The RooFit toolkit for data modeling”, in proceedings of Statistical Problems in Particle Physics, Astrophysics and Cosmology [161](#)
- [79] MINUIT, Function Minimization and Error Analysis,
[http://lcgapp.cern.ch/project/cls/work-packages/mathlibs/minuit/home.html/](http://lcgapp.cern.ch/project/cls/work-packages/mathlibs/minuit/home.html) [161](#)
- [80] (**FEWZ**) K. Melnikov and F. Petriello, Phys. Rev. D74, 114017 (2006), hep-ph/0609070. [190](#), [236](#)
- [81] P.M. Nadolsky and C.-P. Yuan, Nucl.Phys.B666:3-30,2003, hep-ph/0304001 [190](#), [236](#)
- [82] H. L. Lai et al., Eur.Phys.J.C12:375-392,2000

REFERENCES

- [83] M.Glück, E. Reya, M. Stratmann, and W. Vogelsang, Phys. Rev. D 63, 094005 (2001) [193](#)
- [84] D. de Florian, G. A. Navarro, and R. Sassot, Phys. Rev. D 71, 094018 (2005) [193](#)
- [85] (**MSTW08**) A.D. Martin, et al., Eur.Phys.J.C63:189-285,2009 [190](#), [219](#), [234](#), [236](#)

List of Figures

1.1	A Feynman diagram to produce $W^- \rightarrow \ell^- \bar{\nu}_\ell$ in $p^\Rightarrow + p$ collisions.	4
1.2	The PHENIX detector.	6
2.1	Couplings appearing in SU(3) QCD.	8
2.2	Deep inelastic scattering in charged lepton-proton scattering.	10
2.3	Q^2 dependence of $F_2(x, Q^2)$ at various x obtained by many experiments[9].	14
2.4	Summary of various $g_1(x)$ measurements for proton, deuteron, and neutron[9].	17
2.5	Result of the global analysis “DSSV” for the polarized PDFs [8].	18
2.6	Leptonic decay mode $W^+ \rightarrow e^+ \nu_e$	19
2.7	Leptonic decay mode $Z \rightarrow e^+ e^-$	20
2.8	Hadronic production subprocess of W^+	21
2.9	Measurements of production cross section of $W^\pm \rightarrow \ell^\pm \bar{\nu}$ and $Z \rightarrow \ell^+ \ell^-$ in proton-proton and proton-antiproton collisions at various \sqrt{s} [31–42].	23
2.10	Helicity conservation in production and decay of W^\pm boson.	24
2.11	The rapidity distribution of the charged lepton from W decays at the center of mass frame. The solid line is of $W^+ \rightarrow \ell^+$ and the dotted line is of $W^- \rightarrow \ell^-$	25
2.12	Distribution of y_W and η_ℓ for $W^+ \rightarrow \ell^+$ (left) and $W^- \rightarrow \ell^-$ (right).	25
2.13	Geometrical explanation of the Jacobian peak.	26
2.14	The convention of the coordinate system for spin asymmetry.	29
2.15	Estimation of A_L of $W^\pm \rightarrow \ell^\pm$ at $\sqrt{s} = 500$ GeV with the CHE NLO generator[10].	30
2.16	Estimation of A_L of $Z \rightarrow \ell^\pm$ at $\sqrt{s} = 500$ GeV with the CHE NLO generator[10].	30
2.17	A_L for e^\pm from W^\pm/Z^0 boson decays for $ \eta < 0.35$, $30 < p_T < 50$ GeV/ c with PHENIX[43].	31
2.18	A_L for e^\pm from W^\pm boson decays for $ \eta < 1$, $25 < p_T < 50$ GeV/ c with STAR[44].	32
2.19	Global fit result of $\Delta u(x, Q^2)$ and $\Delta \bar{d}(x, Q^2)$ at $Q^2 = 10$ GeV 2 obtained in the DSSV analysis[8].	33
2.20	The same plot as Figure 2.19, but adding pseudo-data points to the DSSV data set which are expected to be obtained by the RHIC experiments (PHENIX and STAR), assuming the integrated luminosity of 200 pb^{-1} [8].	33
2.21	Distribution of muons from W^+ and W^- in p_T and η dimension.	34
2.22	p_T distribution of μ^\pm from W^\pm in $1.4 < \eta < 2.4$	34
2.23	η distribution of μ^\pm from W^\pm in $15 < p_T < 60$ GeV/ c	35
2.24	Simulated $W^+ \rightarrow \mu^+$ process and muon background processes at $1.4 < \eta < 2.4$ with PYTHIA.	36
2.25	Simulated $W^- \rightarrow \mu^-$ process and muon background processes at $1.4 < \eta < 2.4$ with PYTHIA.	36
3.1	Schematic drawing of OPPIS[45].	38
3.2	RHIC accelerator complex.	39

LIST OF FIGURES

3.3 (Left) The spin precession at the Siberian Snake to flip the direction, (Right) The spin precession at the Spin Rotator from vertical to longitudinal direction. The figures are taken from[48].	40
3.4 View of RHIC overemphasizing the interaction regions to show the location of the Siberian Snakes and the spin rotators	41
3.5 A general layout of the H-jet polarimeter. The figure is taken from [52].	42
3.6 A top-view of the scattering chamber of the H-jet polarimeter.	42
3.7 Geometric location of the Local polarimeter (ZDC,SMD) of the PHENIX detector.	43
3.8 Geometrical acceptance of the PHENIX detector.	44
3.9 The coordinate system of the PHENIX detector.	45
3.10 Detector subsystems of the PHENIX detector in year 2011 run setup.	46
3.11 History of the PHENIX detector upgrades related with the measurement of muons form W/Z decays from 2009 to 2012.	48
3.12 Overview of the PHENIX magnets.	49
3.13 PHENIX magnetic field lines in (++) mode.	49
3.14 A layout of extended hadron absorbers.	50
3.15 A drawing of Iarocci streamer tubes in the MuID.	51
3.16 A drawing of one gap of the MuID.	52
3.17 A side view drawing of the MuID gaps. The hatched materials are the steel wall absorbers. Dimensions are in mm.	52
3.18 Block diagram of the MuID readout card (ROC) and front-end module (FEM).	53
3.19 Schematic drawing of one chamber layer of the MuTr.	54
3.20 Drawing of the South Muon Magnet and the MuTr Stations.	55
3.21 Mechanical drawing of the MuTr Station-1.	55
3.22 Illustration of stereo readout of the MuTr.	55
3.23 The azimuthal offset angle of stereo cathode planes with respect to their corresponding non-stereo cathode planes.	55
3.24 (Left) Schematic drawing of a MuTr cell. (Right) Contour plot of drift time in the MuTr cell simulated by Garfield.	56
3.25 The arrival time distribution for different incident angles into MuTr based on Garfield simulation.	56
3.26 Analog readout diagram of the MuTr.	57
3.27 Sampling recording of the waveform of the signal with the MuTr FEE.	57
3.28 Block diagram of Mutrg FEE.	58
3.29 Geometry of the RPC3 strips. The width of the strip is different by regions A,B,C.	60
3.30 An exploded view of the layers of the RPCs.	60
3.31 RPC3 seen from the RHIC beam tunnel.	60
3.32 Diagram of the RPC front-end electronics.	60
3.33 Schematic Drawing of a BBC module.	61
3.34 Picture of a BBC module.	61
3.35 Arrangement of PMTs in the BBC. The blue circle blanks are the positions of laser sources.	61
3.36 Drawing of a ZDC module. Dimensions are in mm.	62
3.37 Illustration of the PHENIX DAQ system[65].	64
3.38 Defining symsets of the MuID trigger.	66
3.39 MuID symset logics.	67
3.40 Explanatory drawings for the clustering.	68
3.41 A schematic drawing of the Mutrg-LL1 trigger logic.	68
3.42 Schematic illustration of the physics trigger for $W^\pm \rightarrow \mu^\pm$ in year 2011 runs.	69
3.43 The configuration of the LL1 timing of the WTRG(S,N) trigger in year 2011 runs.	70
3.44 Illustration of the software framework.	72

LIST OF FIGURES

3.45 Geometry of the PHENIX built in the PISA simulation framework.	72
4.1 Timing histogram of the South and North BBC module for a typical event of double collision candidates.	74
4.2 Diagrams of collision detection and reconstruction patterns of the BBC for typical cases.	76
4.3 Mathieson function with $K_3 = 0.7$	79
4.4 Nomenclatures of MuTr tracking.	79
4.5 A visualization of the reconstruction of an event with a track.	82
4.6 Schematic illustration of the definitions of DG0, DG4, DDG0 and RpcDCA in side view.	85
4.7 Definition of DCA_r	85
4.8 Illustration of RpcDCA in beam view.	86
 5.1 Data taking history of year 2011 runs of proton-proton collisions at $\sqrt{s} = 500$ GeV.	88
5.2 Distribution of data with respect to BBC(novtx) trigger rate.	90
5.3 BBC(novtx) trigger rate as a function of multiple collision parameter μ	92
5.4 RMS of bunch-by-bunch relative luminosity for each run.	92
5.5 Fill-by-fill beam polarizations.	93
5.6 The primary vertex z -distribution of a run measured with the minimum-bias trigger.	94
5.7 Vertex distributions of runs used in this thesis.	95
5.8 Radiograph of the South and North MuTr.	96
5.9 Determination of the timing of the RPC3 hits with data.	96
5.10 Luminosity-normalized raw trigger rate of various triggers as a function of multiple collision parameter.	98
5.11 Schematic illustration of the case that the noise hits allows to trigger an event which is supposed to be rejected without noises.	98
5.12 Mean number of hits per event in the North MuID of runs, sorted by the luminosity.	99
5.13 Mean number of hits per event in the North MuTr of runs, sorted by the luminosity.	99
5.14 Number of reconstructed tracks normalized by luminosity with various triggers.	100
 6.1 (Left) Distribution of $p_T^{\text{reco}}/p_T^{\text{true}}$ for $p_T^{\text{true}} = 10, 30$ GeV/ c . (Right) Simulated momentum resolution as a function of p_T^{true} for the North Muon Arm at $\eta = 1.5$	102
6.2 $J/\psi \rightarrow \mu^+\mu^-$ invariant mass distribution at $\sqrt{s} = 500$ GeV.	103
6.3 Υ mass peak observed in the real data. The data points are fitted with Drell-Yan spectrum shape was assumed as background, and Υ mass peak was fitted by gaussian.	103
6.4 Comparison of mass peak width of resonant states ($J/\psi, \Upsilon$) between the real data and the simulation.	104
6.5 Position resolution of MuTr as a function of the ground noise level of MuTr in the simulation.	104
6.6 Measurement of momentum resolution with cosmic rays as a function of p_T	105
6.7 MuID HV group mapping.	106
6.8 Measured run-by-run MuID hit efficiency for South Arm Gap-0 Horizontal plane sorted by multiple collision parameter.	107
6.9 Evaluation of MuID-1D LL1 efficiency with di-track cosmic ray muons.	108
6.10 Evaluation of MuID-1D LL1 efficiency with $J/\psi \rightarrow \mu^+\mu^-$ tag-and-probe method. $p_T > 2.0$ GeV/ c was required for the probe-side track.	110
6.11 An example of fitting of N_{hit} with parameters p_1, p_2	112
6.12 Fitting result for all runs.	112
6.13 Fitting result for all runs in the space of $\{\varepsilon_{\text{plane}}, \varepsilon_{\text{gap}}^{\text{AND}}\}$	113

LIST OF FIGURES

6.14	The same as Figure 6.13, but the data sample are J/ψ probe muons.	113
6.15	Timing chart of the MuID-1D trigger in year 2011 runs. The BCLK where a hard collision with a muon track is produced is defined as BCLK-0.	117
6.16	Fraction of four categories about MuID-1D trigger for reconstructed muon tracks with BBC(novtx) trigger.	119
6.17	Comparison of MuID-1D trigger efficiency as a function of multiple collision parameter obtained between the ERT trigger data and the toy simulation.	121
6.18	Mutrg-SG1 trigger efficiency estimation with Mutrg simulator for North Arm μ^+ , $2.0 < \eta < 2.1$ as a function of p_T	123
6.19	Estimated Mutrg-SG1 trigger efficiency at plateau and the turn-on p_T and p_z as a function of η for South and North Arm.	124
6.20	Illustration of how the clustering algorithm works for positive and negative charged tracks.	125
6.21	Examples of Mutrg-SG1 trigger efficiency turn-on curve, for South (Left) and North (Right) Arm $1.2 < \eta < 1.6$ obtained with MuID-1D trigger data and the fitting result to the data points.	126
6.22	Rapidity dependence of Mutrg-SG1 trigger measured with MuID-1D trigger data and the prediction of Mutrg simulator for South and North Arms.	126
6.23	RPC efficiency for unlike sign dimuons in RunNumber > 338000	128
6.24	Run-by-run relative RPC efficiency correction for South and North Arms.	129
6.25	Mapping of the result of simulation for different efficiency parameterizations. The data points are overlaid.	130
6.26	Reconstructed yield of $J/\psi \rightarrow \mu^+ \mu^-$ for each reference run in the PYTHIA + PISA simulation sorted by multiple collision parameter μ after taking account of the degradation of MuID-1D trigger efficiency with luminosity.	132
6.27	Luminosity dependence of dimuon yield in real data in $2.5 < m_{\text{inv}} < 4.0 \text{ GeV}/c^2$ with WTRG(S,N) triggers, after subtracting combinatorial backgrounds.	132
6.28	Contour plot of the relative fluctuation of acceptance to the reference configuration for South Arm and North Arm.	133
7.1	Distribution of variables for $W^+ \rightarrow \mu^+$ at $16 < p_T^{\text{reco}} < 60 \text{ GeV}/c$ in the North Arm acceptance.	137
7.2	Contour lines of the distribution of variables for $W^+ \rightarrow \mu^+$ in the North Arm acceptance as a function of p_T^{reco}	138
7.3	Inclusive Differential cross section of hadron production as a function of transverse momentum p_T in proton-antiproton collisions at $\sqrt{s} = 200, 500, 900 \text{ GeV}$ measured by the UA1 experiment[70].	140
7.4	Differential cross section of K^\pm and π^\pm as a function of p_T^{true} for the North Muon Arm acceptance in the simulation.	142
7.5	Yield of hadronic backgrounds as a function of p_T^{reco} in the simulation.	142
7.6	Distribution of decay z -position of producing muons (μ^+ or μ^-) from K^+ flying to the North Arm for various initial p_T , whose reconstructed momentum of the track is in $15 < p_T^{\text{reco}} < 60 \text{ GeV}/c$	143
7.7	Schematic illustration of charged hadrons' muonic decay in flight to be reconstructed as a high p_T track.	143
7.8	Fraction of topologies of events whose reconstructed momentum is in $15 < p_T^{\text{reco}} < 60 \text{ GeV}/c$ for K^+ flying to the North Arm as a function of various initial p_T	144
7.9	Fraction of topologies of events whose reconstructed momentum is in $15 < p_T^{\text{reco}} < 60 \text{ GeV}/c$ for π^+ flying to the North Arm as a function of various initial p_T	144
7.10	Radiograph of reconstructed tracks at $10 < p_T < 60 \text{ GeV}/c$ with some quality cuts.	145

7.11 Reconstructed Yield of $W^\pm \rightarrow \mu^\pm$ and muon background events (left panel), and figure of merit of $W^\pm \rightarrow \mu^\pm$ by changing the momentum selection ranges (right panel) for North Arm μ^\pm	147
7.12 Contour lines of the 2D distribution of variables for $W^+ \rightarrow \mu^+$ at $16 < p_T^{\text{reco}} < 60 \text{ GeV}/c$ in the North Arm acceptance.	149
7.13 Contour lines of the 2D distribution of variables for real data at $16 < p_T^{\text{reco}} < 60 \text{ GeV}/c$ in the North Arm acceptance.	150
7.14 Distribution of $W^\pm/Z \rightarrow \mu^\pm$ signal at $16 < p_T^{\text{reco}} < 60 \text{ GeV}/c$ as a function of f_{cut} , and the cumulative signal efficiency at the given f_{cut} threshold.	151
7.15 Distribution of real data at reconstructed at $16 < p_T^{\text{reco}} < 60 \text{ GeV}/c$ as a function of cut threshold f_{cut}	152
7.16 $W^\pm/Z \rightarrow \mu^\pm$ signal and muon background efficiency as a function of cut threshold f_{cut}	153
7.17 Distribution of $W^\pm \rightarrow \mu^\pm$ in $16 < p_T^{\text{reco}} < 60 \text{ GeV}/c$ in $f_{\text{cut}} > 0.95$	155
7.18 Distribution of data in $0.10 < f < 0.95$	158
7.19 Illustration of geometrical limitation of dw_{ij} with requirement of DCA _r	159
7.20 η -distribution of hadronic backgrounds.	159
7.21 dw_{23} -distribution of hadronic backgrounds at various range of f and extrapolation to the signal region ($f \rightarrow 1$).	160
7.22 Result of the unbinned maximum likelihood fitting.	162
7.23 NLL contour plot of the likelihood fitting.	163
7.24 Scattering plot of run-by-run acceptance and efficiency, and multiple collision parameter.	165
7.25 Simulated p_T , $ \eta $, and dw_{23} distribution of $W^\pm \rightarrow \mu^\pm$ at the basic cut with different tunes of MuTr noise scale.	167
7.26 Relative cross section measurement deviation as a function of the simulated position resolution of the MuTr.	168
7.27 Distribution of relative cross section uncertainty due to the position resolution uncertainty of the MuTr. The gray band shows the range of 68 % interval listed in Table 7.10.	168
7.28 The RMS value of dw_{23} distribution for the hadronic background as a function of f in the simulation. The black bullets are data points in the simulation.	169
7.29 Relative cross section measurement deviation as a function of the assumed f_{ext} value for estimating the dw_{23} distribution of hadronic backgrounds.	170
7.30 Distribution of relative cross section uncertainty due to the estimation of dw_{23} distribution of hadronic backgrounds. The gray band shows the range of 68 % interval.	170
7.31 Likelihood distribution of $W^\pm \rightarrow \mu^\pm$ cross section measurement. All statistical and systematic uncertainties (category A,B,C,D in Table 7.15) are taken into account. The 2D histogram (the left panel) shows the correlation of likelihood between the South and North Arms. The 1D plot (the right panel) shows the projection of the 2D likelihood to the South or North axis for individual measurements (the red and blue histograms) as well as the combined likelihood (the black histogram).	174
8.1 Determination of the signal selection.	181
8.2 An example of event distribution in f'_{S_1}	183
8.3 Result of relative luminosity measurement using low momentum track events. (Left) Number of events per spin combination, (Right) Number of events by Bunch ID.	185
8.4 Result of the maximum likelihood fitting for measuring spin asymmetries.	186
8.5 Systematic uncertainty of the central value of spin asymmetries.	186

LIST OF FIGURES

9.1	Comparison of the obtained cross section in this analysis and other measurements and theoretical calculation. For the theoretical calculation, only MSTW08 NNLO calculation with FEWZ in Table 9.1 is plotted as a representative calculation.	190
9.2	3D layout of the FVTX detector.	192
9.3	$A_L^{\mu\pm}$ measured in this study.	193
A.1	Relative dimuon yield in $2.5 < m_{\text{inv}} < 4.0 \text{ GeV}/c^2$ with WTRG(S,N) trigger for different luminosity groups.	199
A.2	Simulated mass spectrum of open charm process and fit results for South and North Arms.	201
A.3	Simulated mass spectrum of open bottom process and fit results for South and North Arms.	201
A.4	Simulated mass spectrum of Drell-Yan+ Z^0 process and fit results for South and North Arms after applying SG1 trigger efficiency.	202
A.5	Simulated mass spectrum of the sum of Υ family and fit results for South and North Arms.	202
A.6	Dimuon yield comparison between MuID-1D and WTRG(S,N) trigger after normalized with the integrated luminosity of each trigger.	203
A.7	Result of fitting of dimuon data with combining the South and North Arms for the WTRG(S,N) and MuID-1D triggers.	205
B.1	The arrival time distribution for different incident angles into MuTr based on Garfield simulation.	208
B.2	Schematic drawing of the Mutrg simulator	209
C.1	Kinematic variable distributions for J/ψ probe-muons in the data and the simulation. The black bullets are the data, and the green bands are the simulation.	212
D.1	Diagram of merging two collisions in simulation.	213
D.2	(Left) Difference between reconstructed vertex and true vertex for $p + p \rightarrow W^\pm$ process with conventional BBC reconstruction in $\mu = 0.6$ case (simulation). (Right) For BbcMultipleVtx algorithm with binsize = 0.5 ns.	214
D.3	Comparison of accuracy of reconstructed vertex between the conventional BBC reconstruction and BbcMultipleVtx for different multiple collision parameters.	215
D.4	The process diagram of DCA_z afterburner	216
D.5	DCA_z 97% contour line for $p + p \rightarrow W^\pm$ process as a function of reconstructed p_T with multiple collision parameter $\mu = 0.3$. Blue: using the conventional BBC reconstruction, Red: using the BbcMultipleVtx reconstruction, Black: using the true vertex of the MC.	217
E.1	MSTW08 unpolarized PDFs[85].	219
E.2	A diagram of neutrino DIS which accesses to $s(x)$	222
E.3	A Drell-Yan diagram to produce a lepton pair in proton-proton collisions.	222
E.4	A single jet production diagram in proton-proton collisions.	222
E.5	A di-jet production diagram in DIS.	222

List of Tables

2.1	The decay modes and branching ratios of W^+ boson [9].	20
2.2	Results of A_L at mid-rapidity region with PHENIX and STAR[43, 44].	31
3.1	The “spin patterns” used in year 2011 runs.	38
3.2	Detector subsystems installed in year 2011 runs.	47
3.3	The key parameters of the Central Magnet and the Muon Magnets.	48
3.4	Parameters of hadron absorbers in the PHENIX detector.	50
3.5	Parameters of MuID.	51
3.6	Parameters of the MuTr.	54
3.7	Performance requirements of the PHENIX RPC3 detectors.	59
3.8	The list of the level-1 triggers employed for $\sqrt{s} = 500$ GeV proton-proton collisions in year 2011 runs.	65
5.1	The machine parameters of the RHIC during $\sqrt{s} = 500$ GeV polarized proton-proton collisions in 2011. Values are taken from [68].	87
5.2	Errors on the BBC cross section.	89
6.1	Mass peak width of resonant states in the real data.	102
6.2	Summary of BBC efficiency obtained with data for different physics processes at $\sqrt{s} = 500$ GeV case.	115
6.3	Summary of BBC efficiencies estimated with the PYTHIA + PISA simulation. .	115
6.4	Comparison of data points in Figure 6.16 and calculation with the toy MC. .	120
6.5	Measured MuID-1D trigger efficiency for various μ values using ERT trigger data.	122
6.6	The number of events of the denominator of efficiency and the plateau value for unlike-sign, like-sign, and unlike-sign after subtracting combinatorial backgrounds for South and North Arm.	128
7.1	Run filtering cuts used in this analysis.	145
7.2	Cross section of muon backgrounds with PYTHIA simulation and muon yields in $16 < p_T^{\text{reco}} < 60$ GeV/ c per charge at $f > 0.95$ in the North Arm for the integrated luminosity of 24.8 pb^{-1}	156
7.3	Coefficients of the fitting of hadronic background dw_{23} distribution.	157
7.4	Condition of the fitting.	163
7.5	Result of the unbinned maximum likelihood fitting.	163
7.6	Summary of the average acceptance and efficiency $\langle A \cdot \varepsilon \rangle$ for runs used in this study. PYTHIA simulation was used as $W^\pm \rightarrow \mu^\pm$ process generator.	164
7.7	List of uncertainties of acceptance and efficiency.	165
7.8	Estimation of relative cross section deviation for various configuration of the simulated position resolution of MuTr compared to the default.	168

LIST OF TABLES

7.9	Relative systematic cross section error (68 %) due to the uncertainty of the MuTr position resolution.	168
7.10	Relative systematic cross section error (68 %) due to the estimation of dw_{23} distribution of hadronic backgrounds.	169
7.11	Variation of fitting result with changing the selection of sideband data for determining η -distribution of hadronic background.	172
7.12	Relative difference of the cross section estimation of the CHE NLO event generator with the MRT02 PDF set compared to the default PYTHIA LO event generator.	172
7.13	Summary of relative systematic uncertainties related with muon backgrounds.	172
7.14	Expected fraction of $Z \rightarrow \mu^\pm$ events (f_Z) in the signal.	173
7.15	List of statistic and systematic uncertainties which are varied independently in estimating the total cross section uncertainty in the MC sampling.	173
7.16	Result of cross section of $W^\pm \rightarrow \mu^\pm$ for each Arm individually with various inclusions of uncertainty categories in Table 7.15.	175
7.17	Result of cross section of $W^\pm \rightarrow \mu^\pm$ for combining both Arm measurements with various inclusions of uncertainty categories in Table 7.15.	175
7.18	Result of total cross section measurement and of $W^\pm \rightarrow \mu^\pm$ in this study. The central value is the most probable value after taking account of both statistical and systematic uncertainties, and the uncertainty range was determined to exclude 16 % of the likelihood distribution of both sides to the total integral.	176
8.1	f'_{cut} value to give the maximum FOM, and the remaining number of events and the dilution factor using the central value of the cross section measurement. The central value dilution factor, signal efficiency and number are also listed.	180
8.2	Number of events for each spin combination with f'_{cut} -value given in the Table 8.1.180	
8.3	Uncertainty of $n_{\text{sig}}^{\text{sel}}$ in the data set of the final signal selection.	184
8.4	Systematic uncertainties of beam polarization.	184
8.5	Summary of relative efficiency measurement.	185
8.6	Raw asymmetries for the final signal selection. The correction for the relative luminosity is ignored.	187
8.7	Result of the measurement of spin asymmetries. The systematic range shows the uncertainty range of the central value.	187
9.1	Theoretical calculations of total cross section of total cross section times branching ratio [31, 75, 80, 81, 85]. The error in the table comes from uncertainty of PDFs.	190
A.1	Total relative efficiency of dimuon process to the reference run for MuID-1D and WTRG(S,N) trigger.	198
A.2	Results of the fitting.	204
A.3	Table of systematic errors about efficiencies and luminosity	205
A.4	Final results of cross section correction factors in this study.	206

Acknowledgments

This work would not have been accomplished without the support and the consideration of so many people.

First of all, I wish to express my sincere gratefulness to my supervisor Prof. Satoru Yamashita for continuous encouragements and advices with his lucid and deep vision about physics, experiments and educational philosophy through not only the period of this work but the whole duration of my six-year graduate school. When I encountered some issues through the work, and when I discussed about them his suggestions and advices were always clear, and those supported my work as if bright torches in the fog. He always respected my individuality toward the research regardless of the progress visible or not. I am very happy and fortunate to have been his student to learn so many things through this work and other two major works.

I have no words to express my gratitude to Prof. Naohito Saito who invited me to participate in the PHENIX collaboration for this work as the thesis topic after 2011 Tohoku earthquake and tsunami disaster. The topic in this thesis is his over-10-year project since he wrote the proposal of $W \rightarrow \mu$ at RHIC, and he led the construction of Mutrg with many predeceasing staffs and graduate students. His leadership was crystallized in the phrase “we shall hold it *down*” which he gave me at the first day we met, and the dignity of that phrase kept my motivation up to accomplish this work.

I wish to express my gratitude to Dr. Hideto En’yo who is the chief scientist of Radiation Laboratory in RIKEN. His attitude and enlightenment toward physics and experiments inspired me (in)directly in many lessons. I hereby express special thanks to Dr. Yasuyuki Akiba, who is the group leader of the experimental group of RIKEN BNL Research Center. As the group leader he pointed out essential comments for this work from wide overview.

I would like to thank all members of the PHENIX collaboration.

I would like to express my special appreciation to Dr. Ralf Seidl. He is the analysis coordinator of $W \rightarrow \mu$ analysis in 2011 run. He represented great leadership to proceed the analysis work in the collaboration, and I owed many things in the analysis works especially in producing simulation samples and developing track quality variables. He also accepted many of my ideas to include them in the analysis. It was of my pleasure to work and discuss with him.

I would like to express many thanks to Dr. Itaru Nakagawa. As a Mutrg expert he gave me lots of knowledge about Muon Arms, and he made many connections for me with other collaborators for discussion. It was substantial that I discussed many times with him about the performance of the detectors to reach to the conclusion. He gave me immediate responses every time I reported new things and gave me useful questions and comments. I sincerely appreciate that he took a lot of cares of me in staying in BNL and RIKEN in management side as well.

I would like to express my best gratitude to the PHENIX Mutrg team for taking responsibility of the quality of the data used in this thesis as well as for daily discussions about the detector performances and development of analyses: Dr. Yuji Goto, Prof. Kiyoshi Tanida, Prof. Tsumoru Mibe, Prof. Tetsuya Murakami, Prof. Jiro Murata, Dr. Yoshinori Fukao, Dr. Yoshimitsu Imazu, Dr. Joseph Seele, Dr. Katsuro R Nakamura, Ms. Sanghwa Park, Mr. Kentaro Watanabe,

ACKNOWLEDGMENTS

Mr. Inseok Yoon, Mr. Takeru Iguri, Ms. Minjung Kim, Mr. Nobuaki Amano, and Ms. Haruna Murakami. Especially Dr. Yoshinori Fukao has guided me lots of the technical specs of MuTrg and the PHENIX online electronics as well as the software framework, which helped me a lot to construct the MuTrg simulator to understand the trigger efficiency. Dr. Yoshimitsu Imazu gave me lots of suggestions about the basic performances of MuTr. I had many discussions with Dr. Joseph Seele about analysis techniques, evaluation of trigger efficiencies as well as handling of data. I would like to express my special gratitude to Ms. Sanghwa Park for encouraging me to write the thesis, and careful reading and giving precious feedbacks for the manuscripts to me.

I wish to appreciate the PHENIX forward upgrade project group and $W \rightarrow \mu$ analysis group for discussing analysis strategies: Dr. Richard Hollis, Dr. Murad Sarsour, Prof. John Hill, Prof. Matthias Grosse Perdekamp, Prof. Abhay L. Deshpande, Prof. Xiaochun He, Prof. John Lajoie, Prof. Rusty Towell, Dr. Francesca Giordano, Dr. Ihnjea Choi, and Dr. Young Jin Kim.

I would like to appreciate the PHENIX Spin Physics Working Group (SpinPWG). Especially I was happy that I discussed and received many comments from the following collaborators: Dr. K. Oleg Eyser, Dr. Kieran Boyle, Dr. John Koster, Dr. Mickey Chiu, Dr. Cesar Luiz da Silva, Dr. Ming Liu, Dr. Melynda Brooks, and Dr. Jin Huang.

I would like to thank Dr. Kensuke Homma, Mr. Masaya Nihashi, Dr. Takashi Hachiya, Dr. Kensuke Okada, Dr. David Kawall for the development of the new BBC reconstruction as well as its calibration. I would like to appreciate Prof. John Lajoie, Dr. Vince Cianciolo, and Dr. Sarah Campbell for evaluating the MuID trigger efficiency.

I thank Mr. Kohei Shoji and Mr. Yoshimasa Ikeda for preparing computing and data analysis environments in RIKEN CCJ computing facility.

I would like to express special thanks to work with the following collaborators in the PHENIX collaboration for supporting me in many phases: Dr. John Haggerty, Dr. Michael Leitch, Dr. Alexander Bazilevsky, Dr. Stephen Baumgart, Dr. Jamie Nagle and Dr. David Morrison.

I met many PHENIX students in BNL and RIKEN who inspired me a lot in both academic and private aspects to have fruitful days. I would like to thank Mr. Mike Beaumier, Dr. Martin Leitgab, Mr. Chong Kim, Mr. Daniel Jumper, Mr. Ciprian Gal, Mr. Andrew Manion, Ms. Sookhyun Lee, Mr. Josh Perry, Mr. Takahito Todoroki, Mr. Brennan Christopher Schaefer, Mr. Kimiaki Hashimoto, Mr. Ryoji Akimoto, Mr. Hidemitsu Asano, Mr. Akihisa Takahara, Mr. Yosuke Watanabe, Mr. Sotaro Kanda, and Mr. Sanshiro Mizuno. I also would like to thank Dr. Yasushi Watanabe, Dr. Yuki Aramaki, Dr. Kazuya Aoki during the time I was researching in RIKEN. I would like to thank many Japanese researchers in BNL and RIKEN other than the PHENIX collaboration.

This work cannot be achieved without helps and considerations of people out of the PHENIX collaboration.

I would like to express sincere gratitude to the all members of my previous project, the Neutron Optics and Physics (NOP) collaboration. I have learned many experimental techniques and fundamentals through the construction of the experimental apparatus for the neutron lifetime measurement with pulsed cold neutron beam at J-PARC MLF. The experiences at this project definitively formed the core of myself as an experimental physics researcher. I would like to appreciate Prof. Hirohiko Shimizu, Dr. Takashi Ino, Dr. Suguru Muto, Dr. Kaoru Taketani, Dr. Yasushi Arimoto, Prof. Hirochika Sumino, Dr. Yoshichika Seki, Prof. Yoshihisa Iwashita, Prof. Masa-aki Kitaguchi, Prof. Tatsushi Shima, Dr. Masako Yamada, Mr. Sohei Imajo, and Mr. Dai Sakurai.

Under the supervision of Prof. Satoru Yamashita, the Yamashita group at ICEPP in the University of Tokyo has kept to represent remarkable achievements. It is my brilliant honor to have been a member of the group and to have been a colleague of the following talented researchers: Prof. Tamaki Yoshioka, Dr. Tomohiko Tanabe, Dr. Taikan Suehara, Dr. Kenji

Mishima, Dr. Masakazu Kurata, Dr. Takashi Kubota, Dr. Yuichi Morita, Dr. Hidetoshi Otono, Mr. Hitoshi Hano, Mr. Toru Suehiro, Mr. Takuro Murase, Mr. Takeshi Takahashi, Mr. Ryo Katayama, Mr. Takahito Yamada, Mr. Nao Higashi, Mr. Harumichi Yokoyama, and future grad students Mr. Takuaki Mori, and Ms. Sei Ieki. It was my great pleasure to have opportunity to discuss about divergent research topics of each individual at weekly meetings, which has cultivated our interests each other.

I would like to express best appreciation to ICEPP secretaries during my belonging, Ms. Masako Shiota, Ms. Yoko Takemoto, Ms. Akiko Miyazono, Ms. Yoshie Tezuka, Ms. Ritsuko Ambiru, Ms. Chieko Morita, Ms. Megumi Suzuki, Ms. Naoko Kataoka, Ms. Eiko Yuno, Ms. Hiroko Yakushi, Ms. Ikue Tsukamoto, and Ms. Chiyo Ito for kindly taking care of general businesses. I would like to thank the secretaries of Radiation Laboratory in RIKEN, Ms. Noriko Kiyama and Ms. Keiko Suzuki for managements in RIKEN. I would like to thank the account manager for administration Mr. Kazunori Mabuchi, and Ms. Taeko Itoh, Ms. Susan P. Foster for managements in BNL.

I would like to thank all of my friends who supported to work for the thesis.

Finally I would like to thank my grandmother Mitsuko, my mother Hiroko, my father Katsumonbu, and two younger sisters Yumiko and Eriko, for continually encouraging and supporting me to keep concentration on this work.

Index

- χ^2_{track} , 83
- DCA_{*z*}, 213
 - afterburner, 215
- Abort gap, 39
- Absorbers, 50
- AGS (Alternating Gradient Synchrotron), 38
- A_L , 5
- A_{LL} , 2
- A_N (transverse spin asymmetry), 40, 42, 43
- Arms
 - Central, 45
 - Muon, 44, 45
- Asymptotic freedom, 8
- Baryons, 1, 9
- BBC (Beam Beam Counter)
 - BBCLL1, 66
- BBC (Beam Beam Counters), 61
- Bjorken scaling, 1, 12, 13
- Bjorken-*x*, 11
- Blue beam, 38
- BNL (Brookhaven National Laboratory), 37
- Central Arms, 44
- Cluster (BBC), 74
- Cluster (MuTr), 78
- CNI (Carbon-Nuclear Interference), 40
- Color confinement, 8
- Coordinate (MuTr), 78
- Cut parameter (f'), 179
- Cut parameter (f), 148
- DAQ (Data Acquisition), 63
- DCA_{*r*}, 84
- DCA_{*z*}, 84
- DDG0, 83
- Deep inelastic scattering (DIS), 1
- Deep virtual Compton scattering (DVCS), 3
- DG0, 83
- DGLAP evolution equations, 1, 13, 219
- Dilution factor, 179
- DIS, 1–3
 - neutrino-, 221
 - polarized, 3, 4
 - semi-inclusive-, 4
- $d\phi_{ij}$, 84
- Drell-Yan process, 1, 221
- dw_{ij} , 84
- DX magnets, 39, 43
- EMC, 2, 3
- European Muon Collaboration (EMC), 2
- F_1 , 11, 221
- F_2 , 11, 221
- F_3 , 221
- Factorization, 9, 11, 12
 - scheme, 12
 - theorem, 12, 219, 221
- Fill number, 87
- G_1 , 15
- G_2 , 15
- Gap (MuID), 51
- Gap (MuTr), 53
- GL1, 70
- GL1 (global level-1), 63
- GL1P scaler, 64
- Gluons, 1, 7
- GTM (Granule Timing Module), 63
- H-jet (Hydrogen jet), 40
- Helical dipole magnets, 39
- Hit (MuTr), 78
- HV group (MuID), 106
- Iarocci streamer tube (MuID), 51
- Jet, 222
- Lampshade (Muon Arm), 48, 53
- Likelihood

- Extended unbinned maximum likelihood fitting (for signal extraction), 161
- Maximum likelihood fitting (for spin asymmetry), 185
- LL1 (local level-1), 53, 57
- Magnet
- Central, 48
 - DX, 38
 - Muon, 48
- Magnetic moment, 1, 2
- Minimum bias (MB), 66
- MPC (Muon Piston Calorimeter), 44, 47
- MuID, 45
- MuID-1D trigger, 67
 - MuIDLL1, 66
 - Road, 77
- Multiple collisions, 89
- parameter, 91
- Multiple scattering, 135
- Muon Piston, 48
- MuTr, 45
- Mutrg, 57
- Mutrg-LL1, 67
- Mutrg simulator, 207
- Neutrons, 1–3, 221
- Octant (MuTr), 53
- OPPIS (Optically-Pumped Polarized Ion Source), 37
- Parton distribution function (PDF), 1, 3
- polarized-, 3–5, 12
- Partons, 1, 9
- PHENIX, 5, 44
- coordinate system, 44
 - magnets, 48
- PISA, 68, 71
- Polarimeters, 40
- CNI-, 40
 - H-jet-, 42
 - Local-, 43
- Polarization measurement, 93
- Preselection
- Cut parameter (f), 148
- Protons, 1
- PYTHIA, 71
- QCD, 7
- Lagrangian, 7
 - perturbative, 9
- Quadrant (MuTr), 53
- Quantum chromodynamics (QCD), 1, 2, 7
- Quarks, 1, 7
- Reduced azimuthal bending, 154
- Reduced azimuthal bending (dw_{ij}), 84
- Relative luminosity (spin combination), 184
- RHIC, 3, 5
- RHIC (Relativistic Heavy Ion Collider), 37, 38
- RPC (Resistive Plate Chambers), 58
- RPC1, 45
- RPC3, 45, 58
- timing, 95
- RpcDCA, 84
- RpcTime, 84
- Run number, 87
- Running coupling constant, 8
- Sea quarks, 1, 220
- Semi-inclusive DIS (SIDIS), 4
- Siberian snakes, 39
- SIDIS, 4
- Spin asymmetry, 2
- double, 2
 - longitudinal, 5
 - single, 5
 - transverse, 40
- Spin pattern, 38, 58
- Spin rotators, 39
- Spin-1/2, 1
- Splitting functions, 13
- Standard Model, 1, 2
- (non-)Stereo planes (MuTr), 53
- Structure functions, 10, 12, 13, 15, 220, 221
- Stub, 80
- SU(3) (color), 7
- Sum rules
- for unpolarized PDFs, 220
- TOF (BBC), 73
- Tracking, 77
- Bend-plane fitting, 80
 - Kalman fitting, 80
 - Track finding, 80
- Valence quarks, 220
- van der Meer scan, 88
- Vertex
- distribution, 94
- W bosons, 4, 222

INDEX

WTRG(S,N), [69](#)

Yellow beam, [38](#)

Z bosons, [5](#), [222](#)

ZDC (Zero Degree Calorimeter), [43](#), [62](#)